Enhanced Methodologies for Improved Ground Kinematics Interpretation in the Context of Landslide Early-Warning Systems

by

Sohrab Sharifi

A thesis submitted in partial fulfillment of the requirements for the degree of

Doctor of Philosophy

in

Geotechnical Engineering

Department of Civil and Environmental Engineering

University of Alberta

ABSTRACT

Landslides are widespread geohazards in Canada that cause loss of millions of dollars annually directly and indirectly. Such geohazards are prevalent in Canada's landforms which compromise the safe operation of infrastructures and public safety. Not only stabilizing an area with this scale is financially beyond feasible, but many options are also next to insufficient. A reliable risk management strategy would advise to keep observing the ground to ensure the hazard is adequately mitigated. Monitoring programs are therefore becoming indispensable tools and an integrated pillar in the modern practice of geohazards management. Early-warning systems (EWSs) are a robust tool to this end and developing such systems calls for collaborative efforts and scientific exchanges between different fields considering that kinematical inputs into EWSs come from a variety of means of measurements.

Technology has improved landslide monitoring in many aspects by granting high spatio-temporal resolution of readings, millimetric accuracies, (near) real-time acquisition and remote data retrieval. Technology in this context comes with certain limitations as well that impede its further incorporation into EWSs. The quality of received data determines the performance of an EWS and thus effectiveness of mitigative actions. The high sampling rate of some instruments (e.g., Shape-Accel Arrays or GNSS units), subject to the presence of scatter (noise), obscures the true displacement of the ground. As a result, the slope's kinematics will not be fully understood, and the onset of acceleration cannot be simply detected to raise the alarm. Data filtration is then a significant constituent in an EWS yet poorly addressed. In addition to *in-situ* methods of monitoring, remote sensing techniques such as space-borne interferometric synthetic aperture radar (InSAR) are another source of recording ground displacements. InSAR constantly illuminates a footprint by broadcasting microwaves to the ground and records the backscattered waves which can be transformed into displacement values. However, the application of InSAR in landslide monitoring suffers limitations too. SAR sensors are only sighted to displacement along its line-of-sight (LOS). As a result, the velocity map it provides is not a full reflection of the direction and magnitude of movements. The added ambiguity due to this InSAR's limitation prohibits direct incorporation of the results in EWSs. A decomposition of LOS velocity in three dimensions is then necessary. Common decomposition methods are associated with certain assumptions. The reliability of EWSs heavily revolves around the precision of measurements but little insights on the accuracy of these methods exist.

This research aims to devise and pursue methodologies to enhance the kinematics interpretation respecting the present limitations in developing modern EWSs. The first element of this thesis is data analysis in which the simple moving average is compared against Gaussian-weighted moving average and Savitzky-Golay filters. The impact of using each in interpreting the landslide kinematics is studied as well as detecting the onset of acceleration and forecasting failure time using the inverse-velocity method. The second element is dedicated to examining different approaches in decomposing InSAR's LOS velocities: ignoring the northward component, surface-parallel flow method, aspect-parallel flow method and steepest terrain following method. This is carried out by quantifying their accuracy in light of LOS estimations' accuracy and the mathematical impact of assumptions associated with each method. The outcome of this research is expected to assist geoscientists with implementing alternative methodologies in EWSs which leads to an improved reliability by acquiring a more accurate and truthful kinematics of movements.

PREFACE

The present thesis is original research conducted by Sohrab Sharifi, under the supervision of Dr. Michael Hendry and Dr. Renato Macciotta. The structure of the thesis is configured in a paper-based manner with chapters published in peer-reviewed journals. The conference proceedings extracted from this work can be found in the "References" section. The citations of journal papers are as follows corresponding to Chapters 3-6, respectively:

● Sharifi S, Hendry MT, Macciotta R, Evans T, 2022. "Evaluation of filtering methods for use on high-frequency measurements of landslide displacements", *Natural Hazards and Earth System Sciences*, 22(2):411-430. https://doi.org/10.5194/nhess-22-411-2022.

● Sharifi S, Macciotta R, Hendry MT, 2022. "Algorithms to enhance detection of landslide acceleration moment and time-to-failure forecast using time-series displacements", *Engineering Geology*, 106832. https://doi.org/10.1016/j.enggeo.2022.106832.

● Sharifi S, Hendry MT, 2023. "An assessment of surficial velocities by MT-TOPSAR interferometry: Case study of the Oldman River Dam, Alberta, Canada", *Bulletin of Engineering Geology and Environment*, 82(446). https://doi.org/10.1007/s10064-023-03473-0.

● Sharifi S, Macciotta R, Hendry, MT, 2023. "Evaluating topography-based methods in 3D decomposition of InSAR 1D velocities obtained for translational landslides: Thompson River Valley in Canada", *Landslides*, 1:17. https://doi.org/10.1007/s10346-023-02153-0.

DEDICATION

To those who come next that

question,
speculate,
devise,
explain,

and hand it to them who follow.

ACKNOWLEDGEMENTS

Doctoral studies are considered individual research; however, one cannot embark on and accomplish finishing this journey without the help of others. I would like to express my deepest appreciation to my supervisors, Dr. Michael Hendry and Dr. Renato Macciotta. They guided me on research, tutored me on science, and coached me on professionalism. Their insightful feedback and breadth of knowledge shed light on dimensions unchartered to me. Their unlimited patience and unwavering support also let me further explore those dimensions in the hope for buried treasures, awaiting to be unearthed. I also would like to thank the committee members, Dr. Derek Martin, Dr. Albert Liu and Dr. Mustafa Gül as well as other faculty members involved in multiple official and unofficial occasions who graciously spared time and shared their experience with me.

This research could not be conducted without the financial support from (Canadian) Railway Ground Hazards Research Program funded by the Natural Sciences and Engineering Research Council of Canada, Canadian National Railway (CN), Canadian Pacific Railway (CP) and Transport Canada. The assists received from our collaborators, Mr. David Brown from CN and Mr. Danny J. Wong from CP, to accommodate many limitations during field campaigns are much appreciated. Also, special thanks should go to Dr. Huntley and Mr. Rotheram-Clark from the Geological Survey of Canada for providing valuable data and sharing their expertise in remote sensing parts of this research. I am also indebted to the University of Alberta and the many donors who provided me the honour of being awarded multiple scholarships.

My Ph.D. studies gave me opportunities to work closely, seek help, learn from and start friendships with many amazing persons: Akhila Palat, Amir Soltanieh, Chris Bunce, Corey Froese, Danial Behnia, Daxton Dion-Hoffman, Ian Adams, Jennifer Stogowski, Jorge Rodriguez, Kevin

Wallin, Lucas Duerksen, Mahya Roustaie Hossein Abadi, Nima Mirhadi, Parisa Haji Abdulrazegh, Pouya Salem, Prabin Acharya, Reza Mousapour, Saiedeh Fallah Nafari and Vivian Giang.

I would be remiss in not mentioning my family, back home, for their encouragement and belief in me. Thank you Amirhossein, Fatemeh, Mohammad Ebrahim, Salman, Samaneh, Sanaz, and finally my parents, Azar and Mohammad Sharifi who are greatly missed. Lastly, there are no words I can use to express my gratitude to my wonderful wife and lifetime friend, Sara, who amazingly makes the world better by just being herself. She has been all the stabilization I needed against landslides on my path.

TABLE OF CONTENTS

LIST OF TABLES

LIST OF FIGURES

Chapter 1: Introduction

Landslides are widespread natural hazards in Canada. This type of geohazards leads to various levels of damage to the infrastructure, compromising the economic welfare and public safety of Canadians. Figure 1- 1 shows the risk associated with the occurrence of landslides across Canada, colour-coded based on the susceptibility of each point. An adverse combination of slope geometry, weak geological formations, precipitation and permafrost has led to a medium (colour: yellow) to high (colour: red) risk of landslides in the Prairies and southeastern Canada (P. T. Bobrowsky & Dominguez, 2012). Within the past 150 years, the death toll caused by landslides surpasses those caused by other natural hazards in total (Evans 1999). It is estimated that Canada's economy faces a loss of \$200~400 million annually (Clague & Bobrowsky, 2010) with this range increasing to \$281-450 million to address the damages, in Western Canada alone, according to a more recent study (Porter et al., 2019).

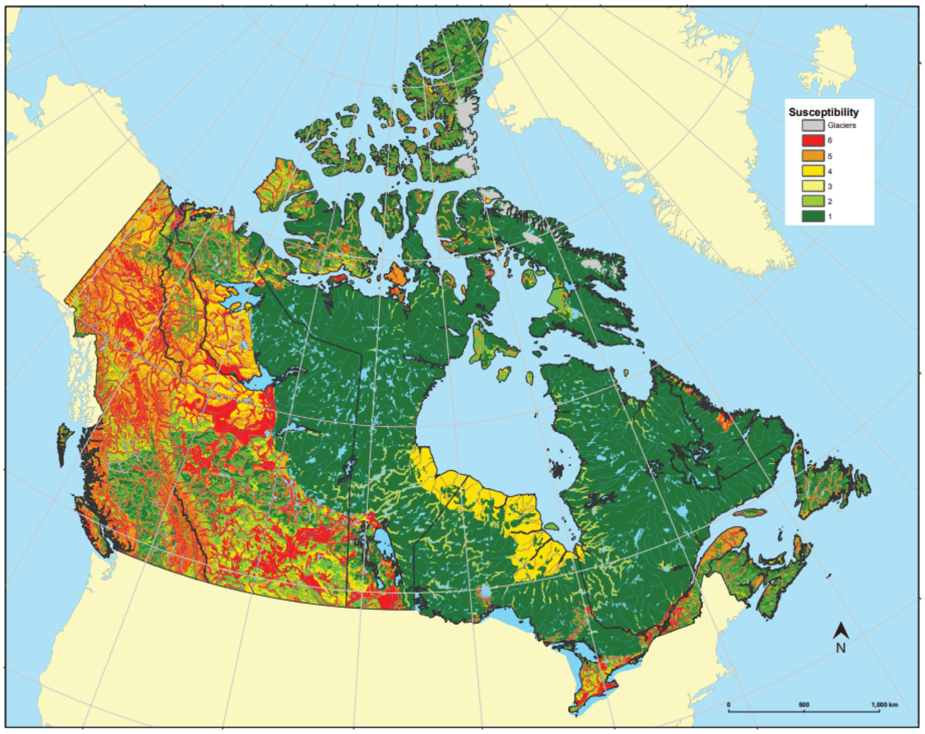

Figure 1- 1. Landslide susceptibility map of Canada (P. T. Bobrowsky & Dominguez, 2012)

Safe and reliable operation of infrastructures carries a high priority in asset management. Linear structures are heavily impacted due to the long nature of the corridor they are embedded within. Alberta Transportation reports about 500 sites traverse landslides. 78% of these cases are categorized as "active" with a significant portion of 60% affecting main provincial highway sectors (Tappenden & Skirrow, 2020). In British Columbia, a highway stretching from Horseshoe Bay to Pemberton hosted 154 landslides from 1856 to 2007 which is responsible for 18% of landslide-related life casualties in that period within Canada (Blais-Stevens & Hungr, 2008). A total of 1277 cases have been documented in a different study along B.C. Highway 99 and Trans-Canada Highway since 1999 (Hungr et al., 1999). Railways are also another linear structure frequently reported to traverse unstable sites. More than 2200 at-risk sites are reported in British Columbia (Hungr et al., 1999). While the exact number of actually affected sites is beyond estimation, managing the damages landslides on railway systems requires $10-18 million annually (Porter et al., 2019). However, the pipeline industry is perhaps the most affected one financially with $205-305 million as a result of leaks, ruptures, re-routing, monitoring and stabilization. Non-linear structures are also impacted by landslide processes and the related mechanisms. The Sainte Marguerite dam in Quebec, Gardiner and Nipawin dams in Saskatchewan, Oldman River and Dunvegan dams in Alberta, and Peace Canyon, Site C, WAC Bennett, Seymour Falls and Cheakamus dams in British Columbia are examples of such in Canada and 153 similar cases also exist in the United States (Jaspar & Peters, 1979; Morgenstern & Simmons, 1982; Sauer, 1984; Houston, 2001; Schuster, 2006; Scammell et al., 2012; Scammell, 2013; Hendry et al., 2019).

Stabilization options are often deemed infeasible as they lead to cost-ineffective, technically insufficient, and/or environmentally harmful solutions. Proactive monitoring strategies instead provide more practical solutions and have become consequently an integrated component of risk management plans. A globally endorsed subset of these strategies is early-warning systems (EWSs). An EWS is defined as a “set of capacities to generate timely and meaningful warning to enable individuals, communities, and organizations to respond appropriately” (International Strategy for Disaster Reduction, 2009). EWSs are fed by measurements coming from various instruments where they are processed, and appropriate warnings will be issued based on the severity of the anticipated risk. In an attempt to increase efficiency, an EWS should be automated to an extent that the reliability of alarms is not impacted. This, however, is challenging considering that characteristics of the fed data span a whole wide spectrum in terms of spatio-temporal frequency as well as measurement precision. The rapid advancement of technologies in recent decades has been advantageous to enrich the collected datasets respecting the volume of measurements.

1.1. Problem Statement

The integration of novel techniques within an EWS should be associated with a comprehensive understanding of the mechanism of data collection and traits of yielded output. This calls for higher involvement of geoscientists with other fields such as data analysis and remote sensing. The first challenge is minimizing the scatter in time-series displacements. Raw readings from electronic devices are characterized by volatility and rapid variations, which is referred to as “scatter” herein after. Figure 1- 2 shows an example of displacement readings reported by a positioning system (Geocube) before and after filtration. Numerous studies reported the use of such scatter-contaminated readings. However, the data management and data analysis methodologies are frivolously treated. A rudimentary filter called simple-moving average (SMA) is frequently employed with no apparent reason but simplicity. In addition, the filtration intensity seems to be often chosen arbitrarily with no in-depth understanding of how it affects the perceived kinematics. This lack of knowledge of SMA's performance becomes even more crucial in determining the moment of onset of acceleration or forecasting the failure time.

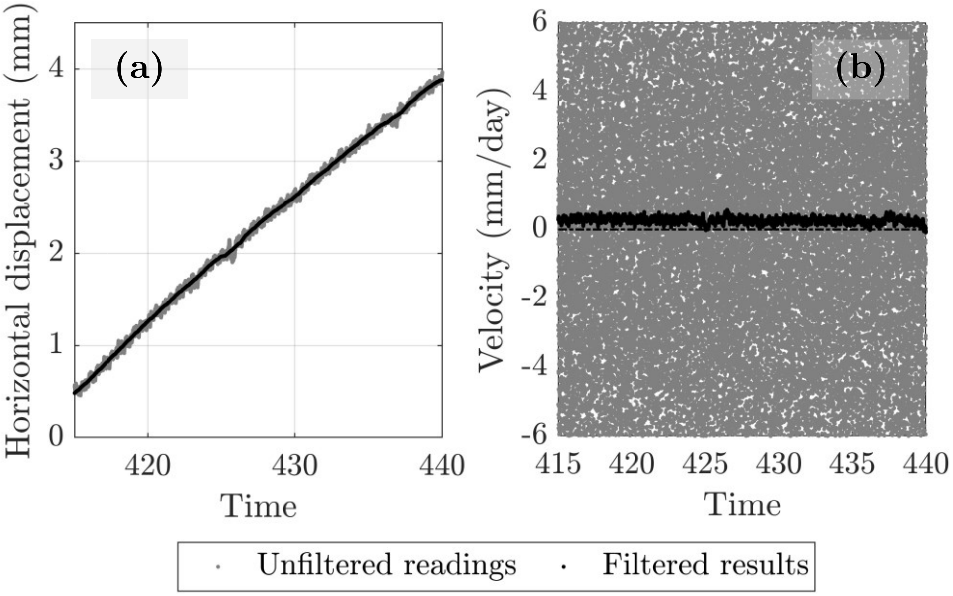

Figure 1- 2. Impact minimizing scatter in displacement readings on the velocity values (NOTE: data is realistic and collected by a Geocube unit on Ten-mile landslide, Sharifi, Hendry, Macciotta, et al., 2022)

In-situ observations have been augmented by data provided through remote sensing methods such as interferometric synthetic-aperture radar (InSAR). It has been well-received in recent decades because of relatively lower associated costs and efforts than in-situ means of monitoring. InSAR is an all-day all-weather sensor that covers a wide area with an acceptable temporal sampling frequency, but it is associated with limitations as well. The SAR sensor is only capable of sensing displacements along a line aiming at the target (scatterer), called line-of-sight (LOS). This leads to a counter-intuitive way of demonstrating 3D movements in 1D. 1D LOS measurements prohibit determining the true magnitude and direction of velocities which complicates their application in an EWS. Decomposing LOS velocities is an ill-posed problem with more unknowns (3 velocity components) than knowns (2 LOS velocities from different satellite orbits). As a result, additional mathematical assumptions are required to successfully decompose LOS velocities in 3D. Within this process, the main obstacle is the lack of an established mathematical methodology with documented accuracy. Many previous researchers have adopted a simplified approach which simply ignores the South-North velocity component given the near-polar orbit of SAR satellites. This suggestion seems to be a pragmatic solution rather than a scientific approach. It implies no movements along the South-North direction which does not agree with reality of landslide movements in a general case.

1.2. Research Objectives

Corresponding to the knowledge gaps discussed above, this study aims to investigate methodologies to determine an enhanced interpretation of the landslides kinematics which directly benefit EWSs. A higher-level category of objectives of this study corresponds to the following elements: data analysis and InSAR. The specific objectives of this study are as follows with the first two associated with data analysis and the remainder associated with InSAR:

1. Investigating the impact of using SMA on the interpreted kinematics and compare its performance against two other filters, Gaussian-weighted moving average (GWMA) and Savitzky-Golay (SG);
2. Investigating the effect of using the above filters on detecting the onset of acceleration moment and forecasting failure time using the inverse-velocity method;
3. Measuring the combined precision of InSAR velocity estimations by ignoring the northward velocity component (simplifying assumption), combined with InSAR's inherent uncertainties;
4. Evaluating other decomposition methods which enforce a relationship between velocity components based on the ground geometry (topography-informed methods).

1.3. Overview of Methodology

1.3.1. Sufficiency of Scatter Filters (Objectives 1 and 2)

1.3.1.1. Approach 1: Numerical Analysis of Synthetic Database

The filtration process is associated with the execution of a mathematical operation. Different filters employ different kernels such as averaging, weighted averaging or linear regression. This inevitably leads to different filtered results and a quantitative comparison of their performance is not possible because the true trend of displacements is not known. A framework called "Numerical Analysis of Synthetic Database" is here developed accordingly. It attempts to create scattered displacements which resemble the raw readings an EWS receives directly from instruments. This framework starts by generating a series of known trends, called "scenario", inspired by the regular trends reported in the literature. The variation of the methodology to reach objectives 1 and 2 is the type of generated scenarios. For the latter, accelerating and failing trends are considered while harmonical trends are mostly considered for objective 1. The scatter, randomly generated, is then added to the scatter-free scenarios at different variability levels which are later filtered using SMA, GWMA and SG at different filtration intensities. Considering the availability of true trends, it is now feasible to evaluate the behaviour of each filter in interpreting the kinematics by calculating the error.

1.3.1.2. Approach 2: Analysis of Documented Landslides

The second approach is applying the filters to the displacement of documented landslides. Although the true scatter-free trend is still unknown, examining the filtered results can provide further support to the first approach. The significant criteria of filter rating are to what degree the application of each filter underrepresents the kinematics while minimizing the volatility, measurement lags, sensitivity to filtration intensity, and success toward outliers as well. The ten-mile landslide, located in southwestern British Columbia is chosen for this purpose as several positioning devices, called "Geocube", are installed at this location. Please refer to "Section 3.3" for further background information on this site. For objective 2, 17 datasets from 9 failed cases are gathered from the literature which correspond to various physical dimensions, geological settings, triggering factors and means of monitoring. For further information on these datasets, please refer to "Section 4.3". Given that the actual failure time is known, it is possible to calculate the error in forecasting such a moment upon employing SMA, GWMA and SG.

1.3.2. Precision of InSAR Decomposition by Simplifying Assumption (Objective 3)

Two sources of uncertainty are considered for InSAR-evaluated kinematics: inherent InSAR precision along LOS and the simplifying assumption (ignoring the northward component). The impact of the latter is studied through the mathematical configuration of LOS projection. Eq. 1. 1 states how true components of ground velocity at vertical (V_V), Eastward (V_E) and Northward (V_N) can be used to calculate LOS velocity using the geometry of acquisition:

$$\begin{pmatrix} \mathrm{V}_{\mathrm{LOS}_{\mathrm{Asc}}} \\ \mathrm{V}_{\mathrm{LOS}_{\mathrm{Des}}} \end{pmatrix} = \begin{bmatrix} \cos\theta_{\mathrm{Asc}} & -\sin\theta_{\mathrm{Asc}}\cos\alpha_{\mathrm{Asc}} & \sin\theta_{\mathrm{Asc}}\sin\alpha_{\mathrm{Asc}} \\ \cos\theta_{\mathrm{Des}} & -\sin\theta_{\mathrm{Des}}\cos\alpha_{\mathrm{Des}} & \sin\theta_{\mathrm{Des}}\sin\alpha_{\mathrm{Des}} \end{bmatrix} \begin{pmatrix} \mathrm{V}_{\mathrm{V}} \\ \mathrm{V}_{\mathrm{E}} \\ \mathrm{V}_{\mathrm{N}} \end{pmatrix}, \qquad (1.\ 1)$$

where *Asc* and *Des* subscripts attribute the parameter to the ascending and descending orbits, and θ and α are the side-looking angle of sensor and satellite trajectory as shown in Figure 1- 3. Reducing the velocity vector dimension to ignore V_N leads to Eq. 1. 2:

$$\begin{pmatrix} \mathrm{V}_{\mathrm{LOS}_{\mathrm{Asc}}} \\ \mathrm{V}_{\mathrm{LOS}_{\mathrm{Des}}} \end{pmatrix} = \begin{bmatrix} \cos\theta_{\mathrm{Asc}} & -\sin\theta_{\mathrm{Asc}}\cos\alpha_{\mathrm{Asc}} \\ \cos\theta_{\mathrm{Des}} & -\sin\theta_{\mathrm{Des}}\cos\alpha_{\mathrm{Des}} \end{bmatrix} \begin{pmatrix} \mathrm{V}_{\mathrm{v}} \\ \mathrm{V}_{\mathrm{e}} \end{pmatrix}, \qquad (1.\ 2)$$

where V_v and V_e are new estimated components following the simplifying assumption. Equating the left-hand sides of Eqs. 1. 1 and 1. 2 leads to the equations that can be leveraged in calculating the error of ignoring V_N. For further information on the procedure, please refer to Appendix B in Chapter 5. The second source of uncertainty is InSAR's ability to track the movements of targets on the ground based on the received backscattered energy of microwaves. Eq. 1. 3 presents the LOS precision of targets as a function of reflectivity (γ – also called "coherence"):

$$\text{Precision}=\frac{\lambda}{4\pi}\sqrt{\frac{1-\gamma^2}{2\gamma^2}}, \tag{1. 3}$$

where λ is the typical microwave length which is about 5.5 cm for a typical SAR sensor operating at the C-band range of microwaves. The chosen study for this objective is Oldman River Dam, located in southern Alberta. Please refer to "Section 5.2" for further information.

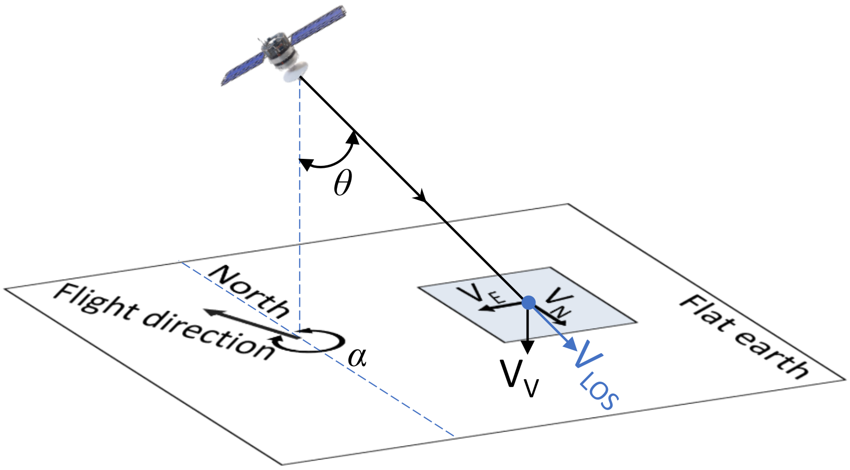

Figure 1- 3. Geometry of acquisition, featuring θ (side-looking or incidence angle) and α (trajectory or heading angle)

More than 200 SAR scenes are processed and then, the LOS precision as quantified by Eq. 1. 3 is added to and subtracted from the LOS matrix in Eq. 1. 2. Given that the direction of movements is governed by the geological structure, the error induced by ignoring V_N was compensated which finally leads to the calculation of combined precision.

1.3.3. Evaluating Topography-Informed Decomposition Methods (Objective 4)

As Eq. 1. 1 suggests, there are 3 unknowns (velocity components in 3D) and two knowns (LOS velocities from ascending and descending orbits). This system of equations is under-determined and simplifying assumption resolves it by reducing the unknowns. An alternative approach is adding to the knowns by enforcing a relationship between components. The surficial geometry of the ground has been a source of inspiration to this end. Eqs. 1. 4-1. 6 which are called the Surface-Parallel Flow Method, Aspect-Parallel Flow Method and Steepest-Terrain Following Method, respectively:

$$V_V = V_E i_E + V_N i_N, \tag{1. 4}$$

$$V_E = V_N \tan\beta, \tag{1. 5}$$

$$V_V = V_E i_E + V_N i_N \text{ AND } V_E = V_N \tan\beta, \tag{1. 6}$$

where i_E and i_N are elevation gradients in eastward and northward directions, respectively and β is the aspect angle of each point on the ground. To reach objective 4, more than 400 SAR scenes archived over Thompson River Valley by Canadian Radarsat-2 (U5 and U21 beams in descending orbit), and European Sentinel-1 (ascending and descending orbits) are analyzed. This corridor carries a significant financial and environmental significance that is compromised by several slow-moving landslides with a record of 9 historic failures. Please refer to "Section 6.2" for more information. 3GPS devices installed on the Ripley landslide can facilitate reaching objective 4. First, InSAR analysis of multiple combinations of SAR stacks mentioned earlier is carried out. The decomposition by topography-informed assumptions is then conducted. Having the GPS measurements, the performance of decomposition methods is examined in terms of interpreting the magnitude and direction of velocity vectors.

1.4. Thesis Outline

The presented thesis is organized into seven chapters. The following provides a summary of what each subsequent chapter presents:

- *Chapter 2* includes a brief overview of the previous studies corresponding to data analysis and InSAR elements of this thesis.
- *Chapter 3 (paper #1)* presents the mathematical framework which is the Numerical Analysis of Synthetic Database using 12 different kinematics scenarios. The results of the application of SMA, GWMA and SG to the Ten-mile landslide displacements as reported by Geocubes are also presented in this chapter. The implication of each filter on the trend distortion, induced lag, fidelity to the true trend, handling outliers and underrepresentation of ground kinematics are discussed in the context of real-time monitoring. Furthermore, this chapter contains practical suggestions for selecting the filtration intensity.
- *Chapter 4 (paper #2)* builds upon the framework discussed in Chapter 3 to specifically weigh the advantages and disadvantages of each filter at/near critical points: onset of acceleration (OOA) and failure. Using appropriate scenarios, the reliability of each in detecting OOA is probabilistically assessed as well as the error in forecasting the failure time. Additionally, this chapter discusses the accuracy of each filter in forecasting the failure time of 9 case histories if they were applied in real-time.
- *Chapter 5 (paper #3)* first provides historical background on Oldman River Dam until 2015 and proceeds to present the InSAR results. The analysis continues by analyzing the error of simplifying assumption, InSAR's LOS error, and finally calculating the combined precision by taking into account both sources of uncertainty. This chapter also identifies an active area on the embankment and then concludes with a discussion on the mechanism of instabilities.

- *Chapter 6 (paper #4)* demonstrates how SPFM, SPFM coupled with the Least-Squares Method, APFM and STFM achieve the decomposed vectors of velocity. This is carried out by comparing the magnitude and geometry of interpreted vectors quantitatively against those shown by GPS devices on the Ripley landslide. This chapter continues to provide mathematical justification for the observed trends using novel methods developed in this study for the first time.
- *Chapter 7* collates the significant concluding remarks from previous chapters and brings this thesis to a close by introducing ideas for future follow-up studies.

Chapter 2: Literature Review

This chapter presents a summary of the background information and published literature regarding both data analysis and InSAR elements of this thesis. A more comprehensive review could be found in the appropriate chapters, specific to each objective. The following sub-chapters address the following:

- The necessity of scatter filtration and various filters used to this end; and
- Different methods to decompose InSAR's LOS velocities.

2.1. Scatter Filtration

The data reported by modern means of monitoring are often contaminated by scatter and the occurrence is beyond control. These unfavourable interferences can be caused by the external environment such as the atmosphere, or the quality of communicating signals due to the perturbation of electronic connections, power sources or other electro-magnetic instruments in the proximity (L. Li, 2011; G. Wang, 2011). Scatter is populated around the "true" displacement trend, such that the average separation is zero. A scatter set also has a finite and constant standard deviation through time. Several previous studies highlighted the impact of scatter on the quality of deductions and issues it can impose on the reliability of monitoring systems such as EWSs (Husaini & Ratnasamy, 2001; Intrieri et al., 2012; Michoud et al., 2013; Intrieri et al., 2017; Tan et al., 2020; Thirugnanam et al., 2020). As a result, the scatter should be reduced as much as possible without distorting the true displacement trends which filtration algorithms aim to achieve.

Scatter minimization can be either performed on the frequency or time domain. The former is typically conducted using the fast Fourier transform (FFT) that aims to find the frequency content of a signal. FFT extracts the frequency content of a signal and by excluding frequencies outside of a certain boundary, scatter filtration can be achieved. However, very raw values of voltage signals are required to follow this approach. This opportunity is not always provided by most instrument manufacturers. Even so, the existence of other external factors such as air temperature and pressure make scatter filtration problematic in this way. Additionally, one level of filtration (e.g., Kalman) is usually already applied and the received scatter in displacements is the residual of this initial filtration which along with previous reasons rejects the suitability of Fourier transform in this context. Additionally, information is provided at discrete frequency steps which calls for interpolation techniques for frequencies in between (Henry, 2022). Non-stationary and non-periodic data (such as displacement or velocity) are also not appropriate to be filtered by FTF (Karl, 1989; Yoshizawa et al., 2011), but if one can manage even to transform the measurements to stationary, it is computationally intensive to transform back and forth for substantial amount of data as is the case for robust monitoring systems. As opposed to this, a short-term Fourier Transformation has been adopted which makes the selection of window time extremely complicated (Kehtarnavaz, 2008). FTF has also a drawback when it comes to finite signals and the energy leaks from adjacent frequency bins that leads to a challenging decision on the filtration frequencies to be filtered out as one small variation leads to a different filtered kinematics (Harris, 1978). Finally, limited applications of using FTF in the landslide community, especially among geotechnical engineers, is a cause of concern in validating the filtered results while others such as filters that work in time domain are well-incorporated into the current practice and the applications in the literature are numerous (Sharifi et al., 2021). Interested readers may refer to the following studies for further information: Duhamel & Vetterli (1990), Luck (2014) , Rajaby & Sayedi (2022).

Filters that work on the time domain often work on a window-basis, meaning that they repeatedly perform an operation point-by-point as an imaginary window slides across the dataset. The mathematical operations executed in this window can be classified as recursive, kernel, or regression filters. Recursive filters, such as the exponential filtering function, calculate the filtered value at a given time based on the previous filtered value. Kernel filters, which include simple moving average (SMA – Eq. 2. 1) and Gaussian-weighted moving average (GWMA – Eq. 2. 1), calculate the filtered values as the weighted average of neighbouring measurements:

$$\widehat{y}_i = \sum_{i-\frac{p-1}{2}}^{i+\frac{p-1}{2}} w_j y_j, \qquad (2.\ 1)$$

where y_j is the jth raw measurement in the sliding window, $\widehat{y}_i$ is the filtered value at ith data and w_j is the weight coefficient. The SMA's weight coefficient is identical for all points in the filtration window. It means that the weighted averaging simplifies into a simple averaging which leads to the same contribution of all points to the filtered value. The GWMA's weight coefficient on the other hand follows its namesake distribution, Gaussian.

Out of GWMA and SMA, the latter is frequently used in the literature largely due to its simplicity (Dick et al., 2015; Macciotta et al., 2016; Carlà, Farina, et al., 2017; Carlà, Intrieri, et al., 2017; Macciotta, Rodriguez, et al., 2017; Bozzano et al., 2018; Carlà et al., 2018; Intrieri et al., 2018; Kothari & Momayez, 2018; Carlà et al., 2019; M. Chen & Jiang, 2020; X.-P. Zhou et al., 2020; Grebby et al., 2021; Y. Zhang, Ma, et al., 2021; Y. Zhang, Tang, et al., 2021; Desrues et al., 2022). Regression filters, another category of filters, calculate the filtered values employing regression analysis on unfiltered values (e.g., Savitzky-Golay, or SG) (Savitzky & Golay, 1964; Cleveland, 1979, 1981; Cleveland & Devlin, 1988; Reid et al., 2021). SG could be transformed into a kernel filter (Appendix 3.A) but the distribution of weight values would be different. Carlà, Intrieri, et al. (2017) applied SMA and exponential filtering to multiple failed landslide cases and concluded the latter is inferior in terms of accuracy of forecasting failure time. On the other hand, Carri et al. (2021) cautioned the designers and users of EWSs against the use of SMA when rapid movements are expected. Published applications of filters other than SMA for landslide monitoring are scarce, and studies dedicated to comparing the functionality of those to that of SMA are limited.

2.2. InSAR LOS Decomposition Methods

Interferometric synthetic-aperture radar (InSAR) is a space-borne earth observation method that uses satellite imagery for applications ranging from fault characterization (B. Smith & Sandwell, 2003) and volcano monitoring (Di Traglia et al., 2021) to mapping subsidence (Motagh et al., 2017; Khorrami et al., 2020; J. Hu et al., 2022) and landslide displacements (X. Liu et al., 2021; Y. Wang et al., 2021). InSAR yields only part of movements which are along the sensor's line-of-sight (LOS). This added ambiguity results in a less intuitive understanding of the kinematics of a landslide (Samsonov et al., 2013; Shi et al., 2018; Cenni et al., 2021). Schlögl et al. (2022) underlined that the incorporation of InSAR into EWSs faces several obstacles. One problem is setting alarm thresholds for regions with several landslides moving at different rates and directions which questions the sufficiency of LOS estimations. Ng et al. (2012), Samsonov et al. (2013), Khorrami et al., (2020), Ma et al. (2021), Chen et al. (2022) and many others suggest ignoring northward component (simplifying assumption) due to the near-polar orbit of satellites (8-10° variance). Although studies adopting this technique are numerous, there are no studies to evaluate the error induced in other components of movements upon ignoring northward. Those who also attempted to quantify the error, like Fuhrmann & Garthwaite (2019), only achieved to express it relative to LOS error without actually quantifying the LOS error. This assumption is most reasonable for phenomena with no significant northward movements, such as ground subsidence or landslides mainly sliding toward east or west. As a result, implications of exercising such assumption should be carefully investigated for other cases.

Others have instead pursued different approaches when the northward component is sizable. Additional information can be incorporated from other variants of SAR analysis, external sources, or an *a priori* deformation model. The first group includes methods such as pixel offset tracking (Shi et al. 2018; Wang et al. 2018) and multi-aperture InSAR (Jo et al., 2017), which intend to determine the velocity along the direction orthogonal to the LOS (i.e., azimuth). However, these methods are less accurate than regular InSAR (on the centimetric order), time-consuming to run, very sensitive to decorrelation, and not as applicable to slow-moving landslides with dim reflectivity (Bechor & Zebker, 2006; Simons & Rosen, 2007; Eriksen et al., 2017; Shi et al., 2018). In the second category of methods, external sources such as *in situ* instruments, mostly GNSS/GPS units, are used to infer 3D movements (Samsonov & Tiampo, 2006; Samsonov et al., 2007; W. Zhu et al., 2014). This approach also faces several challenges including the shortfall of these units in terms of both quantity and uniform spatial distribution, which significantly limits the study area and requires the use of advanced mathematical techniques during post-processing stages (Hu et al. 2014). Finally, the last approach is employing an *a priori* deformation model, which involves exercising compatibility assumptions between the presumed failure kinematics and the calculated 3D velocity vectors. The used compatibility model includes the use of surficial geometry of the terrain and, thus, they are referred to as "topography-informed" assumption. Surface-Parallel Flow Model (SPFM), first introduced by Joughin et al. (1998) and used by others (Sun et al., 2016; Ao et al., 2019; Samsonov et al., 2020; X. Liu et al., 2021; Ren et al., 2022), assumes the velocity components follow the topography as follows (Eq. 2. 2):

$$V_V = i_E V_E + i_N V_N, \tag{2.2}$$

where H is the topography elevation, and i_E and i_N represent the elevation gradients in the eastward and northward directions, respectively. SPFM can be mathematically adjusted to only prompt one LOS geometry, hereafter referred to as Steepest Terrain Following Model (STFM), which has been adopted in previous studies as well (Bianchini et al., 2013; Herrera et al., 2013; Journault et al., 2018; Yi et al., 2022). The last approach proposed to interpret 3D vectors is by dictating the velocity to follow the terrain's aspect, here called the Aspect Parallel Flow Model (APFM), which has been employed by Y. Zhu et al. (2022) and Soltanieh & Macciotta (2022a, 2022b).

Chapter 3: Evaluation of Filtering Methods for Use on High-frequency Measurements of Landslide Displacements

---

Contributions of the Ph.D. Candidate

The material presented in this chapter, including the literature review, conceptualization, methodology development, analysis, draft preparation and revisions, are conducted by the Ph.D. candidate. The supervisors, Dr. Michael Hendry and Dr. Renato Macciotta, have reviewed all pieces presented in the published manuscript, cited below:

Sharifi S, Hendry MT, Macciotta R, Evans T, 2022. “Evaluation of filtering methods for use on high-frequency measurements of landslide displacements”, *Natural Hazards and Earth System Sciences*, 22(2):411-430. https://doi.org/10.5194/nhess-22-411-2022.

Contributions of This Chapter to the Overall Study

Evaluating the performance of scatter filters calls for a knowledge of true trends of kinematics which is not provided in the received measurements by means of monitoring. A framework is introduced in this chapter to address this gap which involves generating scattered trends resembling the raw data. To assure its flexibility, the scatter set is scaled at 6 various levels, and superimposed on 12 kinematics scenarios which are iteratively generated corresponding to 10 scales of monitoring periods. 3 filters – SMA, GWMA and SG – are applied to the synthetic database at various intensities. The error in interpreting the velocity of trends were then calculated to cast light on advantages and disadvantages of these filters. To minimize the lag in the filtered results caused by real-time nature of simulations, a chart is presented which examines the Geocube data received from the Ten-mile landslide. The developed methodology and findings in this chapter deliver the objective #1.

Abstract

Displacement monitoring is a critical control for risks associated with potentially sudden slope failures. Instrument measurements are, however, obscured by the presence of scatter. Data filtering methods aim to reduce the scatter and therefore enhance the performance of early warning systems (EWSs). The effectiveness of EWSs depends on the lag time between the onset of acceleration and its detection by the monitoring system, such that a timely warning is issued for the implementation of consequence mitigation strategies. This paper evaluates the performance of three filtering methods (simple moving average, Gaussian-weighted moving average, and Savitzky-Golay), and considers their comparative advantages and disadvantages. The evaluation utilized six levels of randomly generated scatter on synthetic data as well as high-frequency global navigation satellite system (GNSS) displacement measurements at the Ten-mile landslide in British Columbia, Canada. The simple moving average method exhibited significant disadvantages compared to the Gaussian-weighted moving average and Savitzky-Golay approaches. This paper presents a framework to evaluate the adequacy of different algorithms for minimizing monitoring data scatter.

Keywords: Landslide; Early Warning System; Scatter; Filter; Gaussian-Weighted Moving Average, Savitzky-Golay.

3.1. Introduction

Landslides are associated with significant losses in terms of mortality and financial consequences in countries all over the world. In Canada, landslides have cost Canadians approximately $10 billion since 1841 (Guthrie, 2013) and more than $200 million annually (Clague & Bobrowsky, 2010). Essential infrastructure, such as railways and roads that play vital roles in the Canadian economy, can be exposed to damage if it transverses landslide-prone areas. Attempting to completely prevent landslides is typically infeasible, as stabilizing options and realignment may be cost-prohibitive or lead to environmental damage. This accentuates the significance of adopting strategies that require constant monitoring to mitigate the consequences of sudden landslide collapses (Vaziri et al., 2010; Macciotta & Hendry, 2021).

In recent years, detailed studies have addressed the use of early warning systems (EWSs) as a robust approach to landslide risk management (Intrieri et al., 2012; Thiebes et al., 2014; Atzeni et al., 2015; Hongtao, 2020) . The United Nations defines an EWS as "a chain of capacities to provide adequate warning of imminent failure, such that the community and authorities can act accordingly to minimize the consequences associated with failure" (International Strategy for Disaster Reduction, 2009). Although an EWS comprises various components acting interactively, the core of its performance relies on its ability to detect the magnitude and rate of landslide displacement (Intrieri et al., 2012). Given that the timely response of an EWS determines its effectiveness, an accurate sense of landslide velocity and acceleration is necessary. Monitoring instruments able to provide real-time or near real-time readings such as global navigation satellite systems (GNSSs) and some remote sensing techniques are, satisfactory for this purpose (Yin et al., 2010; Tofani et al., 2013; Benoit et al., 2015; Macciotta et al., 2016; Casagli et al., 2017; Chae et al., 2017; Huntley et al., 2017; Rodriguez et al., 2017; Intrieri et al., 2018; Journault et al., 2018; Rodriguez et al., 2018; Carlà et al., 2019; Deane, 2020; Rodriguez et al., 2020; Woods et al., 2020, 2021). These instruments can record the displacement of locations at the surface of the landslide with a high temporal resolution, which allows the monitoring system to track movements on the order of a few millimeters per year. In practice, the results are usually obscured by the presence of scatter, also known as noise, and outliers that affect the quality of observations. These unfavorable interferences do not reflect the true behavior of the ground motion and stem from sources such as the external environment and the quality of the communication signals and wave propagation in the case of remote sensing techniques (G. Wang, 2011; Carlà, Intrieri, et al., 2017).

Scatter can be defined as measurement data that are distributed around the "true" displacement trend, such that the average difference between the scatter and the displacement trend is zero and has a finite standard deviation. Scatter in displacement measurements can significantly impact the evaluation of slope movements performed on unfiltered data and decrease the reliability of an EWS. This can lead to false warnings of slope acceleration or unacceptable time lags between the onset of slope failure and its identification, and therefore a loss of credibility for an EWS (Lacasse & Nadim, 2009). As a result, scatter should be reduced as much as possible without removing the true slope displacement trends. The application of algorithms that work as filters aims to minimize the amplitude of measured scatter around the displacement trend.

Several approaches have been proposed to filter displacement measurements based on either the frequency or time domain. Fourier and wavelet transformations aim to find the frequency characteristics of the data, then attenuate or amplify certain frequencies. These approaches are discussed in Karl (1989), who suggests they are generally unsuitable for non-stationary data such as monitoring data time series. Filters that work on the time domain can be classified as recursive, kernel, or regression filters. Recursive filters, such as the exponential filtering function, calculate the filtered value at a given time based on the previous filtered value. Kernel filters, which include simple moving average (SMA) and Gaussian-weighted moving average (GWMA), calculate the filtered values as the weighted average of neighboring measurements. Of these two kernel filters, SMA is frequently used in the literature largely due to its simplicity (Dick et al., 2015; Macciotta et al., 2016; Carlà, Farina, et al., 2017; Carlà, Intrieri, et al., 2017; Macciotta, Rodriguez, et al., 2017; Bozzano et al., 2018; Carlà et al., 2018; Intrieri et al., 2018; Kothari & Momayez, 2018; Carlà et al., 2019; M. Chen & Jiang, 2020; X.-P. Zhou et al., 2020; Grebby et al., 2021; Y. Zhang, Tang, et al., 2021; Y. Zhang, Ma, et al., 2021; Desrues et al., 2022). Regression filters calculate the filtered values by means of regression analysis on unfiltered values (e.g., Savitzky-Golay, or SG) (Savitzky & Golay, 1964; Cleveland, 1979, 1981; Cleveland & Devlin, 1988; Reid et al., 2021). Carlà, Intrieri, et al. (2017) studied both SMA and exponential filtering on multiple failed landslide cases and concluded the latter is inferior in terms of accuracy of failure time prediction. On the other hand, Carri et al. (2021) cautioned the designers and users of EWSs against the use of SMA when rapid movements are expected. However, published applications of filters other than SMA for landslide monitoring are scarce, and studies dedicated to comparing the functionality of other filters to that of SMA are limited.

This paper presents an approach to detect and remove outliers, evaluates the performance of three filters (SMA, GWMA, and S-G), and assesses their suitability to be utilized in an EWS. We evaluated three filters against the following criteria: 1) scatter is minimized, 2) true underlying displacement trends are kept with as little modification as possible, and 3) filtered displacement trends detect acceleration episodes in a timely manner. Moreover, the paper investigates the significance of the time lag between a landslide acceleration event and its identification by a monitoring system for the three filters evaluated.

3.2. Methodology

3.2.1. Synthetic Data Generation

A numerical analysis on a synthetic dataset approach was adopted, which consists of synthetic dataset scenarios generated to resemble typical landslide displacement measurements, including acceleration and deceleration periods. These scenarios are idealizations based on observations of typical landslide displacements published in the literature (Leroueil, 2001; Intrieri et al., 2012; Macciotta et al., 2016; M. B. Schafer, 2016; Carlà, Farina, et al., 2017; Scoppettuolo et al., 2020). A total of 12 dimensionless scenarios were built, with all data between the coordinates x=0, y=0 and x=1, y=1. The x value represents time, and normalization between 0 and 1 allows for extrapolation of the findings for variable displacement measurement frequencies (e.g., the full range of x could represent a week, a month, a year). The analysis of synthetic data focuses on the ability of different algorithms to minimize scatter and identify changes in measured trends; therefore, y represents any of the displacement measurement metrics of interest, e.g., displacement, cumulative displacement, velocity, inverse velocity, etc. Mathematical equations and graphical illustrations of the 12 scenarios are shown in Figure 3- 1.

Nine of the scenarios are referred to as harmonic scenarios, which are characterized by gradual changes in the trend of parameter y. The remaining three scenarios show sudden variations at or near x=0.5, and are referred to as instantaneous scenarios. Considering the discrete nature of instrument measurements, and to account for different ranges in measurement frequencies, each scenario was generated several times, each time with a different number of points (Table 3- 1). The next step was adding random scatter to the scenarios to represent unfiltered displacement measurements. Macciotta et al. (2016) show the scatter in displacement monitoring for a GNSS used in their analyses fitted a Gaussian distribution. We validated the scatter distribution fit approximates a Gaussian distribution for the displacement data scatter of the case study in this paper. This assumption, however, has an underpinning theoretical base established by the central limit theorem in probability theory. It states that the mathematical summation of independent variables (such as scatter) goes toward a Gaussian distribution (S. W. Smith, 2013). As a result,

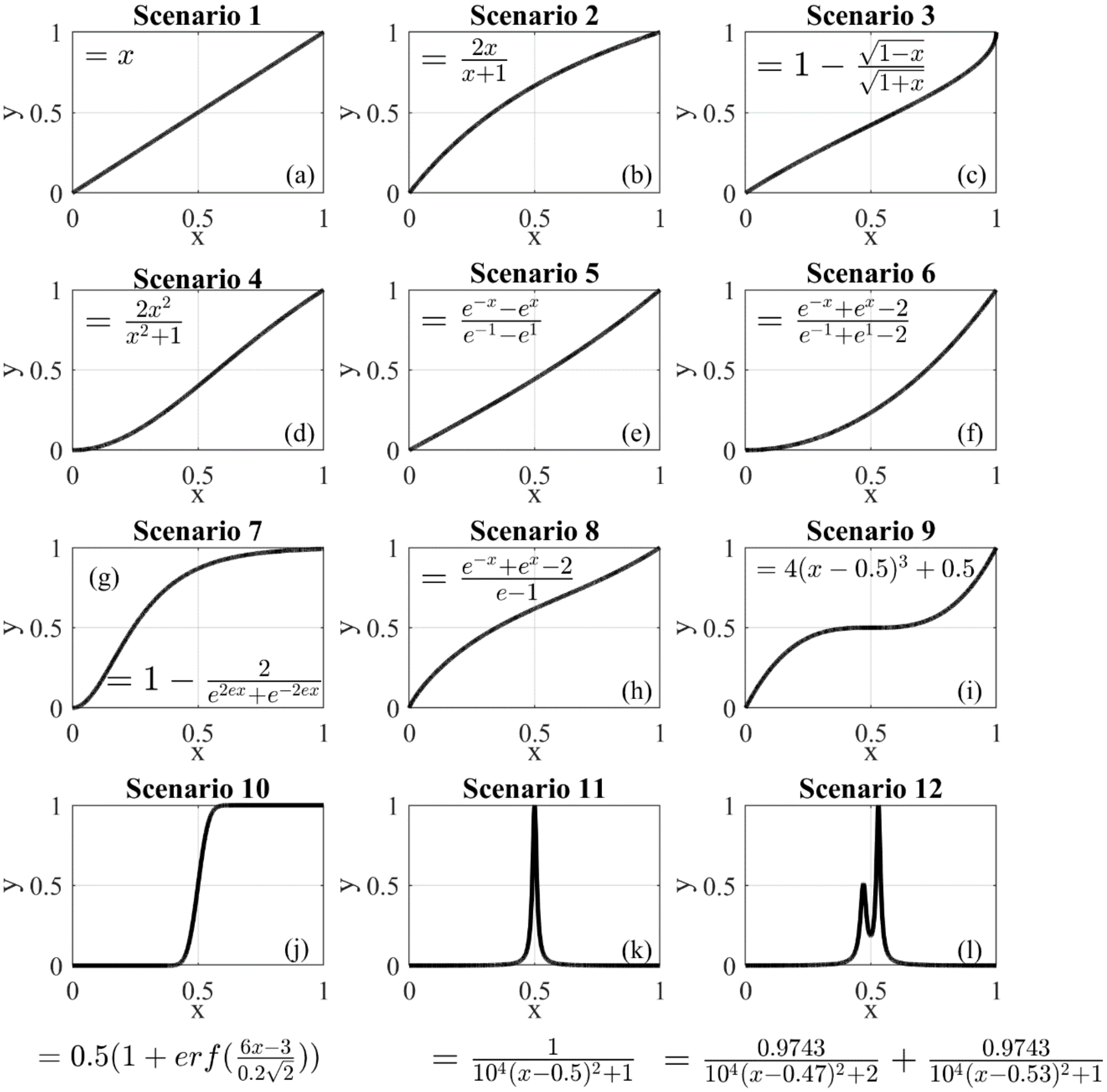

Figure 3- 1. Configuration of all synthetically generated scenarios

the scatter was randomly produced from a normal distribution centered at zero, with extreme values truncated between −1 and 1 and a standard deviation of 0.20. Random generation of the scatter followed the techniques outlined in Clifford (1994) known as the acceptance-rejection method, which generates scatter values through a series of iterations until the algorithm generates the initial normal distribution. The amplitude of the scatter around the trend in parameter *y* was defined for each scenario by scaling the randomly generated scatter. This allowed for the investigation of the effect of different scatter magnitudes on the performance of the filters. Scaling was done by defining the ratio *n/t,* which is the ratio of scatter amplitude (maximum deviation around the trend, termed *n*) to the range of values of the trend (*t*) in each scenario. Six levels of *n*/*t* (0.001, 0.005, 0.010, 0.050, 0.100, and 0.150) were considered when performing the analysis to cover a range of possible levels of scatter in unfiltered measurements. Figure 3- 2 shows two samples of synthetic unfiltered scenarios that are the result of superimposing scatter with *n/t* values of 0.05 and 0.10, respectively, on scenario No. 7.

Table 3- 1. Number of points used to generate scenarios and examples of their corresponding time spans represented by the range of x from 0 to 1, if the measurement frequency is known (1-h and 1-m readings for illustrative purposes)

Number of points	Example monitoring frequency			
	1-h readings		1-m readings	
1000	41.7	Days	16.7	Hours
3000	4.1	Months	2.1	Days
9000	1.0	Years	6.3	Days
20000	2.3	Years	2.0	Weeks
40000	4.6	Years	4.0	Weeks
86000	9.8	Years	2.0	Months
250000			5.8	Months
500000			0.9	Year
750000			1.4	Years
1.00E+6			1.9	Years

3.2.2. Data Processing Approaches

3.2.2.1. Simple Moving Average

SMA is a well-known method for scatter reduction that attempts to reduce scatter by calculating the arithmetic mean of neighboring points' values. A constant-length interval (window or bandwidth) is used for the calculation for each point; this is also termed a "running" average. Eq. 3. 1 is the formulation of this method, which was used by Macciotta et al. (2016) to analyze GNSS data scatter:

$$\widehat{y}_i = \frac{\sum_{i-\frac{p-1}{2}}^{i+\frac{p-1}{2}} y_j}{p}, \tag{3. 1}$$

where $\widehat{y}_i$ is the filtered value, y_j is the unfiltered value, and p is the window length. The window length is constant across the dataset except for regions near the boundaries where fewer points are available. Accordingly, p will be adjusted to the number of available points that are indeed less than the value set by the user. This will cause variation in the effectiveness of the method at the extremes, which needs to be considered when evaluating the results of this approach.

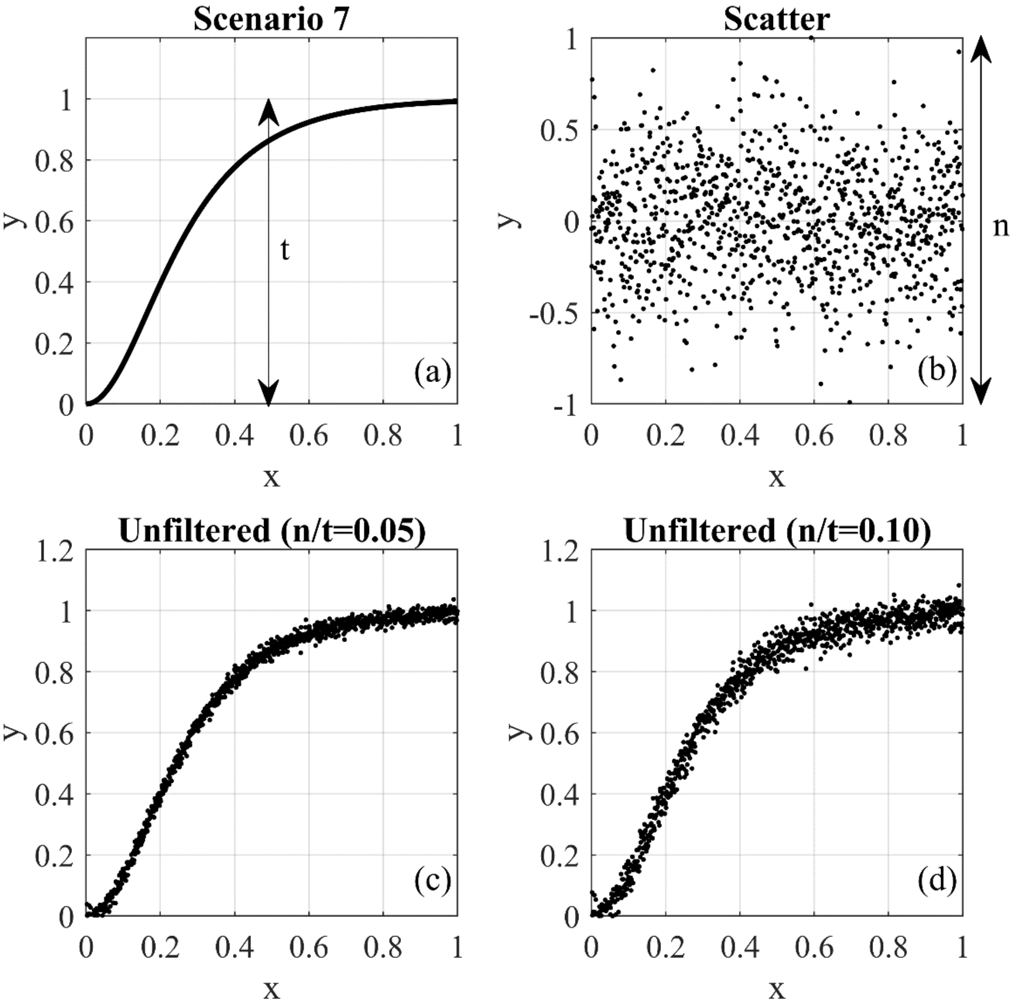

Figure 3- 2. The procedure of generating a scenario with scatter: (a) generated scenario trend, (b) randomly generated scatter, and two scenarios with scatter based on n/t values of (c) 0.05 and (d) 0.10.

3.2.2.2. Gaussian-Weighted Moving Average

Varying the weights of the measurements within the calculation window in SMA can be used to develop different filtering methods. The largest weight can be given to the measurement at the time for which the calculation is being done, with weights decreasing for measurements farther away in time. One simple weighting function that can be adopted is the Gaussian (normal) distribution. Eq. 3. 2 is the formulation of the Gaussian-weighted moving average (GWMA):

$$\widehat{y}_i = \sum_{i-\frac{p-1}{2}}^{i+\frac{p-1}{2}} w_j y_j, \tag{3. 2}$$

where w_j is the weight coefficient based on the Gaussian distribution and the other terms follow the same definition as per SMA.

3.2.2.3. Savitzky-Golay

SG fits a low-degree polynomial equation to the unfiltered measurements within a window and defines the filtered measurements using the fitted curve (Schafer, 2011). Although this procedure seems dissimilar from the weighted averaging as discussed for GWMA, its function can be transformed into a kernel concept using the least-squares method if the data points are evenly spaced. The detailed procedure is presented in Appendix A. Figure 3- 3 shows the weight kernel over a window of seven points attained by fitting a quadratic polynomial. An immediate observation is that some points are given negative weights. If points are not evenly spaced, the weighting kernel cannot be used, and local regression analysis should be periodically conducted for each point. Such filtering is known as locally estimated scatterplot smoothing (LOESS). This decreases the computational efficiency of filter performance and exponentially increases the execution time.

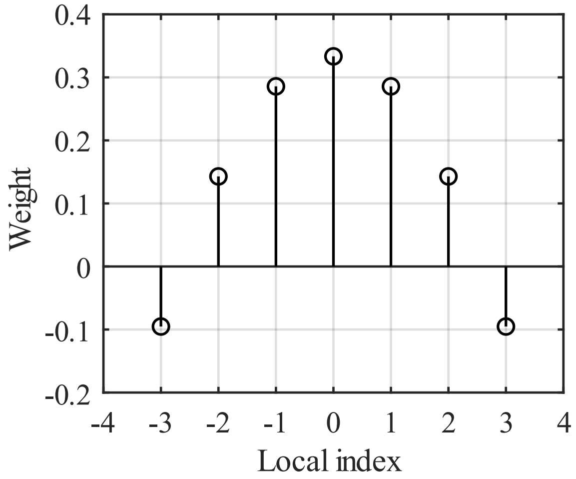

Figure 3- 3. The weighting kernel of the Savitzky-Golay filter for seven points

3.2.3. Evaluation of Processing Algorithms

The synthetic monitoring data and data from the case studies were filtered using SMA, GWMA, and SG techniques. The filters were applied with different lengths of moving windows, from 0.01 (1%) to 0.1 (10%) of all monitoring points, referred to as the bandwidth ratio. These limits for the bandwidth ratio were selected based on literature reports for SMA. In the filtration process, we only used the points prior to the time for which the calculation is being made (point of interest, Figure 3- 4). This is to reflect the reality of displacement monitoring information as applied to EWSs. To this end, filters used the first half of their kernels, but the weights were multiplied by 2 in comparison to a symmetric window in order to keep the sum of weights equal to 1.

All of these filters require the definition of the bandwidth. A roughness factor was defined to aid in the evaluation of the effect of bandwidth in reducing scatter. This factor is defined as (Eq. 3. 3):

$$J_2 = \frac{\int (\hat{y}'')^2 dx}{R_a}, \tag{3. 3}$$

$$R_a = \int (y'')^2 \, dx, \tag{3. 4}$$

where J_2 is the roughness factor, $\hat{y}''$ is the second derivative of filtered measurements, R_a is the absolute roughness computed by Eq. 3. 4, and y'' is the second derivative of unfiltered measurements. The second derivative measures how much the slope of the line connecting two consecutive points changes, which itself is an indication of fluctuation. The greater this second derivative, the greater the variation. J_2 was normalized to the overall curvature of the unfiltered scenario to determine the relative scatter reduction after the application of a filter, eliminating any

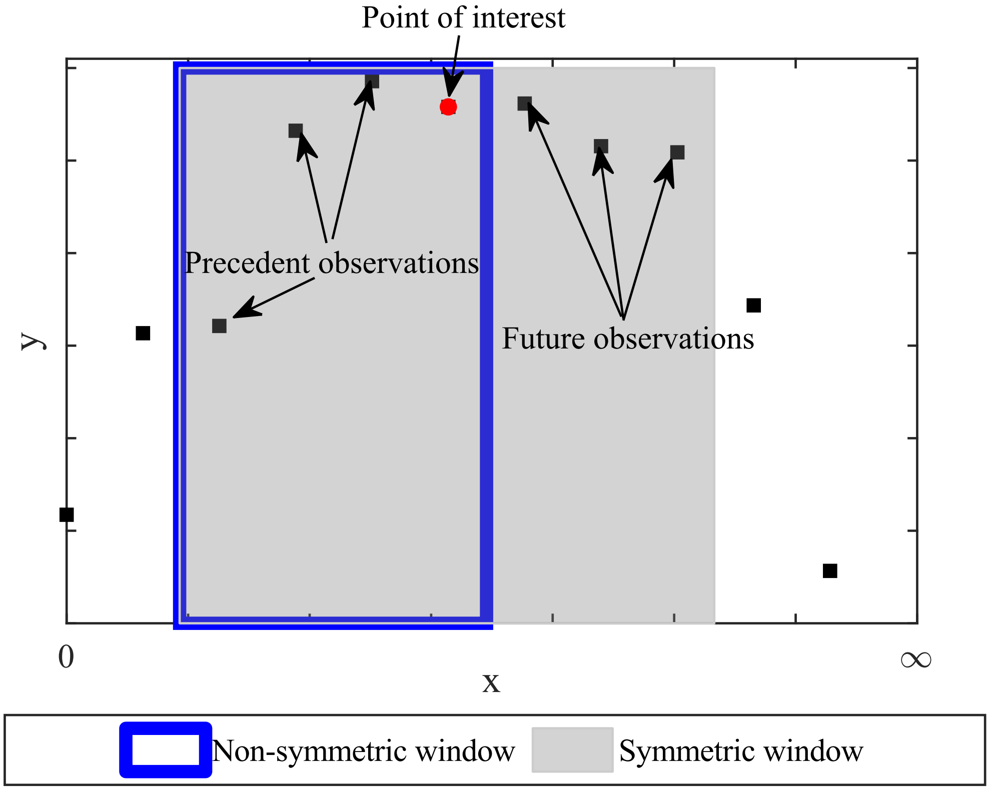

Figure 3- 4. Concept of symmetric and non-symmetric window types in the filtration process

roughness associated with the real trend in the scenario. In limit states, a value of 1 means that fluctuations are similar to the unfiltered dataset, and therefore no improvement has been achieved; a value of 0 suggests the slope of a scenario remains unchanged and indicates a linear trend. Because all the scenarios, except the first, include trends showing concavity or convexity, a residual value for the roughness factor would be expected in the lowest limit state, meaning that a value of 0 is not necessarily a goal. J_2 was used to infer the minimum value of bandwidth ratio after which no significant change in the fluctuation of results is achieved. Considering the second power in the formulation of J_2, all observations are valid if the scenarios are mirrored (when they vary from 1 to 0, instead of 0 to 1).

The filters are not expected to remove all scatter, and the error attributed to the residual scatter can be calculated using the root mean square error (RMSE). Given that velocity values are usually used as thresholds in an EWS, one concern is whether the filter should be applied to displacement values or velocity values derived from unfiltered displacements. To address this issue, two different approaches to filtering were investigated: direct and indirect. As a result, two different approaches using the RMSE were also utilized here.

3.2.3.1. Direct Scatter Filtration

Direct filtration means the filter is applied to the diagram of interest. If the filtered displacement values are the goal, and the filter is applied to unfiltered displacement values, then the filtering process is called direct filtration. The same concept applies when velocity values are derived using unfiltered displacements and the filters are then directly applied to the velocity values. In this approach, the RMSE follows Eq. 3. 5:

$$\mathrm{RMSEd}=\sqrt{\frac{1}{m}\sum_{i=1}^{m}(\widehat{y}_i-y_i)^2}, \tag{3. 5}$$

where *RMSEd i*s the measurement of error in direct filtration, y_i is the value of the true trend (for the synthetic scenario), $\widehat{y}_i$ is the filtered value, and *m* is the total number of points. This approach is often used in the literature (Macciotta et al., 2016; Carlà, Farina, et al., 2017; Carlà, Intrieri, et al., 2017; Carlà et al., 2018; Intrieri et al., 2018; Carlà et al., 2019).

3.2.3.2. Indirect Scatter Filtration

Some EWSs can apply the filter to the displacements but use velocity trends as the metric for evaluation. In this case, the filtered velocity values will be computed using the filtered displacements. Indirect filtration indicates the diagram of interest is the first derivative of the diagram to which the filter is applied. The RMSE, in this case, is defined as (Eq. 3. 6):

$$\mathrm{RMSEi}=\sqrt{\frac{1}{m}\sum_{i=1}^{m}(\hat{y}_i'-y_i')^2}, \tag{3. 6}$$

where *RMSEi i*s the measurement of error in indirect filtration, y_i' is the first derivative of the true trend, $\hat{y}_i'$ is the first derivative of filtered data (derived velocity after the filter is applied to the displacements), and *m* is the total number of points. Similar to J_2, all observations are valid for the mirrored scenarios of those presented in Figure 3- 1. This is a consequence of using the second power in the definition of *RMSEi* and *RMSEd*.

3.2.4. Lag Quantification

Only antecedent measurements are fed into the filters, which is expected to result in a lag between the true trend and its identification by the filters. This lag means the calculated value of velocity or displacement occurred sometime in the past. Consequently, reducing this lag means less time is lost with respect to providing an early warning. To quantify the induced lag, the filtered diagrams of all scenarios at all *n*/*t* ratios and bandwidth ratio values were shifted backwards a number of points equivalent to 0.001 (0.1%) to 0.1 (10%) of all generated points. We refer to this as the shift ratio in the rest of this paper. This shift of filtered diagrams is expected to increase their similarity with the true trend until the best correlation is achieved. The R^2 test was used to determine how well the shifted and filtered results replicate the underlying trend.

3.2.5. Geocube Differential GNSS System

A Geocubes system is a network of differential global navigation satellite system (GNSS) units that work with a single frequency (1572.42 MHz), making it cost-effective (Doberstein, 2012; Benoit et al., 2014; Rodriguez et al., 2018). Geocubes communicate with each other through radio frequency, and a reference unit outside the boundaries of the landslide is assumed as static for differential correction to increase the poor accuracy associated with single frequency GNSSs (Benoit et al., 2014; Rodriguez et al., 2018). The ability of this system to achieve real-time positioning, remote data collection, and processing makes it a suitable candidate for incorporation into an EWS. As a result, Geocube data are used in this study to evaluate the performance of the three mentioned filters.

3.2.6. Outlier Detection

Outliers are defined herein as abnormal inconsistencies (e.g., displacement directions, magnitudes) when compared to the majority of observations in a random sampling of data (Zimek & Filzmoser, 2018). Techniques for outlier detection have been proposed based on the statistical characteristics of datasets. One common example is the Z-score method, which calculates the mean and standard deviation of data within a defined interval and identifies outlier data as those beyond three standard deviations from the mean (Rousseeuw & Hubert, 2011). A limitation of this kind of approach is the sensitivity of the mean and standard deviation to the outlier data points, which has led to the development of other methods that use other indices such as the median (Salgado et al., 2016). One such technique that was adopted in this study is the Hampel filter (Hampel, 1971). In this method, the median of the displacement measurements within a running bandwidth is calculated and data outside a defined threshold from the median are identified as outliers. The threshold is defined as a constant (threshold factor) multiplied by the median absolute deviation. An asymmetric window with a bandwidth ratio of 0.004 (0.4%) and a threshold factor of three were adopted following previous studies (Davies & Gather, 1993; Pearson, 2002; H. Liu et al., 2004; Z. Yao et al., 2019). The data identified as outliers were then removed from the dataset.

3.3. Study Site – Ten-mile Landslide

The Ten-mile landslide is located in southwestern British Columbia (BC), in the Fraser River Valley north of Lillooet (Figure 3- 5a). It is a reactivated portion of a post-glacial earthflow (Bovis, 1985) that was first recognized in the 1970s. The landslide velocity has increased from an average of 1 mm/day in 2006 to 6 mm/day in 2016, with a maximum measured velocity of 10 mm/day (Gaib et al., 2012; BGC Engineering Inc., 2016). The movement of this landslide impacts the integrity of BC Highway 99 and a section of railway operated by Canadian National Railway (CN) (Carlà et al., 2018), with most movement limited to the volume downslope from the railway due to the installation of a retaining wall (Macciotta, Carlà, et al., 2017). Despite the stabilization work done to date, the uppermost tension crack has retrogressed approximately 200 m in 45 years and is now situated 60 m upslope of the railway track. The landslide lateral extents have not expanded since 1981 according to the aerial photographs (Macciotta, Rodriguez, et al., 2017). The

Ten-mile landslide is currently approximately 200 m wide, 140 m high, and has a volume of 0.75 to 1 million m^3, moving towards the Fraser River on a continuous rupture surface with a dip of about 22 to 24°, which is sub-parallel to the ground surface (Rodriguez et al., 2017; Donati et al., 2020). The elevation of the shear surface and mechanism of the landslide have been inferred from the readings of multiple slope inclinometers installed in 2015 (BGC Engineering Inc., 2015).

The bedrock in this region consists of volcanic rocks, such as andesite, dacite, and basalt, and is overlain by Quaternary deposits (Macciotta, Carlà, et al., 2017; Carlà et al., 2018; Donati et al., 2020). The thickness of the landslide varies between 20 and 40 m and the ground profile from the surface to depth comprises medium to high plastic clays and silts overlying colluvium material and glacial deposits, overlying bedrock (BGC Engineering Inc., 2015). The stratigraphy of the sedimented soils in the landslide area notably varies from one borehole to another and reflects the complex stratigraphy of the earthflow.

A total of 11 Geocubes were installed at the Ten-mile landslide in 2016. Figure 3- 5b is a front view of the landslide showing the locations of the Geocube units. Units 44 and 50 are installed near the uppermost tension crack identified as the current landslide backscarp, unit 69 is 30 m above the backscarp, and unit 39 is used as the reference point. Please note that unit 69 is used as the fixed Geocube, and is not shown in Figure 3- 5b. The other units are located within the boundaries of the landslide, with a maximum distance between units of 310 m (Rodriguez et al., 2018). The time step between every two consecutive measurements is 60 s. Figure 3- 6 shows the displacements of units 46 and 47, which were the largest in comparison to other Geocubes.

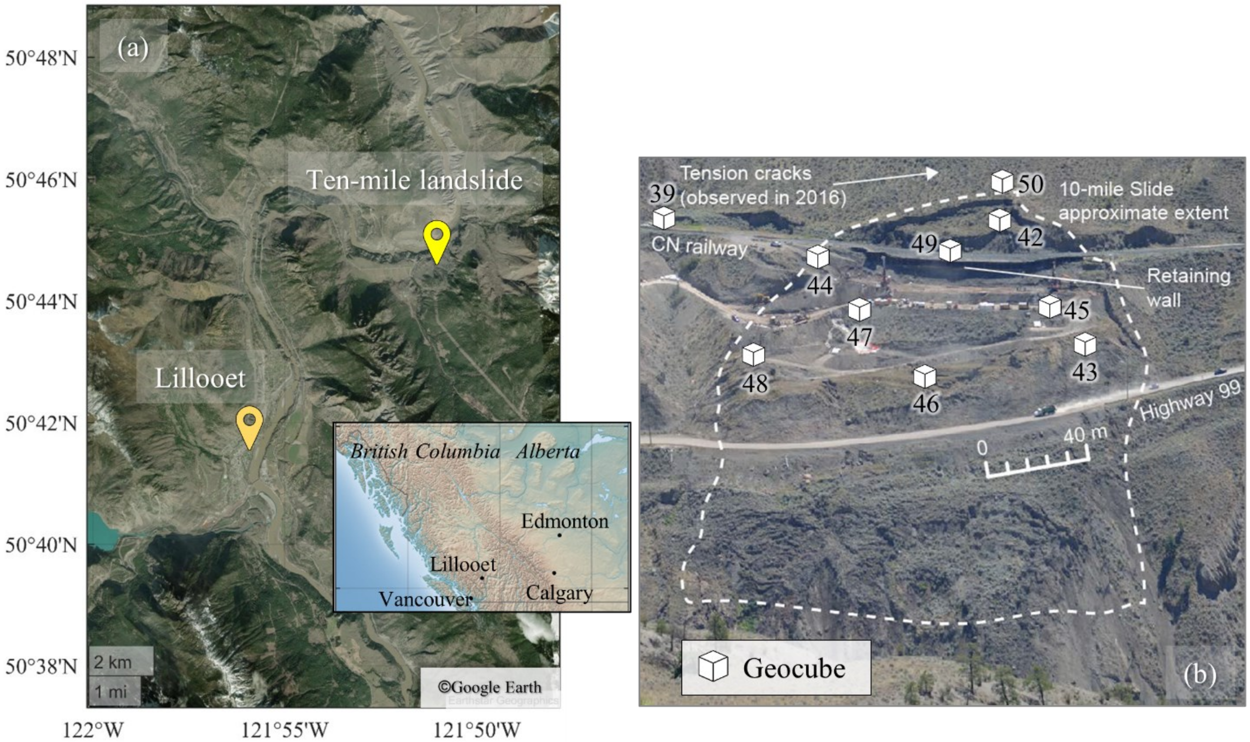

Figure 3- 5. (a) Location of the Ten-mile landslide (© Google Earth) and (b) front view of the Ten-mile landslide and distribution of Geocubes on its surface (Macciotta, Rodriguez, et al., 2017; Rodriguez et al., 2018)

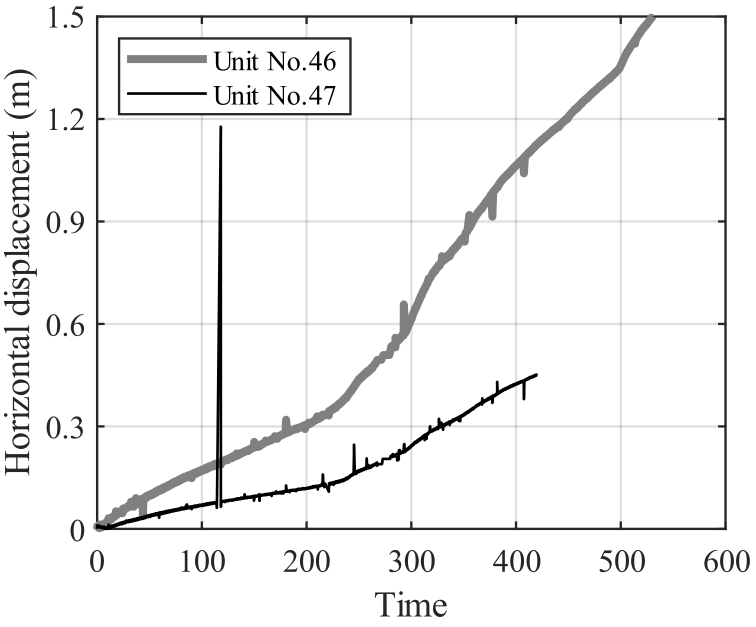

Figure 3- 6. Cumulative horizontal displacement of Geocube units No. 46 and 47

3.4. Results

3.4.1. Synthetic Analysis

Figure 3- 7 shows the roughness value (J_2) of Scenario 6 for SMA, GWMA, and SG on a semi-logarithmic scale. This figure illustrates how, regardless of the *n*/*t* ratio, J_2 substantially decreases as the bandwidth ratio increases to 0.01 and then asymptotically approaches a final value. This means that increasing the bandwidth ratio drastically reduces scatter; however, its effectiveness is restricted as the bandwidth ratio increases above 0.01. This observation was consistent for other scenarios. J_2 values (including Scenario 6 in Figure 3- 7) indicate that J_2 approaches its minimum at bandwidth ratio values of 0.03 to 0.04, regardless of the filter selected.

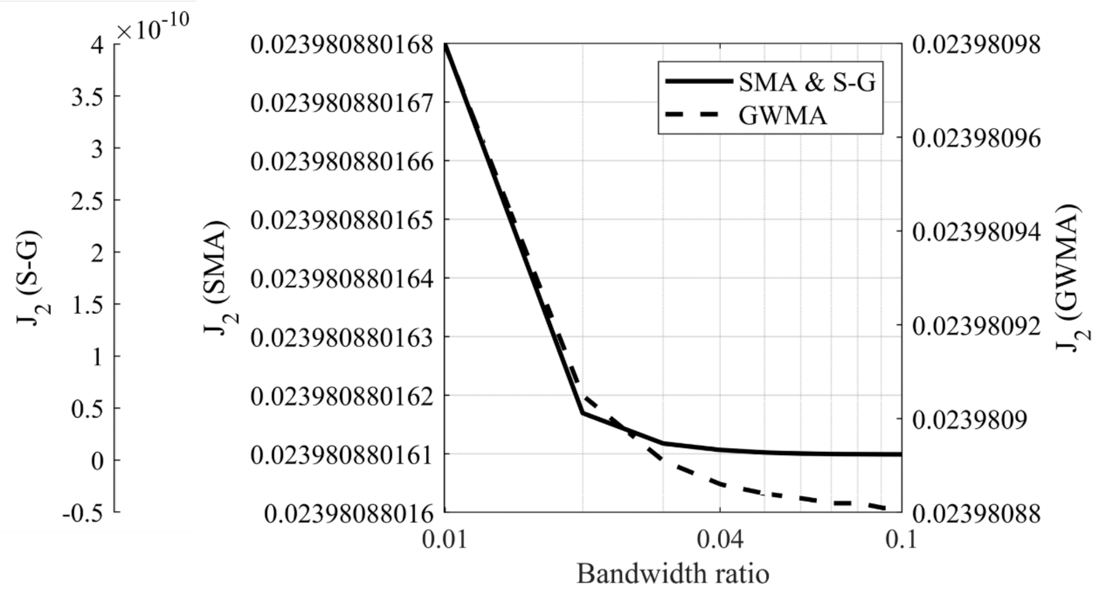

Figure 3- 7. Variation of roughness factor for Scenario 6 with respect to the applied filter on a semi-log scale

3.4.1.1. Effect of Filters on Trend Distortion

Scenarios 11 and 12 were first analyzed to evaluate the degree to which the trend was preserved by these filters, as peaks made it easier for visualization. Figure 3- 8a shows the true trend of Sscenario 11 along with two SMA-filtered scenarios at bandwidth ratios of 0.04 and 0.10, respectively. This figure shows that, as the SMA filter bandwidth increases, the peak in measurements is identified at a later time than the true trend (x=0.5) and the magnitude of the peak is reduced (more than 70% reduction at a bandwidth ratio of 0.10). Furthermore, as the bandwidth ratio increases, the "instantaneous" nature of the peak is lost to a more transitional variation. This highlights a disadvantage of SMA when handling sudden changes in data trends. The calculated *x* value of the peak in Scenario 11 is plotted for different bandwidth ratios and for all three filters in Figure 3- 8b. This figure shows the time at which the peak is identified lags as the bandwidth ratio increases for all filters; however, GWMA and SG identify the peak with a much smaller lag, independent of the *n*/*t* ratio. As an example, for a year of monitoring data at a frequency of 30 s and bandwidth ratio of 0.10, SMA, GWMA, and SG predict the peak point approximately 17, 3.5, and 2.7 days after the real peak, respectively. This lag can be attributed to the utilization of an asymmetric window, which leads to a lagged response of the filter. As more points are included in the filtering procedure (increasing bandwidth ratio), this lag increases because the averaging process is sensitive to window type. The degree of sensitivity, however, depends on the filter. Figure 3- 8c shows the variation of the peak magnitude with respect to the bandwidth ratio for all three filters. SMA and GWMA both underestimate the peak value, and the difference between the calculated peak and real peak increases as the bandwidth ratio increases. SMA calculations underestimate the peak more than twice as much as GWMA. On the contrary, SG intensifies the peak up to a bandwidth ratio of 0.04, with the impact tending to diminish at larger bandwidth ratios; it predicts the true value at a bandwidth ratio value of almost 0.09.

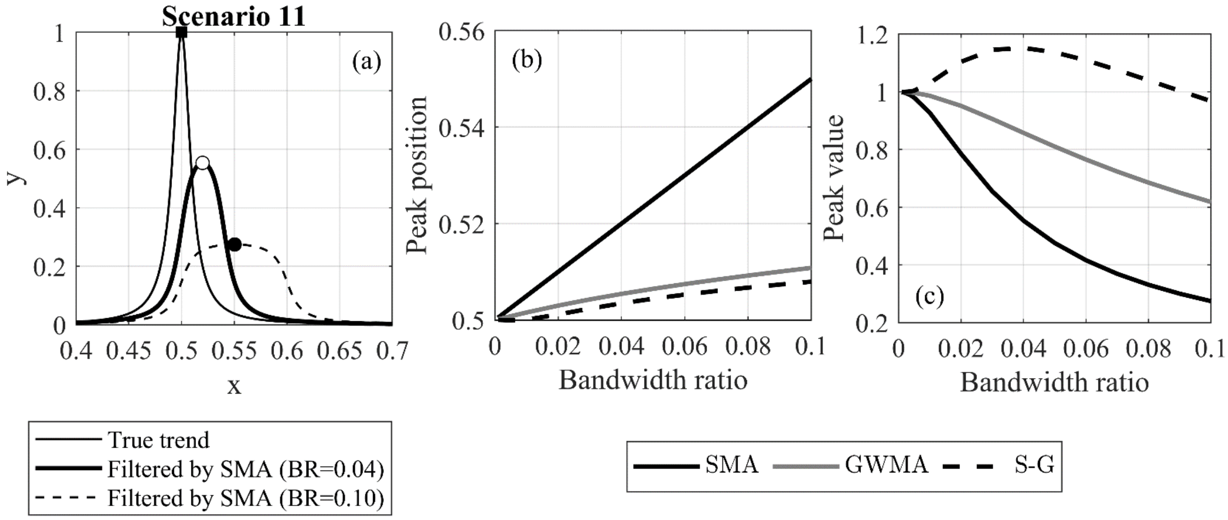

Figure 3- 8. (a) An example of peak displacement by applying SMA, and variation of (b) peak position and (c) peak value with respect to the filter and bandwidth ratio used (original peak at 0.5)

Scenario 12 was used for a detailed evaluation of the ability of these filters to conserve the underlying original trend. Figure 3- 9 shows Scenario 12 and the filtered results for all three filters and an *n*/*t* ratio of 0.15. This scenario and these specific parameters were selected for illustration purposes as they allow visual identification of differences for discussion. The SMA filter considerably underestimates the magnitude of the peak at a bandwidth ratio of 0.04, which should be the minimum bandwidth ratio according to Figure 3- 7. At a bandwidth ratio of 0.10, the filtered diagram is distorted in comparison to the true trend and the initial peak is not identified. GWMA at a bandwidth ratio of 0.04 shows less underestimation of the peak magnitude, and a slight lag is visually observed at a bandwidth ratio of 0.10. This indicates the significantly better performance of GWMA over SMA. SG results for both bandwidth ratios closely identify the time and magnitude of both peaks, indicating yet better performance. However, the peak is artificially intensified at a bandwidth ratio of 0.04, and a significant drop occurs well beyond the true trend immediately after the second peak for both bandwidth ratios (pulsating effect), which was also observed in Scenario 11. Increasing the degree of the polynomial fitted as part of the SG methodology was not completely effective at eliminating this effect. The pulsating effect was also observed when a symmetrical window was utilized and is attributed to the negative weights in the SG kernel.

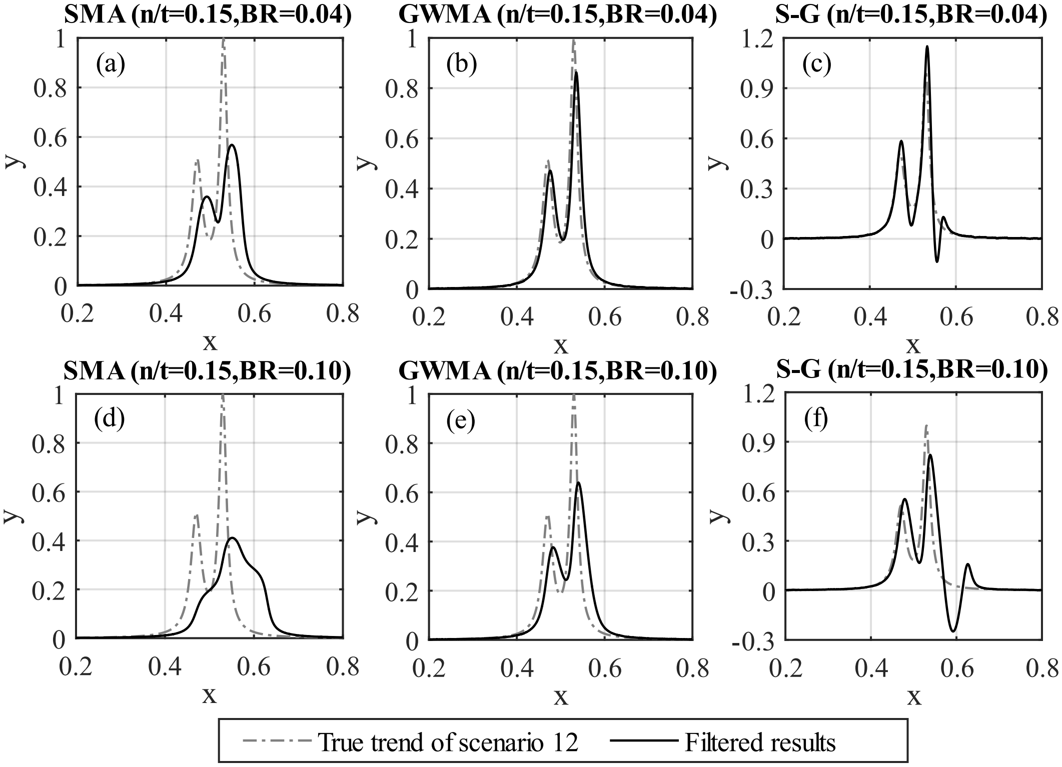

Figure 3- 9. Filtered results of Scenatio 12 with scatter using SMA (a,d), GWMA (b,e), and SG (c,f) at bandwith ratios (BRs) of 0.04 (a-c) and 0.10 (d-f)

3.4.1.2. Results of Direct Scatter Filtration

Figure 3- 10 shows the RMSEd of all three filters for all the harmonic synthetic scenarios. This figure shows that, for these numerical analyses on synthetic scenarios, the error depends linearly on the bandwidth ratio for all of the filters and does not depend on the scenario or *n*/*t* ratio. SMA shows the greatest difference from the true trend, followed by GWMA (approximately 60% less difference than SMA). SG, on the other hand, almost lies on the horizontal axis for all the bandwidth ratios, which means the filtered results yield near-zero error. Figure 3- 10 also shows how the error increases as the bandwidth ratio increases. This can be attributed to the utilization

of an asymmetric window, which leads to a lagged response of the filter. As more points are included in the filtering procedure (increasing bandwidth ratio), this lag increases and, consequently, causes a larger error. The RMSEd of filters for the instantaneous synthetic scenarios are shown in Figure 3- 11. In Scenario 10, the same behavior as noted for the harmonic scenarios can be seen for SMA and GWMA, whereas SG is not as accurate. This is more noticeable in Scenarios 11 and 12 in which SG becomes less accurate than GWMA at larger bandwidth ratios. This result shows that SG cannot handle the instantaneous scenarios as satisfactorily as the harmonic ones. The errors related to SMA and GWMA for the instantaneous synthetic scenarios show non-linear behavior and are greater when compared to the harmonic scenarios. Figure 3- 11 clearly shows all filters are challenged by the instantaneous variations when compared to gradual ones in direct filtration.

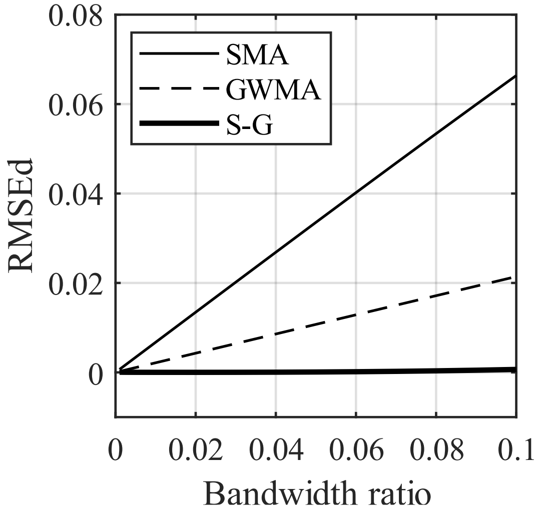

Figure 3- 10. RMSEd fpr the harmonic scenarios

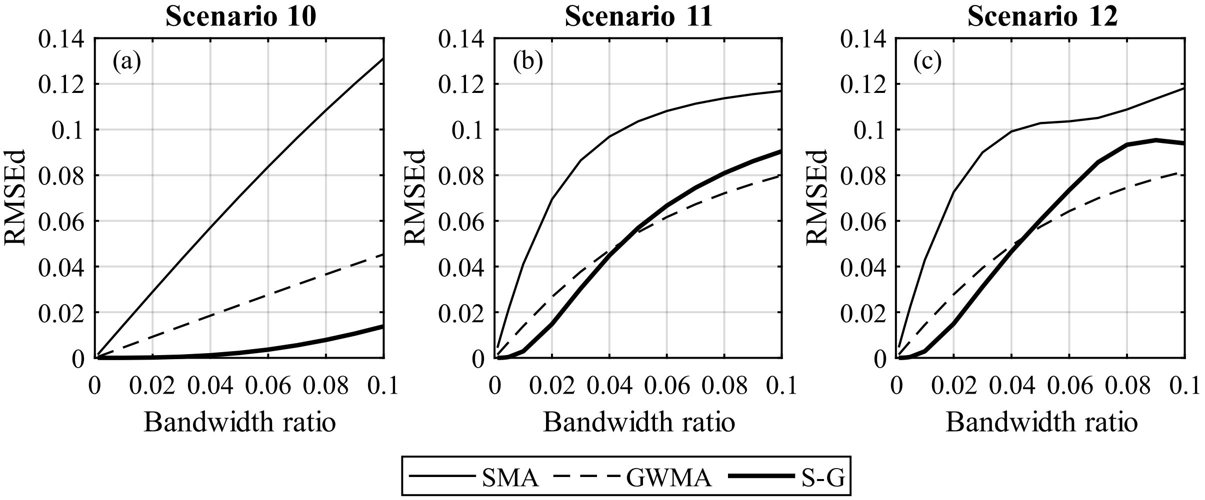

Figure 3- 11. RMSEd for the instantaneous scenarios

3.4.1.3. Results of Indirect Scatter Filtration

Figure 3- 12 shows the RMSEi results for the harmonic scenarios (when performing indirect filtration) on a semi-logarithmic scale. We observed that the error considerably decreases as the bandwidth ratio increases to 0.02; however, to highlight the variation of error in the range of interest for the bandwidth ratio, only RMSEi values corresponding to bandwidth ratios greater than 0.04 are plotted in Figure 3- 12 and Figure 3- 13. In Figure 3- 12, the error for the GWMA is either equal to or slightly less than the error for the SMA, and SG shows the least error for the harmonic scenarios. The RMSEi results for the instantaneous scenarios (Figure 3- 13) are similar to those for the harmonic scenarios for large *n/t* ratios (0.05, 0.10 and 0.15). For small *n*/*t* ratios, the GWMA is superior at bandwidth ratios above 0.06, and SG has the worst performance.

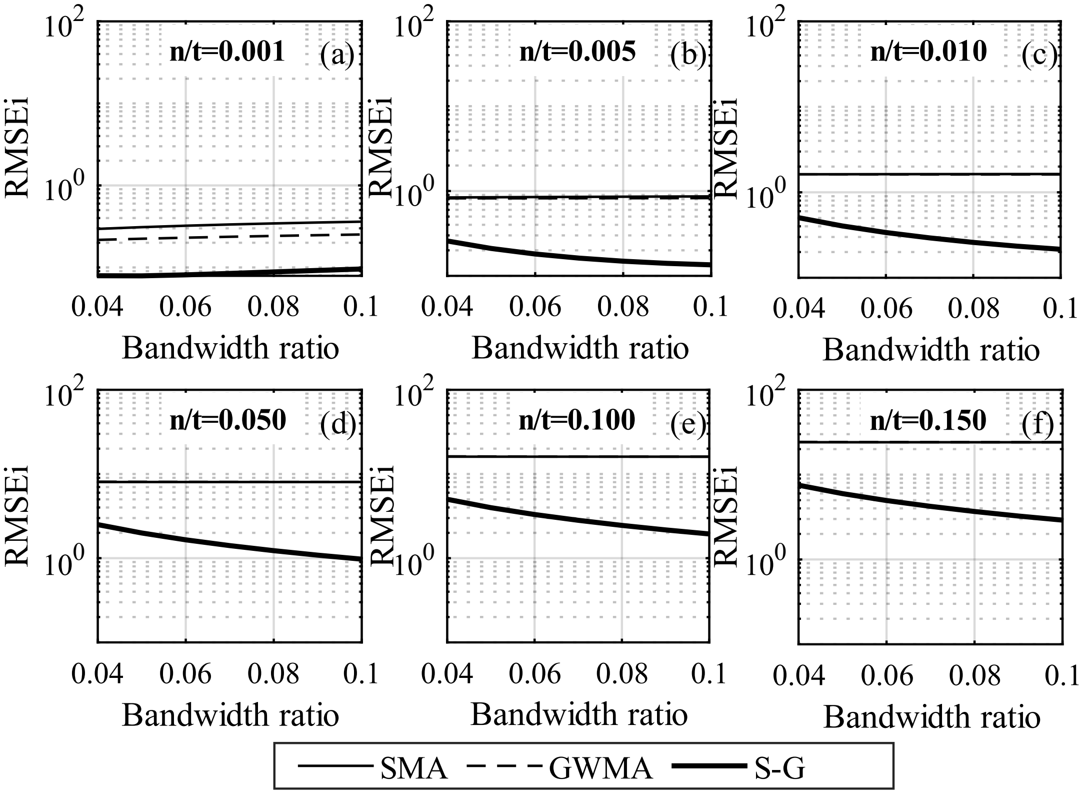

Figure 3- 12. RMSEi for the harmonic scenarios on a semi-log scale

3.4.1.4. Lag Quantification

The non-symmetric inclusion of points causes the identification of a lag in the trend of filtered data. Figure 3- 14 shows Scenario 10 with respect to the original trend, with scatter added (at an *n*/*t* value of 0.15), and the results after filtering with each of the three methods at a bandwidth ratio of 0.04. This figure clearly shows the lag between the results filtered by SMA and GWMA and the true trend. SG results do not have as severe a lag as that resulting from the other filters; we attribute this to the negative weights in its kernel that anchor the filtered values and prevent a lagged response. A minor pulsating effect can be observed in the SG filtered data, decreasing the calculated values at a much earlier time than the true trend. This suggests that SG is robust with respect to identifying initial changes in monitoring trends but overcorrects subsequent changes;

SMA grossly lags with respect to the identification of any change, and GWMA has a reduced lag when compared to SMA.

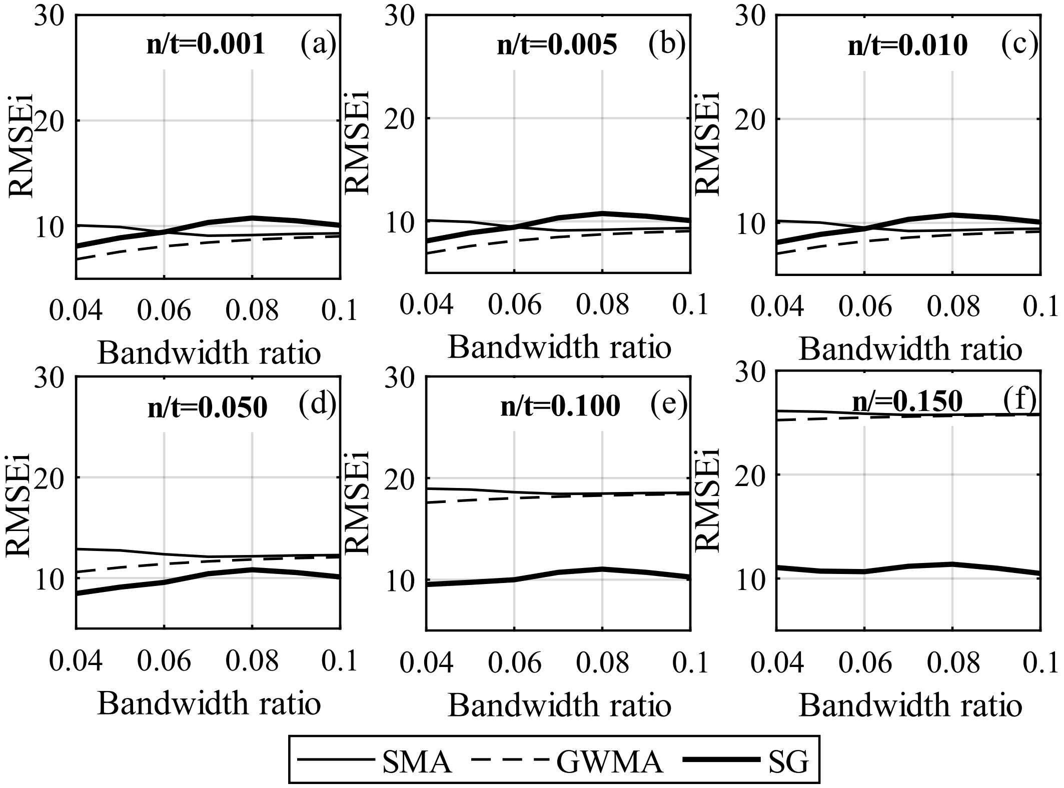

Figure 3- 13. RMSEi for the instantaneous scenarios

Figure 3- 15a shows an example of the R^2 correlation for Scenario 7, comparing the original trend and the results filtered by SMA at an *n*/*t* value of 0.01 and bandwidth ratio of 0.04. The shift ratio is the shift of filtered trends (in the horizontal axis – parameter *x)* relative to the range of *x* values. R^2 calculations are shown for the filtered data (shift ratio of 0) and as the filtered trends are shifted backwards in time (negative shift ratio values). In this analysis, the peak R^2 value (largest correlation between the shifted filtered results and original trend) indicates the shift required to minimize the lag in identifying the original trend changes, therefore providing a quantitative approach to calculating the lag in parameter *x*. In the example in Figure 3- 15a, the lag corresponded to 0.018 (1.8%) of the total points.

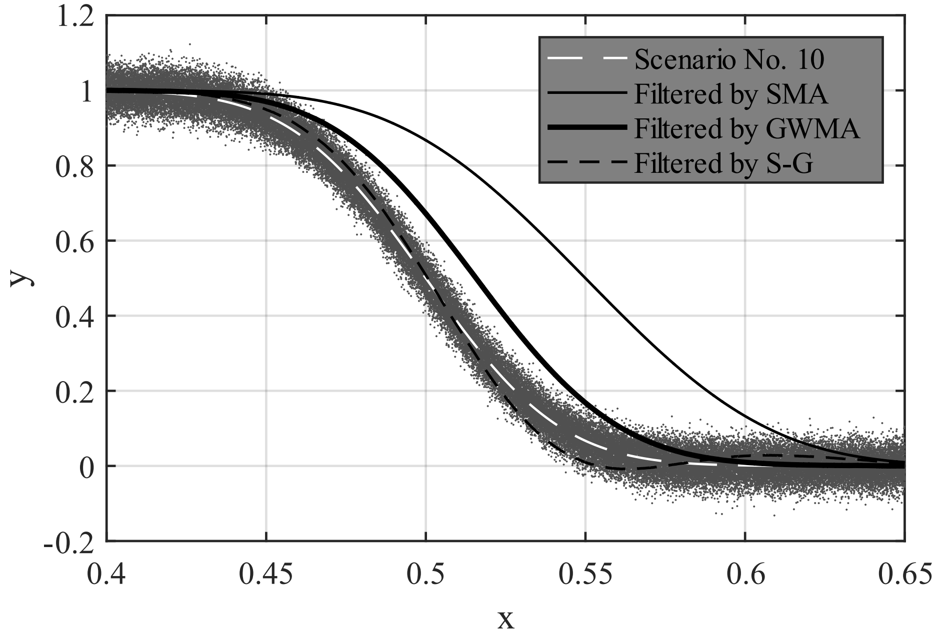

Figure 3- 14. Scenario 10 with and without scatter, and with scattered results filtered by SMA, GWMA and SG for an n/t value of 0.15 and a bandwidth ratio of 0.04

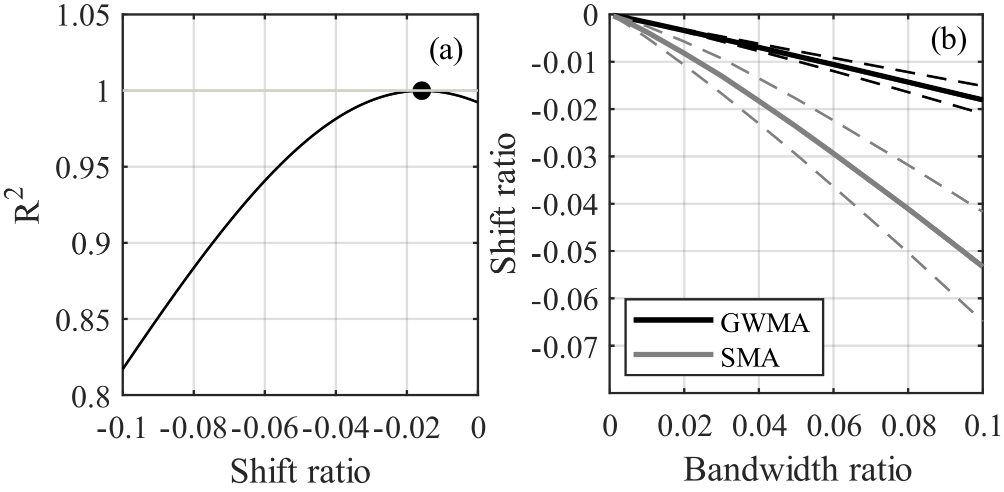

Figure 3- 15. (a) R^2 values for Scenario 7 with filtered and shifted results at an n/t value of 0.01 and bandwidth ratio of 0.04 and (b) shift ratio at peak R^2 for all scenarios and n/t ratios, with the mean (solid line) bounded by one standard deviation (dashed lines)

Peak R^2 values for all scenarios and *n*/*t* values are closely correlated with the bandwidth ratio. The lag, quantified by the shift ratio, is larger when the trend change is more pronounced; therefore, the correlation between the shift ratio and bandwidth ratio is different for different scenarios. Figure 3- 15b shows the mean correlation between the shift ratio and bandwidth ratio, for all scenarios and n/t values, bounded by one standard deviation, for GWMA and SMA. Table 3- 2 shows linear and quadratic regressions of this correlation and the strength of the correlation in terms of R^2 and RMSE. Figure 3- 15b quantitatively shows that GWMA lags less than SMA with respect to identifying changes in measurement trends. Moreover, the uncertainty associated with lag for SMA is greater than for GWMA because of the larger standard deviation. Figure 3- 15b quantifies how increasing the bandwidth ratio increases the lag with respect to identifying true measurement trends and, although large bandwidth ratios decrease the scatter in data, the bandwidth ratio should carefully balance minimizing both scatter (J_2) and lag (shift ratio). SG is not included in this analysis as the method resulted in no significant lag in identifying changes in measurement trends; however, it had the disadvantages previously noted including pulsating effects and overestimating peak values.

Table 3- 2. Regression correlations between shift ratio (SR) and bandwidth ratio (BR) with the strength of the correlation in terms of R^2 and RMSE

	Linear regression		Quadratic regression	
SMA	$SR=-0.5087(BR)$	$R^2=0.9940$ RMSE=0.0014	$SR=-1.323(BR^2)-0.4049(BR)$	$R^2=0.9997$ RMSE=3.24E-4
GWMA	$SR=-0.1783(BR)$	$R^2=0.9996$ RMSE=1.2963E-4	$SR=-0.1171(BR^2)-0.1691(BR)$	$R^2=0.9999$ RMSE=3.5672E-5

3.4.2. Results on the Ten-mile Landslide

Unfiltered results reported by Geocubes 46 and 47 installed on the Ten-mile landslide were processed by all three filters. To illustrate to the reader through visual inspection the difference between the performance of SMA, GWMA, and SG, only a 200-day window of displacement data from Geocube 46 and filtered points produced by direct filtration are shown in Figure 3- 16. Figure 3- 16a also features an inset showing scaled Scenario 4, which resembles the general trend of

Geocube 46 data for the period from day 200 to 400. Figure 3- 16 shows that increasing the bandwidth ratio reduces the scatter, but increases the lag in the filtered results, consistent with observations on the synthetic datasets. For bandwidth ratios larger than 0.04, SMA becomes insensitive to some short-scale (20- to 30-day) trends in the data (qualitative visual inspection). As an example, at a bandwidth ratio of 0.10, SMA suggests the displacement of Geocube 46 follows a bi-linear trend with an inflection point at day 240, while unfiltered points and other filters suggest other periods of acceleration and deceleration. Importantly, SG is sensitive to even subtle variation and does not show significant lag.

Figure 3- 17 shows the filtered velocity values obtained by directly filtering the calculated velocities and by indirectly filtering the displacement values before calculating the velocity from Geocube 46 data. The direct and indirect filtering approaches demonstrated similar performance in terms of scatter reduction for Geocube 46 data. As the bandwidth ratio increases, SMA tends to significantly attenuate the local maximum and minimum points in comparison to results at smaller bandwidth ratios, indicating a probable loss of information about the landslide behavior and sensitivity of this filter to the bandwidth ratio, as also noted in Figure 3- 16 (curvature loss in SMA results). Indirect filtration by SMA seems to be limited near the boundary at time zero, resulting in a subdued replica of direct filtration. The length of this region is found to be governed by the bandwidth ratio, as the necessary number of points for filtering in this portion has not been provided to the filter. This is also observed in SG results. This problem was not found in GWMA results, as direct and indirect filtration both follow the same pattern. GWMA and SG are both able to preserve the velocity variation even at the most intense filtration (bandwidth ratio of 0.10); however, variations between local maxima and minima are more extreme in SG than GWMA results. This is attributed to peak overestimation (Figure 3- 8 and Figure 3- 9) or a pulsating effect

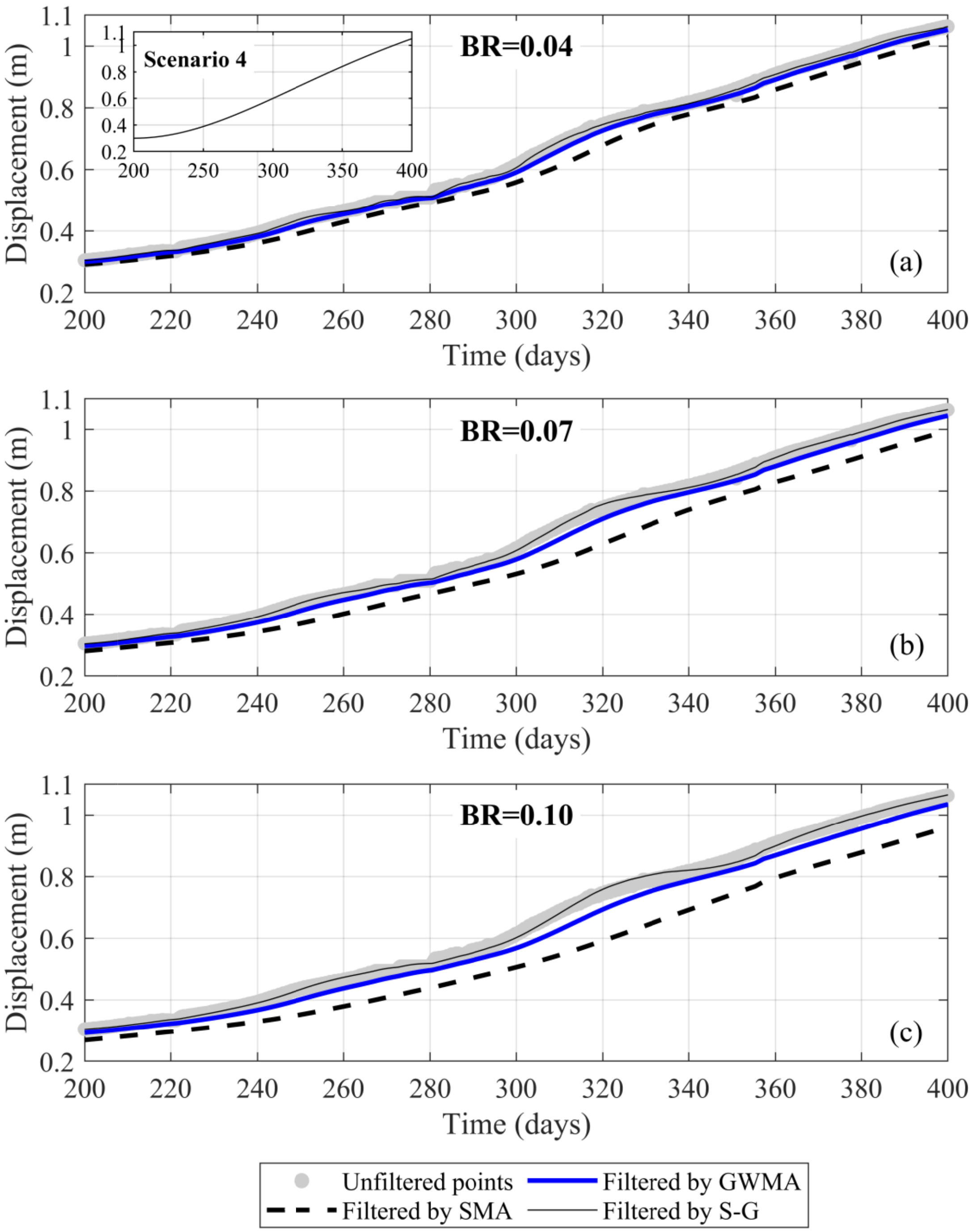

Figure 3- 16. Unfiltered displacement of Geocube 46 data vs. time and data filtered by SMA, GWMA, and SG for bandwidth ratios (BRs) of (a) 0.04, (b) 0.07, and (c) 0.10.

superimposing on the peaks/troughs. Moreover, the SG results still demonstrate relatively large fluctuations even at the largest bandwidth ratio. This means that the application of SG might still trigger false alarms in an EWS if the landslide is moving at a faster rate or experiencing different episodes of acceleration and deceleration. To avoid this, a larger bandwidth ratio should be used but this can be problematic due to the higher computational effort required and issues that might follow, such as the pulsating effect.

Results for Geocube 47 confirm the same observations made for Geocube 46 but also allow for an evaluation of the significance of outliers on the filtered results. Figure 3- 18a displays the outliers detected in the displacement diagram of Geocube 47 data along with the threshold established by the Hampel algorithm using an asymmetric window, a bandwidth of 0.4% and a threshold factor of 3. Figure 3- 18b-d shows a magnified portion of the displacement measurements for Geocube 47 filtered by each of the three filters at three different bandwidth ratios before the elimination of outliers. This highlights the necessity of outlier elimination before the application of any scatter filter. These plots show that detecting and removing outliers significantly impacts the performance of SG, as the presence of the outlier generates a peak that follows the outlier measurement and is followed by a sudden decrease that drops well beyond the data trend. SMA tends to widen the time range affected by the outlier more than GWMA but, for the most part, the SMA-filtered results are almost parallel to the underlying trend. All filters appear to be significantly impacted by the outlier value, suggesting a pre-processing filter is required to remove outliers regardless of the use of SMA, GWMA, or SG to reduce scatter. The outliers were successfully identified and removed after the application of the Hampel algorithm, and the above-mentioned effects were no longer observed in the filtered results.

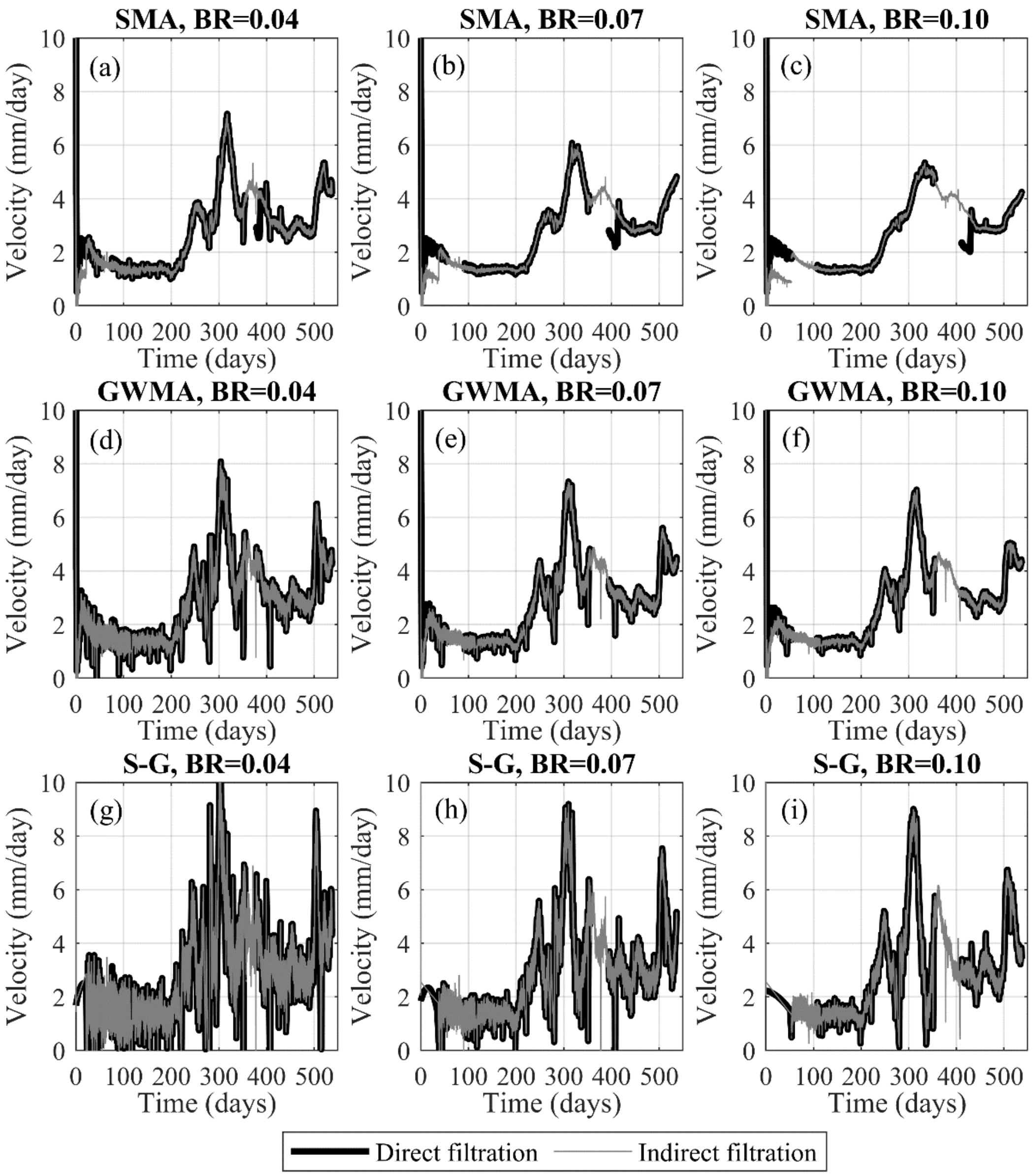

Figure 3- 17. Indirect and direct filtration results of Geocube No. 46 velocity values for bandwidth ratio (BR) values of (a) 0.04, (b) 0.07, and (c) 0.10.

3.4.2.1. Lag Minimization in Filtered Geocube Results

The lag between unfiltered and filtered data for Geocube 46 (Figure 3- 16) is consistent with the synthetic database results. The lag quantification results (Figure 3- 15b) were used to provide a correction value for the filtered Geocube results. The shift ratios used for this purpose with respect to each filter and bandwidth ratio are tabulated in Table 3- 3. To determine whether

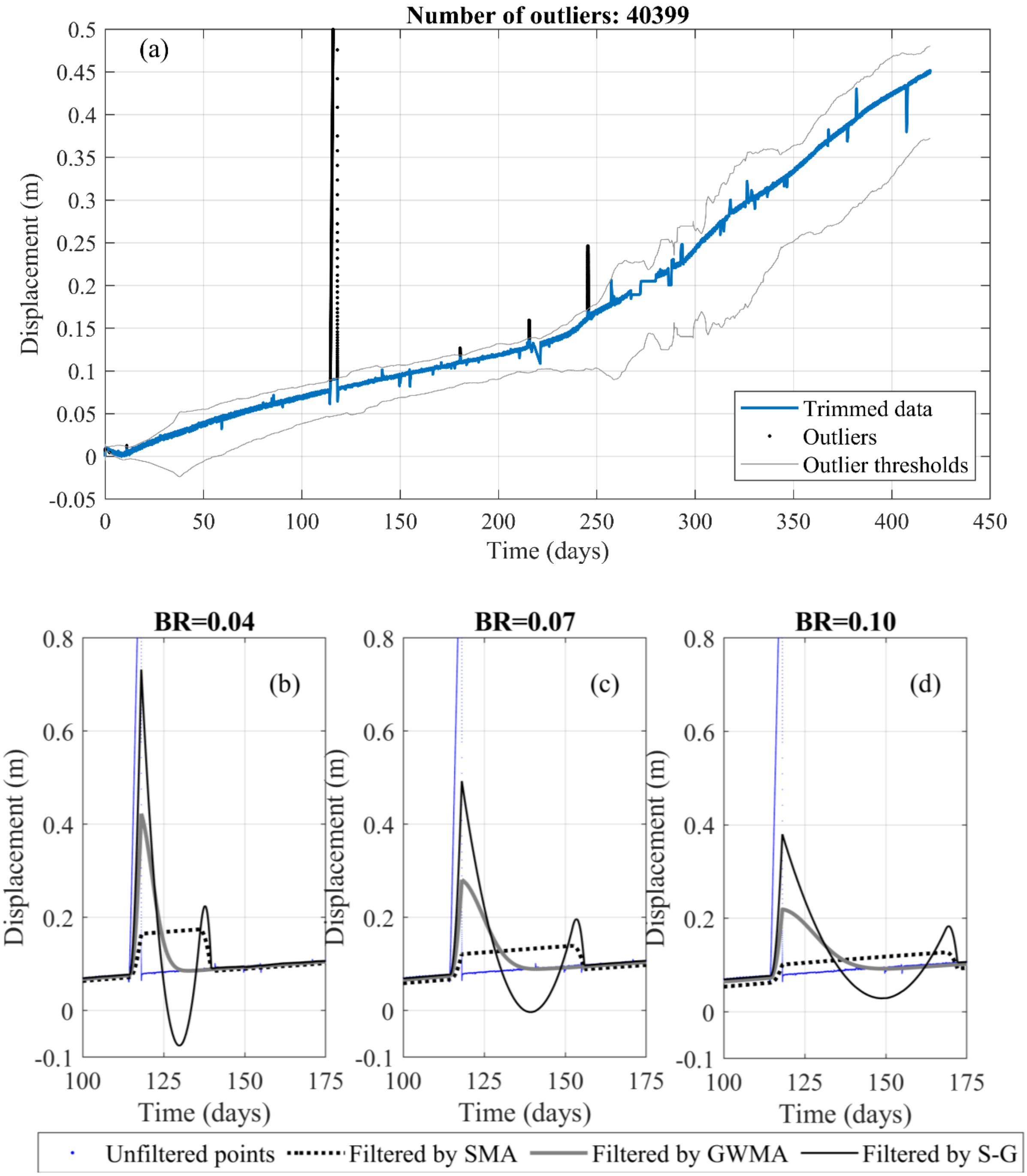

Figure 3- 18. Unfiltered and filtered displacement measurements for Geocube 47 at bandwidth ratios (BRs) of (a) 0.04, (b) 0.07 and (c) 0.10

the results of lag correction using the mean correlations derived from the synthetic scenarios (Table 3- 2) were acceptable, the filtered diagrams were shifted (using the mean line for GWMA and values between the mean and lower boundary for SMA) and different portions of the displacement diagrams for Geocubes 46 and 47 were examined. Some examples are shown in Figure 3- 19. The mean and standard deviation of the scatter around the trend (error distribution) were calculated by assuming a linear trend within the short periods of analysis (considered an approximation of the true displacement trend for the short time interval). These were also calculated for the filtered and shifted diagrams. The closer the mean and standard deviation of the filtered and shifted data are to that obtained from the linear trend, the better the performance of the lag correction based on the results from the synthetic scenarios. As an example, for the period from day 250 to 260, the GWMA resulted in a standard deviation of 0.001 to 0.0015 for bandwidth ratios from 0.04 to 0.10, respectively; corresponding values for SMA to 0.0018 to 0.0021. This illustrates that shifted GWMA results are closer to the true (scatter-free) displacements because the standard deviations of scatter inferred by this filter are closer to the true scatter, although both have good agreement with the true scatter. The means of inferred scatter by both filters are also close enough to the mean of the true scatter (almost zero). The results show the statistical indices of scatter inferred from the filtered shifted displacement measurements closely agree with that considered to be true scatter, and therefore the filtered displacement measurements are corrected for lag. This suggests the correlations stated in Figure 3- 15b and Table 3- 2 based on the synthetic scenarios are applicable to minimize the lag for the Geocube system at the Ten-mile landslide.

Table 3- 3. Shift ratios used for lag minimization of Geocube 46 displacements

Bandwidth ratio	Shift ratio	
	SMA	GWMA
0.04	-0.02	-0.007
0.07	-0.035	-0.012
0.10	-0.06	-0.018

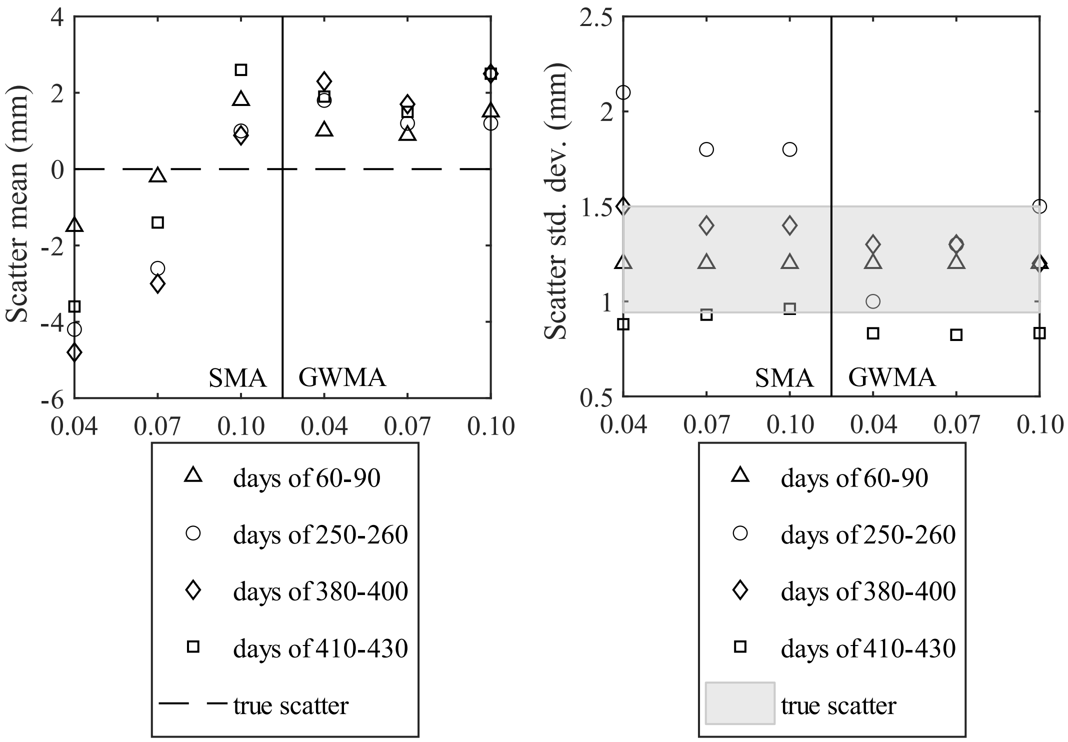

Figure 3- 19. Mean and standard deviation of scatter inferred by SMA and GWMA in comparison with true scatter in the displacement of Geocube 46

3.5. Discussion

Previous studies dedicated to landslide monitoring consistently adopt SMA for scatter minimization in displacement data. However, the adequacy of this filter and the effect of bandwidth selection were not well understood. Analyzes conducted on synthetic databases in this study using a roughness factor (J_2) demonstrate that at least 4% of the total observations should be fed into the filter to ensure fluctuations are sufficiently reduced.

The results of this study show that SMA tends to considerably distort the underlying trend at a bandwidth ratio of 0.10 (Figure 3- 8 and Figure 3- 9), and its lagged response with respect to real-time monitoring is almost three times that of GWMA results. As a result, a bandwidth ratio between 0.04 and 0.07 is suggested. However, we caution that the bandwidth should be selected with complete awareness that SMA is highly sensitive to bandwidth, and sensitivity analyses on bandwidth are recommended when defining an EWS. Corresponding observations were made during the analysis of displacement data from Geocubes installed on the Ten-mile landslide.

Error calculations show that GWMA and SG outperform SMA in both direct and indirect filtration and are more successful in preserving the true displacement trend. The near-zero lagged response of SG makes it a notable candidate for developing an EWS. Nonetheless, its intrinsic shortcoming in handling peaks, leading to a pulsating effect, will pose challenges for its utilization. The bandwidth range used for SMA is also suggested to be applied with the SG filter.

GWMA results suggest a proper trade-off can be achieved between minimizing the lag time and scatter and avoiding the pulsating effect. Compared to SMA and SG, GWMA is less sensitive to changes in the bandwidth. Analyses focused on the Geocube data also confirm that GWMA is capable of constraining the fluctuations in the velocity diagram while not attenuating variations in the displacement rate diagram. Moreover, the lag quantification chart proposed could reliably capture the required shift with a greater degree of confidence in comparison to SMA even at the largest bandwidth ratio studied here (0.10). The bandwidth for GWMA can therefore range from 0.04 to 0.10. Moreover, we observed consistency between direct and indirect filtration results using GWMA but greater differences when using SMA or SG results. This was especially the case in the early parts of the datasets and at some locations where outlier elimination was likely ineffective.

Filter and bandwidth selections should not be arbitrarily or purely empirical, as differences in outcomes can be substantial. An automated surveillance system for landslides demands stability in filter performance for a variety of circumstances, considering the ground can experience irregular sequences of acceleration and deceleration. The results here suggest practice moves away from the adoption of SMA due to the limitations discussed. SG demonstrates some inconsistent or erratic performance for certain displacement trends, which is detrimental although overall the error is smaller than for SMA. On the balance of its strengths and limitations as evaluated in this study, GWMA appears to be the more robust approach.

3.6. Conclusions

This study evaluated the suitability of SMA, GWMA, and SG filters for scatter reduction of datasets targeted for use in an EWS. A total of different 12 scenarios with harmonic and instantaneous changes were synthetically generated and random variations with Gaussian distribution were then added to produce unfiltered results. The three filters considered were then each applied with different bandwidths and the error computed. These filters were also successfully applied to the records from two Geocubes installed on the Ten-mile landslide. The results led to the following conclusions:

- When used for direct filtration of harmonic scenarios, the error resulting from the GWMA approach is approximately one-third that of the SMA approach. The SG approach results in near-zero error regardless of the values of the bandwidth ratio and n/t. When used for direct filtration of instantaneous scenarios, the superiority of SG is no longer unconditional and depends on the bandwidth ratio; this reflects the fact that SG cannot appropriately handle peaks in the velocity diagram.

- When used for indirect filtration of harmonic scenarios, SG again outperforms the other methods. The error associated with GWMA is marginally less than for SMA. These observations are not valid when the filters are applied to instantaneous scenarios, as GWMA results in less error than SG at bandwidth ratios above 0.03.

- Detailed investigations with Scenarios 11 and 12 demonstrate that SMA distorts the underlying trend by displacing and sometimes neglecting peak(s), while GWMA and SG tend to preserve them somewhat similarly.

- Due to the presence of negative weights in the SG kernel, some artificial smaller troughs and peaks are created after major peaks. This phenomenon, referred to herein as a pulsating effect, results in an unfavorable performance of SG on the velocity and displacement diagrams, especially in the presence of outliers.

- Investigations on the roughness factor reveal the bandwidth ratio should be at least 0.04. Taking this into account, GWMA seems to be the most reasonable option as the related uncertainties are much smaller than for SG and the error is acceptable and less than for SMA.

- A consequence of using asymmetric windows in the filtering process is a lag in the SMA and GWMA results that increases with increasing bandwidth ratio. Lag quantification suggests a correlation between the needed shift and bandwidth ratio that can be used to eliminate the lag. SMA requires approximately three times the shift of GWMA on average.

- Application of these filters to displacement data reported by Geocubes shows SMA and SG are unable to properly handle data points at the beginning of the dataset (i.e., near the boundary) in indirect filtration of the velocity diagram. Moreover, SMA and SG are inclined to respectively underestimate and overestimate peaks and fluctuations in the velocity diagram. Overall, GWMA provides the most reliable filtered values for velocity with no distinct difference between direct and indirect filtration.

Appendix 3.A

Consider a polynomial of degree *k* that is intended to be fitted over an odd number of points denoted as *z*. The weighting coefficients of the Savitzky-Golay filter can be extracted from the first row of matrix *C* (Eq. 3. 7):

$$C=\left(J^{T}J\right)^{-1}J^{T}, \tag{3. 7}$$

where *T* operator is the transpose of a matrix and *J* is the Vandermonde matrix, with elements at the *i*th row and *j*th column ($1 \le i \le z$ and $1 \le j \le k+1$) that can be achieved as follows (Eq. 3. 8):

$$J_{ij}=m_{i}^{j-1}, \tag{3. 8}$$

where *m* is the local index of points ($-(z+1)/2 \le m \le (z+1)/2$). As an example, the kernel of an SG filter that fits a quadratic polynomial (k=2) over seven points (z=7) is attained here. In the first step, *J* is set up as follows (Eq. 3. 9):

$$J=\begin{bmatrix} 1 & (-3)^1 & (-3)^2 \\ 1 & (-2)^1 & (-2)^2 \\ 1 & (-1)^1 & (-1)^2 \\ 1 & (0)^1 & (0)^2 \\ 1 & (1)^1 & (1)^2 \\ 1 & (2)^1 & (2)^2 \\ 1 & (3)^1 & (3)^2 \end{bmatrix}. \tag{3. 9}$$

Then, using Eq. 1, matrix *C* is computed as Eq. 3. 10:

$$C=\begin{bmatrix} -0.0952 & 0.1429 & 0.2857 & 0.3333 & 0.2857 & 0.1429 & -0.0952 \\ -0.1070 & -0.0714 & -0.0357 & 0 & 0.0357 & 0.0714 & 0.1071 \\ -0.0595 & 0 & -0.0357 & -0.0476 & -0.0357 & 0 & 0.0595 \end{bmatrix}. \tag{3. 10}$$

The second and third rows of *C* are the coefficients to find the filtered values' first and second derivations at the point of interest, respectively.

Chapter 4: Algorithms to Enhance Detection of Landslide Acceleration Moment and Time-to-failure Forecast Using Time-series Displacements

---

Contributions of the Ph.D. Candidate

The material presented in this chapter, including the literature review, conceptualization, methodology development, analysis, draft preparation and revisions, are conducted by the Ph.D. candidate. The supervisors, Dr. Michael Hendry and Dr. Renato Macciotta, have reviewed all pieces presented in the published manuscript, cited below:

Sharifi S, Macciotta R, Hendry MT, 2022. "Algorithms to enhance detection of landslide acceleration moment and time-to-failure forecast using time-series displacements", *Engineering Geology*, 106832. https://doi.org/10.1016/j.enggeo.2022.106832.

Contributions of This Chapter to the Overall Study

Detecting the onset of acceleration (OOA) and forecasting failure time are the two most critical aims of EWSs, and the application of scatter filters directly influences the outcome. Following the framework discussed in the previous chapter, such influences are studied on failing and accelerating scenarios in this chapter. To include a broad range of circumstances, OOA was varied between the early and late stages of the monitoring period and the curvature of the failing scenario was adjusted as well as all the previous factors explained before. The separation of actual OOA and the interpreted OOA after application of SMA, GWMA and SG is plotted on a cumulative probability diagram to assess the reliability of each filter in detecting OOA probabilistically. The error in forecasting failure time was studied both using a synthetic database and 17 datasets of failed cases from the literature. The findings of this chapter deliver the objective #2.

Abstract

Landslide monitoring data are characterized by scatter that can make the velocity and acceleration of a landslide unclear. The presence of scatter can therefore influence the reliability of an early warning system (EWS) too. Data filters such as simple moving average (SMA) are commonly used to reduce scatter in the data and enhance the reliability of EWSs. Therefore, evaluating the adequacy of these filters to reproduce displacement characteristics representative of the landslide is important. Gaussian-weighted moving average (GWMA) and Savitzky-Golay (SG) filters are examined here against SMA. To this aim, a comprehensive numerical analysis of a synthetic database was carried out on accelerating scenarios to quantify the reliability of each filter to detect the onset of acceleration and forecast the failure time using the inverse velocity method. GWMA and SG applications in the synthetic scenarios reached reliability thresholds of 90% at 30% and 4% of the corresponding time by SMA, respectively, and provided a timelier capture of moment patterns. Specifically, these synthetic cases show the application of GMWA and SG improves failure time forecasting by 60 to 80% and 90 to 100%, respectively, compared to SMA depending on the amount of data used by the filter and the remaining time to failure. Additionally, nine failed cases (17 datasets) from the literature were examined after employing these three filters. Results of these cases show using alternatives to SMA would increase the accuracy of failure time forecasts by 60%.

Keywords: Landslide; Early Warning System; Inverse Velocity Method; Simple Moving Average; Gaussian-Weighted Moving Average; Savitzky-Golay.

4.1. Introduction

Landslides cause significant life and economic loss every year around the world (Schuster & Highland, 2001; Clague & Bobrowsky, 2010). Monitoring and early warning systems (EWS) have been successfully adopted as a strategy to mitigate landslide risks. An EWS acts as a central unit in which measurements (e.g., in-situ and remote displacement measurements, piezometric data) from a variety of monitoring instruments are processed so that the EWS can provide appropriate warnings for decision-makers to take appropriate action (e.g., mining geotechnical teams, municipalities, ministries of highways, railway operators). Based on case histories, published recommendations, and tolerable risk levels, an EWS provides a warning if a transgression is detected against pre-set thresholds of study parameters such as displacement, velocity, acceleration or even precipitation, depending on the EWS's configuration (Ju et al., 2020). Commonly explained by creep theory, the evolution of a landslide deformation from early movements to failure is divided into three phases of primary, secondary and tertiary. The primary or transient phase, characterized by a logarithmically decreasing displacement rate, is followed by the second stage in which the ground travels at a constant velocity (balanced state). In the last stage, its kinematics exponentially evolve when the collapse (rupture) takes place, and the slope fails (S. Wang et al., 2020; X. Hu et al., 2021). The onset of acceleration (OOA), marking the transition from secondary to tertiary phase, can be an alarming sign in monitoring such geohazard (Zavodni & Broadbent, 1978; Carlà, Intrieri, et al., 2017; Chang & Wang, 2022). This is also reflected by Scoppettuolo et al. (2020) in which phenomenological models of 18 well-documented landslides are gathered. Timely detection of OOA and reliable failure time forecasting (FTF) are the two most crucial tasks of a reliable EWS. In this paper, slope failure is recognized as the collapse of the slope followed by rapid downslope movement of the failed mass and serviceability failure modes associated with large slope deformations are outside the scope of this paper.

The relationship proposed by Saito & Uezawa (1961) was an early attempt to deliver FTF in which the logarithm of time to failure was correlated to the strain rate. Later, Fukuzono (1985b, 1985a, 1990), following the work of Saito (1969), developed a methodology, known as the inverse velocity method (INV), by experimenting on artificial slopes and using creep theory (Eq. 4. 1):

$$\frac{1}{v}=[A(\alpha\text{-}1)]^{\frac{1}{(\alpha\text{-}1)}}(t_f\text{-}t)^{\frac{1}{(\alpha\text{-}1)}}, \tag{4. 1}$$

where v is the landslide velocity, t is time, t_f is the failure time, and A and α are empirical constants. α mainly controls the shape of the inverse velocity diagram (linear, convex, or concave; Figure 4- 1) and is typically in the range of 1.0 to 3.0 (Intrieri et al., 2019). As indicated in Figure 4- 1, the diagram is linear when α =2. This makes the FTF simple and previous research suggests that, with some tolerable deviation, this parameter can be generally approximated as 2.0 (Rose & Hungr, 2007; Segalini et al., 2018). Linear INV is not the only graphical method proposed for FTF as other methods have been proposed by, for example, Mufundirwa et al. (2010) and Hao et al. (2017), but these methods have not been as widely adopted as INV because of complicated implementation or somewhat similar accuracy to INV.

Although the INV has the advantage of balancing simplicity and accuracy, it has certain limitations. First, this method is devised based on ideal and controlled laboratory conditions (Rose & Hungr, 2007) to which real situations do not necessarily conform (i.e., heterogeneity in material properties or variation in applied stress). Second, INV is susceptible to the existence of scatter because any variation from the actual displacement is propagated through differentiation and inversion, causing considerable error in FTF (Carlà, Intrieri, et al., 2017; Ju et al., 2020; X.-P.

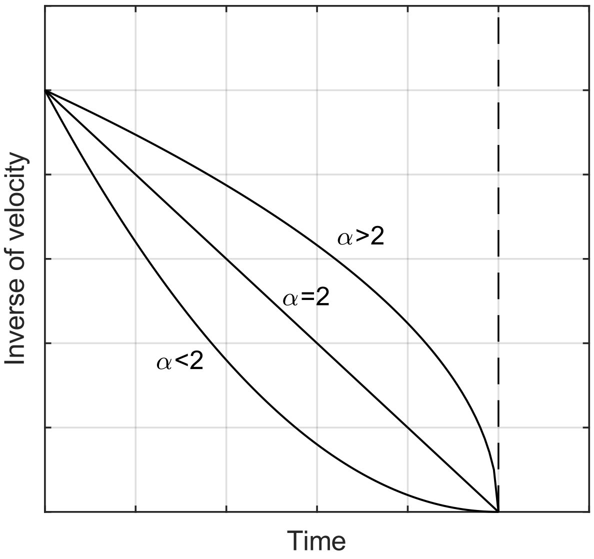

Figure 4- 1. The schematic variation of inverse velocity values for α *values equal to, greater than, and less than 2*

Zhou et al., 2020). Therefore, these two factors lead to dispersed inverse velocity values that make FTF challenging and disputable. To account for these shortcomings, different techniques have been adopted, such as applying filtration algorithms to reduce scatter (Rose & Hungr, 2007; Mufundirwa et al., 2010; Carlà, Farina, et al., 2017; Carlà, Intrieri, et al., 2017; Intrieri et al., 2018; Carlà et al., 2019), following a probabilistic approach rather than offering a deterministic result (Miao et al., 2018; J. Zhang et al., 2020), and abandoning the creep theory to use other physical explanations such as visco-plastic model (Herrera et al., 2009) or employing novel evolutionary computation programming (Lian et al., 2015; W. Yao et al., 2015; C. Zhou et al., 2016; W. Zhang et al., 2019; Deng et al., 2021; X. Hu et al., 2021). Moreover, evolutionary algorithms are known as data-driven methods, meaning they execute predictions based on historical data, and overlook discrepancies with proceeding patterns of landslide movements unless complex, algorithm training techniques are adopted, which can also be computationally intensive. We propose that, when scatter reduction is performed with sufficient understanding of the filter function, this solution can be the most practicable method that provides adequate information about landslide kinematics.

Scatter in readings of *in situ* and remote sensing techniques obscure the true values of displacement and velocity (Benoit et al., 2015; Hendry et al., 2015; Journault et al., 2018; Deane et al., 2020; Woods et al., 2020, 2021; Roy et al., 2022; Sharifi, Hendry, & Macciotta, 2022; Sharifi, Hendry, Macciotta, et al., 2022). To minimize this effect, the simple moving average (SMA) is frequently used to process displacement monitoring data for EWSs. While there is no theoretical limitation to applying SMA to parameters that are different in nature such as pore-water pressure (Pecoraro & Calvello, 2021) or even footing displacements (Sharifi, Abrishami, Dias, et al., 2022), this study only focuses on displacement and its derivatives hereafter. SMA (Eq. 4. 2) simply calculates the average of neighbouring points values and uses it as the filtered value (Macciotta et al., 2016):

$$\hat{y}_i = \frac{\sum_{i-\frac{p-1}{2}}^{i+\frac{p-1}{2}} y_j}{p}, \tag{4. 2}$$

where $\hat{y}_i$ is the filtered value, y_j is the unfiltered value, and p is the averaging window length (also known as bandwidth). SMA has been employed in many previous studies given its simplicity. Intrieri et al. (2018) derived the displacement of the Maoxian landslide (Mao County, Sichuan Province, China) from synthetic-aperture radar (SAR) images attained by the Sentinel-1 satellite and used SMA with a window size of 5 days to process the data. The application of INV to the processed data showed filtration was successful in estimating the failure time with an acceptable degree of accuracy. Carlà et al. (2019) also studied the Maoxian landslide and failure of a tailings dam embankment at Cadia gold mine (New South Wales, Australia) using three-point window SMA and INV. Carlà, Intrieri, et al. (2017) examined the performance of SMA and an exponential filter (Eq. 4. 3) as applied to events including Mount Beni, the Vajont landslide, Stromboli, and the collapse of a medieval city wall in Volterra:

$$\widehat{v}_t=\beta\cdot v_t+(1-\beta)\cdot \hat{v}_{t-1}, \tag{4. 3}$$

where $\widehat{v_t}$ is the filtered velocity at time t, v_t is the unfiltered value, $\hat{v}_{t-1}$ is the previous filtered value, and β is a filtering factor (assumed as 0.5 in Carlà et al. 2017a Carlà, Intrieri, et al., 2017). They show SMA outperforms the exponential filter in terms of FTF. To improve the credibility of EWSs and avoid false FTF, they recommended establishing a failure window in which the failure is considered most probable. This task comprises performing two parallel SMAs with two different bandwidths, called the short-term moving average (p=3) and the long-term moving average (p=7). The extents of these windows are $[t_{\text{short SMA}}-\frac{\Delta}{2};t_{\text{long SMA}}+\frac{\Delta}{2}]$, where $t_{\text{short SMA}}$ and $t_{\text{long SMA}}$ are the forecasted failure time using inverse velocity values filtered by the short- and long-term moving average, respectively, with their difference denoted as Δ . Although this method is a step forward from a purely deterministic approach, it is still not completely probabilistic because no probabilities are quantified. Additionally, it does not state how p values for the short and long term should be chosen if the measurement frequency is different than what is reported in their study. We propose that when a more suitable filter is used in the data processing, the resulting failure window can be reduced or might be unnecessary from a practical perspective. Grebby et al. (2021) also reported they were able to detect precursory deformations of Brumadinho Tailing Dam prior to the collapse in 2019 and practiced INV for FTF. They applied a 3-point SMA to the time-series data inferred from SAR interferometry to minimize the residual scatter from atmospheric phase screening.

The effect of scatter can also be critical when data frequency is high, as it is in the case of most novel monitoring technologies such as a Geocube system working on the global navigation satellite system (GNSS) with an acquisition frequency of one positioning measurement every 60 seconds (Macciotta, Rodriguez, et al., 2017). Sharifi, Hendry, Macciotta, et al. (2022) present a detailed study on high-frequency monitoring data filtration with SMA and two alternative filters called Gaussian-weighted moving average (GWMA – Eq. 4. 4) and Savitzky-Golay (SG – Eqs. 4. 5-4. 6). GWMA is a modified version of SMA, with the inclusion of a weighting constant (*w*) applied to the data within the moving window. The weighting constant follows the Gaussian distribution, giving the largest weight to the point in time when the average is calculated and decreasing weight as the temporal distance increases. SG, on the other hand, fits a low-degree polynomial on a window of points and estimates the filtered value based on the fitted function. SG can be interpreted as a weighted average approach using least-squares equations to define the weights following the low-degree polynomial fit:

$$\hat{y}_i = \sum_{i-\frac{p-1}{2}}^{i+\frac{p-1}{2}} w_j y_j, \tag{4. 4}$$

$$\hat{y}_i = \sum_{i-\frac{p-1}{2}}^{i+\frac{p-1}{2}} C_{1j} y_j, \tag{4. 5}$$

$$C = \left(J^T J\right)^{-1} J^T, \tag{4. 6}$$

where *i* corresponds to all data points, *j* corresponds to the data points in the filtration window, *T* is the transpose operator, *J* is the Vandermonde matrix with 2*n*+1 rows and *m*+1 columns (*n* is the number of points in the filtration window and *m* is the degree of polynomial to be fitted; 2 here), and C_1 is the first row of matrix C that provides the weights considered in the SG filter. Figure 4-2 displays an example of the performance of GWMA (Eq. 4. 4) and SG (Eq. 4. 6) along with their weight distribution for a 13-point filtration window.

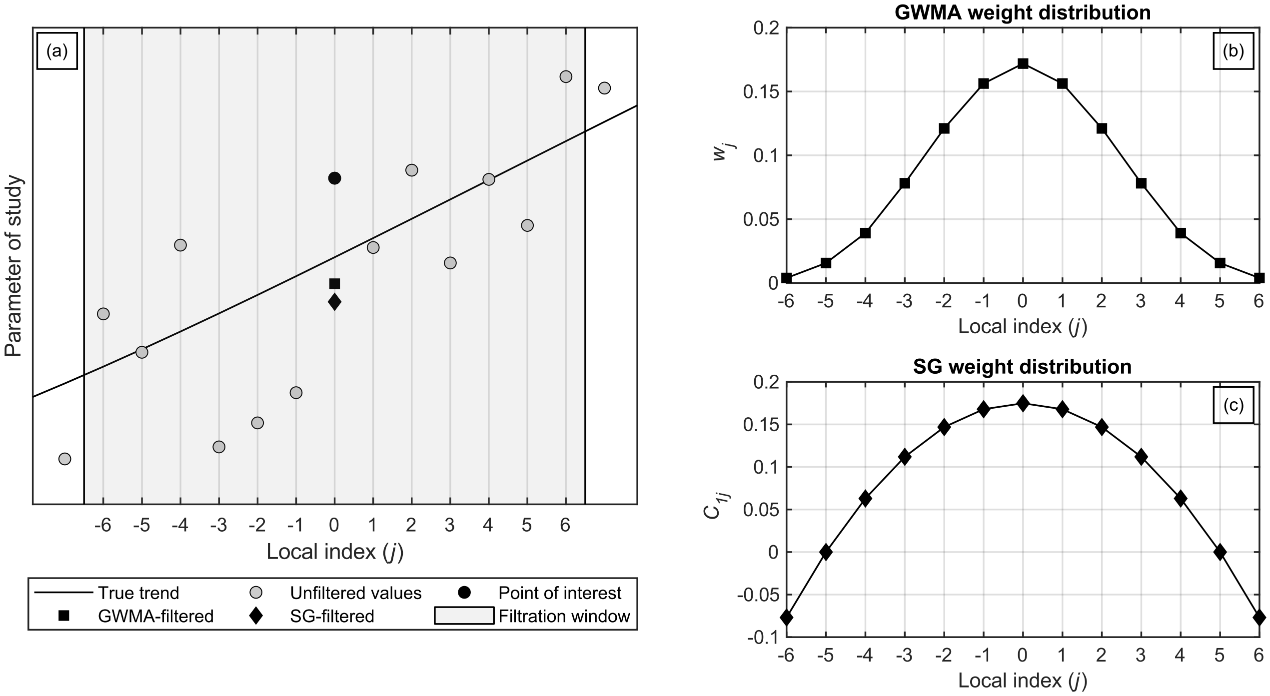

Figure 4- 2. (a) Performance of GWMA and SG on an example dataset using a 13-point window, weight distribution of (b) GWMA and (c) SG

Sharifi, Hendry, Macciotta, et al., (2022) highlighted that the significance of the data filtration step in landslides monitoring has been unheeded in most previous works. To this end, they adopted a method called numerical analysis of a synthetic database in which all three of these filters were applied to synthetically generated scenarios with a variety of acceleration-deceleration trends and temporal resolutions. The Ten-mile landslide located in southwestern British Columbia, Canada was also examined as an example of practical application. To account for real-time monitoring, an asymmetric window was used in their study, meaning that only precedent measurements were considered in the filtration process. They concluded that GWMA and SG managed to minimize the scatter while causing minimum distortion to the data trend, in contrast to SMA which tends to alter the trend significantly.

This paper evaluates the performance of SMA, GWMA, and SG for FTF, and quantifies the reliability of these three filters to identify OOA in the real-time function of an EWS on a local scale. The work uses numerical analysis of synthetic cases and nine case histories (17 datasets) reported in the literature as test data for this purpose.

4.2. Methodology

4.2.1. Synthetic Data Generation

The method of numerical analysis of a synthetic database (Sharifi et al., 2021; Sharifi, Hendry, Macciotta, et al., 2022) is used here to investigate the performance of SMA, GWMA, and SG for FTF. In this technique, a pre-defined trend of the study parameter (e.g., displacement) is generated and a random scatter set is added to simulate a sample of observations similar to what instruments report. This framework allows one to make quantitative comparisons between the performance of different filters by taking advantage of knowing the true (scatter-free) values, which are not available in real monitoring data. The accuracy of conclusions made from this method will, however, primarily depend on: 1) the consistency of the statistical properties between synthesized and true scatter and 2) the representativity of the synthetic scenarios' trends to the kinematics of real landslide events and their pre-failure behaviour.

In this study, the statistical distribution of the random scatter set was assumed as Gaussian. This decision was made based on the central limit theorem in probability theory, stating that the summation of independent random variables goes toward a normal (Gaussian) distribution (S. W.

Smith, 2013), as also shown by Macciotta et al. (2016) and Sharifi, Hendry, Macciotta, et al. (2022) for landslide deformation measurements.

Two different types of landslide scenarios are generated: accelerating and failing. The former is produced by a simplified bi-linear trend (Scoppettlo et al., 2021) as depicted in Figure 4- 3a with the mathematical expression presented in Eq. 4. 7, and the latter is the result of using Eq. 4. 8 (depicted in Figure 4- 3b), which is the back-calculated expression of INV (Eq. 4. 1):

$$d=\frac{1}{2(1-t_{OOA})}[|t+t_{OOA}|+|t-t_{OOA}|]-\frac{t_{OOA}}{1-t_{OOA}}, \tag{4. 7}$$

$$d=\left(\frac{\alpha-1}{2-\alpha}\right)[A(\alpha-1)]^{\frac{1}{1-\alpha}}(t_f-t)^{\frac{2-\alpha}{1-\alpha}}+c, \tag{4. 8}$$

where t and d are dimensionless and normalized time and displacement, respectively; t_{OOA} is the designated time of OOA, which holds a value between 0 and 1; A and α are the same parameters as defined for Eq. 4. 1; t_f is the failure time, which is assumed to be 1 for the synthetic data; and c is an integral constant to make the initial location 0 (Eq. 4. 9):

$$c=\left(\frac{\alpha-1}{\alpha-2}\right)[A(\alpha-1)]^{\frac{1}{1-\alpha}}, \tag{4. 9}$$

The parameter A is assumed as $1/(\alpha\text{-}1)$ to make the inverse velocity diagram normalized between 0 and 1, without overriding any condition. Notably, monitoring instruments provide discrete information in time contrary to the above continuous mathematical equations. The generated scenarios, therefore, consisted of discrete points that follow the equations presented. The number of points generated was varied to evaluate a range of data acquisition frequencies within the normalized time interval of 1. These are presented in Table 4- 1 along with their corresponding time period. These numbers were selected to cover appropriate time ranges with respect to various measurement frequencies.

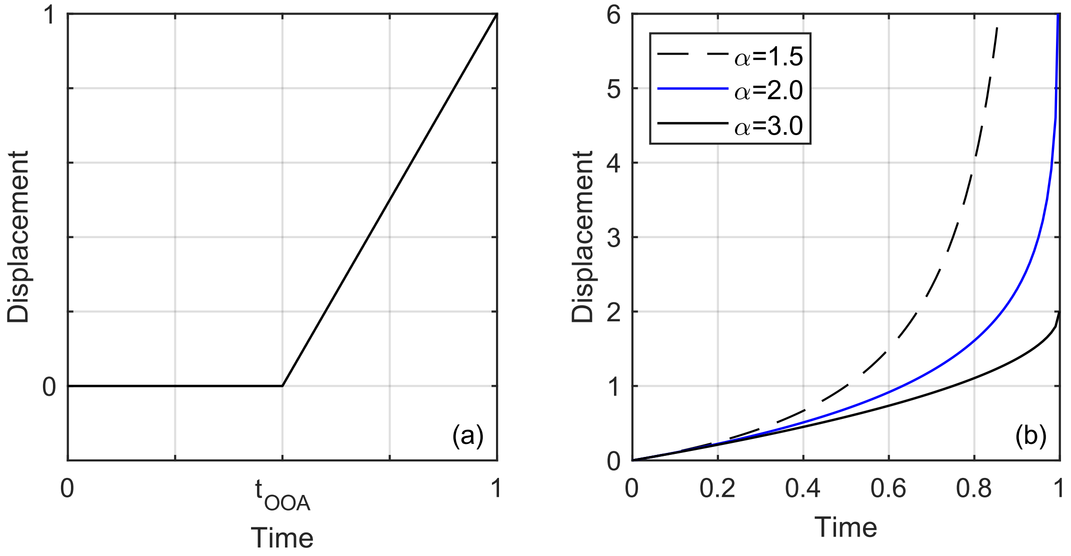

Figure 4- 3. Two categories of synthetically generated cases: (a) accelerating and (b) failing

Table 4- 1. Number of points used to generate synthetic cases and the corresponding time period with regard to frequencies of 1 minute, 1 hour, and 1 day.

Number of points	Example monitoring frequency					
	1-min readings		1-h readings		1-d readings	
50	50	minutes	2.0	days	1.6	months
100	1.6	hours	4.1	days	3.3	months
1,000	16.6	hours	1.3	months	2.7	years
10,000	6.9	days	1.1	years		
50,000	34.7	days	11.5	years		
100,000	2.3	months				
500,000	1	year				
1.00E+6	2	years				

The scatter sets were normalized within a range of values between ±1 and followed a normal distribution with a mean of 0 and a standard deviation of 0.2. Before superimposing the scatter sets on the synthetic scenario trends, they were scaled to represent different variability levels (VLs), with values of 0.001, 0.005, 0.010, 0.050, 0.100, and 0.15 (Sharifi, Hendry, Macciotta, et al., 2022). These six VL values along with the fact that scenarios are normalized and constructed with a variety of point frequencies (Table 4- 1) allow for the evaluation of scenarios that represent a wide range of data scatter and monitoring frequencies. Figure 4- 4 shows examples of an accelerating scenario with t_{OOA}=0.5, and a failing scenario when α=2, after the addition of scatter with *VL*=0.10.

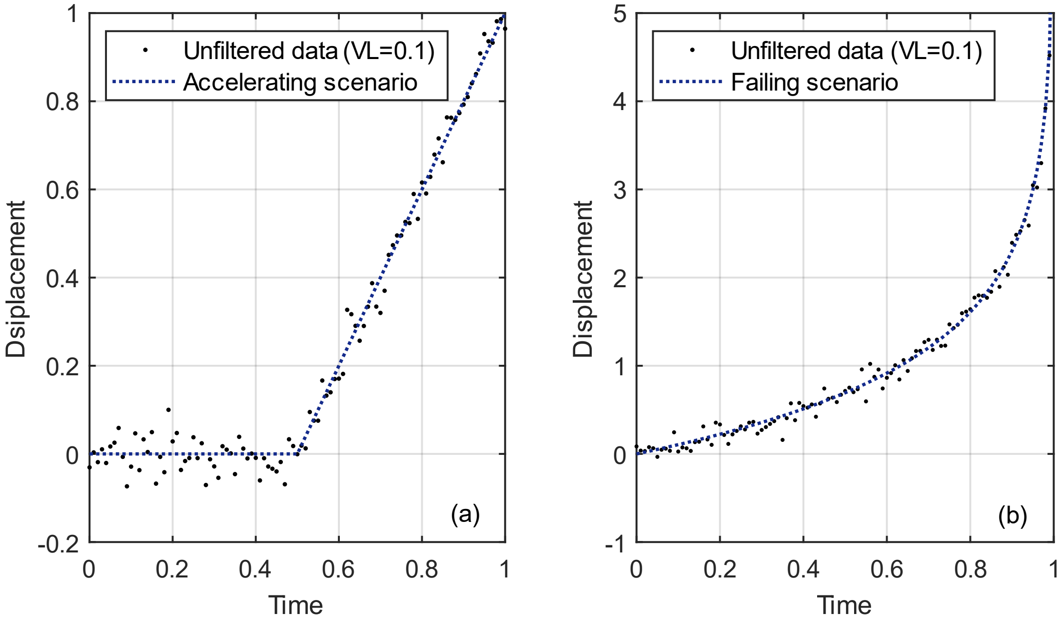

Figure 4- 4. Samples of unfiltered synthetic cases along with their true underlying trend at VL=0.10: (a) accelerating case and (b) failing case (α=2)

4.2.2. Procedure for Evaluating Filter Performance

To quantify the reliability of filters for OOA detection, accelerating scenarios with t_{OOA} values between 0.1 and 0.9 were generated at 0.1 intervals and scatter sets were superimposed to define the unfiltered synthetic databases. Filters were then applied with bandwidths of 0.04, 0.07, and 0.10 of the total number of points, referred to as the bandwidth ratio (BR). These values were selected based on Sharifi, Hendry, Macciotta, et al. (2022), who report this as the most reliable range in which an acceptable minimum fluctuation is achieved while also maintaining the error and lag at tolerable levels. Only preceding data to the time of evaluation of the filter were considered in the filtering process at each point of interest to simulate real-time monitoring.

Application of this asymmetrical window leads to a lagged response of filters, and increasing the bandwidth increases the lag (Sharifi, Hendry, Macciotta, et al., 2022). A function following Eq. 4. 7 was then fitted to the filtered diagram using the least-squares method without imposing the t_{OOA}, and the algorithm was allowed to freely detect the OOA point based on the filtered values. The temporal separation of detected OOA and originally designated OOA is considered the error of the filter with respect to the identification of OOA. The cumulative probability function (CPF) of that error (for all scenarios modelled) illustrates the delay in identifying the OOA when employing each filter. To compute the CPF, a total of 1296 accelerating scenarios were synthesized and analyzed for each filter.

Unfiltered failing scenarios were generated following INV characteristics for α =1.50, 2.0, and 3.0 and the six VL values to investigate the accuracy of the filters for FTF purposes. SMA, GWMA, and SG filters were then applied to these scenarios using the BRs used before (0.04, 0.07, and 0.10). The predicted failure time was then extrapolated using Eq. 4. 1 (inverse velocity curves) as fitted from the filtered values. In an ideal situation, filtration does not cause any lag or trend distortion, the scatter is entirely eliminated, and the predicted failure time would match the designated failure time (t=1). Life expectancy diagrams are usually used to show the time-to-failure at specific times, and Figure 4- 5 is an example. FTF can improve as monitoring progresses towards the defined (for synthetic data) or observed time of failure (Figure 4- 5). The error between the predicted and the "true" time of failure for GWMA and SG can be compared to the error when using SMA (commonly adopted). This is done by calculating an error ratio (Eq. 4. *10*):

$$\text{Error ratio}=\frac{\text{Error in GWMA or SG predictions}}{\text{Error in SMA predictions}}. \qquad (4.10)$$

This same process was adopted to evaluate the case history data, with filters sometimes applied on displacement or velocity values depending on data availability. If velocity is the parameter of interest, the filtered value can be obtained in two ways: direct or indirect filtration. Direct filtration means the filter is applied directly to the velocity values computed from unfiltered displacements; indirect filtration means the displacement values are first filtered and then the velocities calculated. Direct and indirect filtration do not produce significantly different results (Sharifi, Hendry, Macciotta, et al., 2022), and thus the availability of either velocity or displacement values from case history data did not influence the assessments in this paper.

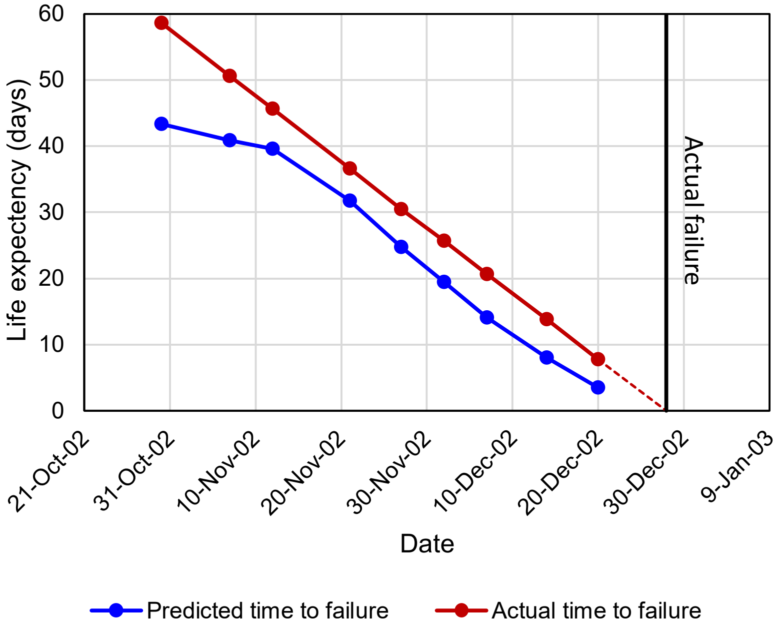

Figure 4- 5. An example of life expectancy diagram (distometric base 1-2 installed on Mt. Beni) (Carlà, Intrieri, et al., 2017)

4.3. Study Sites

Table 4- 2 shows the 17 datasets used for this study, from nine case histories. The objective was to apply and evaluate the filters to different failure characteristics, including geology, failure mechanism, and different values of fitting parameter α for INV. The α value of sets 15 and 16 was

back-calculated as a part of this investigation given they were not reported in the corresponding references. For set 16, the average displacement values of all accelerating points were used. Sets 4, 15, and 16 do not conform to the usual assumption of linearity in the inverse velocity diagram as they hold α values other than 2. Because bypassing such a parameter in FTF is not within the scope of this investigation, back-calculated values as reported in Table 4- 2 were used in the analyses, which means convexity/concavity of the inverse velocity diagram was regarded as a known factor. This will allow for comparisons between filters; however, assumptions of the shape of the INV response can be critical to the reliability of FTF as presented in Figure 4- 6.

Some of the available datasets were omitted as they did not comply with the assumptions in this research of scatter, having an average of 0 around the displacement trend. For example, the raw inverse velocity values of distometric base 15-13 installed on the eastern flank of Mt. Beni are shown in Figure 4- 7 (after Carlà, Intrieri, et al., 2017). Any regression line would lead to an unbalanced distribution of scatter due to the points highlighted within the red circle (mean of scatter for the moving window would not be 0 with respect to the true trend), which is an integrated assumption about scatter (S. W. Smith, 2013; Macciotta et al., 2016). These data points could be the result of measurement bias or human error, or real deceleration from the processes of slope progression towards collapse, not fully captured by the monitoring frequency. To eliminate variables in the comparison between filter reliability for SMA, GWMA, and SG, these datasets were not used for evaluation. Each case tabulated in Table 4- 2 was filtered iteratively by different window sizes in such a way that the BR would fall within the range from 0.04 to 0.10, similar to synthetic scenarios. You may find the collected datasets used for this study in Appendix A as they were published.

Table 4- 2. List of all case studies used in this investigation

Name	Location	Slope Materials	Mechanism	Destabilizing factor	Data used	Set number	α value	References
Mt. Beni	Florence, Italy	Ophiolitic breccias	Rockslide / Toppling	Quarry activities, precipitation	Baseline 1-2	[1]	1.99	(Gigli et al., 2011)
					Baseline 3-2	[2]		(Intrieri & Gigli, 2016)
					Distometric base 1-2	[3]		(Carlà, Intrieri, et al., 2017)
Creep test	Samples from Beijing, China	Granite	Creep failure	Loaded to initial stress and held at the constant stress	Sample 1	[4]	1.77	(Hao et al., 2017)
					Sample 2	[5]	2.03	
					Sample 3	[6]	2.20	
Delabole slate quarry	Cornwall, England	Quartz-chlorite-sericite slates	Progressive multi-block	Rainfall	West face movements	[7]	1.96	(Boyd et al., 1973; Coggan & Pine, 1996)
Vajont (Mt. Toc)	Italian Alps	Limestone and clay	Roto-Translation	Unknown	Benchmark 50	[8]	1.97	(Helmstetter et al., 2004)
					Benchmark 67	[9]		
					Unknown	[11]		(Voight, 1988)
					Benchmark 63	[12]		(Carlà, Intrieri, et al., 2017)
					Benchmark 5	[13]		
Mount St. Helens	Washington, United States	-	Volcano eruption	Magmatic flow	Crater diameter	[10]	1.96	(Voight, 1988)
Liberty Pit Mine	Utah, United States	Quartz monzonite	Rockslide	Blast, pore water pressure	Unknown	[14]	~2.00	(Zavodni & Broadbent, 1978; Rose & Hungr, 2007)

Coal mine	British Columbia, Canada	Mist Mountain and Morrissey formation	Retrogressive rotational failure	Mining activity and waste dump	GPS Point 105	[15]	2.8 ~ 2.9	(Clayton et al., 2020)
Cadia gold mine tailing dam	New South Wales, Australia	Rockfill and clay core	Progressive translational failure	Static liquefaction due to lateral movement of a weak layer near foundation	75 points attained by InSAR analysis	[16]	3.0 ~ 3.5	(Carlà et al., 2019)
Xinmo Maoxian)	Sichuan, China	Heavily jointed metamorp-hic sandstone	Progressive rock avalanche	Intense rainfall, and seismic activities in the region	49 points attained by InSAR analysis	[17]	1.93	(Intrieri et al., 2018; Carlà et al., 2019)

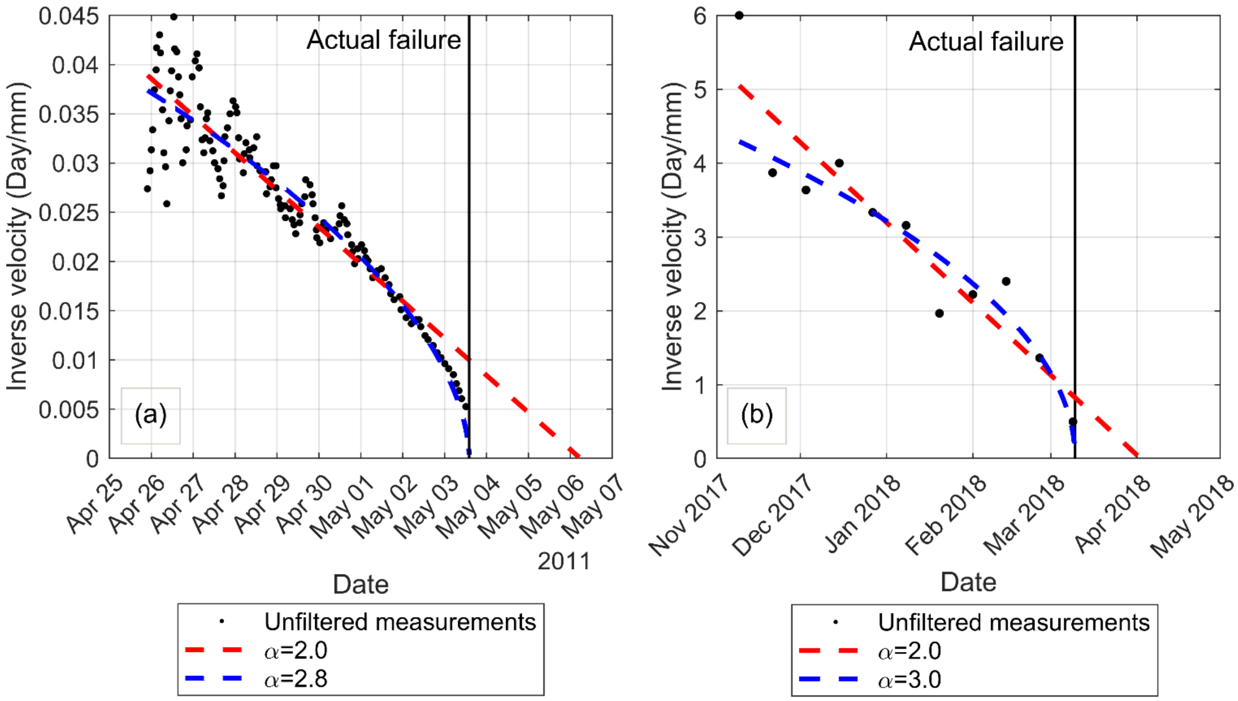

Figure 4- 6. Inverse velocity diagram of (a) case 15 and (b) case 16 along with projected failure time using linear and non-linear fitting

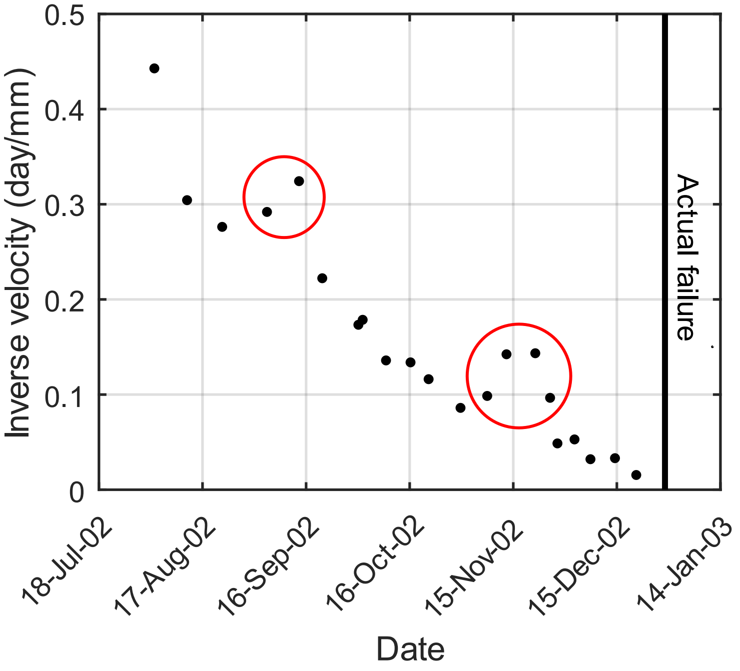

Figure 4- 7. Inverse velocity diagram for data from distometric base 15-13 installed on Mt. Beni (red circles mark data points with outlier trait)

4.4. Results and Discussion

4.4.1. OOA Reliability Results

Figure 4- 8 displays the CPF of error in OOA detection for each filter for all synthetic scenarios. In this figure, the horizontal axis (below) shows the error between the "true" and detected OOA in terms of data points. Normal distribution functions are also fitted to the error distributions for visualization and analysis. Above this diagram, three additional horizontal axes are provided to scale the normalized and dimensionless time to actual values based on the three different time periods (assuming 6 months, 1 year, and 2 years of data are represented by the full extent of data points generated). The mean and standard deviation of the three fitted distributions are provided in Table 4- 3. This table and Figure 4- 8 show SMA has the greatest skewness to the right, indicating that detection of OOA by SMA lags significantly in comparison to GWMA and SG filters. SG observations are somewhat symmetric to the zero-error axis, meaning almost 50% of SG observations have negative values. Importantly, and as shown in Table 4- 3 which contains the statistical indicators of fitted normal distributions, the spread of error (standard deviation) in SMA and GWMA are 8.67 and 3.18 times that of SG, respectively. The error distribution of GWMA and SMA results have considerable positive mean values, which are attributed to the lagged response that is characteristic of the averaging process incorporated in the formulation of SMA and GWMA. As a result, SG is insensitive to the asymmetric window, and partly attenuated sensitivity is seen in GWMA results due to the inclusion of weight constants near the evaluation time, as opposed to the equal weighting in SMA. The 90% threshold adopted for evaluation (90% of OOA identified are within this threshold) shown in Figure 4- 8 corresponds to errors of 0.003, 0.023, and 0.075 for SG, GWMA, and SMA filters, respectively. This means GWMA and SG have only 30% and 4% of the latency of SMA, respectively. These values, for example, correspond to

respective delays of 13 hours, 4 days, and 13.5 days to identify the OOA when the synthetic data represent readings for a 6-month period.

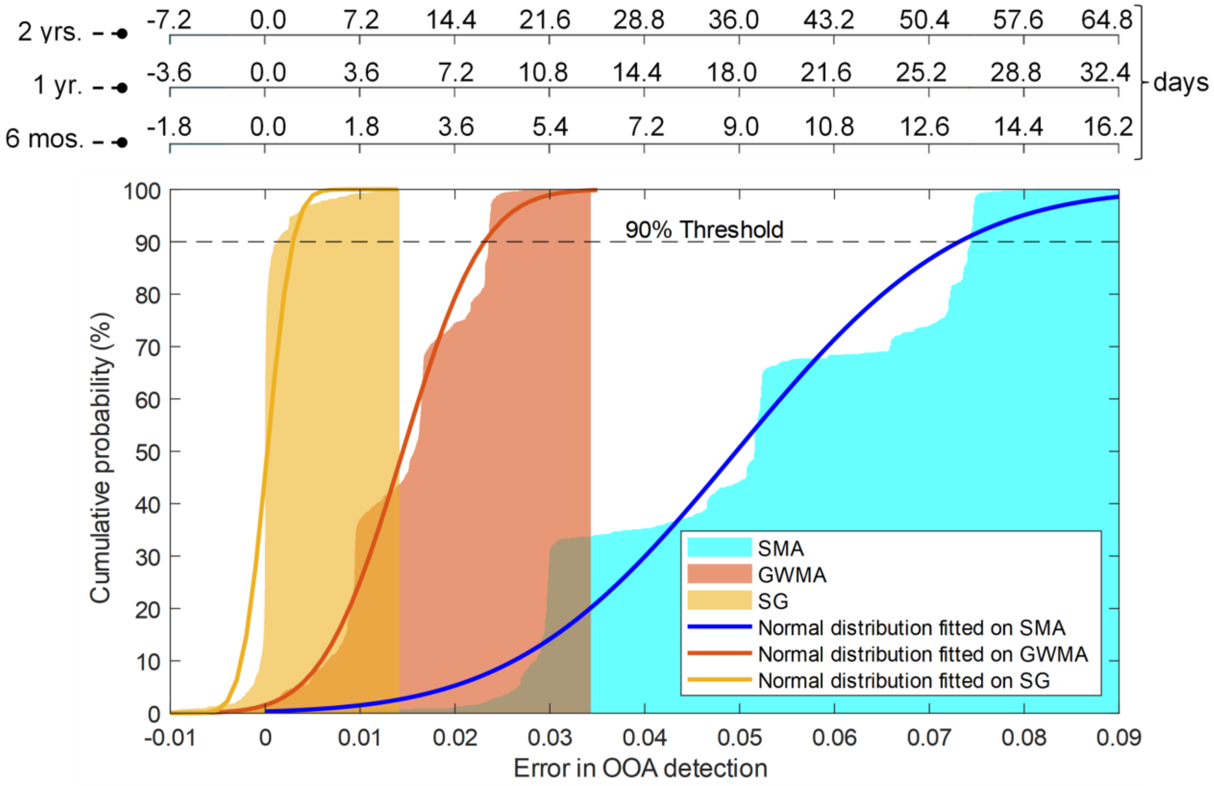

Figure 4- 8. CPF of OOA detection using SMA, GWMA, and SG filters on synthetic accelerating cases (top axes indicate actual time scales for time periods of 6 months, 1 year, and 2 years)

Table 4- 3. Mean (in days) and standard deviation (in days) of the fitted normal distribution for each filter along with the actual time corresponding to time periods of 6 months, 1 year, and 2 years.

	Mean				Standard deviation			
Time scale	Normalized	6 mos.	1 yr.	2 yrs.	Normalized	6 mos.	1 yr.	2 yrs.
SMA	0.04965	8.94	17.87	35.75	0.01831	3.30	6.59	13.18
GWMA	0.01449	2.61	5.22	10.43	0.00671	1.21	2.42	4.83
SG	0.00021	0.04	0.08	0.15	0.00211	0.38	0.76	1.52

4.4.2. Failure Time Forecast

4.4.2.1. Results of Numerical Analysis of Synthetic Database

The results of analysis on synthetic cases are presented in Figure 4- 9. This figure shows the average of errors calculated across different bandwidths as well as errors converted to the equivalent time corresponding to the three different monitoring periods as before (6 months, 1 and 2 years). The figure shows the greater accuracy of the GWMA and SG filters in FTF with little variations over time, with SG predictions being the closest to the true failure time. Figure 4- 9 shows the application of GWMA enhances the FTF by up to 60 to 80% in comparison to SMA; this improvement rises to 90 to 100% for SG depending on the α value and time to failure. In Figure 4- 9b, a deviation from general trend with outlier characteristic is seen at the time-to-failure of 0.01 for all filters. Given that scatters are randomly generated, their stochastic arrangement in the filtration window could lead to complicated interactions that cause these anomalies. Although these outliers were sometimes encountered, we observed that the general behaviour of results would not differ very much from one iteration to another. As a results, tools such as normalization (in case of error ratio), linear regression and statistical indicators (average, standard deviation, etc.) were used, where appropriate, to capture large-scale behaviour of population and minimize the impact of such erratic measurements.

The mean error ratios (Eq. 4. *10*) are plotted against time in Figure 4- 10. Linear fits in this figure show that all the error ratios are close to a linear trend and the discussed outliers are not evident here. The slopes of these lines display that error ratio diagrams of GWMA and SG have positive slopes toward the designated failure. This, according to Eq. 4. *10*, suggests that SMA accuracy improves relative to other filters for FTF as more information about the landslide motion is provided and the time of failure approaches. This trend is more pronounced when α=2.0 due to the synergy of the underlying linear trend in the inverse velocity diagram, with the tendency of SMA to arrange the data in a linear trend (Sharifi, Hendry, Macciotta, et al., 2022). 18% of all generated FTF for the synthetic scenarios, approximately equally distributed between GWMA and SG (9% each) , were not used in Figure 4- 9 and Figure 4- 10 as they held an absolute error ratio greater than 1. Most of the rejected data were generated with *VL* values of 0.10 and 0.15 and the small number of points. This led to insufficiency of BRs lower than 0.10 when either the *VL* value is high or few data are available. Higher BR values as much as 0.15 were used for those and it was partially successful to address the issue. However, the authors would like to caution against using BRs much higher than 0.10 as it would lead to a higher lag in the filtered response as well as imposing a larger computation burden with no or even negative effect on FTF. The latter statement regarding the paradox of bandwidth will be further discussed using the results of case histories in Section 4.2.2. The discarded points also corresponded to the initial points in scenarios, and for that, the boundary effect may be considered a culprit which happens with smaller data points fed into the filter, compared to the bandwidth. As a result, it appears the reliability of each GWMA and SMA to improve the FTF is 91%.

4.4.2.2. Results of Analysis of Case Histories

Error diagrams of all cases are presented in Appendix B. The error of FTF on the set 1, as an example, is shown in Figure 4- 11 with respect to the time-to-failure when applying SMA, GWMA, and SG with *p* values (bandwidth, or the window size of the moving average) ranging from 2 to 4 that on average translate into 10 to 20 days. The FTF error and error ratios of all datasets with respect to different p values as a result of projection at the last available data point are presented in Table 4- 4 and Table 4- 5. The following discussions are based on these tables and Figure 4- 11. Generally, as the remaining extent of the slope advances toward 0, the FTF performance of all filters tends to improve. This figure also illustrates that increasing the bandwidth leads to larger FTF errors, meaning that although increasing the bandwidth aims to reduce the scatter, it leads to a larger error for FTF (bandwidth paradox) caused by the increased lag in identifying changes in displacement trends. The bandwidth paradox is accentuated the most

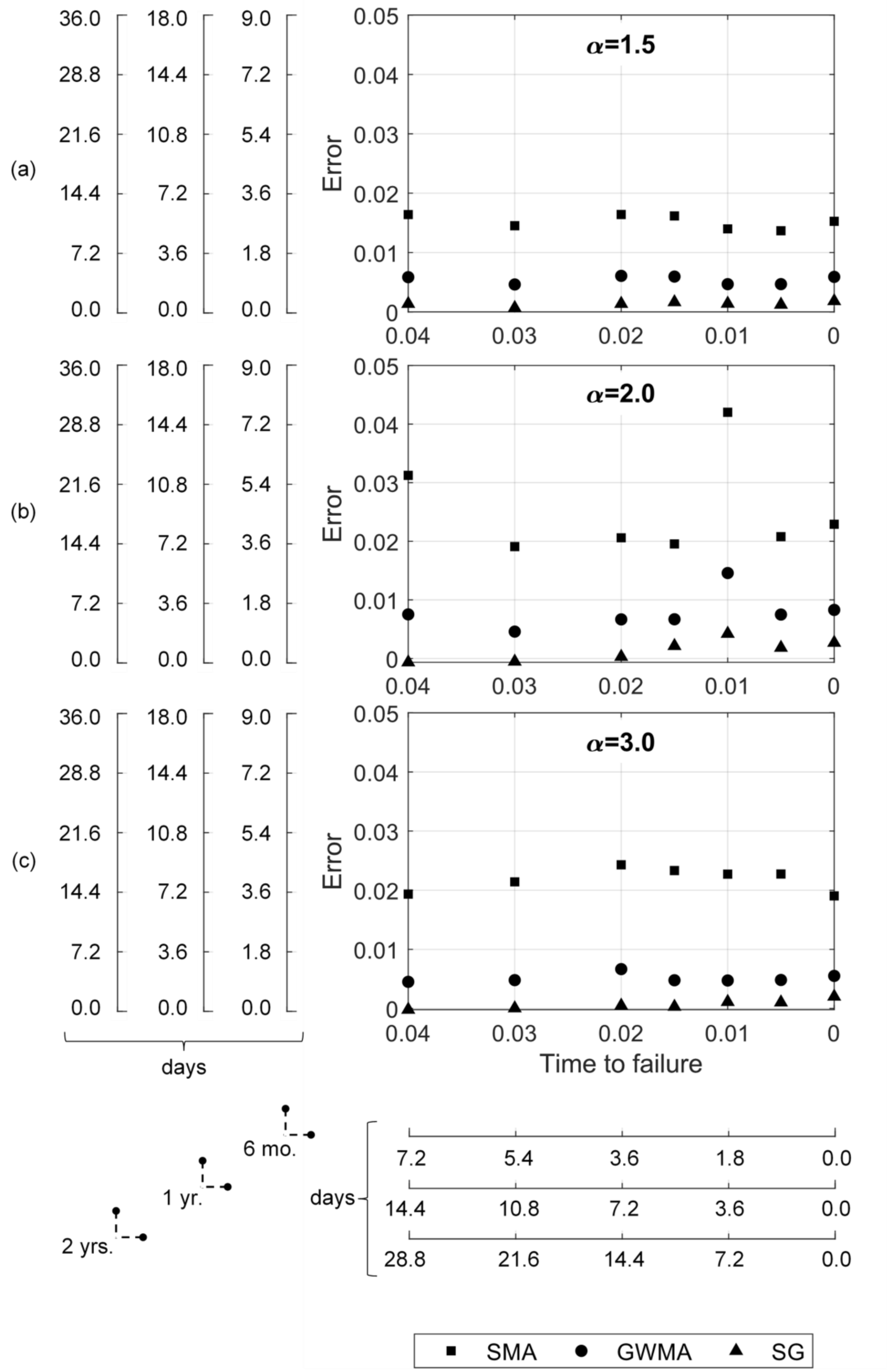

Figure 4- 9. Mean error of failure time forecast for all filters at α =1.50, 2.0, and 3.0 (auxiliary axes indicate actual time scales for time periods of 6 months, 1 year, and 2 years)

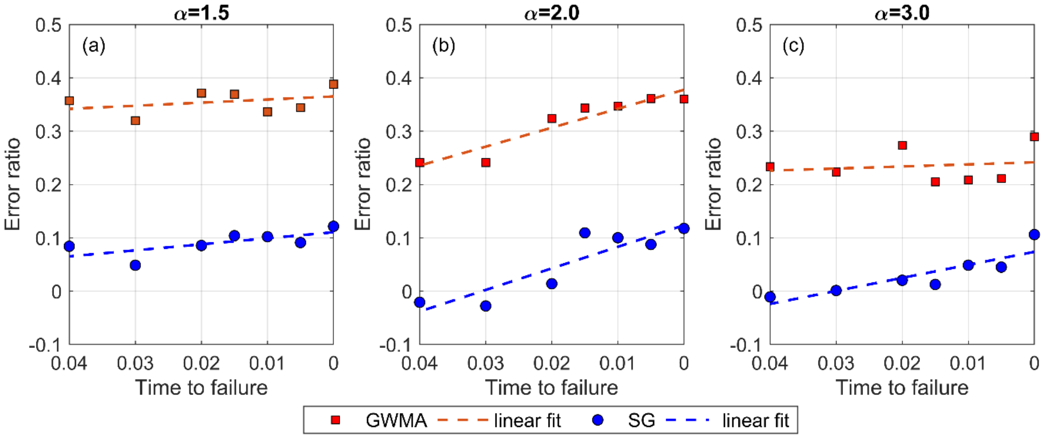

Figure 4- 10. Error ratio of failure time forecast when using GWMA and SG on synthetic cases at α =1.50, 2.0, and 3.0

in SMA, while the performance of SG is almost indifferent to bandwidth. This indicates FTF enhancement and scatter reduction are not competing when using SG. Sharifi, Hendry, Macciotta, et al. (2022) state that using GWMA can lead to a shift in results by only 23 to 45% of the shift calculated using SMA (shift or lag ratio), and one may suggest using these numbers to correct the SMA-forecasted failure moment instead of using the GWMA filter itself. However, it is not recommended since only 15% of the error ratios of GWMA in our results lie within that range, and for a considerable 85% of points, the GWMA's error ratio was out of this range. This is attributed to the use of failure cases studied here, which adds to the randomness of measurements through variability associated with monitoring instrumentation and landslide development mechanisms as opposed to the lag estimations in Sharifi, Hendry, Macciotta, et al. (2022). The results from these case studies, however, support their findings that the enhanced performance of GWMA in FTF is due to the trend distortion caused by applying SMA while GWMA tends to preserve the underlying trend better.

The difference between the results of GWMA at high *p* values with the results of SG is not significant in most cases, suggesting a low bandwidth is preferred for SG to reduce the computation effort and capture trend deviations in short time periods; however, a larger bandwidth is preferred for GWMA. Notably, SG tends to create a depression in filtered values immediately after the measured peaks, which is less pronounced at lower bandwidths (Sharifi, Hendry, Macciotta, et al., 2022), supporting the use of a low bandwidth for SG.

Figure 4- 12 shows a summary of error ratios for the 17 datasets in a polar diagram for ease of comparison between datasets. In this diagram, the distance of each point from the origin (r) represents the error ratio to SMA and the results of each set are arranged at a unique angle (θ). The results are also color coded based on the sign of the error ratio. The error ratios in Figure 4- 12 are the average results of different bandwidth values and each point corresponds to a certain time before failure. Figure 4- 12 shows that using GWMA and SG have improved performances compared to SMA for FTF purposes as all of the points are located at $r < 1$. The furthest points from the origin (r values near 1) correspond to the earliest measurements, later improving as time advances. If those that fall in the earliest 10% of the dataset are excluded, the average error ratio of all cases drops below 0.5 for both filters. This means that using these alternative filters improves the accuracy of FTF by at least 50%, with improvements of 70 to 80% becoming very likely but depending on the characteristics of the monitoring data.

The statistical indicators of the whole dataset consisting of the error ratio of all sets after the application of GWMA and SG are listed in Table 4- 6. This table shows the maximum, minimum, average, and median of SG filters are prone to lower values compared to GWMA filters, which is manifested in more negative average values in Figure 4- 12 and higher negative values in Table 4- 6. On the other hand, the standard deviation is similar for both filters, which implies that GWMA and SG are similar in terms of error ratio uncertainty. Almost 70% of absolute error ratios for both GWMA and SG are less than 0.4.

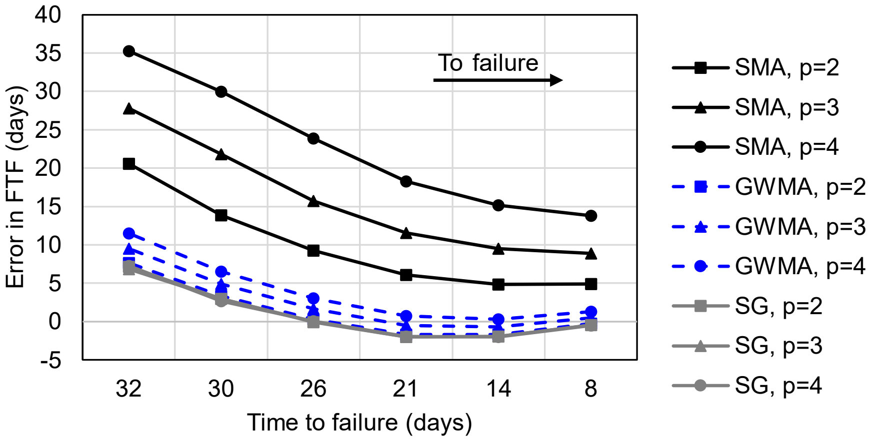

Figure 4- 11. Variation of error in failure time forecast for set 1 using SMA, GWMA, and SG filters vs. time to failure

Table 4- 4. Error and error ratio of all 17 datasets with respect to p corresponding to the latest time to failure

Set No.	Filter	Mis forecast	*p*=2	*p*=3	*p*=4	*p*=5	*p*=6
Set 1	SMA	Error (days)	4.92	8.900	13.78	-	-
	GWMA	Error (days)	-0.26	0.49	1.29		
		Error ratio	-0.05	0.05	0.09		
	SG	Error (days)	-0.463	-0.467	-0.53		
		Error ratio	-0.09	-0.05	-0.03		
Set 2	SMA	Error (days)	-	-	9.92	17.12	25.75
	GWMA	Error (days)			-2.95	-2.05	-1.07
		Error ratio			-0.29	-0.12	-0.04
	SG	Error (days)			-4.11	-3.53	-3.63
		Error ratio			-0.41	-0.20	-0.14
Set 3	SMA	Error (days)	-	-	9.92	17.12	25.75
	GWMA	Error (days)			-2.95	-2.05	-1.07
		Error ratio			-0.29	-0.12	-0.04
	SG	Error (days)			-4.11	-3.53	-3.63
		Error ratio			-0.41	-0.20	-0.14
Set 4	SMA	Error (mins)	0.018	0.031	0.045	0.060	0.077
	GWMA	Error (mins)	-4.36E-05	2.5E-03	5.3E-03	8.3E-03	1.1E-02
		Error ratio	-2.39E-03	8.16E-02	1.18E-01	1.39E-01	1.52E-01
	SG	Error (mins)	-7.2E-04	-1.9E-04	8.09E-05	7.6E-04	1.4E-04
		Error ratio	-3.92E-02	-6.18E-03	1.80E-03	1.27E-02	1.84E-02
Set 5	SMA	Error (mins)	-	0.007092	0.012781	0.019063	0.02593
	GWMA	Error (mins)		-0.00268	-0.00181	-0.00079	0.00036
		Error ratio		-0.37	-0.14	-0.04	0.01
	SG	Error (mins)		-0.00341	-0.00361	-0.0038	-0.00347
		Error ratio		-0.48	-0.28	-0.19	-0.13
Set 6	SMA	Error (mins)	-	0.012771	0.021965	0.032133	0.043384
	GWMA	Error (mins)		-0.005	-0.00327	-0.00136	0.00073

		Error ratio		-0.39	-0.14	-0.04	0.01
	SG	Error (mins)		-0.00656	-0.00658	-0.00515	-0.00503
		Error ratio		-0.51	-0.29	-0.16	-0.11
Set 7	SMA	Error (year)	0.349041	0.479167	0.655989	0.842059	0.962348
	GWMA	Error (year)	0.147913	0.179968	0.212097	0.245115	0.27980
		Error ratio	0.42	0.37	0.32	0.29	0.29
	SG	Error (year)	0.139481	0.144408	0.155877	0.130835	0.106811
		Error ratio	0.39	0.30	0.23	0.15	0.11
Set 8	SMA	Error (days)	-	12.29302	14.66625	17.33832	20.44267
	GWMA	Error (days)		7.535246	8.068908	8.601707	9.154141
		Error ratio		0.61	0.55	0.49	0.44
	SG	Error (days)		6.937242	6.966858	6.914076	6.917222
		Error ratio		0.56	0.47	0.39	0.33
Set 9	SMA	Error (days)	-	7.143295	9.241116	11.67486	14.48605
	GWMA	Error (days)		3.059772	3.498314	3.949269	4.427070
		Error ratio		0.42	0.37	0.33	0.30
	SG	Error (days)		2.522733	2.527320	2.531317	2.521038
		Error ratio		0.35	0.27	0.21	0.17
Set 10	SMA	Error (days)	-	-	2.309319	4.12451	6.201187
	GWMA	Error (days)			1.894528	1.574035	1.227203
		Error ratio			0.82	0.38	0.19
	SG	Error (days)			2.565527	2.584055	2.613131
		Error ratio			1.11	0.62	0.42
Set 11	SMA	Error (days)	-	2.93316	4.454480	6.222090	8.257520
	GWMA	Error (days)		0.35956	0.55787	0.81021	1.10893
		Error ratio		0.12	0.12	0.13	0.13
	SG	Error (days)		0.15829	0.1795	0.01148	0.03701
		Error ratio		0.05	0.04	1.0E-3	4.0E-3
Set 12	SMA	Error (days)	-	-	23.4549	32.3327	43.1302
	GWMA	Error (days)			4.12988	5.56195	7.05906
		Error ratio			0.17	0.17	0.16
	SG	Error (days)			1.02297	0.96505	0.68636
		Error ratio			0.04	0.03	0.01
Set 13	SMA	Error (days)	-	2.850862	4.665007	6.760283	9.167468
	GWMA	Error (days)		-0.68895	-0.30938	0.082252	0.49769
		Error ratio		-0.24	-0.06	0.01	0.05
	SG	Error (days)		-1.16031	-1.14906	-1.14052	-1.16465
		Error ratio		-0.40	-0.24	-0.16	-0.12
Set 14	SMA	Error (days)	10.7808	16.7713	-	-	-
	GWMA	Error (days)	3.4791	4.66449			
		Error ratio	0.32	0.27			
	SG	Error (days)	3.19432	4.96647			
		Error ratio	0.29	0.29			
Set 15[1]	SMA	Error (days)	-	2.03818	2.192728	3.36595	2.559269
	GWMA	Error (days)		1.153719	1.173601	1.280897	1.336571

		Error ratio		0.56	0.53	0.54	0.52
	SG	Error (days)		0.834468	0.684181	0.624921	0.637146
		Error ratio		0.40	0.31	0.26	0.24
Set 16[2]	SMA	Error (days)	7.514682	10.36665	12.39547	12.34299	13.13021
	GWMA	Error (days)	2.872128	4.438498	4.901791	5.45333	5.784523
		Error ratio	0.38	0.42	0.39	0.44	0.44
	SG	Error (days)	2.735168	3.281445	3.827722	5.183299	5.972365
		Error ratio	0.36	0.31	0.30	0.41	0.45
Set 17[2]	SMA	Error (days)	1.817428	2.548136	3.631645	3.952903	6.414177
	GWMA	Error (days)	0.313583	0.930811	1.413272	1.521274	1.421061
		Error ratio	0.17	0.36	0.38	0.38	0.22
	SG	Error (days)	-1.38101	-1.29136	-1.3189	-1.16766	-0.19107
		Error ratio	-0.75	-0.50	-0.36	-0.29	-0.02

1. The remaining records for set 15 are presented in *Table 4- 5* under high *p* values
2. Error-values are the average of all detected points by InSAR

Table 4- 5. Continued of Table 4- 4 for Set 15 at high p values

Set No.	Filter	Mis forecast	*p*=7	*p*=8	*p*=9	*p*=10	*p*=11
Set 15 (cont.)	SMA	Error (days)	2.784326	3.000708	3.192642	3.335847	3.457953
	GWMA	Error (days)	1.416918	1.382435	1.526133	1.644441	1.734951
		Error ratio	0.50	0.46	0.47	0.49	0.50
	SG	Error (days)	0.588089	0.514632	0.474210	0.398132	0.391581
		Error ratio	0.21	0.17	0.14	0.11	0.11

Table 4- 6. Statistical indicators of error ratio after forecasting failure time of case histories

Indicator	GWMA	SG
Maximum	0.838	0.666
Minimum	-0.738	-0.925
Average	0.113	-0.023
Standard deviation	0.323	0.304
Median	0.128	0.043
Negative values (%)	32%	40%

Figure 4- 13 shows the absolute error ratio in the log scale vs. the time-to-failure of distometric base 15-13 installed on the eastern flank of Mt. Beni (Figure 4- 7). As mentioned before, this set was among the datasets dismissed for analysis due to a violation of the zero-mean criterion. In this specific instance, GWMA and SG filters underperformed in comparison to SMA given that the error ratio is greater than 1 for most of the extent of the slope. This can be attributed to those points located in the red circle in Figure 4- 7 which significantly affect the scatter

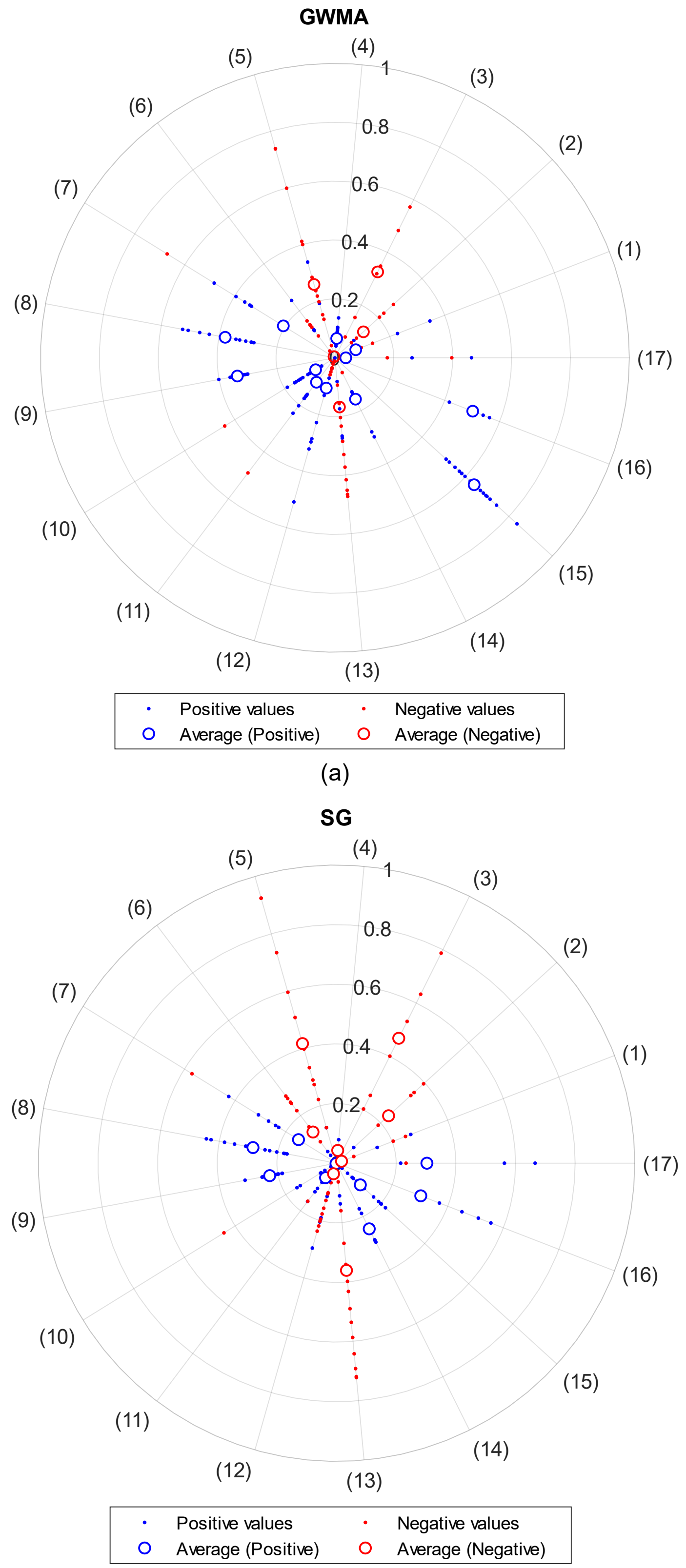

(a)

(b)

Figure 4- 12. Polar exhibition of error ratios for all 17 studied sets

dispersion such that these points would have to be treated as outliers rather than scatter for data processing purposes, or due to decelerating factors not properly captured by the frequency in data acquisition. Because SMA is a low-pass filter or in other words, tends to intensively attenuate the anomalies such as sharp peaks and troughs in the data (Sharifi, Hendry, Macciotta, et al., 2022), these points did not impact the FTF results from the SMA as much as the adverse effects seen in the GWMA and SG results. This highlights the need to apply algorithms designed to capture outliers prior to employing any filter to reduce scatter, such as the Hampel filter (Hampel, 1971).

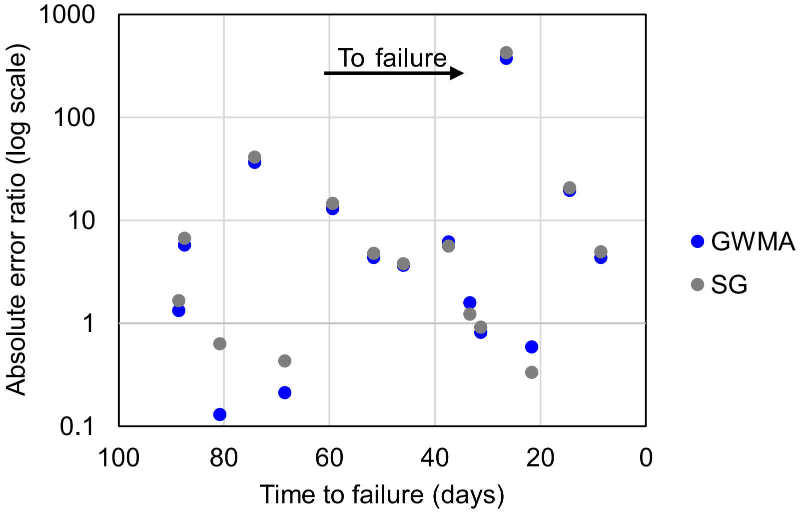

Figure 4- 13. Absolute error ratio values of distometric base 15-13 installed on Mt. Beni after application of GWMA and SG filters

4.5. Conclusions

Detecting the time when a landslide initiates an acceleration period and forecasting the time to a potential failure are crucial for landslide risk management and control. EWSs use monitoring data as a means to meet these goals. Considering the scatter in landslide monitoring data, employing a filter becomes necessary to minimize any adverse impact on interpreted velocity and acceleration values of the landslide. In this paper, the performance of three different filters (SMA, GWMA, and SG) was studied to evaluate how their application affects the detection of onset of acceleration and failure time forecast using the inverse velocity method. To this end, a set of synthetic accelerating and failing cases, as well as nine case histories (17 datasets) from the literature, were used. The analysis of 1296 synthetic cases for each filter showed SMA predicts the onset of acceleration with 90% confidence 3.2 and 25 times later than GWMA and SG, respectively. The standard deviation for detecting the onset of acceleration for SMA and GWMA was 8.67 and 3.18 times that of SG, respectively. These findings all indicate the alternatives considered herein to SMA can lead to improvements in the capacity of EWSs with respect to the timely detection of changes in landslide patterns and the onset of acceleration. Failure time forecasting using the inverse velocity method and synthetic cases showed GWMA and SG can enhance the accuracy of such prediction by 60 to 80% and 90 to 100%, respectively, depending on the kinematics of the landslide (characterized by the curve in the inverse velocity before failure and quantified by the α value in the fitted curve). The results of inverse velocity FTF with case history data filtered by SMA, GWMA, and SG also confirmed these alternative filters outperform SMA at least by 60% in terms of FTF accuracy. Our results suggest the adoption of GWMA and SG can improve the reliability of EWSs over the current prevalent use of SMA, as they enable an EWS to capture the acceleration moment with reduced lag time and forecast time to failure with a narrower range of error.

Appendix 4.A – Case Histories Data

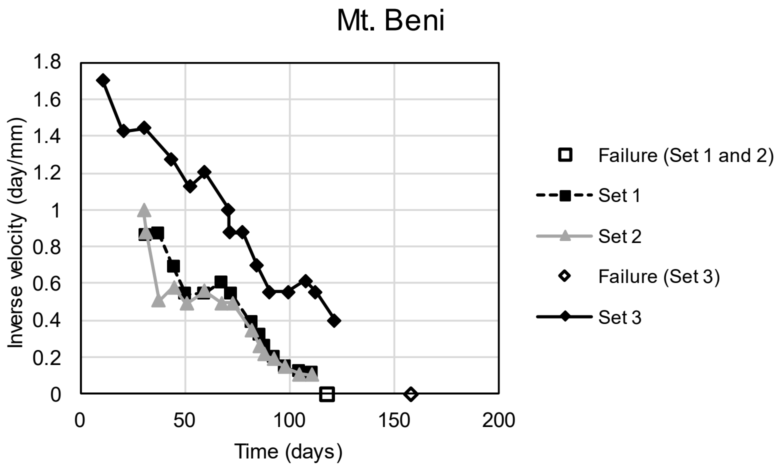

Figure 4- 14. Inverse velocity diagram of Sets 1 to 3

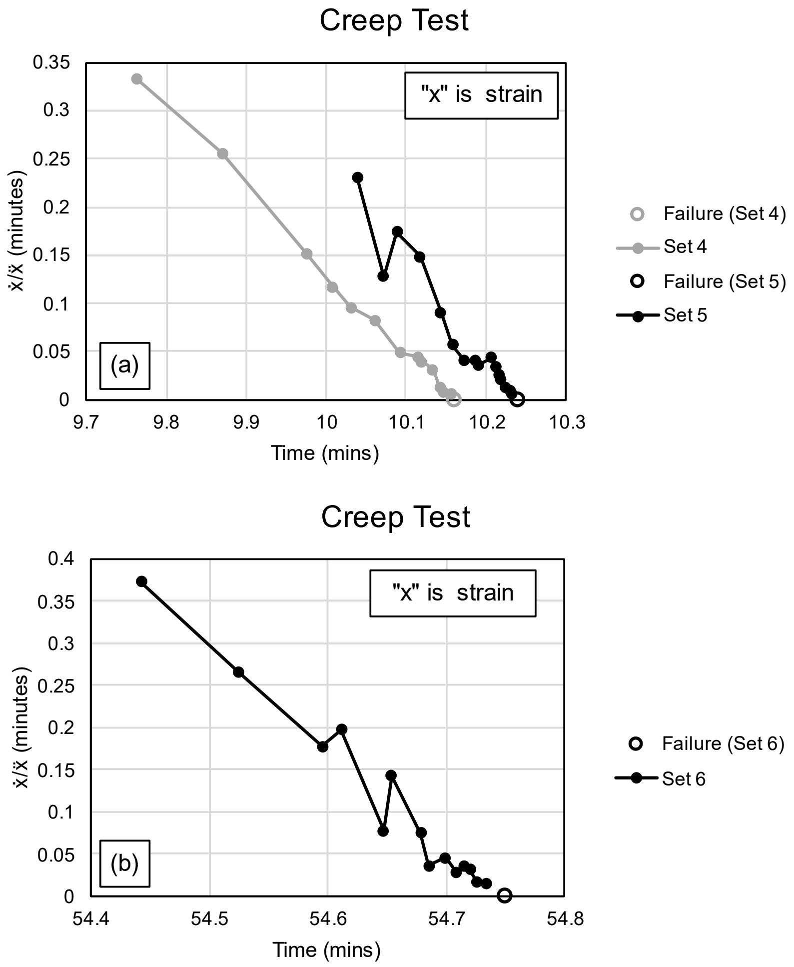

Figure 4- 15. Strain rate representative diagram of Sets (a) 4 and 5, and (b) 6

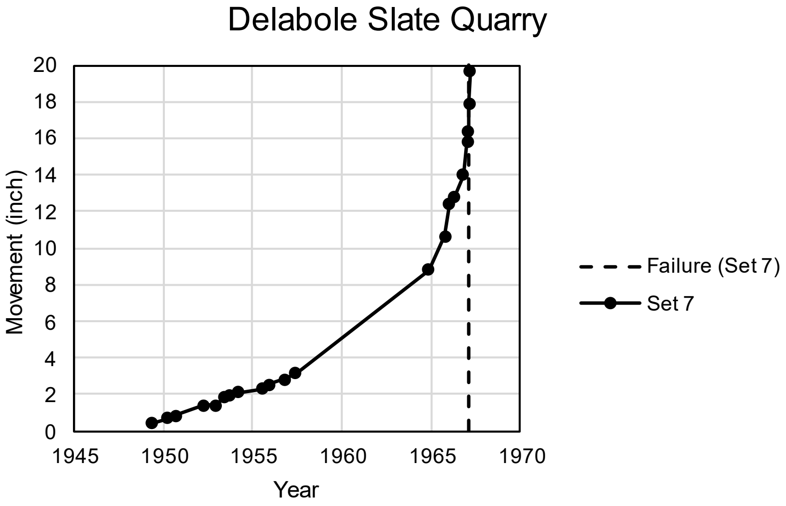

Figure 4- 16. Movement diagram of Set 7

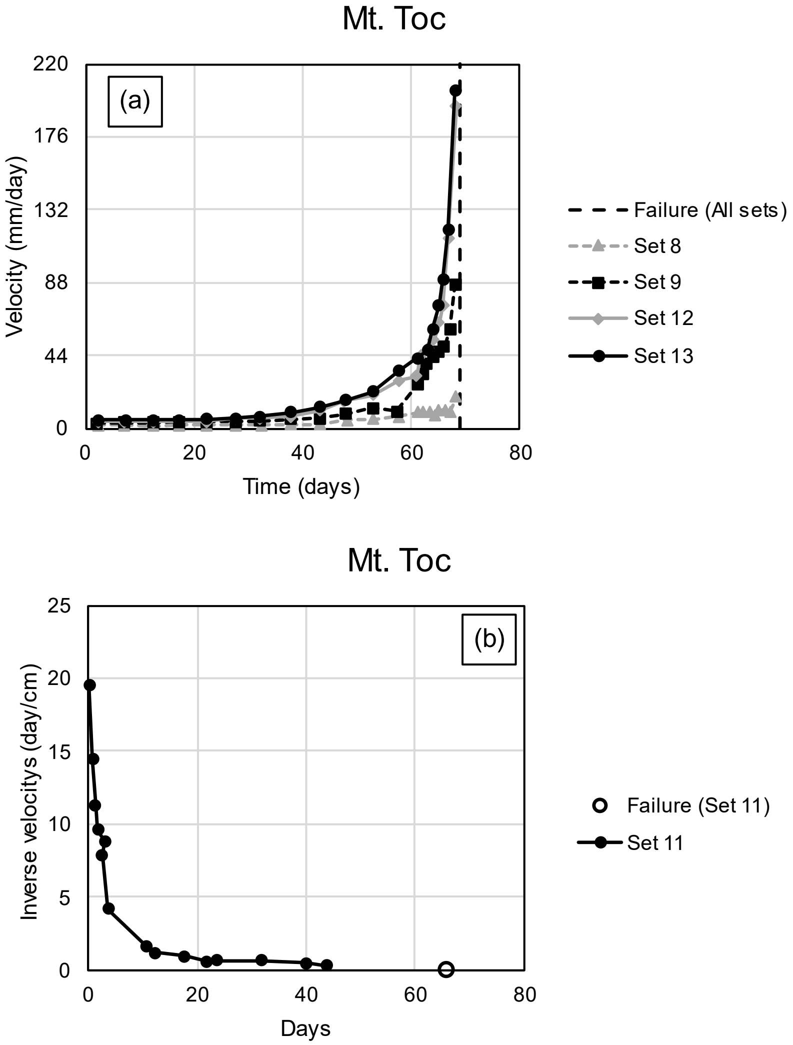

Figure 4- 17. Inverse velocity diagram of Sets (a) 8, 9, 12, 13, and (b) 11

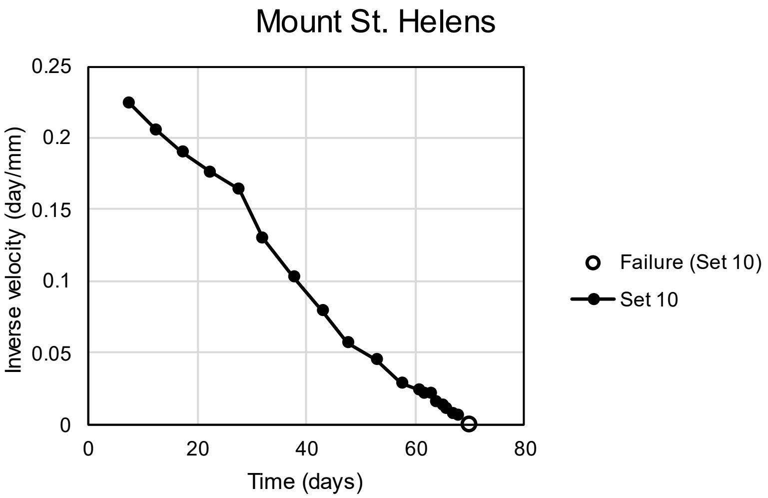

Figure 4- 18. Inverse velocity diagram of Set 10

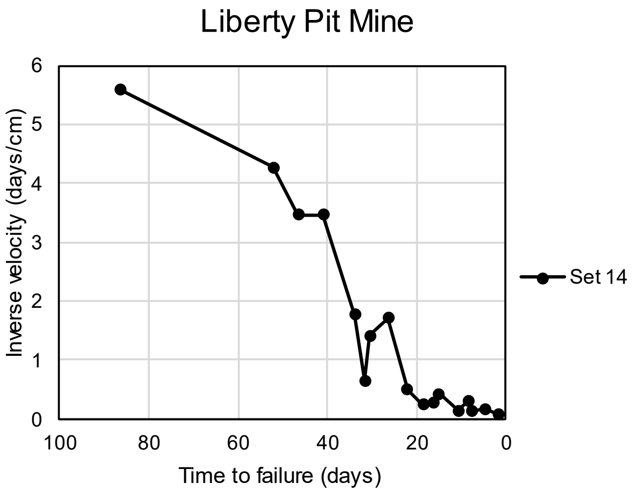

Figure 4- 19. Inverse velocity diagram of Set 14

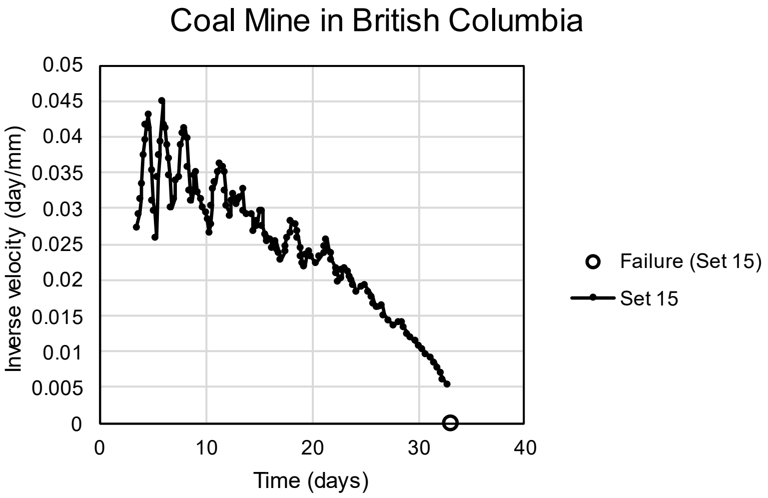

Figure 4- 20. Inverse velocity diagram of Set 15

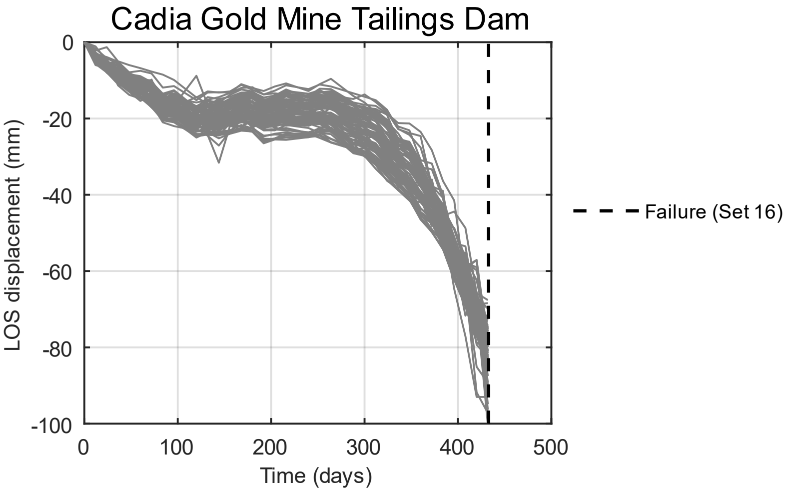

Figure 4- 21. Line-of-sight (LOS) displacement diagram of Set 16

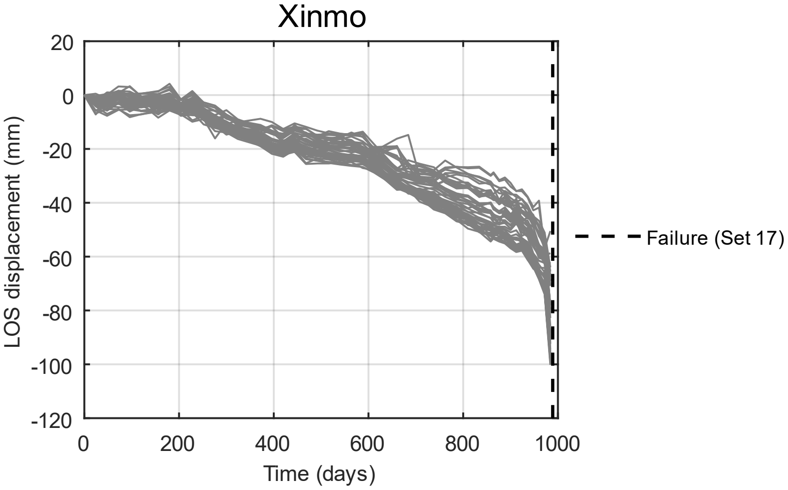

Figure 4- 22. Line-of-sight (LOS) displacement diagram of Set 17

Appendix 4.B – FTF error vs. time-to-failure of all case histories

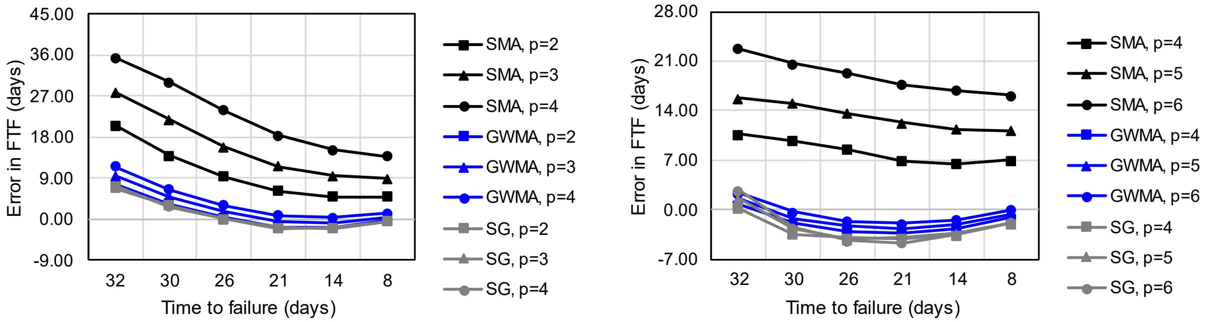

(a) Set 1 (b) Set 2

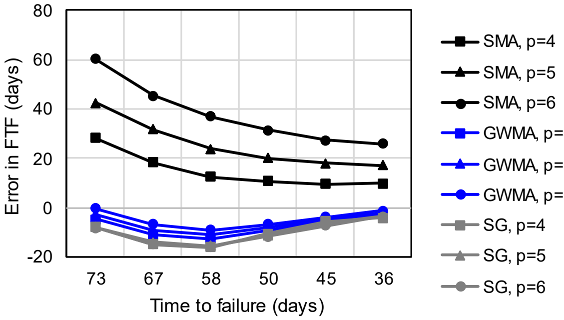

(c) Set 3

Figure 4- 23. Error in FTF vs. time to failure for different baselines in Mt. Beni landslide (Florence, Italy)

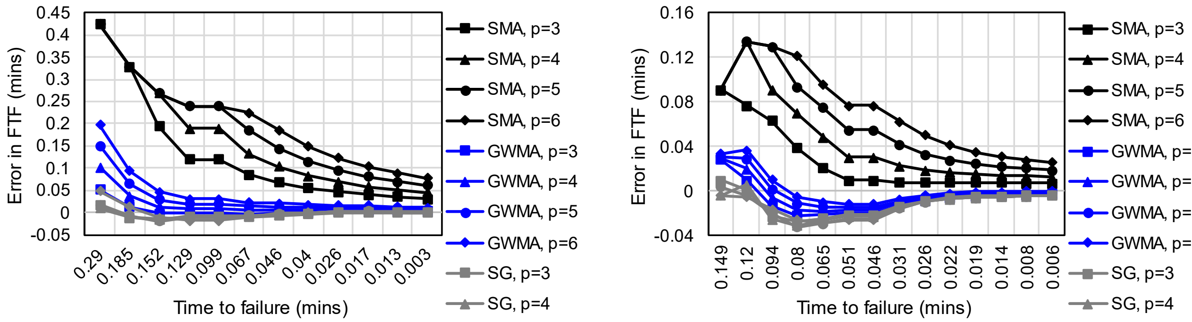

(a) Set 4 (Sample1) (b) Set 5 (Sample2)

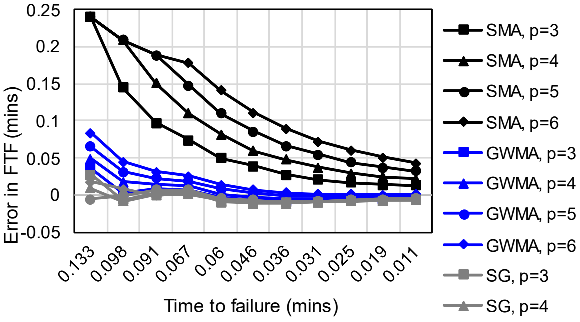

(c) Set 6 (Sample3)

Figure 4- 24. Error in FTF vs. time to failure for creep test (samples acquired from Beijing, China)

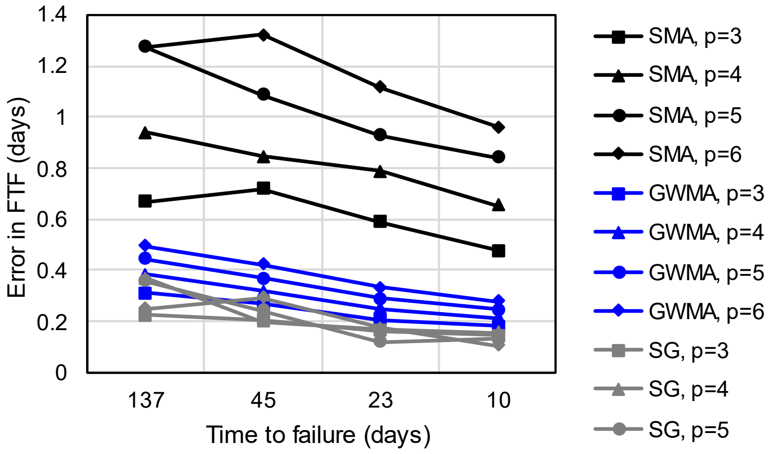

Figure 4- 25. Error in FTF vs. time to failure for set 7 (Failure in Delabole slate quarry, Cornwall, England)

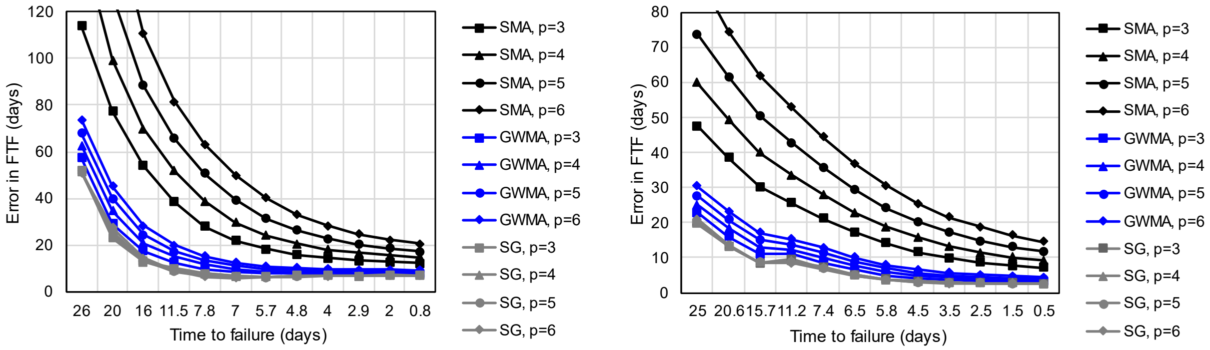

(a) Set 8 (Benchmark50)

(b) Set 9 (Benchmark67)

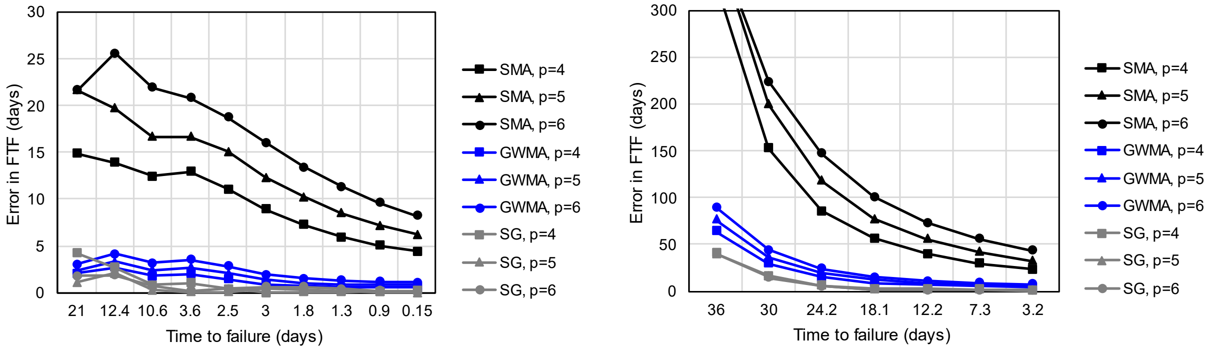

(c) Set 11

(d) Set 12 (Benchmark 63)

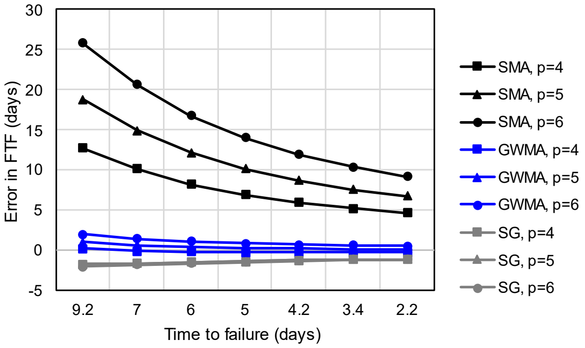

(e) Set 13 (Benchmark5)

Figure 4- 26. Error in FTF vs. time to failure for different benchmarks of the Vajont failure (Italian Alps)

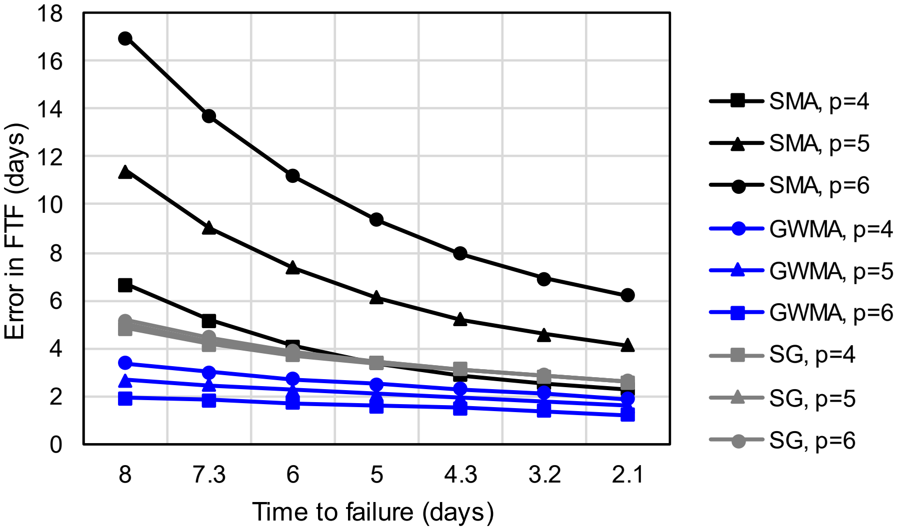

Figure 4- 27. Error in FTF vs. time to failure for set 10 (Mount St. Helens failure, Washington, USA)

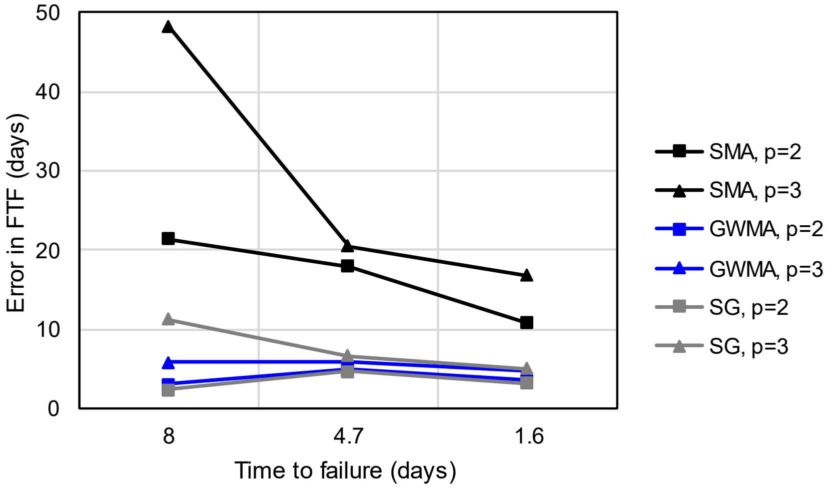

Figure 4- 28. Error in FTF vs. time to failure for set 14 (Failure in Liberty pit mine, Utah, USA)

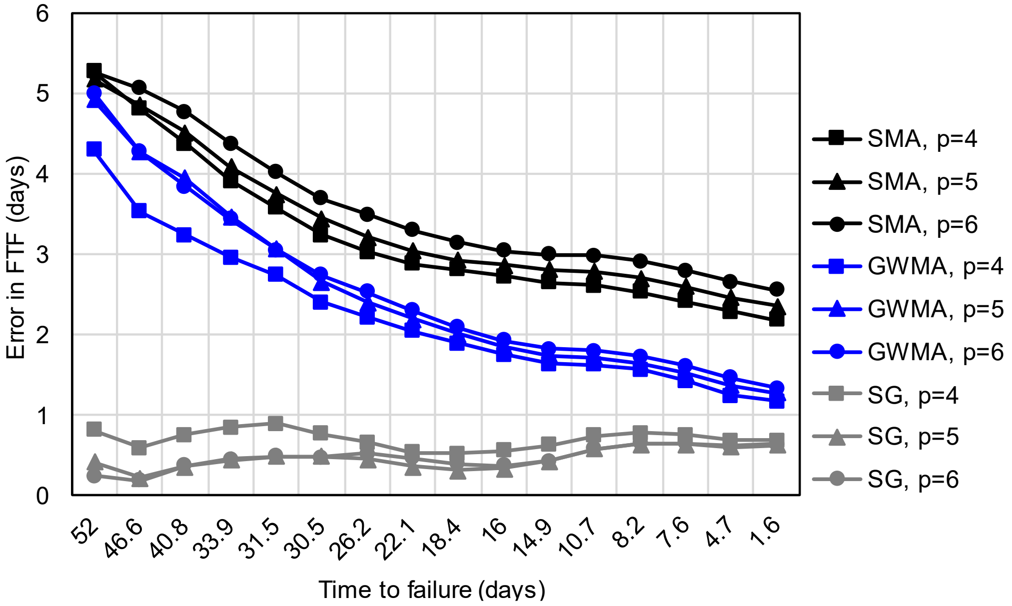

Figure 4- 29. Error in FTF vs. time to failure for set 15 (failure in a coal mine, British Columbia, Canada)

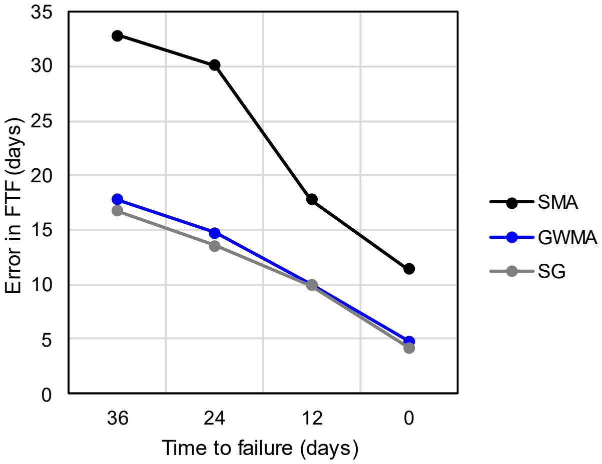

Figure 4- 30. Error in FTF vs. time to failure for set 16 (Cadia gold mine tailings dam embankment failure, New South Wales, Australia)

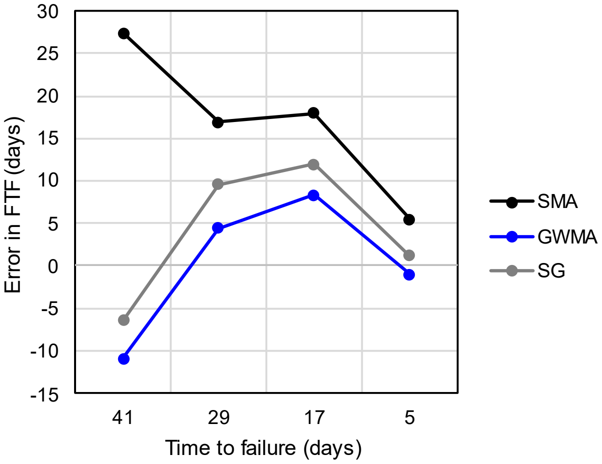

Figure 4- 31. Error in FTF vs. time to failure for set 17 (Xinmo landslide, Sichuan, China)

Chapter 5: An Improved Estimation of Surficial Velocities Obtained by MT-TOPSAR Interferometry: A Case Study of Oldman River Dam, Alberta, Canada

---

Contributions of the Ph.D. Candidate

The material presented in this chapter, including the literature review, conceptualization, methodology development, analysis, draft preparation and revisions, are conducted by the Ph.D. candidate. Dr. Michael Hendry has reviewed all pieces presented in the published manuscript, cited below:

Sharifi S, Hendry MT, 2023. "An assessment of surficial velocities by MT-TOPSAR interferometry: Case study of the Oldman River Dam, Alberta, Canada", *Bulletin of Engineering Geology and Environment*, 82(446). https://doi.org/10.1007/s10064-023-03473-0.

Contributions of This Chapter to the Overall Study

Decomposing InSAR 1D LOS velocities has been long conducted in 2D by ignoring the northward velocity component. Adopting such an assumption is not infallible and leads to erroneous estimations of vertical and eastward velocity components. This chapter introduces a method to combine the variance caused by this assumption in combination with InSAR's inherent uncertainty respecting the reflectivity of objects on the ground. The obtained mathematical expressions of errors along vertical and eastward axes provide guidelines on choosing the scenes if the simplifying assumption is to be practiced. An investigation on the surficial velocity of the ground at the Oldman River Dam, southern Alberta, is carried out. Due to the presence of sheared slip surfaces and expansive materials, the spillway has been a target of monitoring in the past two decades. The variety of ground targets from stable to active moving in different directions make this site an informative case study to deliver objective #3.

Abstract

Numerous dams in North America are constructed on foundations and/or abutments consisting of unstable weak materials or low-friction pre-sheared surfaces such as the Oldman River Dam (ORD), in southern Alberta, Canada. The objective of this paper is to examine the performance of Interferometric Synthetic Aperture Radar (InSAR) on the slow-moving ORD site by comparing the mapped velocities obtained through InSAR analysis in 2015-2022 with velocities from previous investigations. Additionally, the study aims to determine the precision of estimated velocities by analyzing InSAR temporal decorrelation and incorporating the error of simplifying assumption necessary to decompose line-of-sight velocities. The results indicate the spillway, covering an area of ∼26×10^3 m^2, has been moving at an average total velocity of 1.26 mm/yr. On the slope of the embankment, measuring ∼160×10^3 m^2, an active area next to the left abutment is also experiencing a higher average velocity of 8.29 mm/yr (both rates in millimetres per year). An analysis of the precision of the estimations showed an accuracy of 0.72 and 2.78 mm/yr for the spillway and embankment, respectively. Overall, the spillway velocities have not deviated much from 1 mm/yr in the study period but the embankment's active area decelerated from >20 to 5 mm/yr toward the end of 2022. Eventually, a lagged spillway displacement in response to seasonal variation of the reservoir level was also observed.

Keywords: Ground hazard; Dam; InSAR; Monitoring; Velocity; Precision

5.1. Introduction

Ground movements can threaten the integrity and operation of essential infrastructures (Journault et al., 2018; Khorrami et al., 2019; Ma et al., 2021; Macciotta & Hendry, 2021; Wasowski & Pisano, 2020; Woods et al., 2021; C. Zhou et al., 2022). In situ instruments are used to record and monitor ground movements, but they require considerable resources (Cenni et al., 2021; Rodriguez et al., 2021). Different variants of remote sensing techniques, accordingly, have been widely adopted as a complementary component in monitoring plans to minimize expenditures (Bekaert et al., 2020; Deane et al., 2020; Macciotta & Hendry, 2021; Rodriguez et al., 2020; Woods et al., 2020).

Interferometric Synthetic-Aperture Radar (InSAR) is a space-borne remote sensing technology that uses satellite imagery for a better understanding of the kinematics of ground activities. Synthetic-Aperture Radar is a sophisticated sensor that operates within the microwave range and utilizes a short-length antenna to receive data. These waves illuminate a footprint and depending on the objects' reflectivity, a portion of waves are reflected toward the sensor (X. Hu et al., 2016; Mondini et al., 2021). When a second backscattered acquisition is made, the phase difference can be calculated between these two scenes. The outcome is called an interferogram which is a superimposed product of various factors including displacements and atmospheric effect. Minimizing the latter has been a challenge and modern algorithms, called multi-temporal (MT) analyses, were developed to deliver this task more reliably. Rather than only two scenes, they take advantage of a stack of images. This is because such interferences have a weak correlation in time (Roy et al., 2022; Y. Wang et al., 2022). Understanding the temporal development of ground movement has been a further motivation for studies using MT analysis. MT interferometry has been shown as a successful tool for a variety of applications such as fault characterization (B. Smith & Sandwell, 2003), volcano modelling (Di Traglia et al., 2021), mapping subsidence (Ghazifard et al., 2016; J. Hu et al., 2022; Khorrami et al., 2020; Motagh et al., 2017) and landslide monitoring (X. Liu et al., 2021; Y. Wang et al., 2022)

Infrastructures are exposed to ground movements, such as dams and their related structures which carry a considerable hydrological, environmental, financial and safety significance. These instabilities can compromise the integrity of dam structures to various degrees. Seepage problems in the short term or a probable total failure in the long-term resulting in devasting aftermaths are instances of concern in at-risk dams. Schuster (2006) gathered more than 160 of such cases from North America such as the dams on Calaveras Creek, Castaic Creek, Grande Creek, and Cuyama River in the USA (Cotton, 1972; Glover et al., 1997; Hall, 1978; Hanegan, 1973; Kintzer, 1980; Nilsen, 1972). In Canada, the Gardiner Dam and Nipawin Dam in Saskatchewan, Oldman River Dam and Dunvegan Dam in Alberta, and Peace Canyon Dam, Site C Dam, and WAC Bennett Dam in British Columbia are also affected by ground movements (Hendry et al., 2019; Houston, 2001; Jaspar & Peters, 1979; Morgenstern & Simmons, 1982; Sauer, 1984; Scammell, 2013; Scammell et al., 2012; Schuster, 2006). Of factors contributing to the movements, the following can be mentioned: weak unstable materials susceptible to expansion, pre-sheared bedding surfaces due to valley rebounds or glacier thrust, the existence of previous landslides in the foundation and the presence of erodible materials.

Even though concerns for dams' safety in North America are prevalent and *in situ* monitoring means face many limitations, no systematic study on the applicability of InSAR for these cases has been conducted. To examine the performance of InSAR for such cases, the Oldman River Dam (ORD) in southern Alberta, Canada has been chosen. The ORD, underlain by mudrock formations and pre-sheared clay shale seams, has been selected because of the availability of displacements recorded since 1990. In this paper, 288 Sentine-1 scenes are analyzed, and line-of-sight velocities are obtained for ORD's spillway and embankment. LOS velocities are then decomposed here using the common practice of ignoring northward velocity component. A detailed mathematical investigation on the impact of this simplifying assumption and InSAR's inherence precision is also conducted for the first time. The objective of this paper is (1) to assess the feasibility of InSAR application on this slow-moving site by comparing the mapped velocities with previous in situ investigations and (2) to determine the precision of InSAR estimations by considering all known sources of errors (combined precision).

5.2. Site Background

The ORD is located approximately 10 km north of the town of Pincher Creek, and its reservoir is fed by the Oldman River as well as the tributary Crowsnest River and Castle River. The elements and structures of the ORD referred to in this study are shown in Figure 5- 1. The crest elevation is 1125.6 masl with an average slope of 1(vertical):3.5(horizontal) both upstream and downstream. The dam is designed for a maximum reservoir level of 1118.6 masl, which corresponds to 500 Mm^3, but normally operating levels are 1108 to 1118.6 masl. Figure 5- 2 displays the variation of reservoir level measured at hydrometric station 05AA032 (49°36'43" N 114°03'11" W) on the dam's upstream (Government of Canada, 2022).

Situated on the west limb of the Alberta syncline, the ORD is constructed on the Porcupine Hills Formation (upper mudrock and basal sandstone sequences) of the Paleocene epoch, which itself is disconformably underlain by the late Cretaceous Willow Creek Formation (lower mudrock sequence) at an approximate elevation of 1005 masl under the dam centerline (Bally et al., 1966; Jackson, 2002). All units are recognized as non-marine deposits with a sub-horizontal dip of 0.6°N 17°E, which agrees with the adjacency of the site to the Alberta syncline axis 5 km to the west (Sinclair et al., 1989; Figure 5- 3). Davachi et al. (1991) report encountering several shear planes in clay shale seams during their field investigation. These features are common in the Western

Canadian Sedimentary Basin and several dams with similar foundation and abutments are also impacted, such as the Gardiner Dam and Nipawin Dam in Saskatchewan, Dunvegan Dam in Alberta, and Peace Canyon Dam, Site C Dam, and WAC Bennett Dam in British Columbia (Jaspar & Peters, 1979; Morgenstern & Simmons, 1982; Sauer, 1984; Houston, 2001; Schuster, 2006; Scammell et al., 2012; Scammell, 2013). Due to the glaciotectonic thrusts and valley rebound upon river downcutting and stress relief, the planes have undergone extensive shearing that has led them to the residual state (Morgenstern, 1989). These planes have a strike from northwest to southeast and a 0.5° to 1.5° dip towards the northeast. The elevation and design values for the residual friction angle of shear planes identified beneath the spillway are shown in Figure 5- 4. Interested readers may refer to Davachi et al. (1989) for further information regarding other shear planes in the abutments and at the valley bottom.

Monitoring at the ORD includes reading a collection of SIs up to six times per year, extensometers four to six times per year, and surface displacement surveys by a total station eight times from 1991 to 2015. Hendry et al. (2019) compiled and interpreted the datasets obtained by these instruments as follows. Figure 5- 5 shows the average direction and average magnitude of horizontal displacements obtained by SIs for the years 2013-2017 for most units along with their corresponding most active shear plane. Except for one unit on the northeast, the general direction of the shear planes is northeast on the west side of the spillway and approximately southeast on the other side. Moreover, the most active plane is R1 at almost all locations and the variation of velocity magnitudes is limited within the range of 0.8 to 1.7 mm/yr. A total of 38 extensometers are also installed at locations shown in Figure 5- 5. Similar to the SI results, data from the extensometers for the R1 shear plane show maximum velocities of 1.1, 1.6, 0.7, and 0.2 mm/yr in the headworks, upper and lower half of the chute, and flip bucket, respectively.

Figure 5- 1. Layout of different areas and elements of the ORD

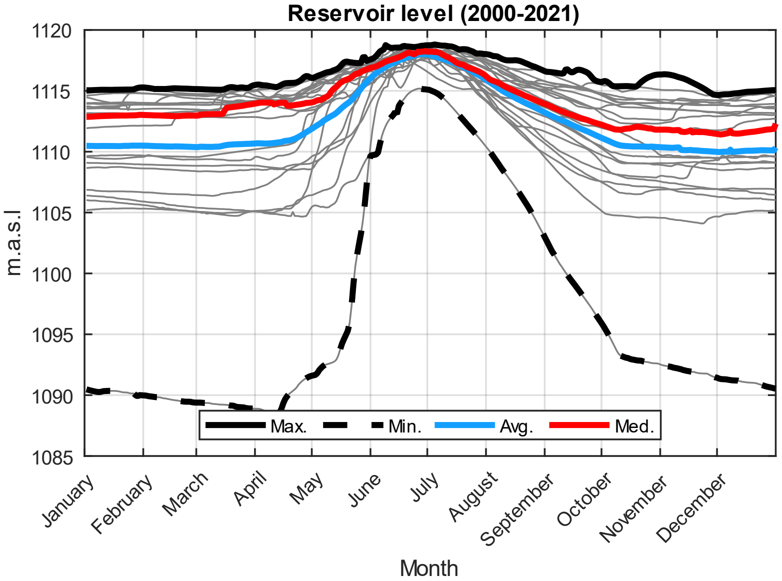

Figure 5- 2. Variation in the ORD reservoir level from 2000 to 2021 (data from Government of Canada, 2022)

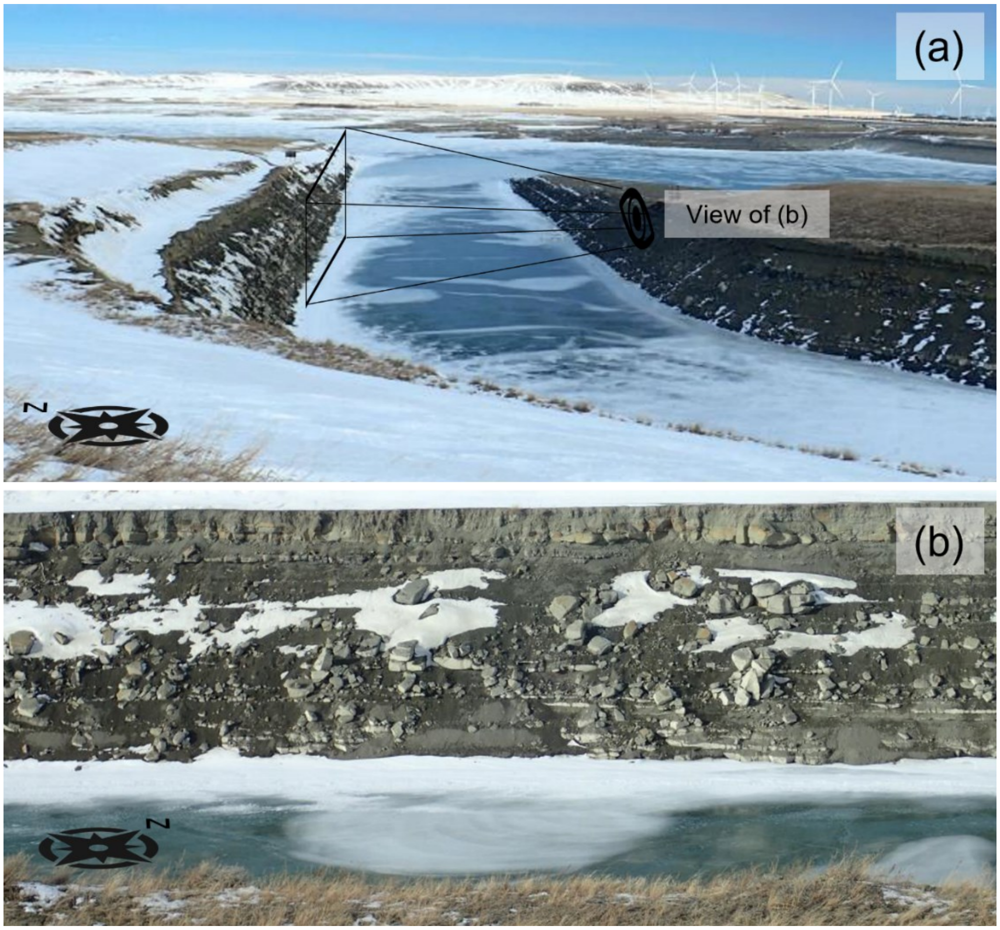

Figure 5- 3. (a) View of spillway approach channel along with (b) a closer look at the geological formations shown at the outcrop (January 17, 2018)

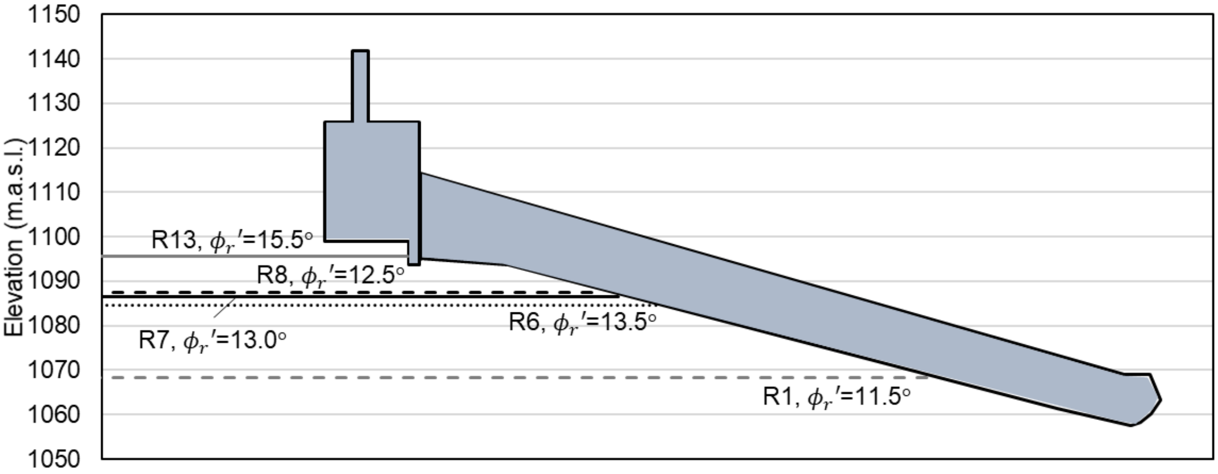

Figure 5- 4. Cross-section of the spillway at its centerline featuring the elevation and design friction angle of shear planes (not to scale)

The average velocities calculated by total station surveys are presented in Figure 5- 6. This figure shows the surficial velocity of the spillway generally decreases from northeast to southwest and from the headworks toward the flip bucket. The azimuth of the movement direction affected by the formation dip is strongly eastward at the headworks and rotates toward almost 135° at lower elevations. The velocities on and around the flip bucket are lower than the accuracy of measurements and are accordingly deemed unreliable. Time-series data of instruments, Figure 5-7, up to 2015 demonstrate the ongoing displacements have been decelerating since the first filling of the reservoir. Hendry et al. (2019) established a long-term trend of 1 mm/yr for the spillway velocities until 2015 and hypothesized the most probable cause of the instability is swelling in the mudstone rock formation associated with a shear strength reduction due to moisture absorption.

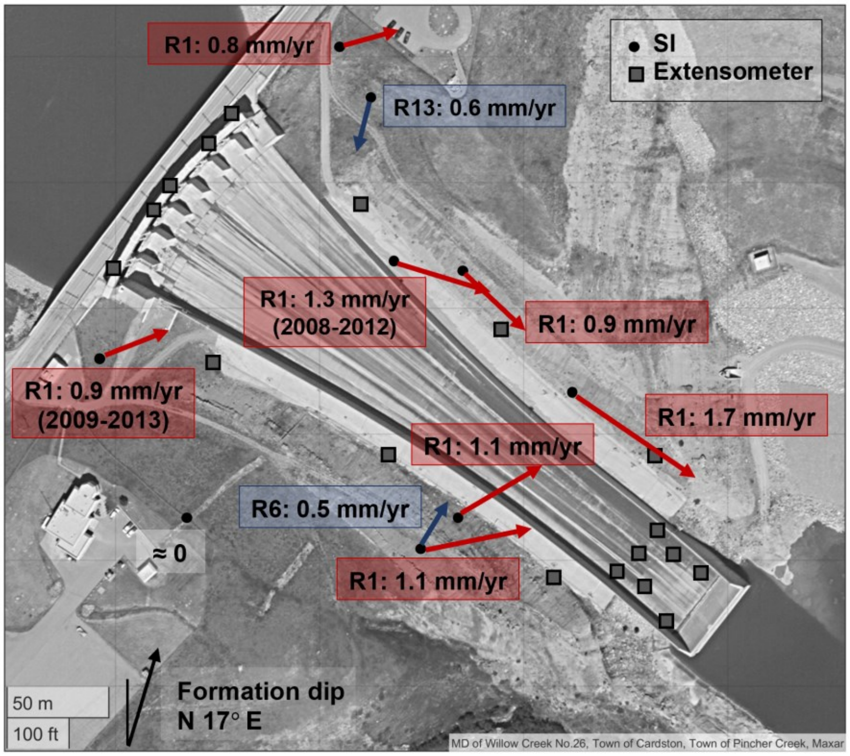

Figure 5- 5. Average direction and magnitude of the most active shear plane based on SI data collected from 2013 to 2017 unless indicated otherwise, and the location of extensometers (after Hendry et al., 2019)

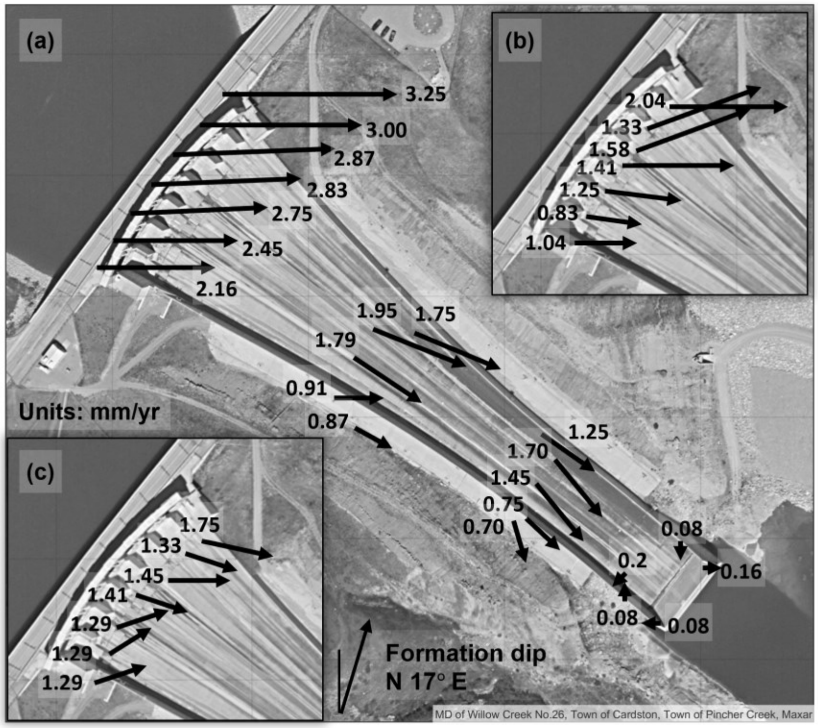

Figure 5- 6. Average velocities obtained by a total station from 1991 to 2015 at (a) top of headworks, the mid and lower portions of the chute and flip bucket, (b) base of headworks, and (c) top of the chute (after Hendry et al., 2019)

5.3. Methodology

Figure 5- 8 presents a flow chart of the applied workflow which is comprised of 3 major blocks of calculation: InSAR analysis, LOS velocities decomposition and calculation of combined precision. Upon analyzing Sentine-1 scenes in the first block, the mapped velocities are spatially interpolated to reconcile the spatial disparity between detected points from ascending and descending orbits. These LOS velocities are decomposed using the prior knowledge in the direction of movements discussed previously. The inherent precision of InSAR LOS velocities (temporal decorrelation) is then calculated which leads to four different combinations of LOS velocities obtained from ascending and descending scenes. These four systems of equations are solved for decomposition followed by compensating the error caused by the simplification assumption needed to solve the equations. The maximum difference of four total velocities from

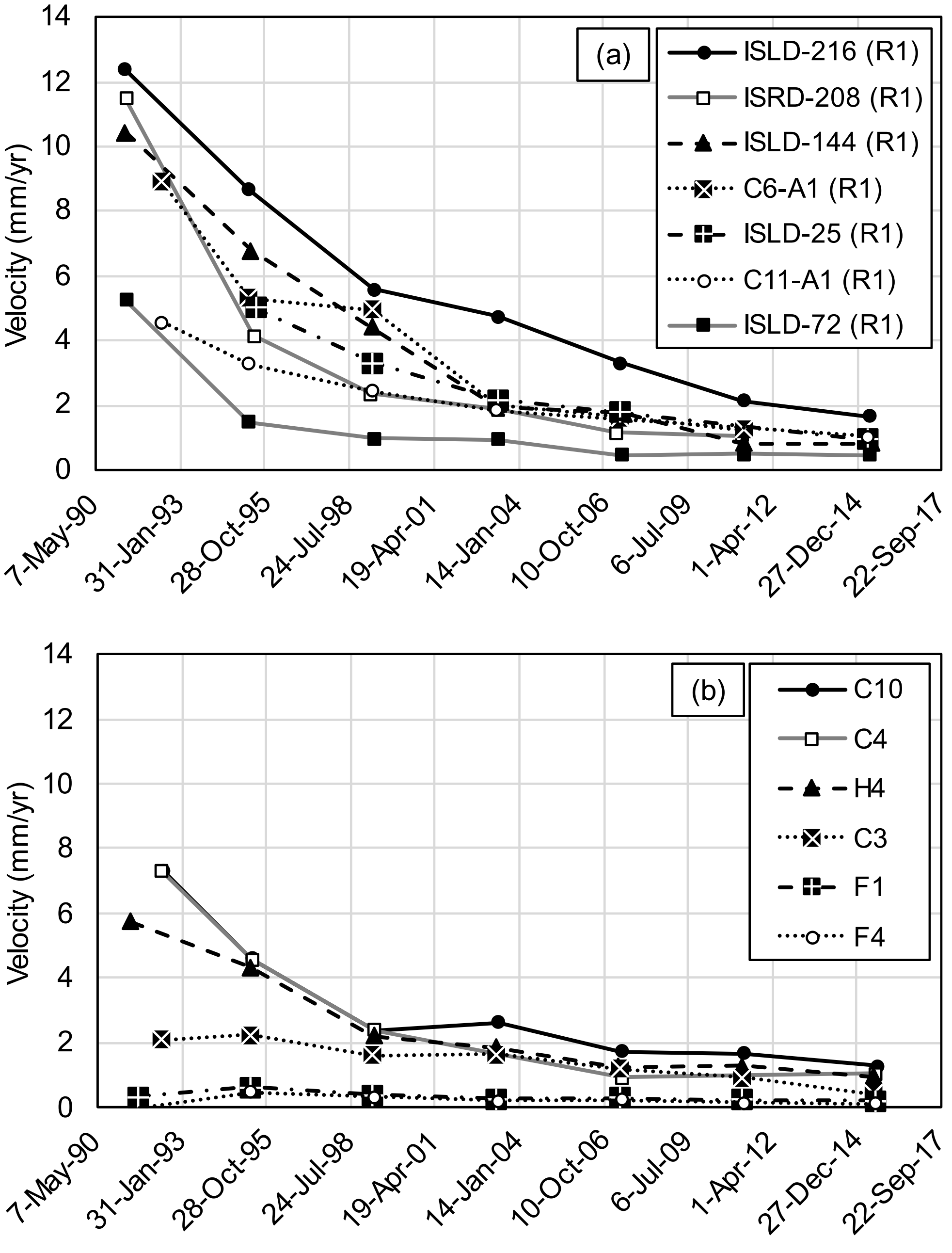

Figure 5- 7. Time-series variation of ground velocity as measured by example (a) SIs and (b) extensometers (NOTE: location of these instruments are marked on Figure 5- 5)

the initially calculated one is considered the precision of estimation. Given that this precision is calculated by considering all known sources of variance, it is referred to as "combined" precision. In the following, each block is presented in detail.

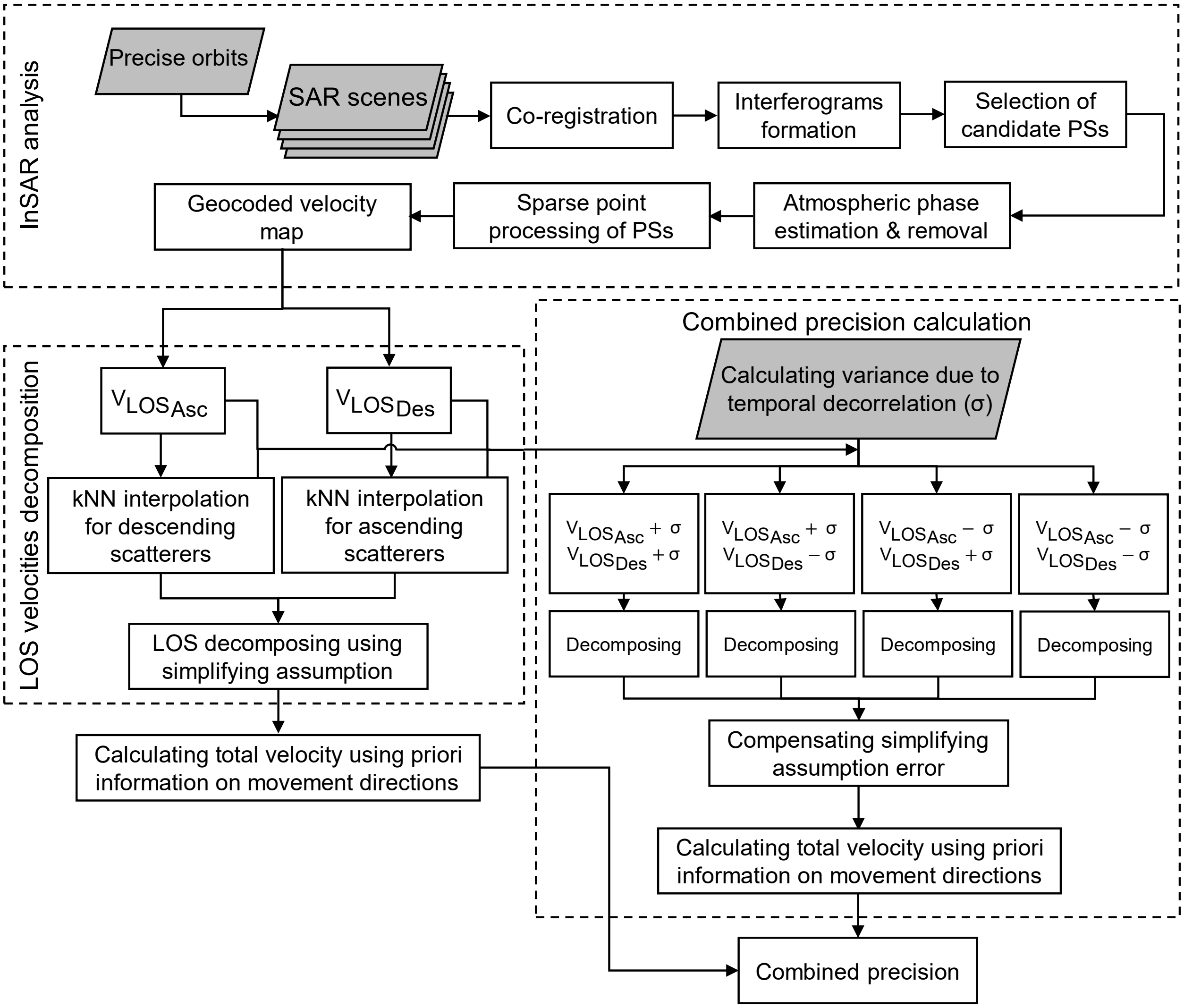

Figure 5- 8. Applied workflow in this study to conduct InSAR analysis, decomposing LOS velocities into total velocities and calculating combined precision

5.3.1. InSAR Analysis

A total of 129 ascending and 159 descending scenes in the imaging mode of Terrain Observation by Progressive Scans (TOPS) and Interferometric Wide (IW) archived by Sentinel-1 were downloaded from the Alaska Space Facility Data Search Vertex (https://search.asf.alaska.edu/#/, which is the full mirror server of Copernicus Open Access Hub:

https://scihub.copernicus.eu/dhus/#/home). A metadata summary of scenes is provided in Table 5-1.

Table 5- 1. Characteristics of images used in this study

Orbit	Path	Frame	Beam mode	Polarization	Scenes	Sensing Period (YYYY/MM-DD)
Ascending	122	158	IW	VV	129	2014/10/26-2021/12/18
Descending	71	429	IW	VV	159	2015/04/20-2021/12/14

The differential SAR interferometry seeks to construct the displacement map by practicing the conjugation of scenes (i.e., the calculation of phase difference). Eq. 5. 1 summarizes all of the factors that contribute to the phase difference between two SAR scenes:

$$\Delta\varphi_{\mathrm{dIn}}=\Delta\varphi_{\mathrm{disp}}+\Delta\varphi_{\mathrm{topo}}+\Delta\varphi_{\mathrm{orbit}}+\Delta\varphi_{\mathrm{atm}}+\Delta\varphi_{\mathrm{noise}}, \tag{5. 1}$$

where $\Delta\varphi_{dIn}$, $\Delta\varphi_{disp}$, $\Delta\varphi_{topo}$, $\Delta\varphi_{orbit}$, $\Delta\varphi_{atm}$, and $\Delta\varphi_{noise}$ are respectively the phase of differential SAR interferometry, interpreted displacement, topography, orbital error, atmospheric perturbations and residual speckle noise due to thermal effects, arbitrary distribution of different objects in each pixel, or residual values from other terms. The goal in InSAR analysis is to suppress the last four terms on the right side of Eq. 5. 1 and isolate the phase of displacement for which pre-developed digital elevation models (DEMs), orbital tube coordinates, and filters are procured. The displacement can be then computed using Eq. 5. 2:

$$\mathrm{Displacement}=\Delta\varphi_{\mathrm{disp}}\cdot\frac{\lambda}{4\pi}, \tag{5. 2}$$

where λ is the wave-length which is 5.54 cm for Sentinel-1.

Multi-temporal (MT) interferometry is a sequel to differential SAR interferometry and is developed to detect the most stable targets and minimize the impact of atmospheric interferences. In this study, SARPROZ software version 2021 (Perissin and Wang 2011; www.sarproz.com/) is used that employs a method called Persistent Scatterer InSAR (PS-InSAR; Ferretti et al. 2001). PS-InSAR starts with choosing a master scene to which other SAR scenes are co-registered. With respect to this master, all possible interferograms are generated. A series of candidate PSs with user-enforced reflectivity are chosen which can be used to estimate and screen the atmospheric contribution using the criteria of strong correlation in space but weak correlation in time. In the next step, by relaxing the threshold of PSs selection, more scatterers are selected and their phase value is transformed into the displacements which facilitates the calculation of velocity. The applied workflow followed the steps discussed in Goorabi et al. (2020), Khoshlahjeh Azar et al. (2021) and partly X. Liu et al. (2019). A threshold of 0.6 was used to mask poor coherent scatterers. Although a value of 0.75~0.8 is usually suggested (Di Traglia et al., 2021; Roque et al., 2021), lower values as used here are also reported for studying rural areas, especially on a local scale (Sun et al., 2015; X. Hu et al., 2016; Samsonov et al., 2020; Kang et al., 2021; H. Chen et al., 2022; Roy et al., 2022).

5.3.2. LOS Velocities Decomposition

To minimize any remaining noise, displacements of scatterers were filtered by Gaussian-weighted moving average with a bandwidth of 7% of the total number of scenes (Sharifi et al., 2021; Sharifi, Hendry, Macciotta, et al., 2022; Sharifi, Macciotta, & Hendry, 2022), then the average velocities were mapped using linear regression. However, these values are only projected values on the satellite line-of-sight (LOS). Its unit vector, LOS velocity (V_{LOS}), can be related to the true components of velocity as follows (Motagh et al., 2017; Sharifi, Hendry, & Macciotta, 2022):

$$V_{LOS}=V_V \cos\theta - (V_E \cos\alpha - V_N \sin\alpha) \sin\theta, \tag{5.3}$$

where V_V, V_E, and V_N are the vertical, eastward, and northward velocity components, respectively, α is the heading angle, and θ is the incidence angle. α is the azimuth of the satellite's orbiting direction with respect to true north and θ is the side-looking angle of the sensor toward the target (Figure 5- 7). Eq. 5. 3 is an ill-posed problem and, to address this, images obtained in two opposite orbits (ascending and descending) are used. However, this does not fully resolve the issue of decomposing the LOS velocity and the V_N component is typically ignored at this point. This is usually justified by considering that the satellite is sweeping the ground in near-polar orbits, which makes it almost unsighted to movements in the south-north direction (González, 2022). Therefore, V_V and V_E can be back-calculated upon making this simplifying assumption. These are, nevertheless, estimated components as the satellite is not completely insensitive to the south-north velocities; otherwise, the term would not appear in Eq. 5. 3 at all. The error of simplification by discarding V_N would be mathematically propagated toward V_V and V_E, making them an estimation of true values. These estimated values are denoted by small subscripts hereafter (V_v and V_e). The error of such an assumption for the ORD and other sites under comparable α and θ can be quantified using Eqs. 5. 4 and 5. 5, which are derived for this specific site as follows (the proof and general equations are presented in Appendix B):

$$\eta_V=-0.1706 \cdot V_N, \tag{5. 4}$$

$$\eta_E=0.0031 \cdot V_N, \tag{5. 5}$$

where $\eta_V=V_v-V_V$ and $\eta_E=V_e-V_E$ denote the error terms of the vertical and eastward components, respectively. To measure the effect of the true horizontal direction on the results, a sensitivity analysis was conducted using an angle β defined between the true horizontal velocity and V_N, which can be approximated as $\tan^{-1}(|V_e/V_N|)$ (please refer to Appendix B for further discussion). To conduct this analysis, Eqs. 5. 4 and 5. 5 can be transformed into the following:

$$\eta_V = -0.1706 \cdot V_e \cdot \tan\beta, \tag{5. 6}$$

$$\eta_E = 0.0031 \cdot V_e \cdot \tan\beta \,. \tag{5. 7}$$

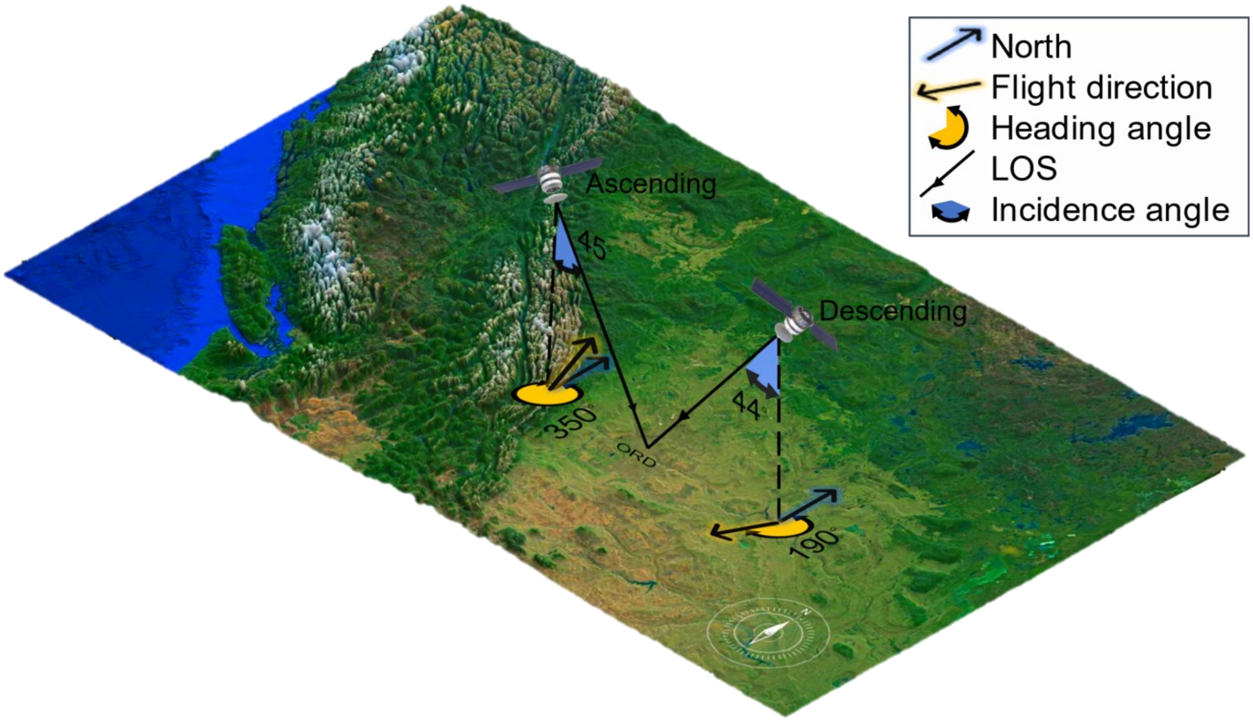

Figure 5- 9. Geometric characteristics of SAR images captured for ascending and descending orbits

To find the maximum error for a conservative quantification, equating the derivations of η_V and η_E to zero was not possible because they are proportional to $\sec^2\beta$. Based on the geometry of the geological formations, the angle β was varied in a known range of E0° to E45°S for points with an eastward direction of movement, mainly on the spillway. E45°S was found to result in the largest error and thus the most conservative estimations. For movements on the embankment, which are mostly under the influence of the slope-driven instability, we assumed the direction to be S18°W, which is perpendicular to the dam's crest. This orientation was selected because it yields the largest error within the range of S18°W to S90°W, and a further south-inclined direction seems unlikely due to the slope geometry.

For a successful decomposing practice, the ascending and descending velocities must correspond to the same point on the ground yet it is rather unlikely to have scatterers from these two sets that geographically overlie. We accordingly borrowed an alternative method from computational geometry called the k-nearest neighbours (kNN) search algorithm (Guo et al., 2003). For every single scatterer from one orbital geometry, kNN searches for k neighbouring scatterers from the opposing geometry and a weighting kernel based on the distance of these scatterers is enforced to address their different contributions. For instance, Figure 5- 9 shows a scatterer from an ascending set (red circle) surrounded by $k=7$ descending scatterers (blue circles), numbered from the nearest to the farthest (i.e., 1 is the closest). Eqs. 5. 8 and 5. 9 demonstrate how kNN is adopted in this example:

$$\widehat{\mathrm{V}}_{\mathrm{LOS}_{\mathrm{D_j}}}=\frac{\sum_{\mathrm{i}=1}^{7}\mathrm{w_i}\mathrm{V}_{\mathrm{LOS}_{\mathrm{D_i}}}}{\sum_{\mathrm{i}=1}^{7}\mathrm{w_i}}, \tag{5. 8}$$

$$\mathrm{w_i}=1-\frac{\mathrm{d_i}}{\mathrm{d_7}}, \tag{5. 9}$$

where $\widehat{V}_{LOS_{D_j}}$ is the equivalent descending LOS velocity corresponding to the jth ascending scatterer, $V_{LOS_{D_i}}$ is the LOS velocity of ith descending scatterer, and w_i is the averaging weight as calculated using Eq. 5. 9. Because the point numbers are sorted in accordance with the distance from the red circle, d_7 is the largest distance and the weights of other points are normalized with respect to it, which automatically leads to the zero significance of point 7 itself. The red and blue points in this procedure can be switched to find all of the equivalent ascending scatterers neighbouring the descending scatterers. The kNN algorithm appreciates the discrete nature of scatterers that would not lead to a reduction in resolution, obscuring the spatial trend, and complications regarding the geometrical aspect of its implementation. Contrary to square down-sampling (Carlà et al., 2019; M. Li et al., 2020), this method does not require an evaluation of the gridding sufficiency, orientation, and size of cells because the kNN algorithm only prompts the number of points (*k*), which can be deduced from a simple sensitivity analysis considering that a distance-damping kernel is employed.

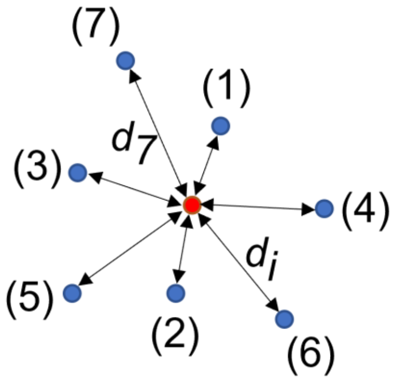

Figure 5- 10. An example of kNN algorithm application (red and blue circles belong to ascending and descending sets, respectively)

5.3.3. Combined Precision Calculation

To quantify the inherent precision of InSAR measurements, an approach using temporal coherence (γ) was adopted using Eq. 5. 10 (Y. Zhang et al., 2018; Kellndorfer et al., 2022):

$$\text{Precision}=\frac{\lambda}{4\pi}\sqrt{\frac{1-\gamma^2}{2\gamma^2}}, \tag{5. 10}$$

where λ is the wavelength, equal to 5.54 cm for C-band sensors such as Sentinel-1. The precision computed by Eq. 9 was added to and subtracted from the cumulative displacements to obtain the maximum and minimum range of LOS velocities for each scatterers. Four different combinations of LOS velocities with respect to two orbiting geometries (ascending and descending) were incorporated into decomposition process to assess Eastward and vertical components after compensating for the error associated with the simplifying assumption (Eqs. 5. 6 and 5. 7). The largest difference between the resultant components with the initially estimated velocities is regarded as the combined precision, which is comprehensive enough in evaluating the reliability of InSAR-driven velocities given all known sources of errors are taken into account.

5.4. Results and Discussion

5.4.1. Estimated InSAR velocities

The k in the kNN algorithm was varied iteratively from 2 to 21, and V_v and V_e were estimated at each iteration for the scatterers. The mean changes of these components bounded by 1-σ for one unit of increase to k (from k-1) are plotted in Figure 5- 11a. This figure shows changes in the V_v and V_e are agreeably close and unstable at low k values, but the range of the changes gradually decreases after a k of 7 or 8. A k of 11 was selected for this study; however, variations of results in response to changing k from 7 to 13 showed negligible impacts on the results. Figure 5- 11b presents the weight distribution of 11 surrounding scatterers around each scatterer of interest. The trend of the weight kernel for all scatterers starts from an initial high value (0.22 on average) and exponentially decreases to zero for the 11th point. The average diagram in Figure 5- 11b provides a sense of how w_i changes and was not used in the analysis; each scatterer was studied using its specific kernel (grey lines).

A total of 740 scatterers with an approximate density of 1 per 320 m^2 were identified in the process of InSAR analysis. Figure 5- 12 shows the temporal coherence of these scatterers both in space and as a histogram distribution. The mean coherence is 0.86 with a standard deviation of 0.10, meaning almost 80% of the scatterers have a coherence of greater than 0.75 as typically recommended, and the remaining scatterers with a coherence between 0.60 and 0.75 are in the expected range given the lower reflection of geo-materials (Sun et al., 2015; X. Hu et al., 2016; Samsonov et al., 2020; Kang et al., 2021; H. Chen et al., 2022; Roy et al., 2022). Early LOS velocity values are also provided in Appendix A.2 for further interests of readers.

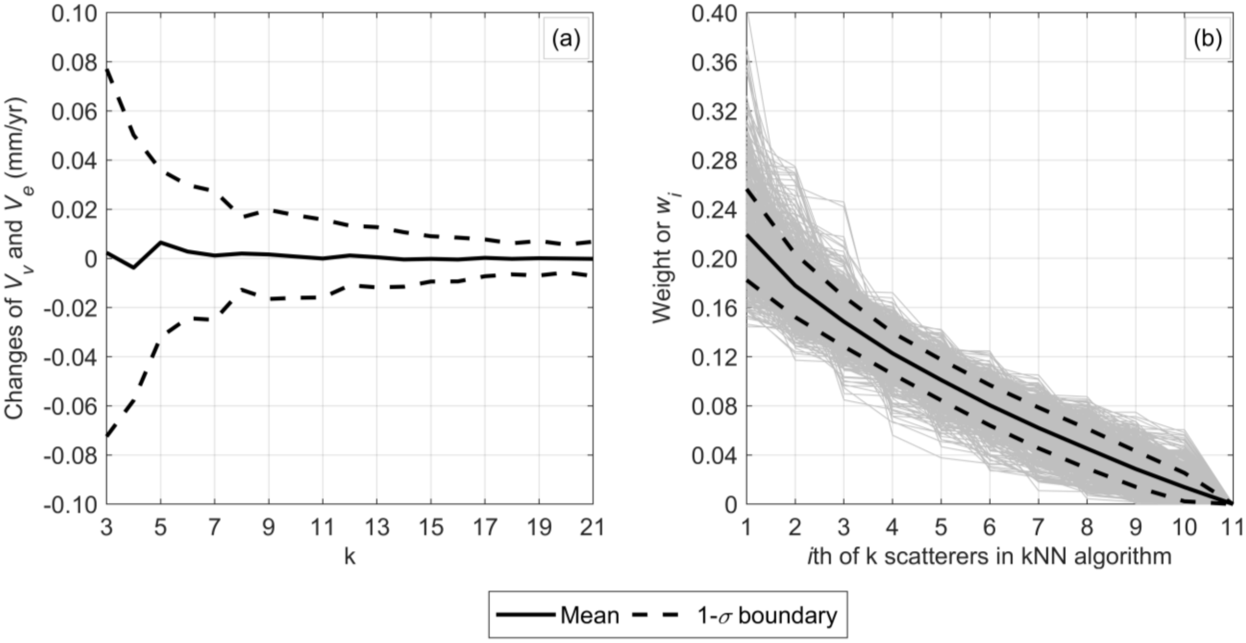

Figure 5- 11. (a) Sensitivity of estimated velocity components with a unit increase to k, and (b) weight distribution for scatterers in kNN for k=11

Figure 5- 13 displays the spatial distribution of scatterers on the spillway, colour-coded by the magnitude of estimated velocity components, as well as a histogram portraying the statistical distribution of velocity magnitudes. The detected scatterers largely populate the headworks of the spillway and the mid-chute part toward the flip bucket. The sign convention is upwards and eastward for positive values of V_v and V_e, respectively. Figure 5- 13a,b demonstrates almost all of the scatterers are showing subsidence except for three scatterers with negligible vertical velocities of 0 to 0.02 mm/yr. The spatial trend of V_v is increasing subsidence, from values of almost -0.3

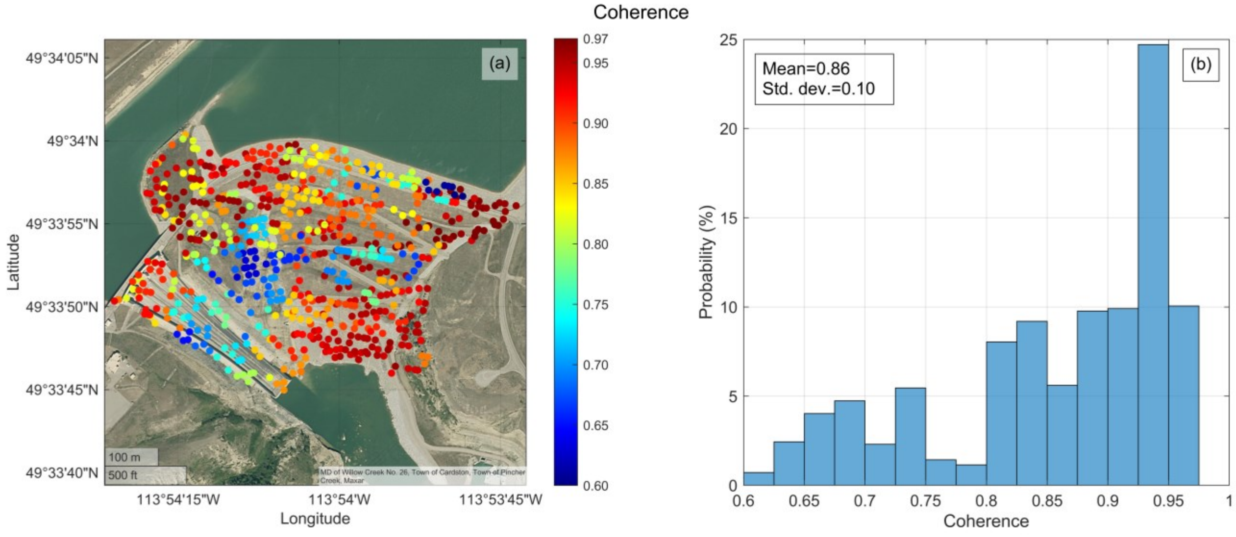

Figure 5- 12. (a) Spatial distribution of detected scatterers colour-coded based on the coherence value and (b) histogram of these values

mm/yr at the headworks toward peak values of -1.17 mm/yr at the mid-chute and again decreasing to -0.3~-0.4 mm/yr at the flip bucket. V_e is approximately 0.35, 1.10, and 0.6 mm/yr at the headworks, mid-chute, and flip bucket, respectively. The total station surveys indicated an eastward tendency of spillway velocities with a decreasing trend in their magnitudes from northeast to southwest and high to low elevations along the spillway fall line. The eastward direction of V_e is parallel to the survey results and also confirmed by our geological knowledge of the formations' strike. However, as seen in Figure 5- 13, the general spatial trend in V_e is increasing from the headworks to the flip bucket with no distinct pattern of lateral variation. Possible explanations for this discrepancy can relate to the residual noise, simplifying assumption error, and InSAR precision that distorted these V_e estimations to a level such that the spatial trend is no longer discernible even though the values themselves are in a credible range. This calls for a detailed error and precision study, which is discussed later. As a result of these uncertainties, the average values are regarded as representative values for V_v and V_e estimations. Figure 5- 13b,d suggests such values are -0.65 and 0.69 mm/yr for the vertical and the eastward velocities while

V_e values are slightly more concentrated around the mean value. Involving the coherence values shown in Figure 5- 12 in the averaging as a weighting function and granting a larger contribution to more coherent scatterers was considered, but did not significantly change the average values. Considering -0.65 and 0.69 mm/yr for V_v and V_e, the total velocity can be approximated between 0.95 and 1.20 mm/yr for horizontal movements between purely eastward and E45°S based on the *in situ* data. This range of velocities is in good agreement with Hendry et al. (2019), who reported a long-term velocity of 1 mm/yr (Figure 5- 6).

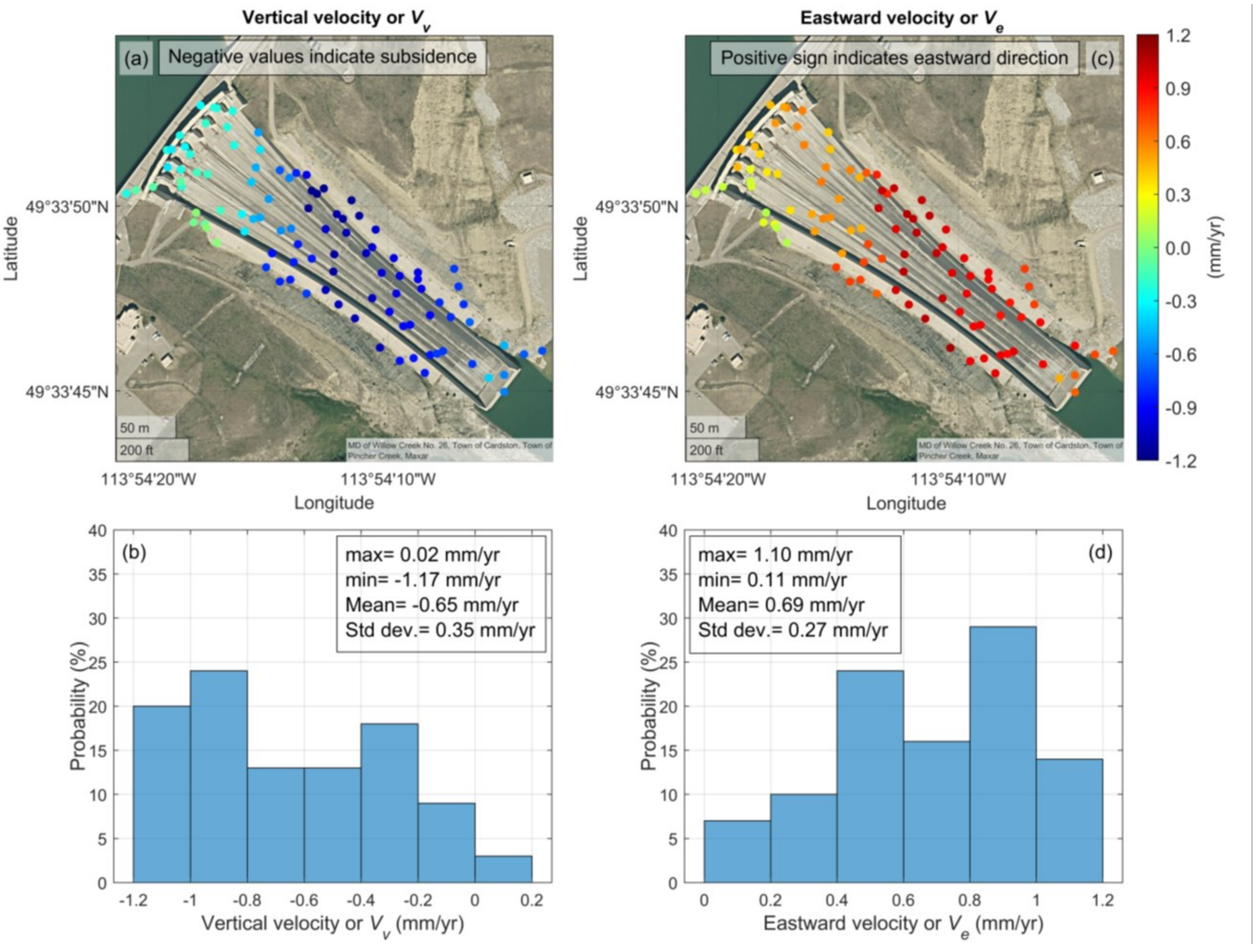

Figure 5- 13. Spatial distribution and velocity histogram of the spillway scatterers in vertical (a & b) and eastward (c & d) directions

Figure 5- 13 illustrates the spatial distribution and histogram of V_v and V_e estimations for the scatterers identified on the embankment. All points have negative V_v values, implying pervasive subsidence with most points subsiding at rates less than 2 mm/yr on the headland, rock outcrop, riprap, and sides of the dam's crest. However, a confined region on the top two-thirds of the embankment adjacent to the left abutment is settling at greater than 2 mm/yr, with a few points with low coherence reaching extreme values of 7 mm/yr (Figure 5- 11). A similar bimodal distribution is also seen in the histogram of V_e, again suggesting the points within the same active area are travelling westward at higher rates up to 3 mm/yr while the remaining scatterers on the embankment and in the adjacent areas are moving toward the east at rates less than 2.01 mm/yr. For the active area, higher vertical velocities near the crest and a fairly uniform V_e in the middle would imply the affected area is bowl shaped. The average V_v and V_e for scatterers on the embankment are computed to be -1.81 and -0.11 mm/yr (Figure 5- 13b,d), with little effect of coherence. However, differentiating the active area from the inactive areas is better in terms of proposing a representative value. The average V_v and V_e values for the active and inactive areas were calculated as -3.92 and -2.04 mm/yr and -0.9 and 0.71 mm/yr, respectively . Adopting an assumption regarding the horizontal velocity direction being the same as the spillway resulted in the total velocity of inactive areas estimated to fall within the range of 1.14 to 1.68 mm/yr. Assuming a horizontal velocity direction of the active area orthogonal to the dam's crest leads to a total velocity of 7.68 mm/yr for this area.

5.4.2. Quantification of Error and Combined Precision

The error associated with the simplifications as calculated by Eqs. 5. 6 and 5. 7 is shown in Figure 5- 14a. The error associated with the simplifying assumption is insignificant for the majority of scatterers, being limited to 0.4 and 0.0072 mm/yr for V_v and V_e, respectively. The average values of η_V and η_E for the scatterers on the spillway are 0.12 and 0.0021, which is 13% and 0.3% of the representative values discussed before (V_v= -0.9 mm/yr and V_e= 0.71 mm/yr). The active area on the embankment, however, is exposed to larger errors with a maximum of 1.51 and 0.0274 mm/yr in the vertical and eastward directions; the average values in this area of 1.07 and 0.02 mm/yr, respectively, are 27% and 1% of the representative velocity values (V_v=-3.92 mm/yr and V_e=-2.04 mm/yr). The vertical component is identified as the most susceptible to the simplifying assumption. After quantifying the error associated with the simplifying assumption, a more accurate calculation of the total velocity was possible as shown in Figure 5- 14b. The average

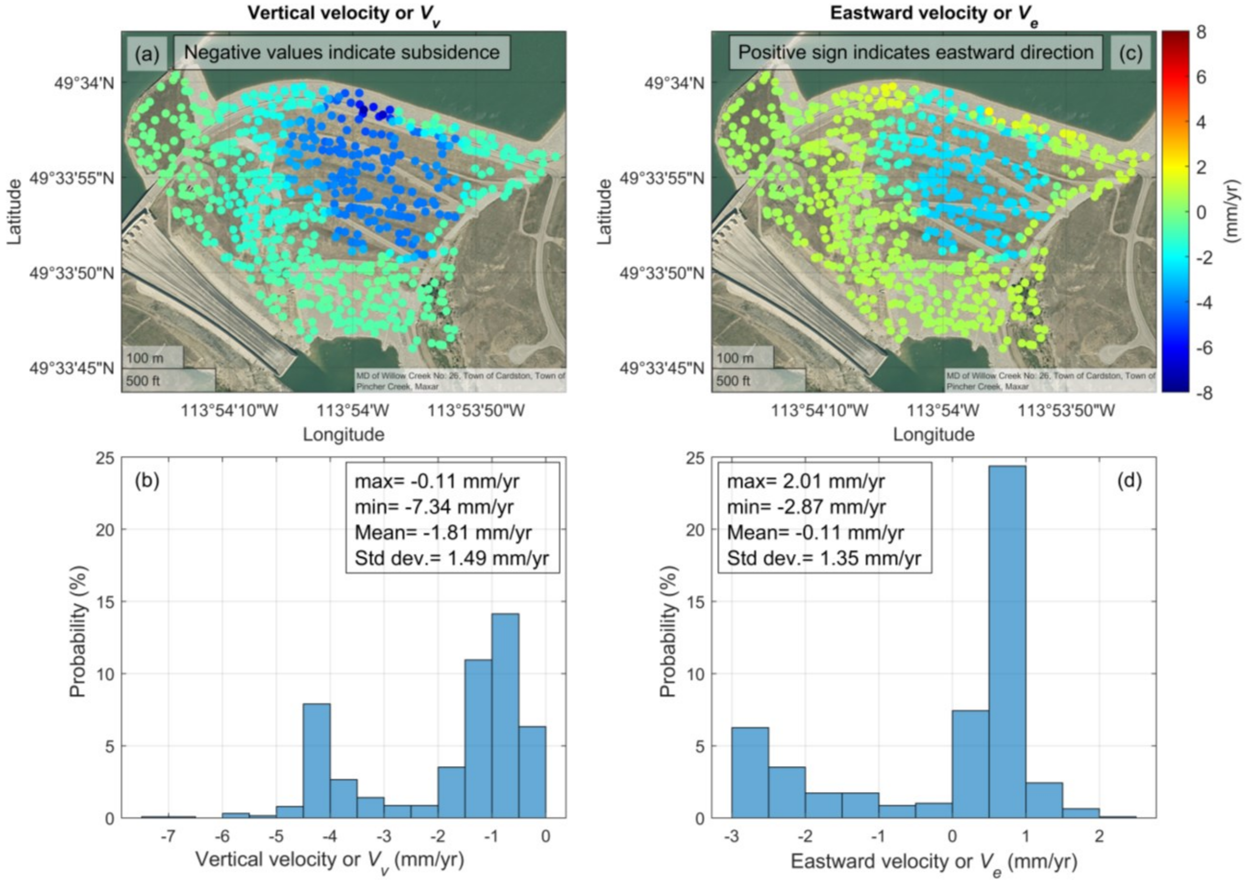

Figure 5- 14. Spatial distribution and velocity histogram of the embankment scatterers in the vertical (a & b) and eastward (c & d) directions

total velocity is calculated as 1.26 and 8.29 mm/yr for the spillway and active area, respectively, and 1.50 mm/yr for the remaining scatterers.

Based on Eq. 5. 10, Figure 5- 15 features a histogram of the precision of LOS velocities and the corresponding LOS velocities. The mean and standard deviation of the precision values are calculated as 0.23 and 0.12 mm/yr, respectively. The resultant combined precisions are illustrated in Figure 5- 16a-c for the vertical, eastward, and total velocities. The majority of scatterers located in the inactive areas have a combined precision in V_v estimations of less than 0.75 mm/yr, while those on the rock outcrop are subjected to larger precision values (1.5 mm/yr). This rises to 2.5 mm/yr for the active area on the embankment, indicating a higher uncertainty in the vertical velocity than for the spillway (Figure 5- 12a,b) that may increase the V_v estimations of the active area (Figure 5- 13a,b) to almost 10 mm/yr. On the other hand, the combined precision for V_e (Figure 5- 16b) indicates estimations for this component (Figure 5- 12c,d and Figure 5- 13c,d) have a greater level of uncertainty. Most of the area is showing a precision of 1.5 to 4 mm/yr, except for the headland, headworks, and top of the spillway chute. This could substantiate why the spatial trend of the estimated V_e for the spillway (Figure 5- 12c) did not conform to the total station surveys (Figure 5- 6). The former showed an increase from the headworks to the flipbucket while the opposite was observed in the latter. The combined precision of V_v and V_e, and especially V_e, was subjected to non-negligible changes with respect to the small variations in the assumed horizontal direction of movement (β) while this was less accentuated for the total velocity. To take this observation into account and also report a single consolidated parameter, we decided to regard the combined precision of the total velocity as the final precision. Figure 5- 16c shows the spatial trend of the total velocity precision reconciles better with V_v and distinctly

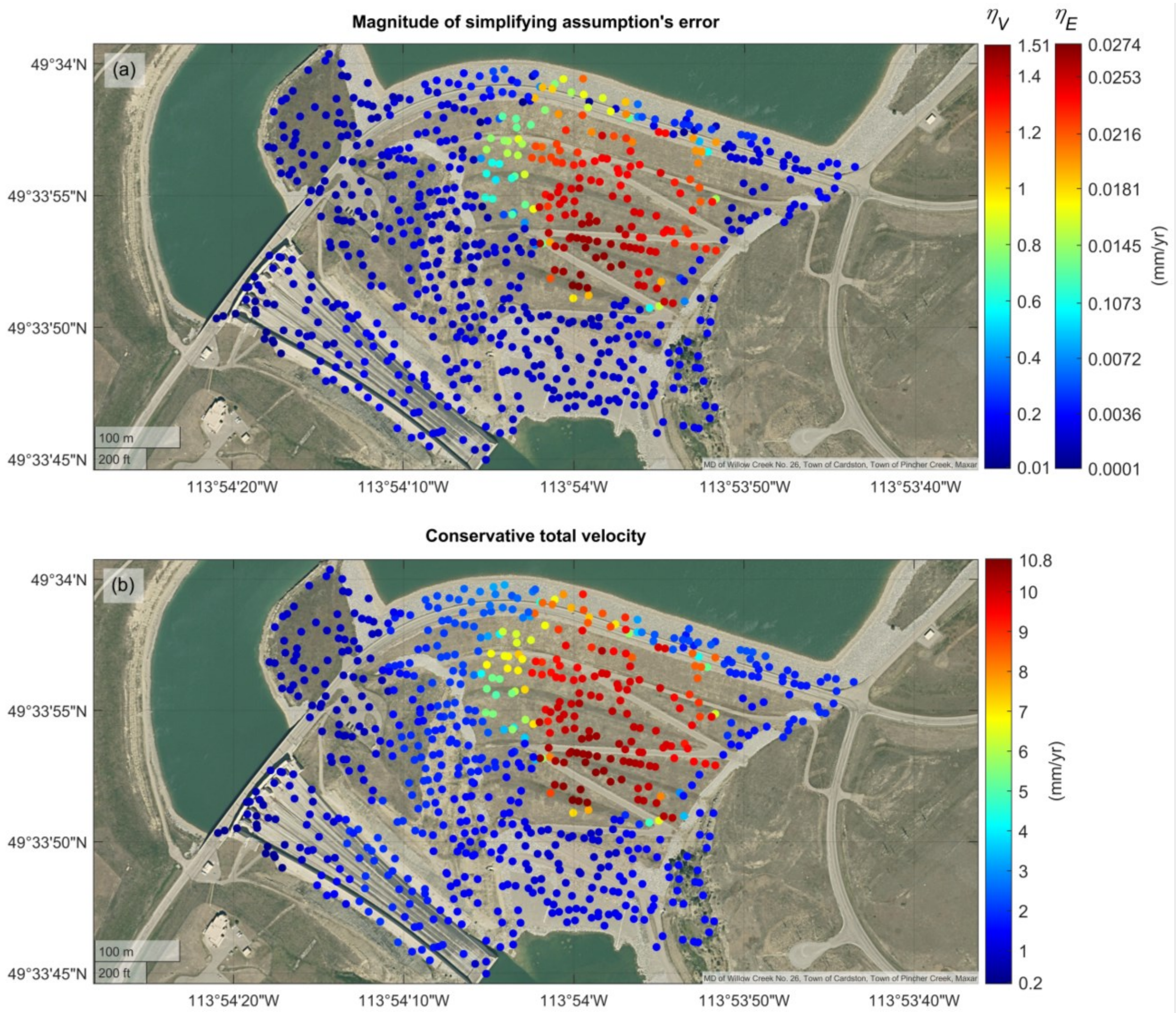

Figure 5- 15. (a) Magnitude of simplifying assumption error on V_v and V_n, and (b) the total conservative velocity upon the assumed horizontal direction of movement (E45°S and S18°W for the eastward and westward-moving scatterers, respectively)

separates the active area from the remaining inactive area. Therefore, the histograms of total velocity precision for these two areas are plotted independently (Figure 5- 16d) with mean values of 0.72 and 2.78 mm/yr for the inactive and active areas, respectively.

5.4.3. Time-series Velocities and Displacements

In addition to average velocities in the study period (late 2014 to late 2021), velocity assessments broken down into shorter periods would be beneficial to establish new projections regarding long-term trends. The yearly averaged total velocities of scatterers on the spillway and

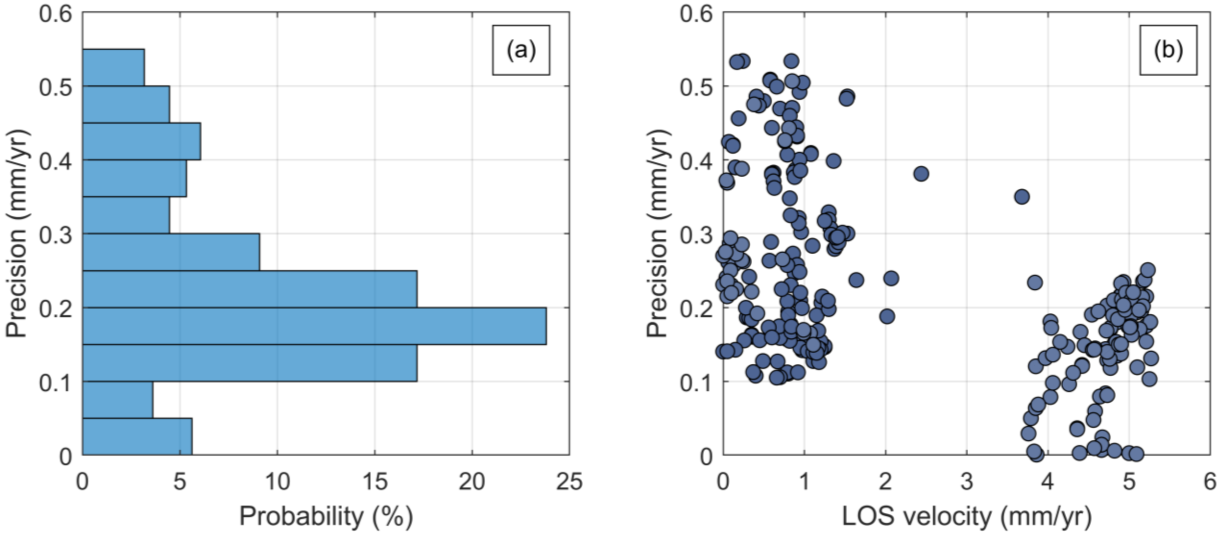

Figure 5- 16. (a) Histogram of LOS velocity precision and (b) precision vs. corresponding LOS velocities

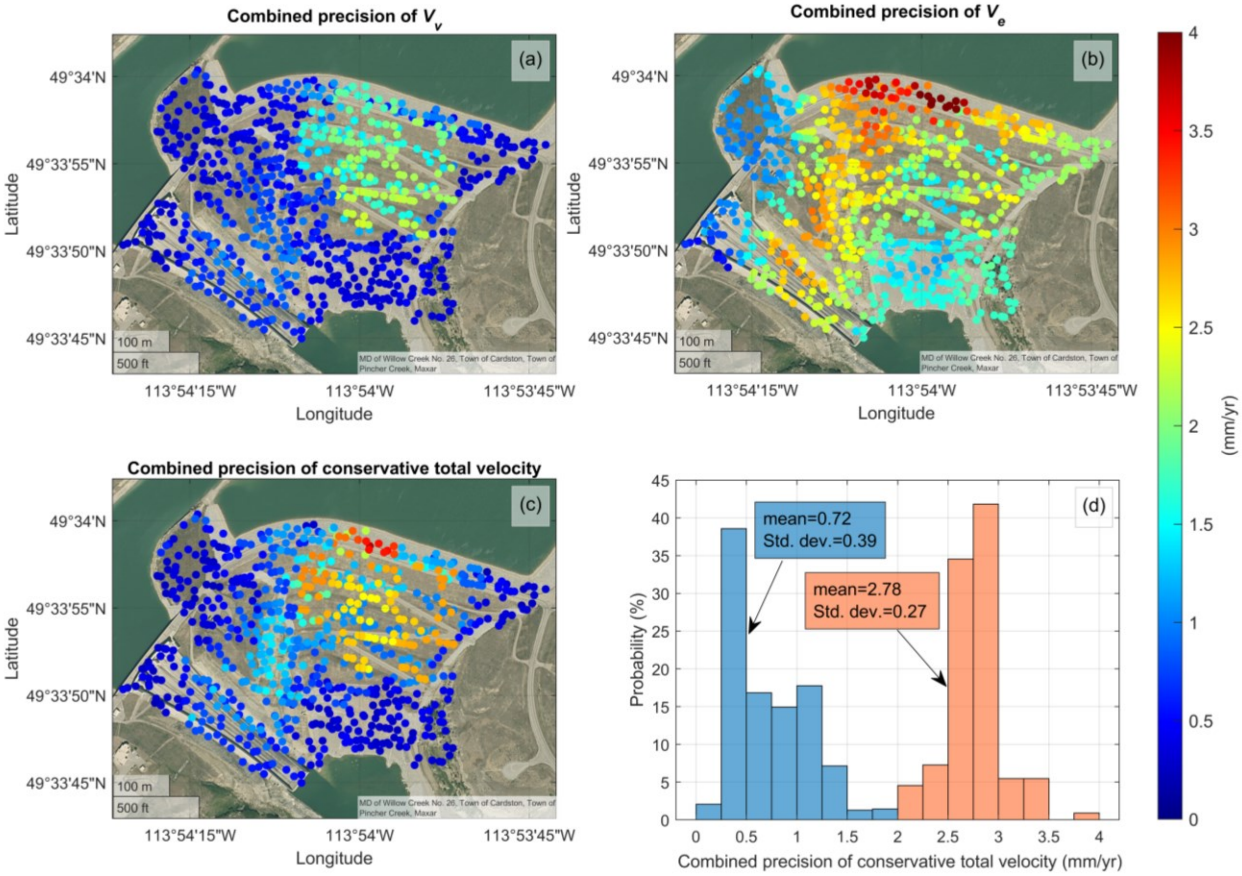

Figure 5- 17. Spatial distribution of combined precision of (a) V_V, (b) V_e and (c) total velocity, and (d) the histogram of total velocity combined precision

the embankment’s active area are plotted in Figure 5- 18. The general trend of the active area is decreasing, reaching values of 5 mm/yr with a lower range of variations after 2018. The spillway, on the other hand, is somewhat consistently moving at about the rate of 1 mm/yr, similar to long-term trends established by (Hendry et al., 2019) (Figure 5- 6). These variations in average velocities could not be correlated to seasonal variations in the reservoir level. The average velocity discussed throughout this paper stems from a non-seasonal cause and is calculated by fitting a line. The residual displacement varying around this fitted line is composed of noise and seasonal effects. We attempted to minimize the noise by employing the Gaussian-weighted moving average, which leaves the seasonal variations as the dominant component in the seasonal displacements. The displacements of headworks’ scatterers were averaged because they indicated a coherent radar response (Figure 5- 12), and then linearly detrended, which is shown against the reservoir level in Figure 5- 19. Around July of each year, the reservoir level reaches its maximum and the seasonal LOS displacement shows a lagged response of a local maximum. The same observation is also evident for the troughs in the diagram. The characteristic points marking the same local maxima and minima in the reservoir level diagram and seasonal LOS displacements are heuristically identified and numbered in Figure 5- 19. Neither the absolute values nor the magnitude of changes of reservoir level and LOS displacements of identical points could be quantitatively correlated. However, the uncanny similarities between the trends of these two diagrams suggest the reservoir level is one major factor that contributes to the seasonal displacements of the spillway.

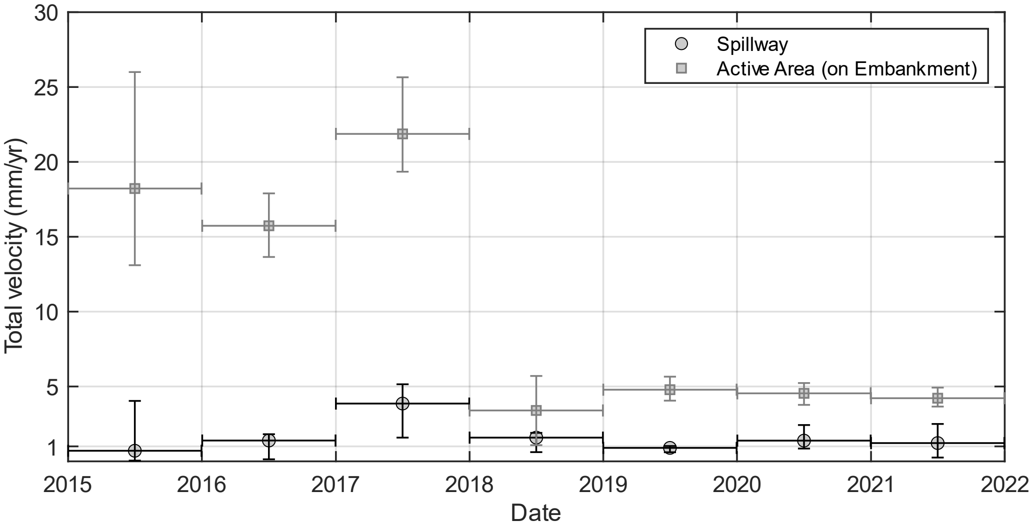

Figure 5- 18. Yearly-averaged velocities for the spillway and the active area on the embankment (horizontal and vertical lines characterize the average span and range of values, respectively)

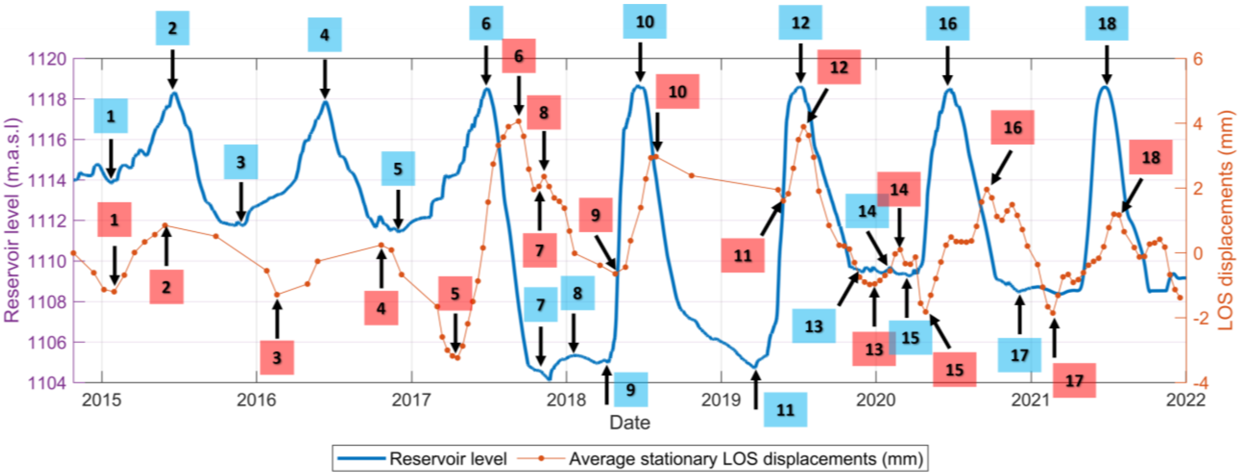

Figure 5- 19. Average LOS displacements of the headworks' scatterers (right axis) against the reservoir level measured at hydroclimatic station No. 05A032 (left axis) for November 2014 to the end of 2021 (numbered points indicate comparable characteristic points in two diagrams)

5.5. Discussion

Previous investigations conducted by industry firms hypothesized the following mechanisms for continuous movements of the spillway: (1) a progressive failure with strength reduction due to ongoing strain and (2) swelling of the mudstone rock formation in the foundation. Hendry et al. (2019) argue that the latter is likely the reason for the continuous movements of the spillway and the surrounding areas. They refute the progressive failure mechanism since there is no evidence of correlations between pore pressures measured by piezometers with the velocities measured by extensometers. Responses of piezometers at the elevation of clay shales to the changes in reservoir level indicate that these weak materials have ready access to water. This triggers the swelling mechanism which is also manifested by the upward movements reported by the extensometers beneath the spillway's headwork as much as 0.3 to 1.2 mm/yr. In this study, however, we could not observe these upward movements which shows these sub-millimetric velocities may not be detected by coarse-resolution SAR scenes.

We suggest that changes in water level leads to a variation in the effective stress given the reported hydraulic connection between the reservoir level and piezometer readings. The observed lag between the diagrams in Figure 5- 19 also arises from the time it takes for water to percolate or dissipate until the groundwater table reflects the reservoir level. Therefore, it is conjectured that two driving mechanisms are at work. The first one is the swelling mechanism, as per Hendry et al. (2019), that continuously prompts the ground to move but the effect of which has decelerated toward 1 mm/yr (Figure 5- 7). The second one is the shear strength reduction in the shear planes caused by seasonal reservoir level changes that is partially responsible for the seasonality in the displacements. This latter observation was not recognized in the displacements of the active area on the embankment, implying another mechanism is responsible. However, a decreased velocity of the active area since 2018 may suggest the activity has ceased and reached an equilibrium. Future measures to keep tracking the movements on the embankment are suggested.

5.6. Conclusions

In North America, numerous dams and their associated structures are susceptible to ground movements caused by weak materials or pre-sheared surfaces. One notable example is the Oldman

River Dam, located in southern Alberta, Canada. This study focused on analyzing the period from 2015 to the end of 2021 using multi-temporal SAR analysis of 288 scenes archived by Sentinel-1.

The history of ground movement detection at the Oldman River Dam dates back to its initial filling in 1991. Previous studies have indicated a deceleration in the velocity of the spillway and its adjacent areas, reaching an average of 1 mm/yr in the long term. In this study, we aimed to validate this conclusion using SAR interferometry and assess the activity state of the embankment. We quantified the error of estimations resulting from temporal decorrelation and simplifying assumptions in the velocity decomposition. We also examined the relationship between seasonal movements of the spillway's headwork and variations in reservoir level to understand their contribution to ground movements.

The spillway is experiencing subsidence at an average velocity of 0.65 mm/yr and displacement towards the east at an average velocity of 0.69 mm/yr. Considering the formation strike reported in the site investigation, the total velocity is estimated to be between 0.95 and 1.20 mm/yr. The average subsidence and westward velocity of the embankment area were calculated at 1.81 and 0.11 mm/yr, respectively. Notably, an oval-shaped active area was identified, exhibiting subsidence at a velocity of 3.92 mm/yr and westward movement at 2.04 mm/yr. In contrast, the remaining inactive areas show subsidence at a rate of 0.9 mm/yr and an eastward velocity of 0.74 mm/yr.

We present ad hoc equations to calculate the error resulting from simplifying assumptions, which can be modified for other cases. After compensating for this error, the total velocities of the spillway and the active area on the embankment were determined to be 1.26 and 8.29 mm/yr, respectively. Considering both the simplifying assumption error and temporal decorrelation, the combined precision of estimations was calculated as 2.78 mm/yr for the active area and 0.72 mm/yr for the rest of the site.

Regarding the yearly average velocities, the active area on the embankment seems to have decelerated to 5 mm/yr from toward the end of 2021, while the spillway velocity remains relatively stable at around 1 mm/yr with minor variations. The analysis revealed that the reservoir level affects the seasonal displacement of the spillway, but no significant correlation was found for the active area on the embankment.

Overall, this study provides valuable insights into the performance of InSAR for monitoring ground movements at the Oldman River Dam site. The findings highlight the importance of considering error sources, such as simplifying assumptions and temporal decorrelation, in velocity estimations. The knowledge gained from this research can contribute to improving monitoring and management strategies for infrastructure affected by ground movements.

Appendix A – Quantification of Simplifying Error

Eq. 5. *11* shows the complete system of equations relating both knowns (ascending and descending LOS velocities) to the unknowns (three components of real velocity), which is simplified to Eq. 5. *12* upon discarding the south-north component:

$$\begin{pmatrix} V_{LOS_{Asc}} \\ V_{LOS_{Des}} \end{pmatrix} = \begin{bmatrix} \cos\theta_{Asc} & -\cos\alpha_{Asc}\sin\theta_{Asc} & \sin\alpha_{Asc}\sin\theta_{Asc} \\ \cos\theta_{Des} & -\cos\alpha_{Des}\sin\theta_{Des} & \sin\theta_{Des}\sin\theta_{Des} \end{bmatrix} \begin{pmatrix} V_V \\ V_E \\ V_N \end{pmatrix}, \tag{5. 11}$$

$$\begin{pmatrix} V_{LOS_{Asc}} \\ V_{LOS_{Des}} \end{pmatrix} = \begin{bmatrix} \cos\theta_{Asc} & -\cos\alpha_{Asc}\sin\theta_{Asc} \\ \cos\theta_{Des} & -\cos\alpha_{Des}\sin\theta_{Des} \end{bmatrix} \begin{pmatrix} V_v \\ V_e \end{pmatrix}, \tag{5. 12}$$

where *Asc* and *Des* subscripts pertain to ascending and descending orbits, respectively, V_{LOS} is the LOS velocity, θ is the incidence angle, α is the heading angle, V_V, V_E, V_N are the true vertical, eastward, and northward velocity components, respectively, and V_v and V_e are the estimated vertical and eastward velocity components, respectively. Equating the right-hand sides of Eqs. 5. *11* and 5. *12* and solving the matrixes leads to Eq. 5. 13, which describes the relationship between the true and estimated velocity components:

$$\begin{pmatrix} \mathrm{V_v} \\ \mathrm{V_e} \end{pmatrix} = \begin{bmatrix} 1 & 0 & \dfrac{-(\sin(\alpha_{\mathrm{Asc}}-\alpha_{\mathrm{Des}}) \sin\theta_{\mathrm{Asc}} \sin\theta_{\mathrm{Des}})}{\cos\alpha_{\mathrm{Asc}} \cos\theta_{\mathrm{Des}} \sin\theta_{\mathrm{Asc}} - \cos\alpha_{\mathrm{Des}} \cos\theta_{\mathrm{Asc}} \sin\theta_{\mathrm{Des}}} \\ 0 & 1 & \dfrac{-(\sin\alpha_{\mathrm{Asc}} \cos\theta_{\mathrm{Des}} \sin\theta_{\mathrm{Asc}} - \sin\alpha_{\mathrm{Des}} \cos\theta_{\mathrm{Asc}} \sin\theta_{\mathrm{Des}})}{\cos\alpha_{\mathrm{Asc}} \cos\theta_{\mathrm{Des}} \sin\theta_{\mathrm{Asc}} - \cos\alpha_{\mathrm{Des}} \cos\theta_{\mathrm{Asc}} \sin\theta_{\mathrm{Des}}} \end{bmatrix} \begin{pmatrix} \mathrm{V_V} \\ \mathrm{V_E} \\ \mathrm{V_N} \end{pmatrix}. \tag{5. 13}$$

Substituting values of 45°, 350°, 44°, and 190° for the ascending incidence angle, ascending heading angle, descending incidence angle, and descending heading angle, respectively, results in V_v-V_V=-0.1706V_N and V_e-V_E=0.0031V_N, which can be used to study the effect of discarding the south-north component on the estimated velocity components (V_v and V_e). In general, the simplifying assumption's error is linearly correlated to V_N by a coefficient. Tables Table 5- 2 to Table 5- 4 show the variation of coefficients of error in vertical and eastward components as well as their ratio, respectively for a typical range of incidence angle (30-45°) and heading angles (350 and 190° for ascending and descending orbits, respectively). Table 5- 2 indicates low incidence angles are preferred to minimize the simplifying assumptions' error while Table 5- 3 displays the incidence angles between ascending and descending orbits should be as close as possible. Table 5- 4 confirms that vertical component is always the most compromised component. This, in particular, can be critical for translational landslides moving sub-horizontally which are very common in Western Canadian Sedimentary Basin.

Table 5- 2. Coefficient of simplifying assumption's error (%) along vertical axis

		Ascending			
	Incidence angle	30	35	40	45
Descending	30	-10.03	-10.99	-11.88	-12.71
	35	-10.99	-12.16	-13.26	-14.30
	40	-11.88	-13.26	-14.57	-15.85
	45	-12.71	-14.30	-15.85	-17.36

Table 5- 3. Coefficient of simplifying assumption's error (%) along eastward axis

		Ascending			
	Incidence angle	30	35	40	45
Descending	30	0.00	1.70	3.26	4.72
	35	-1.70	0.00	1.59	3.11
	40	-3.26	-1.59	0.00	1.54
	45	-4.72	-3.11	-1.54	0.00

Table 5- 4. Ratio of simplifying assumption's error in vertical axis over eastward axis

		Ascending			
	Incidence angle	30	35	40	45
Descending	30	N/A	-6.48	-3.65	-2.69
	35	6.48	N/A	-8.33	-4.60
	40	3.65	8.33	N/A	10.27
	45	2.69	4.60	10.27	N/A

In this study, an angle of $\beta_1 = \tan^{-1}(V_E/V_N)$ is defined to study the effect of the horizontal velocity direction on the assessments. In the following, β_1 is shown to be agreeably close to $\beta_2 = \tan^{-1}(V_e/V_N)$, which is helpful as V_E is not known but V_e is known:

$$\tan\beta_1 = \frac{V_E}{V_N} = \frac{V_e\text{-}0.0031V_N}{V_N} = \frac{V_e}{V_N}\text{-}0.0031 = \tan\beta_2\text{ -}0.0031, \tag{5. 14}$$

$$\tan(\beta_2\text{-}\beta_1) = \frac{\tan\beta_2 - \tan\beta_1}{1+\tan\beta_1\tan\beta_2} = \frac{0.0031}{1+\tan\beta_2(\tan\beta_2\text{ -}0.0031)}. \tag{5. 15}$$

Plotting Eq. 5. *15* reveals this function varies between 0.0031 and zero, which means:

$$0 \leq \tan(\beta_2 - \beta_1) \leq 0.0031 \Longrightarrow 0 \leq \beta_2 - \beta_1 \leq 0.18°. \tag{5. 16}$$

This means the separation between β_1 and β_2 is less than 0.2° in the worst-case scenario, implying $\beta_1 \approx \beta_2 = \beta$ (as referred to in the main body). The importance of this outcome, as mentioned above, is that it enables us to conduct a sensitivity analysis by varying the angle of β, the azimuth of horizontal velocity:

$$V_V = V_v + \frac{0.1706}{\cos\beta} V_e, \tag{5. 17}$$

$$V_T = \sqrt{\left(V_v + \frac{0.1706}{\cos\beta} V_e\right)^2 + \left(\frac{0.1706}{\cos\beta} V_e\right)^2}, \tag{5. 18}$$

where V_v, V_e, and β are known and V_T is the true total displacement.

Appendix B – InSAR LOS Velocity

Figure 5- 20 presents the LOS velocity of scatterers detected in analyzing ascending and descending scenes.

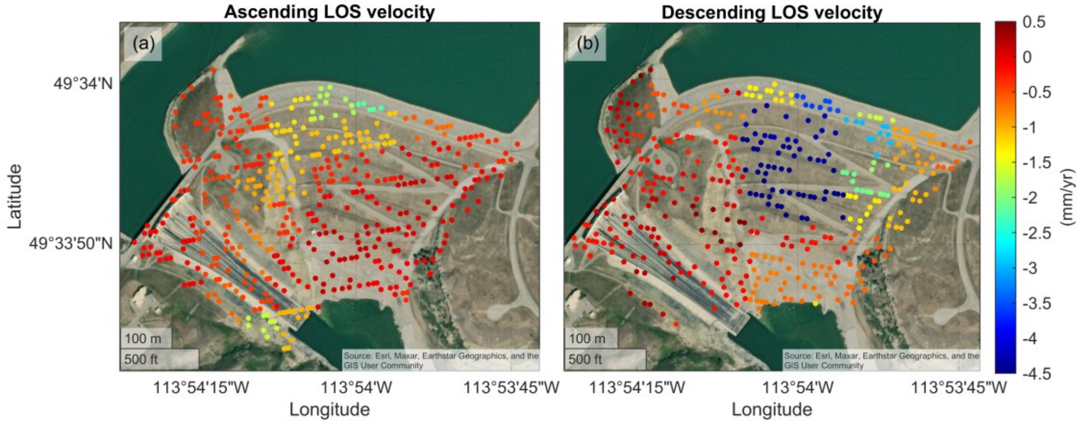

Figure 5- 20. LOS velocity obtained by analyzing SAR scenes in (a) ascending and (b) descending orbital geometries

Chapter 6: Evaluating topography-based methods in 3D decomposition of InSAR 1D velocities obtained for translational landslides: Thompson River Valley in Canada

---

Contributions of the Ph.D. Candidate

The material presented in this chapter, including the literature review, conceptualization, methodology development, analysis, draft preparation and revisions, are conducted by the Ph.D. candidate. The supervisors, Dr. Michael Hendry and Dr. Renato Macciotta, have reviewed all pieces presented in the published manuscript, cited below:

Sharifi S, Macciotta R, Hendry, MT, 2023. “Evaluating topography-based methods in 3D decomposition of InSAR 1D velocities obtained for translational landslides: Thompson River Valley in Canada”, *Landslides*, 1:17. https://doi.org/10.1007/s10346-023-02153-0.

Contributions of This Chapter to the Overall Study

Another approach to decomposing InSAR’s LOS velocity is exercising assumptions inspired by the ground geometry. This establishes a compatibility assumption between velocity components. However, very few insights exist on the accuracy and detriments of each, especially for applications on landslides with translational mechanisms. Four different methods, SPFM, SPFM-LSM, APFM and LSTM are examined on analyzed SAR scenes over Thompson River Valley. The GPS devices on the Ripley landslide facilitated a mathematical evaluation of decomposition methods. Based on the observed trends in biasing the interpretations, mathematical experiments were developed and successfully employed to explain the observed large errors in the interpreted magnitude and geometry of vectors. The findings in this chapter deliver the objective #4.

Abstract

Interferometric synthetic aperture radar (InSAR) has gained considerable attention as a landslide monitoring strategy owing to its high accuracy, large coverage, and relatively low associated costs. A crucial drawback of InSAR, however, has limited its further incorporation: one-dimensional estimations along the sensor's line-of-sight (LOS). This leads to an ambiguity in results and a less intuitive understanding of landslide kinematics. A frequently exercised approach to address this issue has been taking inspiration from the topography to establish compatibility assumptions between velocity components, yet little insight exists on the performance of these methods. The objective of this paper is to investigate the performance of four renowned topography-based methods—Surface Parallel Flow Model (SPFM), SPFM coupled with least-squares method (SPF-LSM), Aspect Parallel Flow Model (APFM), and Steepest Terrain Following Model (STFM)—in evaluating the magnitude and geometry of total velocity vectors. To this end, the analysis is performed on 202 Radarsat-2 and 243 Sentinel-1 scenes acquired over a section of the Thompson River valley, a critical railway corridor in Western Canada traversing 14 landslides. The results indicate the APFM provides estimations with the lowest magnitude error (15~19 mm/yr or 18.75~23.75% of *in situ* measurements) compared to the other approaches. SPFM and SPF-LSM are highly sensitive to LOS variance and tend to bias the interpreted vectors toward the north orientation. However, APFM and STFM reflect more realistic aspect angles, with the former inclined to steeper travel angles and the latter suffering from erratic upward travel angles due to local topographies.

Keywords: InSAR; LOS; 3D decomposition; Topography; Translational Landslides; Thompson River Valley.

6.1. Introduction

Remote sensing techniques have become an integrated component of landslide monitoring plans, with interferometric synthetic-aperture radar (InSAR) gaining a considerable share of attention in recent decades (Komac et al., 2015; Lannacone & Falorni, 2016; Intrieri et al., 2018; Shi et al., 2019; Bentivenga et al., 2021; Cenni et al., 2021; Bar et al., 2022; Jia et al., 2022). InSAR is a widely used technique for tracking ground movements due to relatively lower costs and efforts than in-place instrumentation, as it covers a wider area and has a higher temporal sampling frequency (Bianchini et al., 2013). The development of modern multi-temporal algorithms, aimed at minimizing atmospheric perturbations into InSAR results, also contributed to its popularity given the improved accuracy of measurements to the millimetric level and a finer spatial resolution of detected points (Berardino et al., 2002; Ferretti et al., 2001, 2011). However, a crucial limitation of this robust tool is that the SAR sensor is sighted only to part of the movements that are visible along the line-of-sight (LOS) but not orthogonal to it (Ferretti, 2014). The LOS measurement is a product of both magnitude and direction of velocity and, thus, this added ambiguity results in a less intuitive understanding of the kinematics of a landslide (Samsonov et al., 2013; Shi et al., 2018; Cenni et al., 2021), especially for velocities oriented toward the north/south, which become less visible to the sensor considering the near-polar trajectory of satellites (Wasowski & Bovenga, 2014). This limitation becomes even more significant when setting alarm thresholds in a monitoring system for regions that host several landslides moving at different rates and directions or for a single landslide with different slope aspects (Bianchini et al., 2013; Schlögl et al., 2022).

Numerous studies have addressed the problem of reconstructing a 3D velocity vector out of a 1D LOS measurement (J. Hu et al., 2014). As satellites orbit the earth in two directions (ascending and descending), the relationship between the three components of velocity (V_V, V_E, and V_N representing vertical, eastward, and northward components, respectively) and LOS velocity (V_{Asc} and V_{Des} representing LOS velocity seen in ascending and descending geometry, respectively) is as follows:

$$\begin{pmatrix} V_{Asc} \\ V_{Des} \end{pmatrix} = \begin{bmatrix} \cos\theta_{Asc} & -\sin\theta_{Asc}\cos\alpha_{Asc} & \sin\theta_{Asc}\sin\alpha_{Asc} \\ \cos\theta_{Des} & -\sin\theta_{Des}\cos\alpha_{Des} & \sin\theta_{Des}\sin\alpha_{Des} \end{bmatrix} \begin{pmatrix} V_V \\ V_E \\ V_N \end{pmatrix}, \qquad (6.1)$$

where θ and α represent the geometry of SAR scene acquisition, i.e., the sensor's incidence angle (side-looking angle) and the satellite trajectory, respectively (as shown in Figure 6- 1).

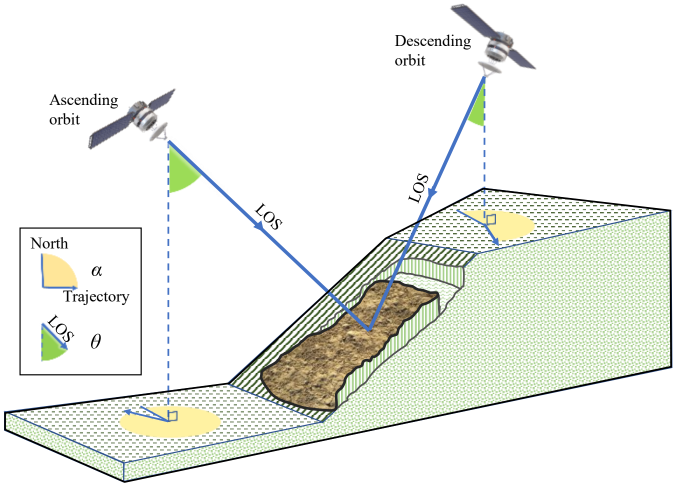

Figure 6- 1. Geometry of SAR scene acquisition in ascending and descending viewing geometries

Eq. 6. 1 is an under-determined system of equations and, to resolve this, V_N was simply disregarded in many early studies due to the orbital geometry of satellites that detects the least ground velocity along south/north orientations (Ng et al., 2012; Samsonov et al., 2013; Khorrami et al., 2020; Ma et al., 2021; H. Chen et al., 2022). This assumption is the most reasonable for phenomena with no significant northward movements, such as ground subsidence or landslides mainly sliding toward the east or west. Others have instead pursued different approaches when the northward component is sizable, incorporating additional information that can be procured from other variants of SAR analysis, external sources, or an *a priori* deformation model. The first group includes methods such as pixel offset tracking (Shi et al., 2018; Z. Wang et al., 2018) and multi-aperture InSAR (Jo et al., 2017), which intend to determine the velocity along the direction orthogonal to the LOS (i.e., azimuth). However, these methods are less accurate than regular InSAR (on the centimetric order), time-consuming to run, very sensitive to decorrelation, and not as applicable to slow-moving landslides with dim reflectivity (Bechor & Zebker, 2006; Simons & Rosen, 2007; Eriksen et al., 2017; Shi et al., 2018). In the second category of methods, external sources such as *in situ* instruments, mostly GNSS/GPS units, are used to infer 3D movements (Samsonov & Tiampo, 2006; Samsonov et al., 2007; W. Zhu et al., 2014). This approach also faces several challenges including the shortfall of these units in terms of both quantity and uniform spatial distribution, which significantly limits the study area and requires the use of advanced mathematical techniques during post-processing stages (J. Hu et al., 2014). Finally, the last approach is employing an *a priori* deformation model, which involves exercising compatibility assumptions between the presumed failure kinematics and the calculated 3D velocity vectors. As an example, Fan et al. (2021) assumed the symmetrical horizontal and vertical movements of the ground along the strike and dip of the working face in a sub-horizontal coal seam mine. Their study built upon the probability integral method, in which 3D velocity vectors are assumed to show a normal distribution around the mining strike based on the symmetrical nature of movements (Yang et al., 2017; Milczarek et al., 2021). A *priori* compatibility model underpinning the kinematics of the landslide is often reflected in the surficial geometry of the terrain and, thus, the topography can be leveraged toward this end. Surface-Parallel Flow Model (SPFM – Eq. 6. 2), first introduced by Joughin et al. (1998) and used by others (Sun et al., 2016; Ao et al., 2019; Samsonov et al., 2020; X. Liu et al., 2021; Ren et al., 2022), assumes the velocity components follow the topography as follows:

$$V_V = \left(\frac{\partial H}{\partial x_E}\right) V_E + \left(\frac{\partial H}{\partial y_N}\right) V_N, \tag{6.2}$$

where *H* is the topography elevation, and $\partial H/\partial x_E$ and $\partial H/\partial y_N$ represent the elevation gradient in the eastward and northward directions, respectively. SPFM can be mathematically adjusted to only prompt one LOS geometry, hereafter referred to as Steepest Terrain Following Model (STFM), which has been adopted in previous studies as well (Bianchini et al., 2013; Herrera et al., 2013; Journault et al., 2018; Yi et al., 2022). The last approach proposed to interpret 3D vectors is by dictating the velocity to follow the terrain's aspect, here called the Aspect Parallel Flow Model (APFM), which has been employed by Y. Zhu et al. (2022) and Soltanieh & Macciotta (2022a, 2022b).

Few studies are available in the literature that focus on retrieving 3D velocity vectors of slow-moving translational landslides. Moreover, the accuracy of such methods is not clear in terms of interpreting both the magnitude and geometry of vectors compared to one another. Given the glacial morphology in Canada, translational and compound landslides are very common (Biagini et al., 2022) and, therefore, applying the most suited algorithm in this region can significantly enhance landslide surveillance systems for managing associated risks. The objective of this paper is to examine the performance of four methods—SPFM, SPFM coupled with the least-squares method (SPFM-LSM), STFM, and APFM—in the context of translational landslides for the most active landslides along Thompson River Valley, a critical railway corridor in Western Canada. To this end, 202 Radarsat-2 scenes (U5 and U21 beams in descending orbit) and 243 Sentinel-1 scenes (ascending and descending orbits) are analyzed using Persistent Scatterer Interferometry. The spatial interpolation of the 3D vector maps obtained from the four topography-based methods facilitated the calculation of error in the magnitude and geometry of total velocity vectors compared to other *in situ* measurements. Further discussion is then presented on the sources of variance and their contribution to the interpreted geometry of vectors.

6.2. Study Area

The Thompson River valley is located in the Canadian Cordillera between the towns of Ashcroft and Spences Bridge, British Columbia, Canada. A long history of landslides has been documented within a 10-km section of this valley, as shown in Figure 6- 2. The tracks of both the Canadian Pacific Railway (CP) and Canadian National Railway (CN) pass through this corridor and traverse 12 out of 14 landslides. These trans-continental high-traffic railways are of great financial significance in Canada and are proactively monitored for risk management (Macciotta et al., 2016). A collection of government agencies, universities, and industry partners have engaged in studies and field campaigns, especially on the Ripley landslide that is recognized by the International Programme on Landslides (IPL – Project 202) of the International Consortium on Landslides (ICL) (P. Bobrowsky et al., 2017; Han et al., 2021).

The landslides along the valley show retrogressive behaviour, vary in volume from 0.4 to 15 million m^3, and typically move at rates slower than 200 mm/yr (Eshraghian et al., 2007). Despite the historical events that led to fatalities and short-term river impoundment, previous studies concluded the likelihood of such scenarios is low for slow-moving landslides other than Ripley (Eshraghian et al., 2008a; Hendry et al., 2015). The surficial geology of this valley comprises Quaternary deposits formed by a series of glaciation events separated by episodes of incision and erosion in the Pleistocene sequence. Clague & Evans (2003) identified eight formations overlying andesitic bedrock; four of these units are reported to be present at unstable slopes with Units 6 and 8 found close to uplands (Figure 6- 3) (Clague & Evans, 2003; Hendry et al., 2015). A weak, highly plastic clay seam at the residual state with friction angles of 9-16° within Unit 2 accommodates

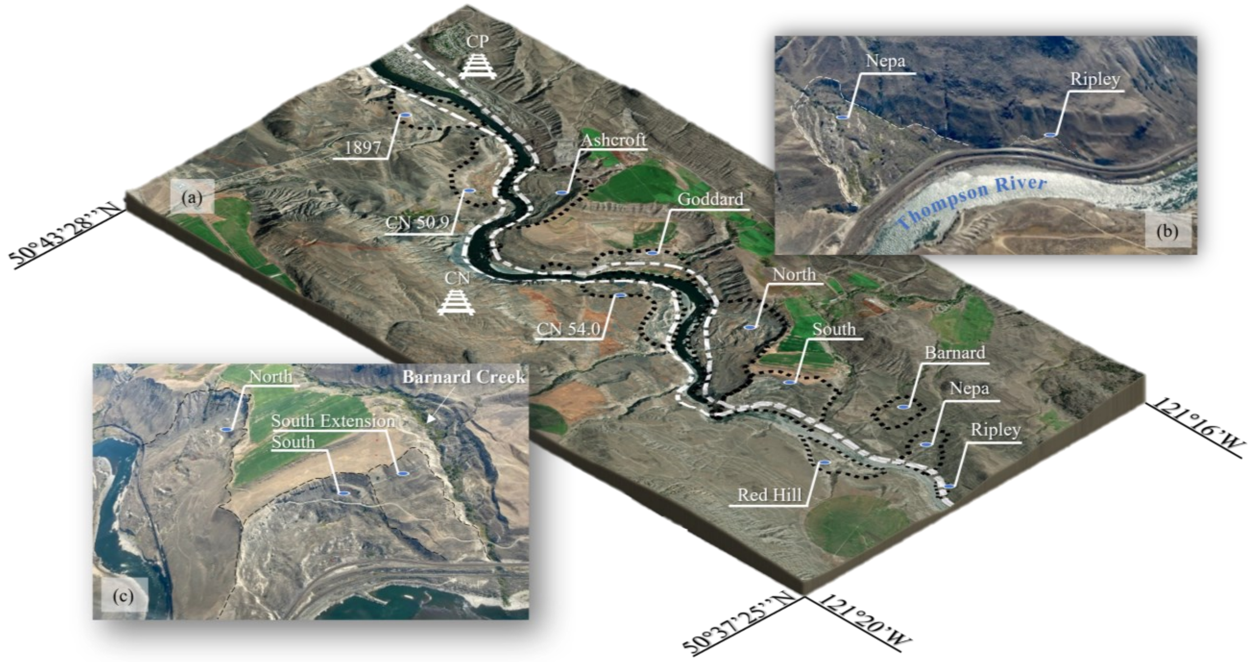

Figure 6- 2. Approximate daylighted boundaries of recognized landslides along the Thompson River valley with CP and CN tracks shown (a), and aerial images of the Nepa and Ripley (b) and North and South (c) landslides.

the sub-horizontal basal shear surface of the landslides within the Thompson River valley. Several hypotheses have been presented on the triggering reasons, including the role of precipitation filling back scarps or irrigation water sourced from agricultural activities in the uplands (Stanton, 1898; Porter et al., 2002). However, later studies indicated the elevation of the Thompson River is the main factor contributing to de/stabilizing the slopes and the effect of previously speculated triggers is limited (Eshraghian et al., 2005, 2008b; Bishop et al., 2008; Hendry et al., 2015). The buttressing effect of the river has a constructive effect when rising, which can potentially halt the movement, but can also trigger movements when drawing down due to seasonal variations (Hendry et al., 2015). The river is also involved in stability by altering the geometry of the sliding block through toe erosion (Eshraghian et al., 2008b; Macciotta et al., 2016).

The Ripley landslide is the most heavily instrumented case, and its movements have been monitored using a variety of surficial and sub-surface methods, including shape-accel arrays, slope inclinometers, GPS units, corner reflectors, and multiple geophysical methods (e.g., electrical resistivity tomography). With approximate dimensions of 200 m × 300 m × 40 m (length × width × height) and a volume of 0.75 million m^3, Ripley is close to the smallest instability in the valley yet is one of the most active cases, reaching movement rates as high as 2 mm/d in the short term (Macciotta et al., 2014). Three GPS units are installed at the site, with two units (GPS1 and GPS2) close to the tracks and a third unit on the retaining wall between the CP and CN tracks. Figure 6-4 shows the location of these units, acquired time-series displacements from April 2008 to February 2020, and the magnitude and direction of average velocities in the horizontal and vertical planes (V_H and V_T are horizontal and total velocities, respectively). GPS1 and 2 are travelling at an aspect of N62-66°W at a travel angle of 14 to 17° below the horizon while GPS3 is illustrating a more pronounced total velocity of 117 mm/yr at N56°W at a travel angle of 35°. GPS3 is theorized to be situated on a different block than the other two, acting as a graben and pushing the facing block to slide sub-horizontally (M. B. Schafer, 2016). However, it is also believed that excessively local phenomena such as wall deflections and base scouring are superimposed on the reported displacements and GPS3 measurements do not reflect only the landslide kinematics.

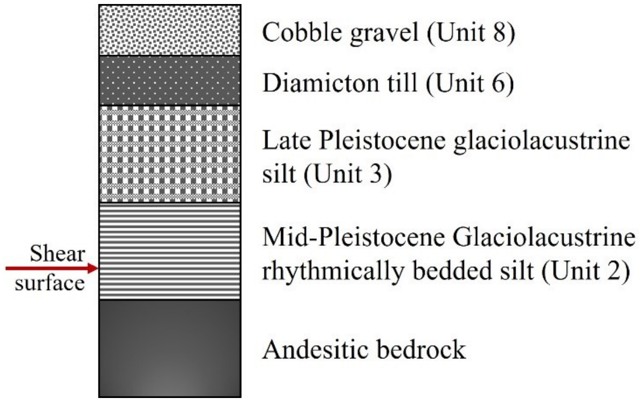

Figure 6- 3. Most common geological units in the Thompson River Valley

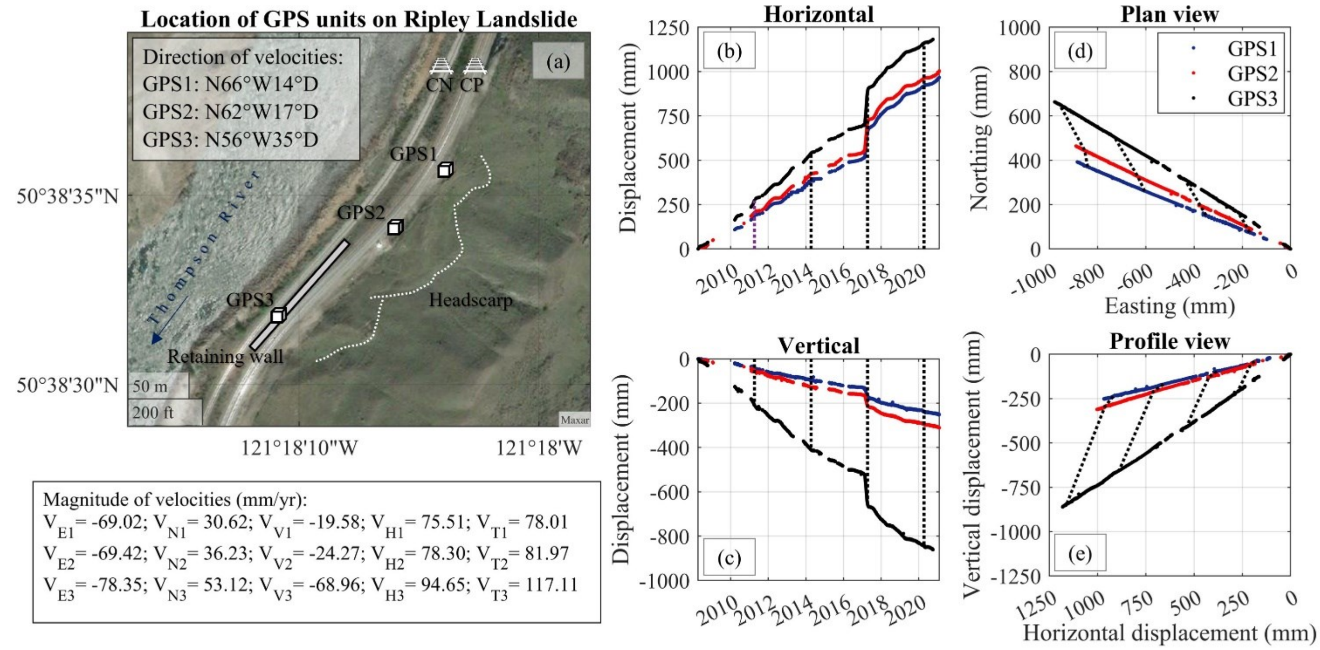

Figure 6- 4. Location of GPS units on the Ripley landslide and average velocities (a), observed time-series of horizontal (b) and vertical (c) displacements, magnitude, and direction of velocities in horizontal (d) and vertical (e) planes (dashed lines mark 3-year intervals)

The Geological Survey of Canada recently launched a series of field studies using remote sensing techniques to document and monitor the regime of movements of the North landslide as well. The most active part of this landslide is its toe, also known as the “Solar Slump,” which was a part of a rapid failure in October 1881 (Stanton, 1898) as a result of over-steepening due to construction and excessive erosion (Porter et al., 2002). North landslide is an ancient roto-translational landslide with a similar geological setting as discussed above and dominated by the variation of pore pressures in the confined aquifer above the bedrock close to the river. Historical records show a peak velocity of 15 cm/yr at the site (Huntley et al., 2021); however, surveys by a real-time kinematic global navigation satellite system (RTK-GNSS) at ground control points (GCPs) indicate this can increase to more than 20 cm/yr. Ortho-photos taken by a remotely piloted aircraft system (RPAS) between September 2019 and September 2021 were also analyzed by digital image correlation (DIC) (Lucieer et al., 2014); the results presented in Figure 6- 5 demonstrate the magnitude and aspect of horizontal velocities.

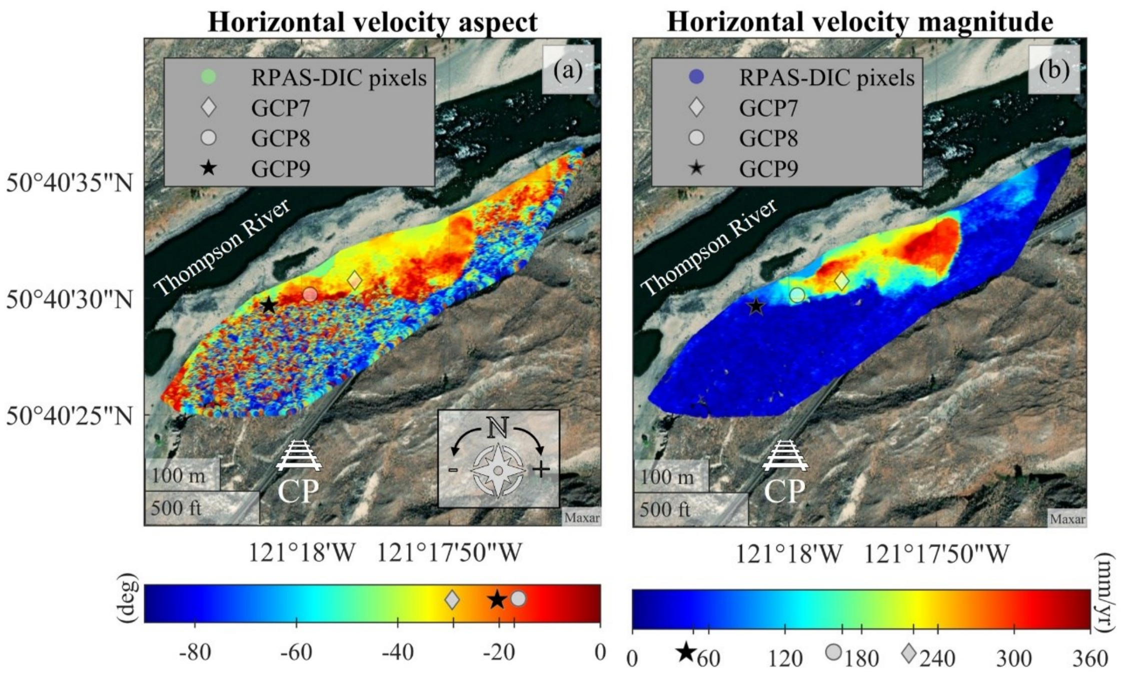

Figure 6- 5. Aspect (a) and magnitude (b) of horizontal velocities at ground control points (GCPs) and remotely piloted aircraft system-digital image correlation (RPAS-DIC) pixels on the toe of North landslide from September 2019 to September 2021 (Rotheram-Clarke et al., 2022)

6.3. Methodology

Figure 6- 6 shows the general framework applied in this study to determine the accuracy of SPFM, SPFM-LSM, APFM, and STFM in terms of total velocity magnitude and geometry (aspect and travel angles). The following describes the major steps in the methodology.

6.3.1. InSAR Analysis

Sentinel-1 (S1) SAR scenes obtained by both A/B sensors were downloaded from Alaska Space Facility Data Search Vertex (www.search.asf.alaska.edu), which is a mirror server to the original Copernicus Open Access Hub (www.scihub.copernicus.eu). Radarsat-2 (RS2) images were also procured by the Canadian Space Agency through the Geological Survey of Canada. A total of 243 S1 single-look complex scenes were acquired in interferometric wide swath mode with VV polarization along ascending and descending orbits spanning from March 2016 to November 2021 with a nominal revisiting time of 12 d. RS2 scenes are only from descending orbits with a revisiting time of 24 d, but have an ultra-fine resolution at two different beams (U5 and U21) that provide radar back-scattered reception at two different incidence angles. Table 6- 1 presents a metadata summary of scenes.

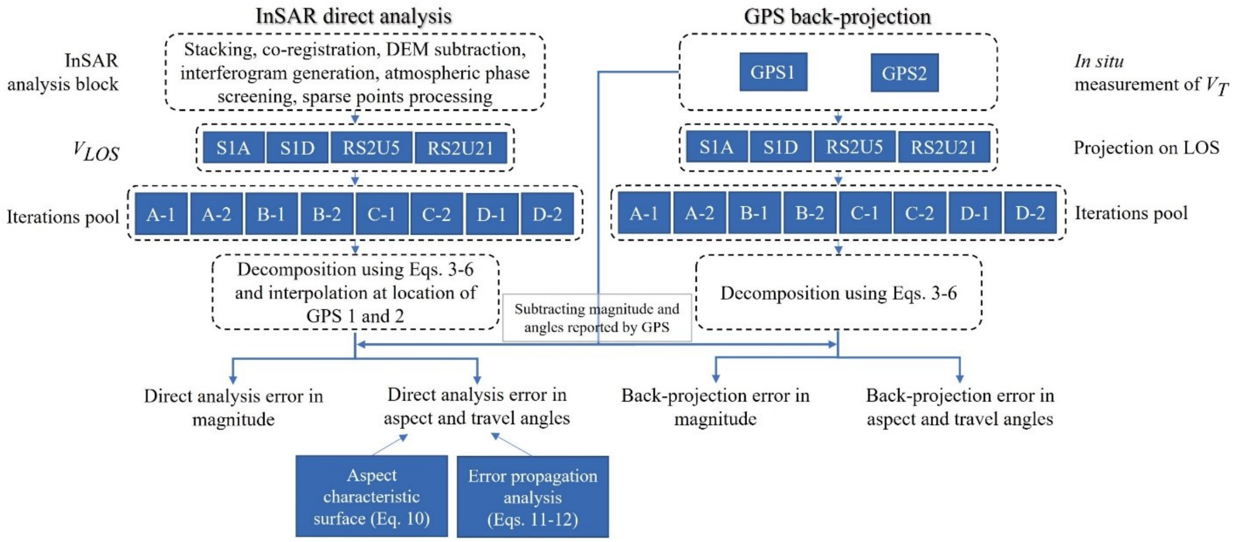

Figure 6- 6. Applied framework to evaluate the accuracy of decomposition methods in terms of magnitude and geometry (aspect and travel angles)

Table 6- 1. Metadata summary of SAR scenes used in this study

Sensor	Sentinel-1		Radarsat-2	
Viewing geometry	Ascending	Descending	Descending	Descending
Polarization	VV		HH	
No. of scenes	119	124	100	102
Nominal revisiting time (d)	12		24	
Spatial resolution	Wide-swath (20×5)		Ultra-fine (3×3)	
Heading angle (°)	350	190	190	190
Incidence angle (°)	40	45	34	45
Sensing period (YYYY/MM/DD)	2016/03/09-2021/11/08	2017/07/11-2021/10/03	2013/09/08-2020/07/09	2013/11/16-2020/07/06
SAR Set identifier	S1Asc	S1Des	RS2U5	RS2U21

The Persistent Scatterer InSAR algorithm was employed to process the SAR scenes in a typical single-master STAR scheme by SARPROZ software (Perissin & Wang, 2012; www.sarproz.com/). The master (reference) scene was chosen for all datasets at almost the middle of the study period to minimize its temporal and spatial separation from other scenes. The applied workflow started by applying precise orbit coordinates, if necessary, to geocode the pixels and for co-registration purposes to assure pixels are accurately aligned. Upon extracting the area of interest, the Shuttle Radar Topography Mission digital elevation model (DEM) was downloaded to remove the elevation effect from the SAR scenes. A linear phase ramp was then employed to estimate and remove the atmospheric perturbations, followed by identification of persistent targets on the ground to calculate the average velocities following the frameworks discussed in Azadnejad et al. (2019), Khoshlahjeh Azar et al. (2021), and Tarighat et al. (2021). The noise in time-series displacements was deemed negligible and filtration algorithms were not employed (Sharifi, Hendry, Macciotta, et al., 2022; Sharifi, Macciotta, & Hendry, 2022).

6.3.2. LOS Velocity Decomposition

The outcome of the InSAR process, at this point, is LOS velocities acquired from four different datasets (S1A, S1D, RS2U5, and RS2U21), which were used to develop combinations of satellite orientations. This would allow the implementation of the discussed post-processing algorithms to calculate the 3D velocity vectors. Different approaches were given category letters A through D and different combinations of satellite LOS velocities were given iteration numbers 1 and 2, leading to eight combinations as presented in Table 6- 2. Each iteration will be referred to using the category letter followed by iteration No. (e.g., A-1 or C-2). The mathematics of SPFM, SPFM-LSM, APFM, and STFM to decompose LOS velocities into 3D are given as Eqs. 6. 3-6. 6, respectively:

$$\begin{pmatrix} V_v \\ V_e \\ V_n \end{pmatrix} = \begin{bmatrix} \cos\theta_1 & -\sin\theta_1\cos\alpha_1 & \sin\theta_1\sin\alpha_1 \\ \cos\theta_2 & -\sin\theta_2\cos\alpha_2 & \sin\theta_2\sin\alpha_2 \\ -1 & i_E & i_N \end{bmatrix}^{-1} \begin{pmatrix} V_{LOS1} \\ V_{LOS2} \\ 0 \end{pmatrix}, \qquad (6.\ 3)$$

$$\begin{pmatrix} V_v \\ V_e \\ V_n \end{pmatrix} = \left(G^T G\right)^{-1} G^T \begin{pmatrix} V_{LOS1} \\ V_{LOS2} \\ V_{LOS3} \\ 0 \end{pmatrix}, \tag{6. 4}$$

$$\begin{pmatrix} V_v \\ V_e \\ V_n \end{pmatrix} = \begin{bmatrix} \cos\theta & 0 & \sin\theta\sin\alpha - \tan\beta\sin\theta\cos\alpha \\ 0 & 1 & -\tan\beta \\ \cos\theta & 0 & \sin\theta\sin\alpha - \tan\beta\sin\theta\cos\alpha \end{bmatrix}^{-1} \begin{pmatrix} V_{LOS1} \\ 0 \\ V_{LOS2} \end{pmatrix}, \tag{6. 5}$$

$$\begin{pmatrix} V_v \\ V_e \\ V_n \end{pmatrix} = \frac{V_{LOS}}{A} \begin{pmatrix} -i_T\sqrt{1+\tan^2\beta} \\ \tan\beta \\ 1 \end{pmatrix}, \tag{6. 6}$$

where V_v, V_e, and V_n are velocity estimated along vertical, eastward, and northward axes, respectively; θ and α describe the geometry of acquisition as before (Figure 6- 1); i_E and i_N are the topographical gradient in eastward and northward directions, respectively; V_{LOS} is the LOS velocity estimated from each SAR stack depending on the iteration (please refer to Table 6- 2); G (Eq. 6. 7) is the design matrix of the over-determined system, which contains the geometry of acquisitions similar to Eq. 6. 3; T is the transpose operation; β is the aspect angle; $i_T=\sqrt{i_E^2+i_N^2}$ is the total gradient; and A is just a defined constant for brevity (Eq. 6. 8):

$$G = \begin{bmatrix} \cos\theta_1 & -\sin\theta_1\cos\alpha_1 & \sin\theta_1\sin\alpha_1 \\ \cos\theta_2 & -\sin\theta_2\cos\alpha_2 & \sin\theta_2\sin\alpha_2 \\ \cos\theta_3 & -\sin\theta_3\cos\alpha_3 & \sin\theta_3\sin\alpha_3 \\ -1 & i_E & i_N \end{bmatrix}, \tag{6. 7}$$

$$A = i_T\cos\theta\sqrt{1+\tan^2\beta} - \tan\beta\sin\theta\cos\alpha + \sin\theta\sin\alpha . \tag{6. 8}$$

Figure 6- 7 displays a schematic sketch of how each of these four topography-based methods takes the geometrical restrictions into the decomposition. In this study, the elevation map

as provided by 1-arcsecond SRTM DEM was interpolated using the spline method (Ajvazi & Czimber, 2019; Desmet, 1997; Her et al., 2015). Elevation gradients were found to be reasonable and well-matching with the topography of landslides. Moreover, a too-high-resolution DEM is not necessarily in favour of LOS decomposition since much of the surficial features do not conform to the geometry of the sliding plane beneath the ground and low-pass filters to avoid capturing very local geometry are advised in these cases (X. Liu et al., 2021; Samsonov et al., 2020). SRTM also has the advantage of considerable coverage and public access which is beneficial for developing regional monitoring systems.

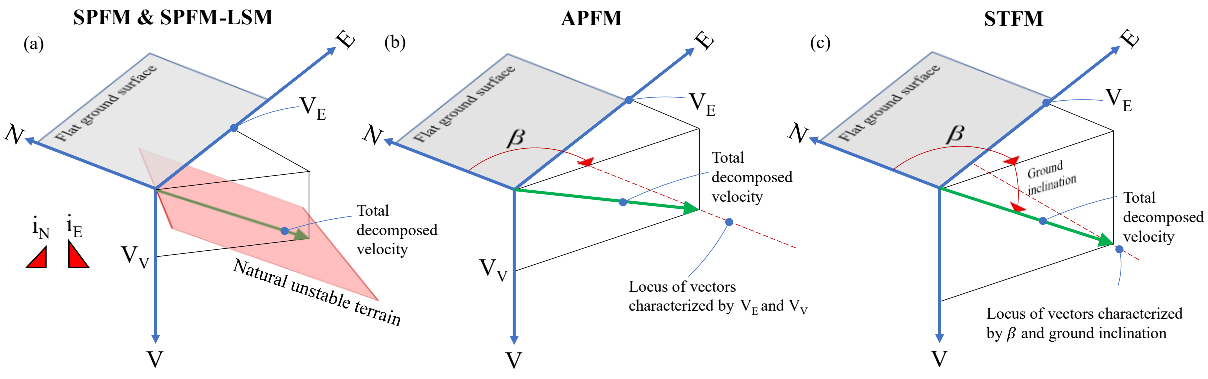

Figure 6- 7. Schematic sketch of decomposition using (a) SPFM & SPFM-LSM, (b) APFM and (c) STFM (the green vector is the total decomposed velocity and red features are the geometrical constraints posed by each method)

Table 6- 2. Post-processing analysis program broken down for each assumption

Category	Assumption	Iteration No.	Combination of used SAR sets
A	SPFM	1	S1A, RS2U21
		2	S1A, S1D
B	SPFM-LSM	1	S1A, S1D, RS2U21
		2	S1A, S1D, RS2U5
C	APFM	1	S1A, RS2U21
		2	S1A, S1D
D	STFM	1	RS2U21
		2	S1D

Decomposition must be done using LOS velocities obtained from different SAR stacks that spatially correspond to similar locations. Given the varied reflectivity of objects from different viewing geometries, the location of scatterers in between stacks would differ. The literature reports down-sampling the ground surface to large cells, with the average LOS velocities of scatterers falling in an identical cell as the representative value, and performing decomposition on the cell level (Carlà et al., 2019; M. Li et al., 2020; Soltanieh & Macciotta, 2022a, 2022b). However, this approach leads to obscuring the spatial trend and under-representation of LOS velocities given this method acts like a low-pass filter. Furthermore, the scatterers in each cell should also be comparable to others in the neighbouring cell, both in number and reliability (i.e., coherence). Considering all of these limitations, the cell configurations should be non-uniformly altered (e.g., non-quadrilateral or warped-sided shapes), which calls for knowledge of the landslide moving blocks of the study site as well. The k-nearest neighbouring (kNN) search algorithm (Taunk et al., 2019) with a damping weight kernel was used in this study to automate this process; this is advantageous for regional studies or for developing an automated monitoring system. The details of this method are presented in Appendix A.

6.3.3. Accuracy Evaluation at Ripley Landslide

6.3.3.1. Error in Magnitude of Total Velocity Vectors

Upon the calculation of total velocity magnitudes at eight iterations, these parameters were then spatially interpolated at the locations of GPS1 and 2 using the kNN algorithm and taking into account the scatterers within a range of 20 m. GPS3 data were abandoned because of the impact of very local phenomena that cannot be captured by S1 and RS2 sensors given their resolution. Considering GPS measurements to be the closest estimations to the true vectors, the performance of each of the four topography-based decomposition methods could be then assessed at the Ripley landslide by subtracting the interpolated magnitude and geometry of linear-fit velocities from the InSAR-decomposed velocities by calculating the error (called “direct analysis error”). Many previous investigations suggested that the active block of Ripley is behaving as a unit and rather similar GPS measurements can also attest to that (Macciotta et al., 2016; Soltanieh & Macciotta, 2022b, 2022a). However, judgment on the accuracy of these methods for interpreting the magnitude of velocities should be made in light of this limitation. Different sources of variance co-act in the direct analysis error; it is also beneficial to isolate the impact of exercising each compatibility assumption from practical limitations (e.g., different spatial resolution, spatial disparity of scatterers, and efficiency of InSAR analysis itself). A second approach is used in parallel, providing an opportunity to study the accuracy of decomposition methods when other exogenous variances are excluded. The total velocity vectors of GPS units (Figure 6- 4) were first back-projected on the LOS of the sensors (using their geometries stated in Table 6- 1) and the decomposition again conducted using Eqs. 6. 3-6. 6. The difference between total velocity magnitude and geometry interpreted in this analysis with GPS measurements is referred to as the "back-projection error." Figure 6- 6 demonstrates the step-by-step visualization of processing tasks.

6.3.3.2. Error in Geometry of Total Velocity Vectors

Underestimation of a specific component may be compensated and obscured by overestimation of another, leading to a rather similar magnitude of total velocity, but this counter-balancing effect is always reflected in either aspect or travel angle. As a result, investigating the alteration of vector geometry caused by LOS variance is essential when evaluating the performance of decomposition methods. Each scatterer is characterized by a certain value of coherence (γ), which is a quantification of the phase stability of that scatterer throughout the entire monitoring period (Ferretti, 2014). In rural areas, such as the Thompson River valley, artificial targets that possess high reflectivity are not found and the γ threshold should be lowered to mask fewer unreliable scatterers. A lower coherence implies less reliable LOS velocity estimations, i.e., the root cause for lower levels of LOS accuracy. Variance (σ) is correlated to γ as follows:

$$\sigma \propto \sqrt{\frac{1-\gamma^2}{\gamma^2}}. \tag{6. 9}$$

Early results demonstrated a tendency of SPFM and SPFM-LSM to rotate the vectors toward north orientation due to LOS variance. Eq. 6. *10* is developed based on Eq. 6. 2, and describes how inaccurate estimations in vertical and eastward directions may lead to new aspect angles (please refer to Appendix B.1 for proof):

$$\tan \beta_e = \frac{a+1}{b\left(\frac{1}{i_N}\right) - a\left(\frac{i_E}{i_N}\right) + c}, \tag{6. 10}$$

where β_e is the error-contaminated aspect angle, $a = dV_E/V_E$, $b = dV_V/V_E$, $c = 1/\tan\beta$, and dV_E and dV_V are errors in V_E and V_V estimations, respectively. The coefficients (a, b, c) are obtained by regression analysis after Eq. 6. *10* is fitted on the Ripley scatterers in the space $<\beta, 1/i_N, i_E/i_N>$, which will be referred to as the aspect characteristic surface.

An over-steepening tendency of travel angle in APFM, also revealed in early results, is investigated by evaluating how much LOS variance leads to variance in V_V compared to V_H. A lower coherence threshold in S1 stacks was chosen than in RS2 stacks to obtain comparable scatterers in terms of number and distribution due to the lower spatial resolution of S1 scenes. This led to 2.1 and 1.47 times the variance in velocity of S1Asc and S1Des, respectively, compared to RS2U21. These ratios were substituted in Eqs. 6. 3-6. 6 for LOS vectors (i.e., 2.1 and 1.47 for the

V_{LOS} of S1Asc and S1Des, respectively) to calculate the propagation of error in LOS velocity into three components as well as the horizontal and total velocities calculated by Eqs. 6. *11* and 6. *12*:

$$\mathrm{dV_H}=\frac{\mathrm{dV_E}\cdot\mathrm{V_E}+\mathrm{dV_N}\cdot\mathrm{V_N}}{\mathrm{V_H}}, \tag{6. 11}$$

$$\mathrm{dV_T}=\frac{\mathrm{dV_E}\cdot\mathrm{V_E}+\mathrm{dV_N}\cdot\mathrm{V_N}+\mathrm{dV_V}\cdot\mathrm{V_V}}{\mathrm{V_T}}, \tag{6. 12}$$

where dV_N, dV_H, and dV_T are errors in V_N, V_H, and V_T, respectively. Once dV_T was calculated, dV_V and dV_H were normalized to it to then compute the values of dV_V and dV_H in response to a unit of dV_T.

6.4. Results

6.4.1. Magnitude of Total Velocity Vectors

Table 6- 3 presents the direct analysis error of total velocity magnitude (V_T) resulting from different InSAR post-processing approaches. It is highlighted that due to the limited differences observed in early results between locations of GPS 1 and 2, the averages are reported here as the representative values. In the first iteration, the lowest error in total velocity belongs to APFM (15 mm/yr or 18.75%) followed by SPFM (19 mm/yr or 23.76%), SPFM-LSM (29 mm/yr or 36.25%), and finally STFM (37 mm/yr or 46.26%). A similar trend is also observed in the second iteration, with values of 19 (23.75%), 24 (30.00%), 32 (40.01%), and 45 (56.26%) mm/yr for APFM, SPFM, SPFM-LSM, and STFM, respectively. In iteration 2, more Sentinel-1 scenes were used and γ had to be lowered for this sensor, leading to 10-26% larger errors than in iteration 1. This can be also viewed in Figure 6- 8 which shows the GPS time-series displacements projected on different LOS geometries used in this study. It is seen that Radarsat-2 was more successful in providing average

velocities close to GPS results and Sentinel-1 tends to under-represent the kinematics of Ripley at the location of GPS units. The back-projection errors, which only indicate the performance of each method, are also presented in Table 6- 3. Given that RS2U21 and S1Des have similar incidence angles (Table 6- 1), the back-projection errors between iterations 1 and 2 in categories A, C, and D are the same. Back-projection errors are also consistent with direct analysis errors, with the lowest error for APFM (5 mm/yr) and the highest for STFM (47 mm/yr). It generally indicates that the direct analysis, which is affected by the InSAR analysis algorithm itself and coherence thresholds, has induced an error close to the ideal values (i.e., back-projection results). Looking at the back-projection errors of two iterations of SPFM-LSM, it seems that replacing RS2U21 with RS2U5 had a negative impact in raising the error from 22 to 27 mm/yr. Therefore, a lower incidence angle seems to be detrimental to the accuracy of estimations. The direct analysis errors are generally 2 to 14 mm/yr different than the back-projection errors, which is attributed to the efficiency of atmospheric phase screening, LOS variance, and kNN spatial interpolation in post-processing stages. The highest error for STFM is attributed to the relatively steep terrain, especially upslope of the track, which induced higher magnitude velocities.

Table 6- 3. Average direct analysis and back-projection error of total velocity magnitude averaged at the locations of GPS1 and 2 for each iteration

Approach	Iteration	Direct analysis error in magnitude of V_T (mm/yr) [relative to average GPS velocities]	Back-projection error in magnitude of V_T (mm/yr) [relative to average GPS velocities]	Absoloute difference in error of direct analysis and back-projection (mm/yr) [relative to direct analysis error]
SPFM	A-1	19 [23.76%]	21 [26.25%]	2 [10.52 %]
	A-2	24 [30.00%]		3 [12.5 %]
SPFM-LSM	B-1	29 [36.25%]	22 [27.50%]	7 [24.13 %]
	B-2	32 [40.01%]	27 [33.75%]	5 [15.63 %]
APFM	C-1	15 [18.75%]	5 [6.25%]	10 [66.67 %]
	C-2	19 [23.75%]		14 [73.68 %]
STFM	D-1	37 [46.26%]	47 [58.76%]	10 [27.02 %]
	D-2	45 [56.26%]		2 [4.44 %]

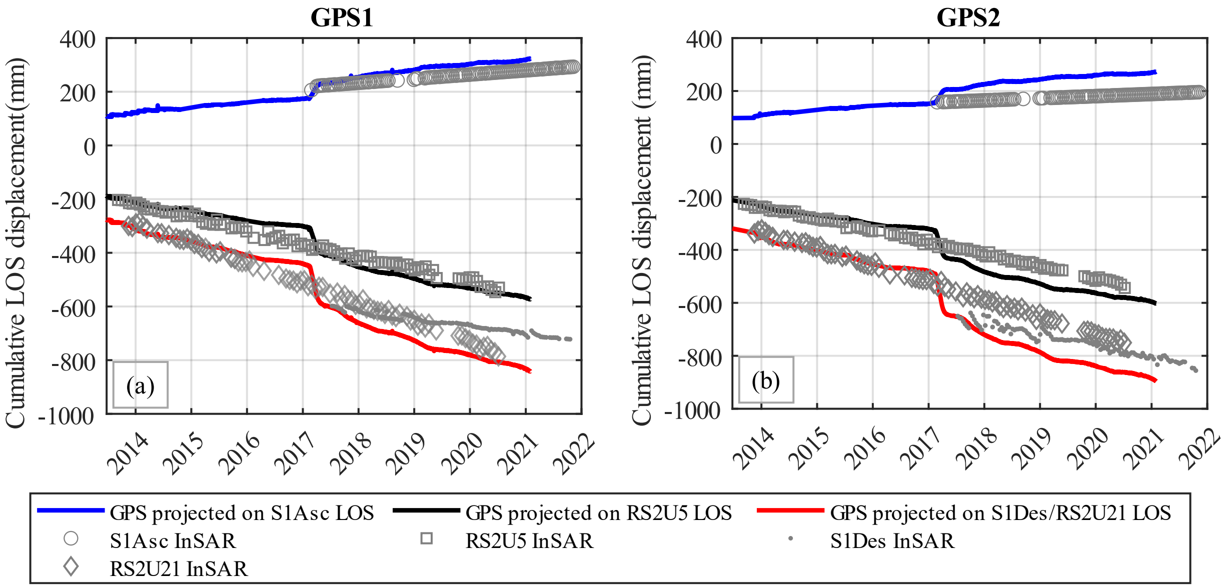

Figure 6- 8. Cumulative displacements of GPS1 (a) and 2 (b) along LOS geometries of all used SAR sensors as well as median time-series displacement of scatterers within the range of 20 m (NOTE: S1Des and RS2U21 are plotted on a similar diagram given the similar acquisition geometry)

6.4.2. Geometry of Total Velocity Vectors

Table 6- 4 presents the direct analysis and back-projection error in aspect and travel angles, averaged at the locations of GPS1 and 2. Table 6- 4 shows the direct error in aspect angle notably increases for SPFM and SPFM-LSM to values more than 30° while APFM and STFM map the direction of velocity in the horizontal plane almost accurately with an error of less than 7°. There are no meaningful differences between iterations 1 and 2 for the same category from the perspective of aspect angle as indicated by the direct analysis error. The back-projection error in aspect angle also aligns with the direct analysis error, showing an error of 20 to 41° for SPFM and SPFM-LSM, respectively, while the other two methods show a limited error of 7.1°. The error in travel angle, except for APFM which is about 14°, is also limited to a maximum of 4.9° regardless of iteration number, which shows the success of SPFM, SPFM-LSM, and STFM with respect to interpreting the travel angle agreeably close to reality. However, the back-projection error in travel is low for all methods, even APFM that shows a low error of 2.1°. Table 6- 4 suggests a significant

difference of more than 10° between the direct and back-projection error with respect to the aspect angle performance of SPFM and SPFM-LSM and the travel angle performance of APFM, which is investigated through aspect characteristic surface and error propagation analysis.

Table 6- 4. Direct and back-projection error of total velocity geometry averaged at the locations of GPS1 and 2 as calculated in different iterations (GPS1 and 2 reported a movement direction of N66°W14°D and N62°W17°D, respectively)

Approach	Iteration	Direct analysis error in aspect angle (°)	Back-projection error in aspect angle (°)	Direct analysis error in travel angle (°)	Back-projection error in travel angle (°)
SPFM	A-1	36.7	20.0	3.2	6.8
	A-2	32.4		1.6	
SPFM-LSM	B-1	33.8	20.3	2.9	6.9
	B-2	36.3	41.0	4.9	8.0
APFM	C-1	1.5	7.1	14.4	2.1
	C-2	6.9		14.5	
STFM	D-1	2.1	7.1	2.4	6.6
	D-2	6.9		1.0	

Figure 6- 9 displays the velocity map of the Ripley landslide with superimposed unit vectors of velocity as well as histograms presenting the distribution of magnitude and geometry of vectors subject to each decomposition method. In this figure and similar ones for other landslides in the valley (Figure 6- 12-Figure 6- 15), only results of iteration 1 are presented as they provide better accuracy in total velocity magnitude but rather similar geometries to iteration 2. Table 6- 4 suggests that, even in an ideal back-projection case, the aspect angle error of SPFM and SPFM-LSM is large, which is rooted in its mathematical configuration in Eq. 6. 3 (please refer to Appendix B.2), and the direct analysis error is generally larger than the back-projection error. However, Figure 6-9 shows the higher error of SPFM and SPFM-LSM in aspect angle is not only limited to the locations of GPS1 and 2, and that the vectors are collectively biased toward the north for both SPFM and SPFM-LSM. The regression analysis of Eq. 6. 10 on SPFM data using the least-squares method led to the function illustrated in Figure 6- 10. The fitted function has an R-squared value

of 0.78, implying the tendency of the vector towards a north orientation in SPFM results from a high sensitivity to LOS velocity variance. Figure 6- 10b also demonstrates the fitted function in a 2D in-plane view of the most sensitive input, $1/i_N$, which shows β exponentially departs from the true aspect (-64°) when i_N decreases. The calibrated coefficients of the fitted function are presented in Table 6- 5 and are back-calculated into V_E, V_N, and β values of 71 and 44 mm/yr and -58°, respectively. These values are on average 2 and 10 mm/yr and 6° apart from average GPS measurements (Figure 6- 4). It is underlined that interpreted V_E in Table 6- 5 is calculated by computing dV_E through comparing SPFM result against GPS values and V_N is subsequently obtained by having V_E and β. Here, these measures are taken to validate the aspect characteristic surface; however, in a general case with no GPS or similar measurements, interpreting β through the value of c is sufficient to correct the geometry of SPFM vectors and account for polar-biasing error.

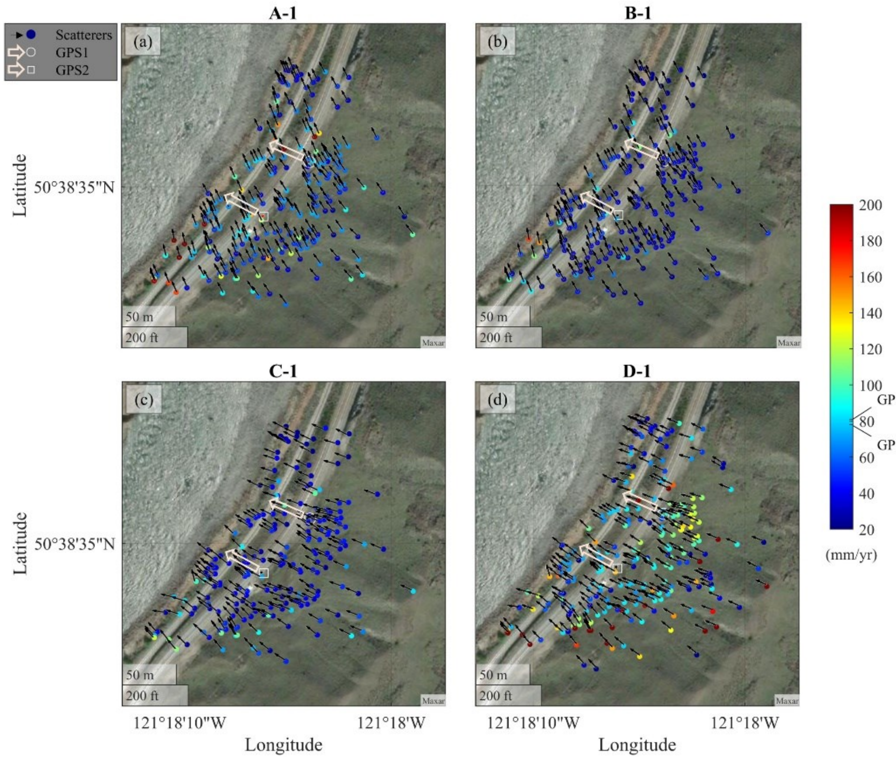

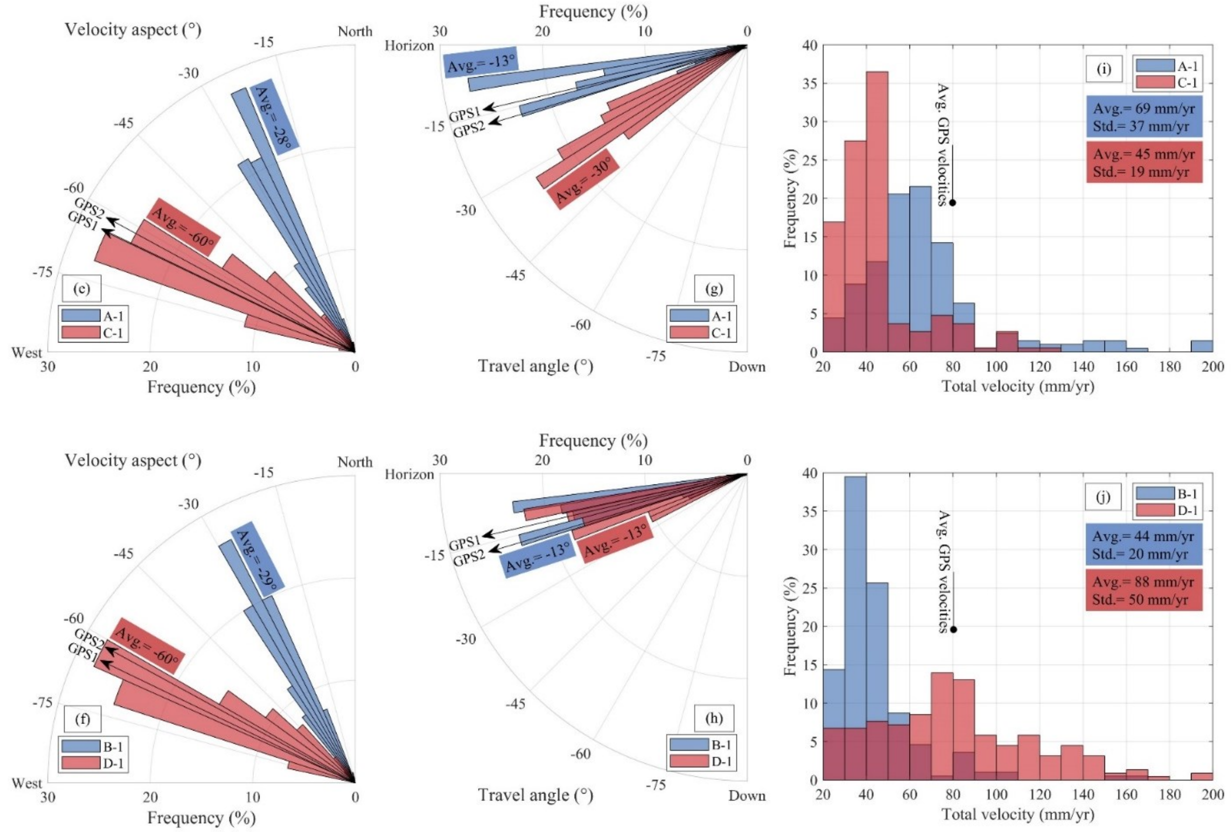

Figure 6- 9. Map of total velocities and their unit vectors for iterations A-1 (a), B-1 (b), C-1 (c), and D-1 (d) and histograms of velocity aspect (e-f), travel angles (g-h), and magnitude (i-j) for scatterers for the Ripley landslide (Note: GPS vectors are not to scale).

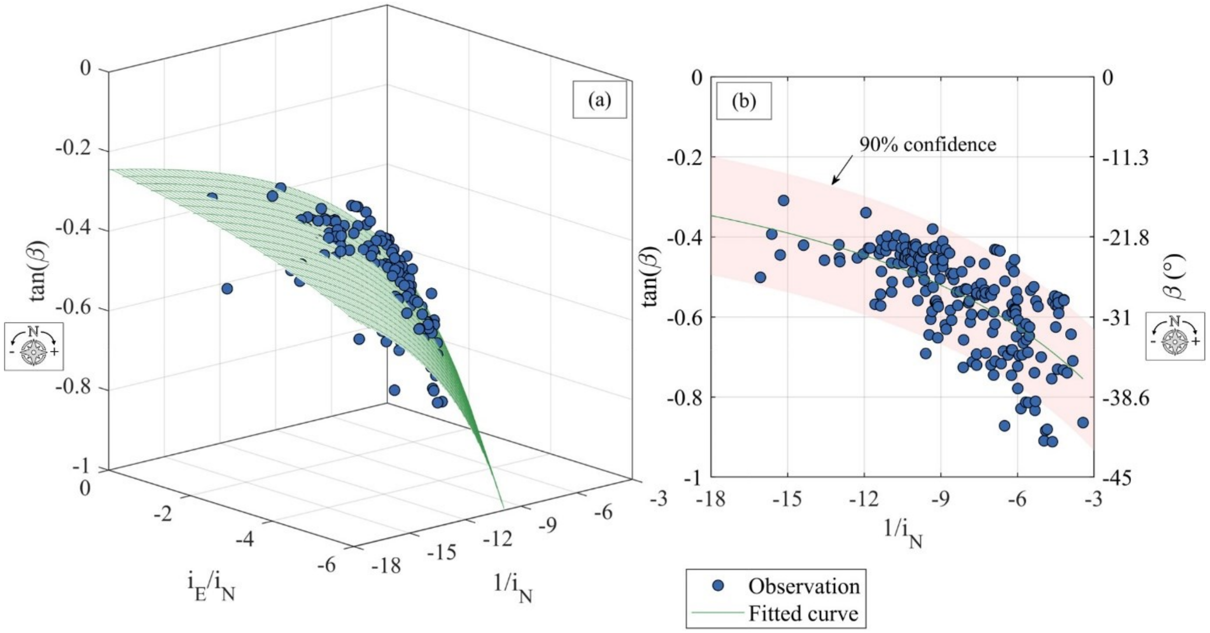

Figure 6- 10. Visual representation of the fitted aspect characteristic surface for A-1 in 3D (a) and 2D in-plane (b) view of the most sensitive input ($1/i_N$)

Table 6- 5. Calibrated coefficients of aspect characteristic surface after regression analysis on A-1 results along with the average back-calculated V_E, V_N, and β values at the location of GPS units on the Ripley landslide and their reported values

Fitted a	Fitted b	Fitted c
0.60	0.23	-0.61
Interpreted V_E (mm/yr)	Interpreted V_N (mm/yr)	Interpreted β (°)
71	44	-58
GPS-reported V_E (mm/yr)	GPS-reported V_N (mm/yr)	GPS-reported β (°)
69	34	-64

Figure 6- 9g also shows that a steeper estimation of travel angle in APFM is not only limited to the GPS locations. The error propagation analysis was performed using Eqs. 6. 11 and 6. 12 which indicates how much error in each component of the velocity is reflected by having a unit of error in the total velocity while considering the coherence threshold. Table 6- 6 indicates V_H and V_V respectively receive 0.95 and 0.18 per 1 unit of error in V_T in SPFM and SPFM-LSM, almost similar to STFM. On the other hand, the portion of error in V_H and V_V interpreted by APFM is on average 3.13 and 11 times the unit error in V_T, respectively. This shows that, as a result of LOS variance, the error in V_V is 3.5 more than the error in V_H, resulting in an over-steepened interpretation of travel angle; other methods do not display this effect. A higher portion of error in V_V of APFM results (10.35 and 11.65) may be attributed to the fact that this method does not impose any restrictions on the V_V and LOS variances are more likely to reflect along this component. While V_H also receives a high portion relatively (3.95 and 2.32), given that the ratio of V_E and V_N should still follow the dictated aspect angle, they proportionately vary together.

The scatterer maps and velocity magnitude and geometry histograms obtained for other active landslides in the valley are presented in Online Resource 1 as well as maps of scaled horizontal velocity vectors in Online Resource 2.

Table 6- 6. Portion of error in vertical (V_V) and horizontal (V_H) velocities per unit of error in total velocity (V_T)

Approach	Iteration	Portion of error in V_V magnitude	Portion of error in V_H magnitude	Portion of error in V_T magnitude
SPFM	A-1	0.18	0.95	1
	A-2	0.18	0.95	
SPFM-LSM	B-1	0.18	0.95	
	B-2	0.18	0.95	
APFM	C-1	10.35	3.95	
	C-2	11.65	2.32	
STFM	D-1	0.15	0.96	
	D-2	0.15	0.96	

6.5. Discussion

Back-projection and direct analysis at the Ripley landslide both indicate APFM provides the most accurate estimations of total velocity magnitude, followed by SPFM and SPFM-LSM and then STFM with the largest error. Looking at the entire valley, STFM leads to an overestimation of magnitude when the terrain is steep. This is because the assumption that vectors follow the steepest terrain simply does not conform to the mechanisms of sub-horizontal landslides with limited travel angles. However, SPFM and SPFM-LSM occasionally suffer from overly large estimations due to geometrical distortions toward north/south. This could affect secluded locales such as at the Red Hill landslide or be more universal as in the case of the Goddard and South landslides. This highlights why examining the performance of each method solely on the accuracy of interpreting total velocity magnitude is not sufficient because all of these methods heavily rely on the geometry of the terrain. Therefore, the geometrical sensitivity of these methods is also a major contributor to their accuracy.

The back-projection analysis showed SPFM and SPFM-LSM generally lead to large errors in interpreting the aspect angle. The direct analysis showed yet a larger error, and detailed mathematical investigations demonstrated SPFM's sensitivity to LOS variance, as also reported by Ao et al., (2019). The aspect characteristic surface showed the mathematical configuration of SPFM is very susceptible to LOS variance, leading to an overestimation of V_N and thus biasing the vectors toward the north orientation. This phenomenon was more accentuated for lower slope gradients in the north direction, which highlights a susceptibility to polar biasing for strong west- or east-aspected slopes. Therefore, SPFM and SPFM-LSM might be less preferred approaches in valleys with quasi-polar azimuths. Incorporating a weight matrix in SPFM and SPFM-LSM to adjust the contribution of different LOS velocities in light of their coherence could be a remedy but not a solution, as these methods are inclined to polar biasing even with no LOS variance as seen in the back-projection analysis (please refer to Appendix B.2). A more practical approach to tackle this limitation of SPFM could be fitting the aspect characteristic surface on a group of scatterers known or speculated to be moving about the same direction even when there are no *in situ* measurements. To mitigate the error in aspect angle, the aspect angle interpreted from this fitted function can be used to correct the geometry of vectors.

In contrast, APFM forces the vectors to align parallel with the aspect of the valley, which is a reasonable assumption for translational instabilities sliding along the valley fall line. However, APFM's strict compatibility assumption, dictating the relationship between V_E and V_N, leads to magnifying the variance in V_V and a steep interpretation of travel angle.

In the case of STFM, which prompts one SAR stack, variance in LOS velocity does not impact the geometry of velocity as the ratios between components make the geometry of vectors merely a function of topography and not LOS velocity (Eq. 6. 6). Nonetheless, STFM should be employed with caution because the geometry of decomposition is completely at the mercy of topography. Very large total velocities could be interpreted for steep terrains and a cut-off for the slope inclination should be defined. For example, Herrera et al. (2013) considered 72° for their study site; however, this threshold should be much lower for unstable slopes sliding on a sub-horizontal shear surface and further evaluations are recommended in this regard. Moreover, the landscape in Western Canada is often described as hummocky, and thus a local upward elevation gradient would result in a positive vertical velocity if STFM is exercised. This leads to an interpretation of upslope velocities or bulging, and potentially an incorrect interpretation of movements. This is highlighted in settings similar to the Thompson River valley where the retrogressive mechanism has led to the formation of horsts with surficial geometry slightly tilted rearward. As an example, a considerable portion of scatterers in the case of the North landslide, which features both bulging at the toe (Figure 6- 11a) and hummocky terrain (Figure 6- 11b), were interpreted to show upward velocity while only the former is a valid scenario.

6.6. Conclusion

InSAR is becoming more integrated into landslide monitoring programs. However, the ambiguity of line-of-sight (LOS) velocities impedes a full and realistic understanding of the landslide kinematics that is necessary for both risk management strategies and setting alarm thresholds when developing early warning systems. As a result, LOS velocities should be decomposed from 1D estimations into 3D. Among many approaches adopted to this end, topography-based methods have been well received in terms of feasibility, accuracy, and resource management. However, the choice of specific method should be informed because the shortfalls of each method are manageable if the user is aware of the consequences. In this paper, 202 Radarsat-2 and 243 Sentinel-1 scenes acquired from various viewing geometries over landslides along the Thompson River valley were processed and 1D LOS velocities were decomposed using four different methods: Surface Parallel Flow Method (SPFM), SPFM coupled with the least-

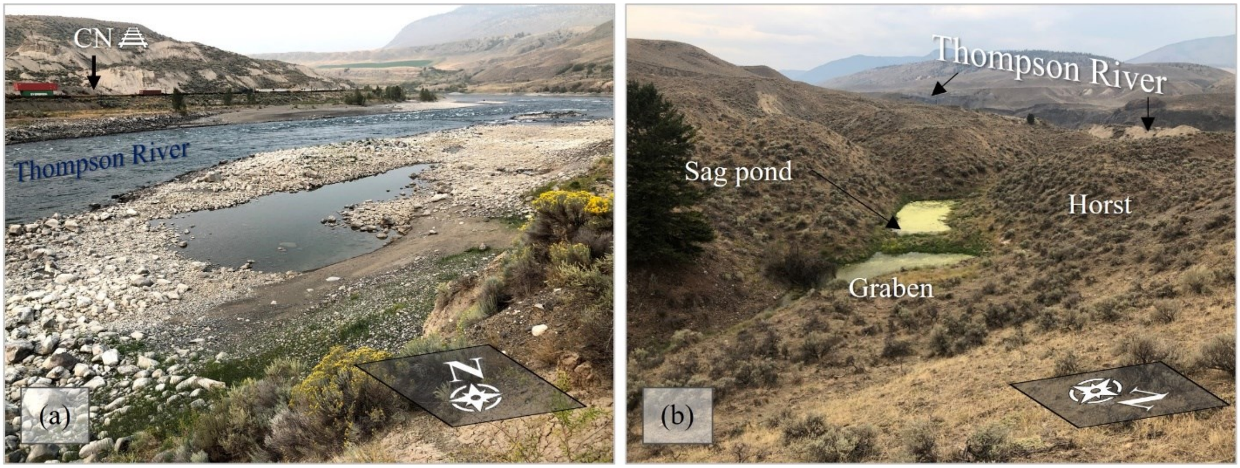

Figure 6- 11. Toe bulge (a) and a view of the hummocky topography (b) at the North landslide

squares method (SPFM-LSM), Aspect Parallel Flow Method (APFM), and Steepest Train Following Method (STFM). The following are concluding remarks:

- In the best combination of SAR stacks, the incorporation of SPFM, SPFM-LSM, APFM, and STFM in decomposition resulted in an error of 19 (23.76%), 29 (36.25%), 15 (18.75%), and 37 mm/yr (46.26%), respectively, in the case of the Ripley landslide.
- The vectors obtained by SPFM and SPFM-LSM are biased toward the north orientation because V_N is exaggerated in response to their sensitivity to LOS variance. Such sensitivity was successfully characterized by a proposed “aspect characteristic surface,” which showed a higher error at lower i_N values.
- SPFM and SPF-LSM showed sporadic overestimation of total velocity magnitude where variance in V_N was not compensated by counterbalancing variance in V_E, leading to artificially large estimations of V_T.
- APFM was more successful in appreciating the velocity aspect with less sensitivity to LOS variance compared to SPFM and SPFM-LSM. However, a restrictive assumption to force V_E

and V_N to align with the valley's aspect led to the manifestation of LOS variance mostly in V_V, inducing erroneous and steep travel angle estimations.

- The geometry of STFM vectors remained somewhat unaffected by LOS variance given its compliance with the terrain geometry. This feature narrows the role of LOS velocities in STFM solely to the magnitude of the decomposed velocity and introduces a vulnerability related to rearward-tilted terrain that can result in the interpretation of upslope velocities. STFM also has a weakness on steep terrain that causes synthetically large total velocities, resulting in the need to define a cut-off in the elevation gradient.

In conclusion, employing a stand-alone method would result in foregoing an accurate understanding of velocities in at least one attitude of the magnitude, aspect, or travel angle. A hybrid approach in the 3D decomposition of 1D LOS velocities is therefore suggested to analyze translational landslides. Different decomposition methods should contribute to the interpretation of a specific vector attitude when they outperform others from that perspective. We propose using APFM to estimate the magnitude and aspect angle of total velocity vectors, and using SPFM or SPFM-LSM for reliable interpretation of the travel angle. Constraining the geometry of vectors using Ground-based InSAR or Unmanned Aerial Vehicle (UAV) would also help but it limits the monitoring area.

Appendix 6.A – kNN Algorithm

The k-nearest neighbouring (kNN) search algorithm is a subset of computational geometry that is mainly used for classification purposes (Guo et al., 2003). It was re-purposed here to interpolate the LOS velocity spatially at an opposing geometry. For this, a damping weight kernel was implemented to adjust the contribution of different scatterers depending on their distance from the location of interest; the farther the distance, the lower the significance. This algorithm is applied to each scatterer from one SAR set and finds k surrounding scatterers from other geometry(ies) that will be averaged adaptively. At the location of ith scatterer from a specific orbit geometry, the LOS velocity of opposing geometry at the location of the scatterer of interest is calculated as follows (Eq. 6. *13*):

$$\widehat{\mathrm{V}}_{\mathrm{LOS}_\mathrm{i}}=\frac{\sum_{\mathrm{j}=1}^{\mathrm{k}} \mathrm{w}_\mathrm{j} \mathrm{V}_{\mathrm{LOS}_\mathrm{j}}}{\sum_{\mathrm{j}=1}^{\mathrm{k}} \mathrm{w}_\mathrm{j}}, \tag{6. 13}$$

$$\mathrm{w}_\mathrm{j}=1-\frac{\mathrm{d}_\mathrm{j}}{\mathrm{d}_\mathrm{k}}, \tag{6. 14}$$

where $\widehat{V}_{LOS_i}$ is the equivalent LOS velocity at the opposing geometry of the ith scatterer, V_{LOS_j} is the LOS velocity of the jth-ordered scatterer (based on the distance in the ascending order) around the scatterer of interest, and w_i is the averaging weight (Eq. 6. *14*) normalized based on the largest distance. Given that the surrounding scatterers are ordered by the distance, the weight of the kth point will be zero, leading to automatic discarding of the farthest point. This method only prompts k as an input, which can be interpreted with the aid of a simple sensitivity analysis on any components of velocity. Sharifi, Hendry, & Macciotta (2022) increased k from 3 to 14 and calculated the variation of V_v and V_e by increasing a unit in k value. They reported an asymptotic trend in such parameters that agreeably started to converge linearly after a certain value, which was used for the final value of k in their analysis. In this study, the sensitivity analysis was performed on the variation of total velocity magnitude and the kNN was modulated to the post-processing script.

Appendix 6.B – SPFM Polar Biasing Characteristic

B.1. Error-contaminated Aspect Angle in Direct Analysis

The compatibility relationship in SPFM-based assumptions is as follows (Eq. 6. *15*):

$$\mathrm{V_V = i_E V_E + i_N V_N}, \tag{6. 15}$$

which can be derived into error terms as in Eq. 6. *16*:

$$\mathrm{dV_V = i_E dV_E + i_N dV_N}, \tag{6. 16}$$

where dV_V, dV_E, and dV_N are errors in the vertical, eastward, and northward directions, respectively. If InSAR analysis itself or post-processing stages superimpose an error in the eastward component or vertical component as much as a unit, such deviations lead to a dV_N of $1/i_N$ and i_E/i_N, respectively, based on Eq. 6. *16*. The magnitude of i_E/i_N is between 2 and 4 for Ripley, 10 and 50 for Red Hill, and 10 and 20 for South landslides while the magnitude of $1/i_N$ increases to range from 5 to 10 for Ripley and 50 to 100 for both the Red Hill and South landslides. These values explain the exaggeration of V_N that leads to vectors inclined to the north orientation in SPFM and SPFM-LSM. However, this explanation isolates the effect of error in only one direction (either vertical or eastward). A more complex interaction of errors in both directions simultaneously would result in an error-contaminated aspect angle (β_e) as a function of elevation gradient ratios ($1/i_N$, i_E/i_N). By re-arranging terms in Eq. 6. *16*, dV_N can be expressed by error terms along other axes:

$$\mathrm{dV_N = \frac{1}{i_N}(dV_V - i_E dV_E)}. \tag{6. 17}$$

The erroneous velocity aspect as a result of superimposing the error along all axes can be calculated as follows (subscript *e* indicate erroneous parameters of such that do not have the subscript):

$$\tan\beta_e = \frac{V_{E_e}}{V_{N_e}} = \frac{dV_E + V_E}{dV_N + V_N} = \frac{dV_E + V_E}{\frac{1}{i_N}(dV_V - i_E dV_E) + V_N} = \frac{\frac{dV_E}{V_E} + 1}{\frac{1}{i_N}\cdot\frac{dV_V}{V_E} - \frac{i_E}{i_N}\cdot\frac{dV_E}{V_E} + \frac{V_N}{V_E}} \quad , \tag{6. 18}$$

which can be simplified into:

$$\tan\beta_e = \frac{a+1}{b\left(\frac{1}{i_N}\right) - a\left(\frac{i_E}{i_N}\right) + c} , \tag{6. 19}$$

where $a = dV_E/V_E$, $b = dV_V/V_E$, and $c = 1/\tan\beta$. Eq. 6. *19* is a homographic function of $1/i_N$ and i_E/i_N and coefficients *a*, *b*, and *c* can be estimated by regression analysis. Given that the velocity aspect of scatterers on Ripley landslide is controlled by geological structures, *c* can be estimated as constant across different scatterers considering it is another form $\tan\beta$. Other coefficients are also approximated as constant considering the scale of Ripley landslide, which was demonstrated to be a reasonable assumption considering the R-squared value of the fitted surface and back-calculated velocity components (Table 6- 5). This analysis can be beneficial as an error mitigation method to interpret an improved estimation of aspect angle.

B.2. Aspect Angle in Back-Projection Analysis of Ripley Landslide

After substituting appropriate values in Eq. 6. 3, the velocity components are given in Eq. 6. 20 for A-1:

$$\begin{pmatrix} V_v \\ V_e \\ V_n \end{pmatrix} = \begin{bmatrix} \frac{0.13i_E+0.71i_N}{0.02i_E+i_N-0.16} & \frac{-0.11i_E+0.64i_N}{0.02i_E+i_N-0.16} & \frac{0.16}{0.02i_E+i_N-0.16} \\ \frac{-0.721i_N+0.114}{0.0007i_E+i_N-0.151} & \frac{0.781i_N-0.114}{0.0007i_E+i_N-0.151} & \frac{0.007}{0.0007i_E+i_N-0.151} \\ \frac{0.721i_E+0.71}{0.007i_E+i_N-0.151} & \frac{-0.781-0.645}{0.007i_E+i_N-0.151} & \frac{1}{0.007i_E+i_N-0.151} \end{bmatrix} \begin{pmatrix} V_{S1A} \\ V_{RS2U21} \\ 0 \end{pmatrix}, \qquad (6.20)$$

which can be used to calculate the aspect angle (Eq. 6. *21*):

$$\tan\beta = \frac{\left(0.721\frac{i_E}{i_N}+0.71\frac{1}{i_N}\right)V_{S1A}+\left(-0.781\frac{i_E}{i_N}+0.645\frac{1}{i_N}\right)V_{RS2U21}}{\left(-0.721+0.114\frac{1}{i_N}\right)V_{S1A}+\left(0.781-0.114\frac{1}{i_N}\right)V_{RS2U21}}. \qquad (6.21)$$

For the Ripley landslide, by substituting i_E/i_N=(-4~-2) and $1/i_N$=(-10~-5) and knowing that $V_{RS2U21}<0<V_{S1A}$, the denominator of Eq. 6. *21* will be larger than the numerator (while the contrary should be true given the true β is less than 315°). A similar conclusion can be made for other iterations of categories A and B. Depending on LOS velocities, Eq. 6. *21* shows that, when i_N is larger than i_E (similar to the Thompson River valley with strong east/west aspects), the aspect angle might be still biased toward the north, even in an ideal case (as seen in back-projection) in which no LOS variance is included in the decomposition.

Online Resource 1 – Results of Other Active Landslides in Valley

For the Red Hill landslide, the SPFM and SPFM-LSM results in Figure 6- 12 show sporadic areas with high velocities reaching 200 mm/yr near the head scarp in the northern half of the landslide and its toe; however, APFM and STFM results indicate only the toe, with smaller very active areas. SPFM and SPFM-LSM show the largest average velocities of 66 and 55 mm/yr, respectively, with a standard deviation larger than 40 mm/yr; such parameters decrease to 45 and 22 mm/yr for APFM and to 48 and 28 mm/yr for STFM. Similar to the discussion above regarding

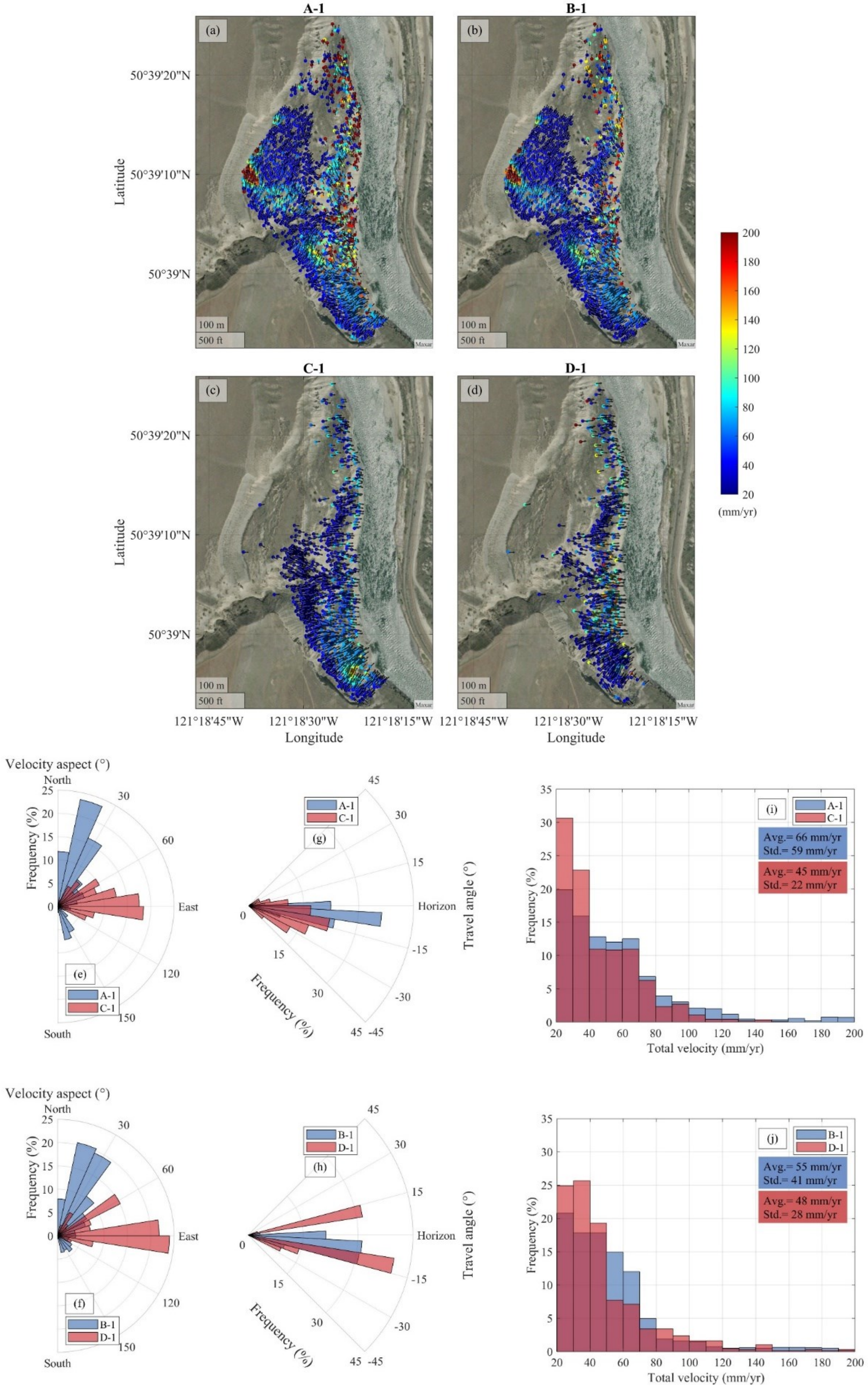

Figure 6- 12. Map of total velocities and their unit vectors for iterations A-1 (a), B-1 (b), C-1 (c), and D-1 (d) and histograms of velocity aspect (e-f), travel angles (g-h), and magnitude (i-j) for scatterers for the Red Hill landslide

the Ripley landslide, the aspect angle of SPFM and SPFM-LSM for the Red Hill landslide show a strong tendency toward the north orientation, even near the head scarp where an eastward orientation is suggested by the geomorphology. Finally, APFM indicates steeper travel angles and STFM shows upward travel angles for more than 30% of scatterers.

For the South landslide, Figure 6- 13 illustrates that SPFM and SPFM-LSM interpreted a larger area to be active with more scatterers reaching values greater than 120 mm/yr; this is contrary to APFM and STFM that report the South extension is the most active part. The average and standard deviation of total velocity magnitudes reported by SPFM (62 and 43 mm/yr) and SPFM-LSM (55 and 38 mm/yr) are larger than reported by APFM (37 and 23 mm/yr) and STFM (42 and 30 mm/yr). Figure 6- 13 further supports the polar biasing characteristic of SPFM and SPFM-LSM as the vectors of the South extension (Figure 6- 2a) show it is merely moving southward. The arcuate features in the southwest overlooking the gully incised by Barnard Creek imply the areas bordering this gully should be under the influence of landslide processes toward the south. However, this effect should diminish for regions further away and be superseded by the predominant landslide process in Thompson River valley, with instabilities toward the southwest similar to that shown by APFM and STFM. Almost 50% of scatterers, as reported by STFM, have an upward component (Figure 6- 13h).

For the North landslide, the rates of movements vary considerably both annually and seasonally so its kinematics cannot be reliably extrapolated to years before the monitoring period (starting September 2019). The activity state therefore cannot be quantitatively compared to Figure 6- 5b. However, Figure 6- 14 shows SPFM-LSM cannot successfully recognize the spatial trend whereas SPFM, APFM, and STFM show a clearer distinction between the most active part of the Solar Slump and less active regions in the southwest. The difference between the aspect angle of

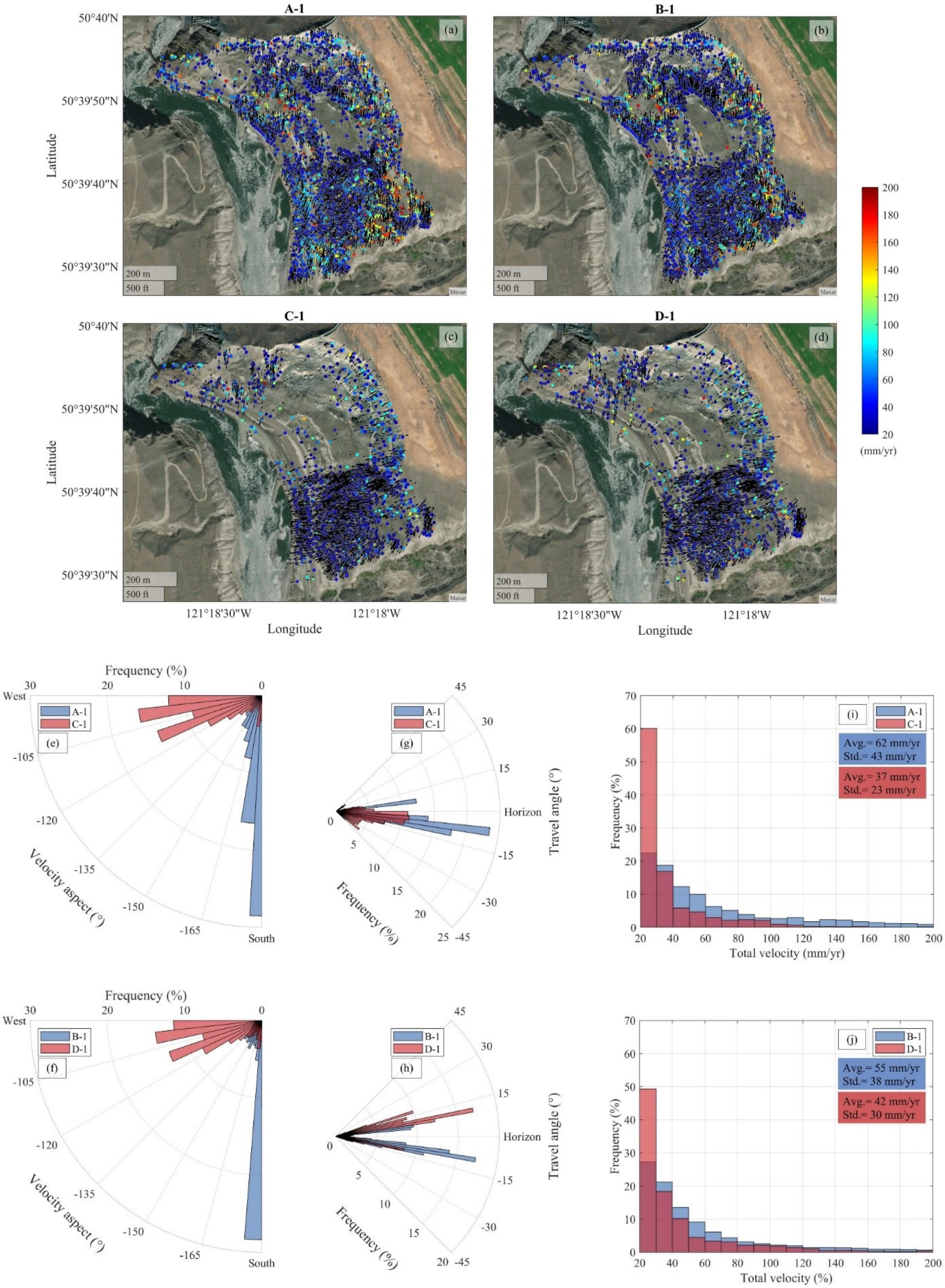

Figure 6- 13. Map of total velocities and their unit vectors for iterations A-1 (a), B-1 (b), C-1 (c), and D-1 (d) and histograms of velocity aspect (e-f), travel angles (g-h), and magnitude (i-j) for scatterers for the South landslide

each method becomes more conspicuous in the southwest of the Solar Slump where the river course runs closer to the south and APFM and STFM suggest a more perpendicular aspect to the river, contrary to SPFM and SPFM-LSM. Moving from northeast to southwest, the velocity aspect in Figure 6- 14c-d rotates from values within the range of N10°W and N30°W to more westward aspect angles of N40°W and N90°W and more assorted aspect angles in southwestern parts similar to Figure 6- 5a. On the other hand, SPFM and SPFM-LSM consistently report an aspect angle of about N10°W throughout the entire region of the Solar Slump. STFM also reports more than 50% of points showing upward movement.

Figure 6- 15a,b shows SPFM and SPFM-LSM interpret a universal high activity state for the Goddard landslide, also reflected by a severe right skewness and large kurtosis in Figure 6- 15i,j. This does not conform to the frequency of track maintenance, as this landslide's velocities would be reaching velocities of 100 mm/yr on average. Moreover, the polar biasing of SPFM and SPFM-LSM becomes so predominant that, counter-intuitively, they indicate a robust and extensive southward movement; this could explain the overestimations in the total velocity magnitudes.

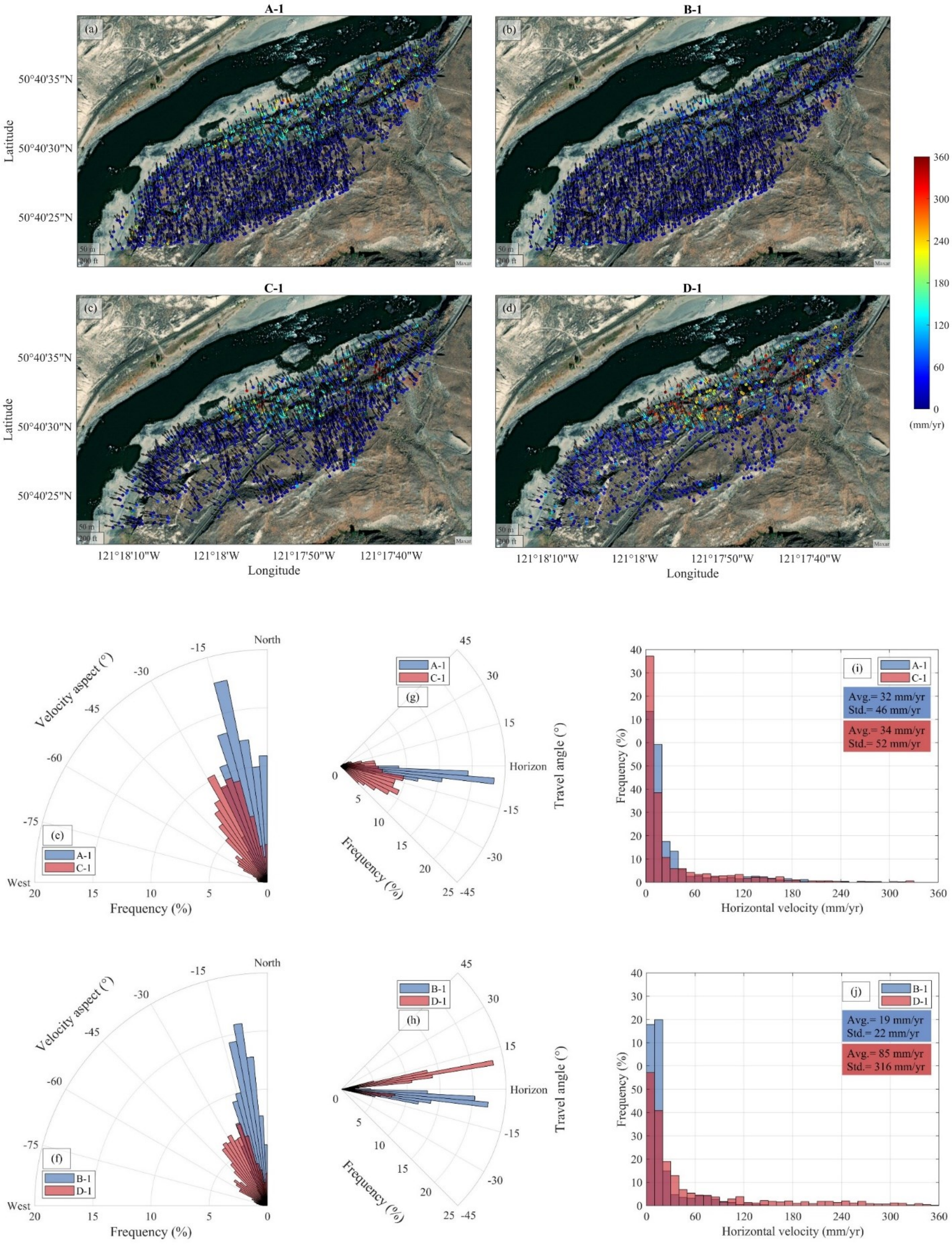

Figure 6- 14. Map of horizontal velocities and their unit vectors for iterations A-1 (a), B-1 (b), C-1 (c), and D-1 (d) and histograms of velocity aspect (e-f), travel angles (g-h), and magnitude (i-j) for scatterers for the North landslide

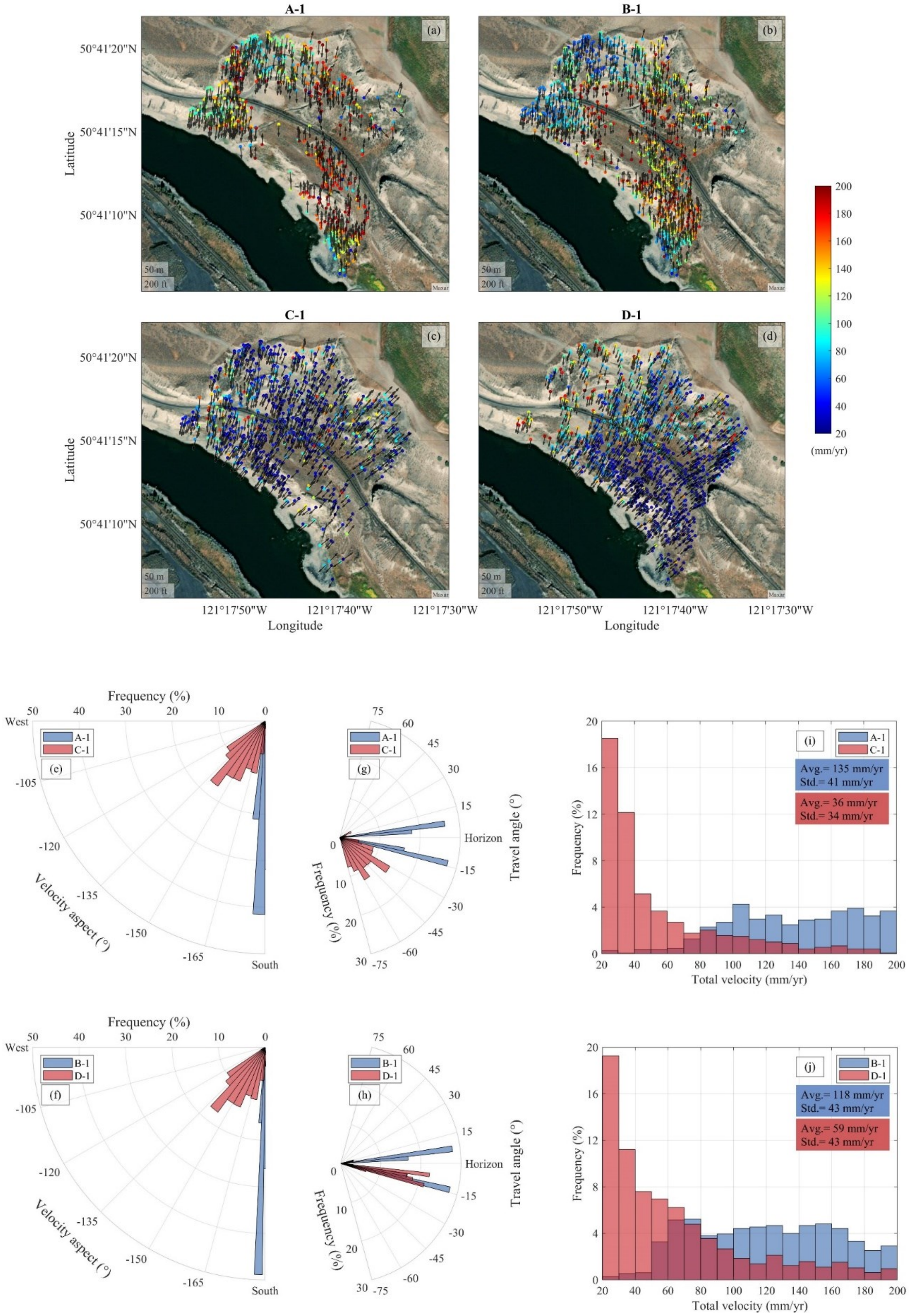

Figure 6- 15. Map of total velocities and their unit vectors for iterations A-1 (a), B-1 (b), C-1 (c), and D-1 (d) and histograms of velocity aspect (e-f), travel angles (g-h), and magnitude (i-j) for scatterers for the Goddard landslide

Online Resource 2 – Horizontal Velocities Vectors

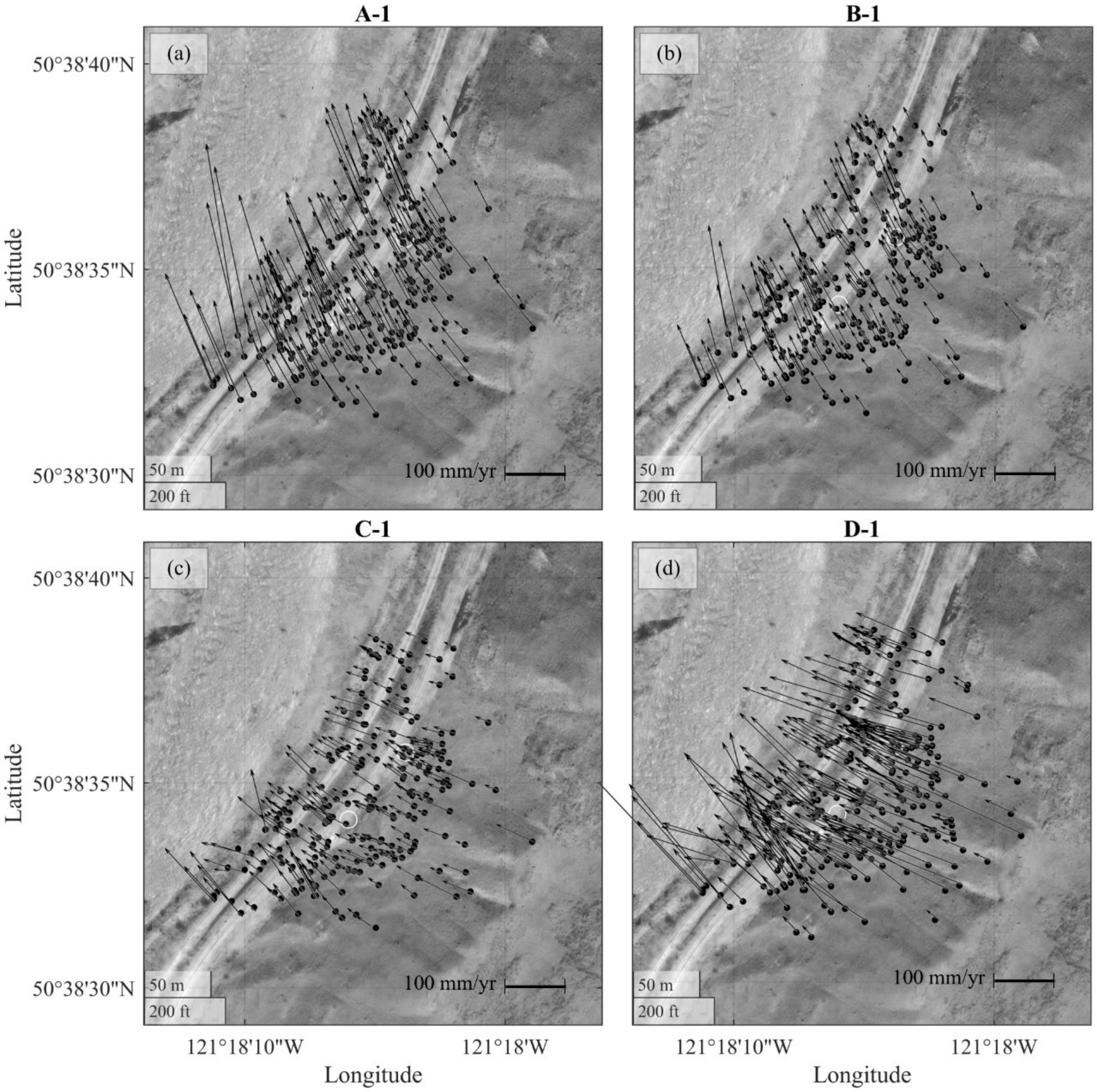

Figure 6- 16. Horizontal velocity vectors at Ripley landslide as interpreted by (a) SPFM, (b) SPFM-LSM, (c) APFM and (d) STFM

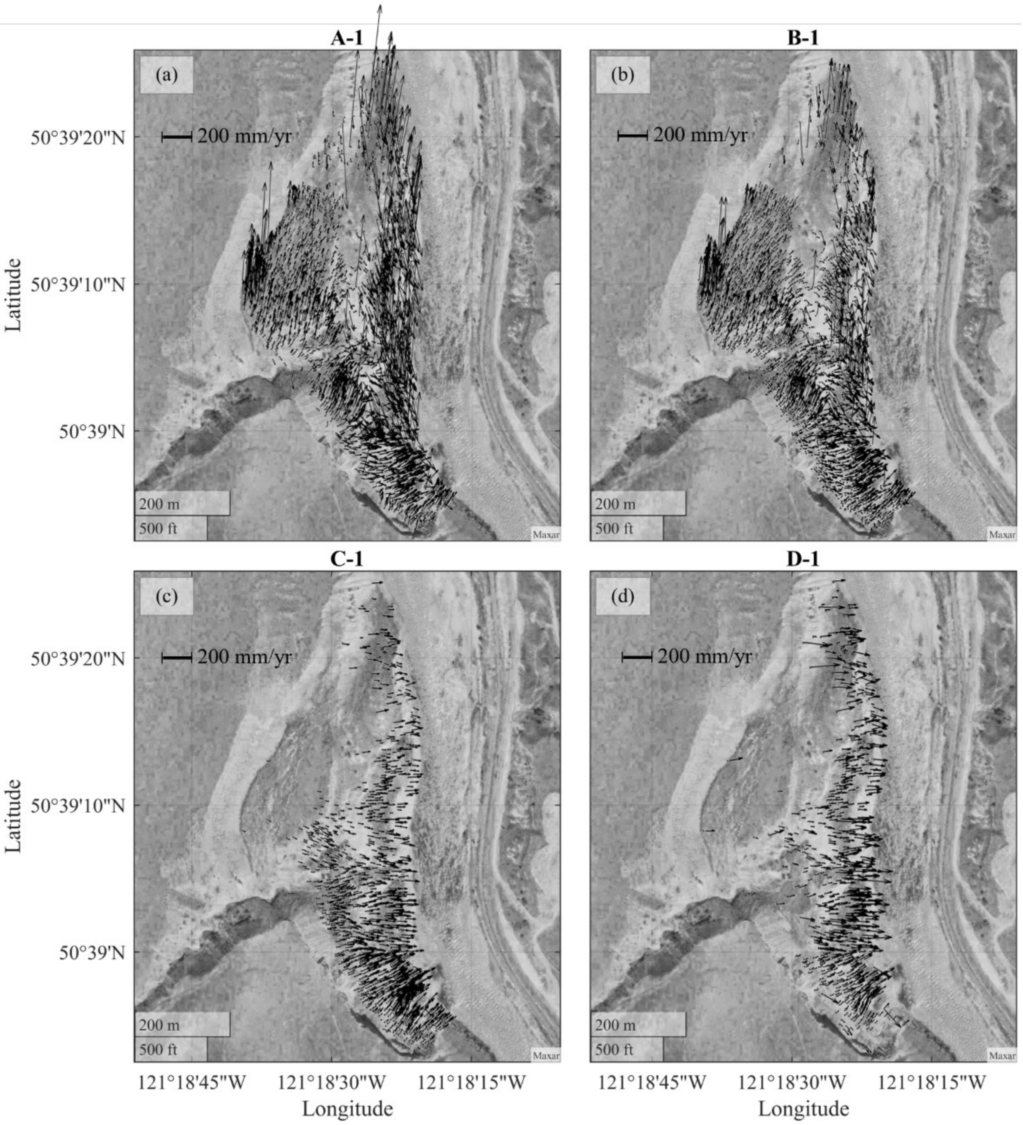

Figure 6- 17. Horizontal velocity vectors at Red Hill landslide as interpreted by (a) SPFM, (b) SPFM-LSM, (c) APFM and (d) STFM

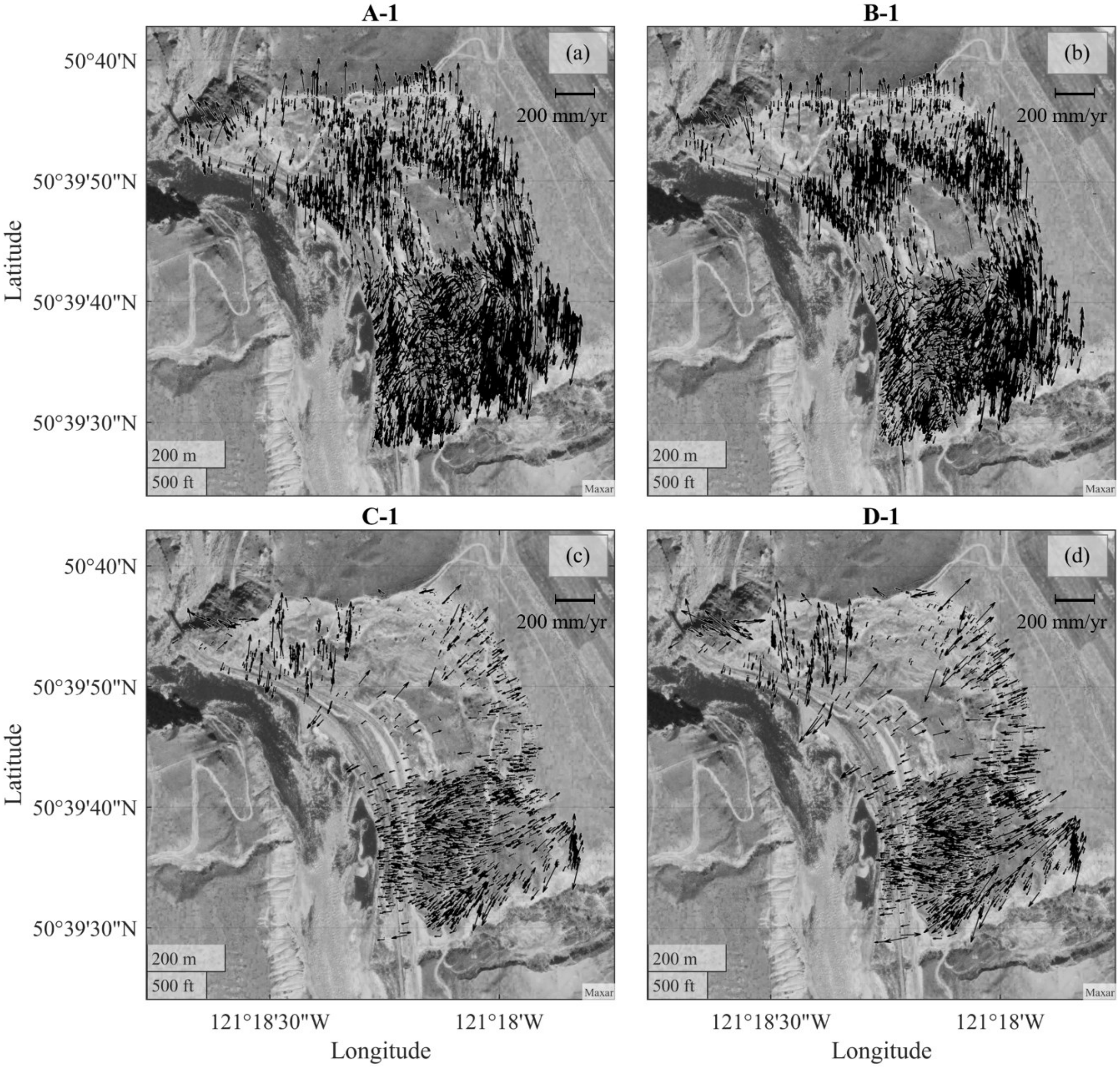

Figure 6- 18. Horizontal velocity vectors at South landslide as interpreted by (a) SPFM, (b) SPFM-LSM, (c) APFM and (d) STFM

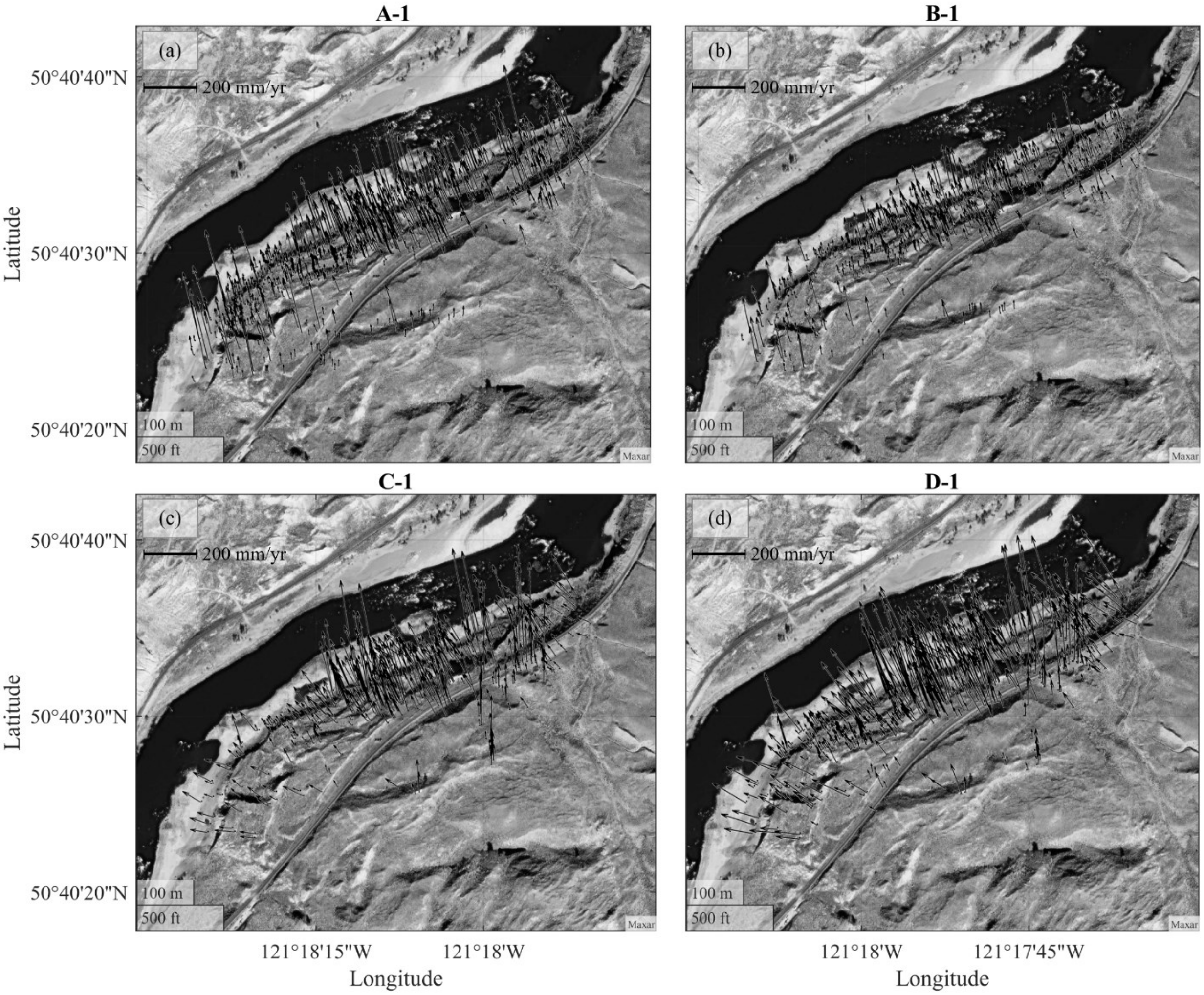

Figure 6- 19. Horizontal velocity vectors at Solar Slump of North landslide as interpreted by (a) SPFM, (b) SPFM-LSM, (c) APFM and (d) STFM

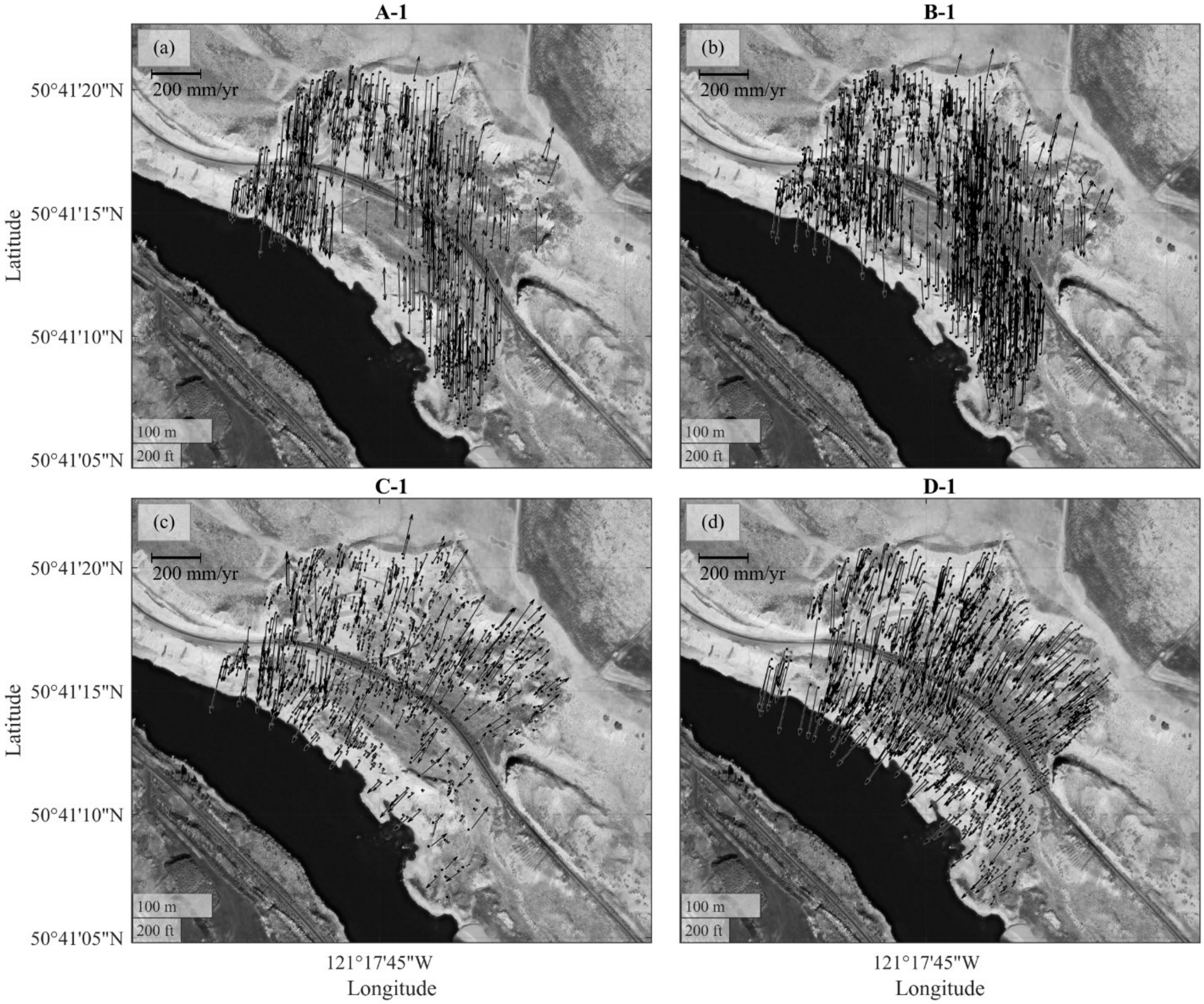

Figure 6- 20. Horizontal velocity vectors at Goddard landslide as interpreted by (a) SPFM, (b) SPFM-LSM, (c) APFM and (d) STFM

Chapter 7: Conclusions and Recommendations

The general goal of this research was to address knowledge gaps pertaining to the development of EWSs by acquiring an improved understanding of ground kinematics. The first two objectives, classified as the element of "data analysis", pursued methodologies to separate the true underlying trend of landslide displacements from unfavoured data artifacts, scatter. Another element of this study is relevant to the application of Interferometric Synthetic-Aperture Radar (InSAR). The incorporation of InSAR into monitoring systems faces a critical impediment to velocity estimations along the sensor's line-of-sight (LOS). The LOS velocity is the product of projecting true velocity along the LOS arm that makes InSAR's results a convoluted mixture of magnitude and geometry manifested in 1D.

In the next sections, a summary of findings, detailed in Chapters 3-6, is presented. This chapter comes to a conclusion by introducing suggestions for future follow-up studies.

7.1. Concluding remarks

7.1.1. Data Analysis Element

7.1.1.1. Advantages and Disadvantages of SMA, GWMA and SG

The filtration bandwidth (window width) should be at least 4% of the total monitoring time to ensure fluctuations are sufficiently minimized. SMA does not preserve the trends and a complete distortion was observed when encountering sudden changes in velocity values even at the bandwidth of 7%. However, 7% may not provide sufficiently less variance in velocity values and a 10% bandwidth could be carefully used in light of its all limitations. SMA also tends to attenuate the changes in velocity relatively more which results in an under-representation of a landslide kinematics.

In the Numerical Analysis of Synthetic Database, an asymmetric filtration window was employed to resemble real-time monitoring since future observations are unknown. This induced a lag in the filtered displacements. Among the three filters, SMA displayed the largest lag while a near zero-lag was noted in SG results. This was due to the negative values in its kernel but they also created artificial fluctuations (pulsating effect). The extent of the pulsating effect depends on the bandwidth and consequently, a large value, such as 10% or more is not recommended. The pulsating effect can also cause fluctuations in the velocity values if SG is directly applied to the velocity diagram.

GWMA results were found to be free of the mentioned artifacts. The pulsating effect was not observed because of all-positive values in the GWMA kernel. It also does not suffer from lagged response as much as SMA since GWMA's kernel grants less significance to points farther away. The velocity values interpreted after the application of GWMA possessed medium volatility while managing to reduce the scatter. GWMA is also less sensitive to bandwidth compared to SMA, giving it the advantage of less computational capacity needed for pre-processing. Results displayed that it is capable of preserving the true trend even at the bandwidth of 7%.

In conclusion, the application of SG is not recommended due to its erratic performance despite a satisfactory performance in terms of lag and lower associated error. SMA is also outperformed by GWMA in many aspects as discussed above. The application of GWMA at the bandwidth of 7% provides an optimal solution, striking a trade-off between lagged response, and residual scatter, preserving the trend and consistent performance in different scenario circumstances. A chart is also presented in section "3.4.1.4. Lag Quantification" which can be used in practice to minimize the lagged response of GWMA.

7.1.1.2. Filters Performance on Acceleration and Failure

Results signified a timelier response from GWMA and SG to detect the onset of acceleration. The mean and standard deviation of SMA's error were found to be 3.42 and 2.72 times GWMA's, and 236.42 and 8.67 times SG's. It is understood that the application of SMA's alternatives would lead to more accurate detection of the onset of acceleration with more confidence. As an example, SMA, GWMA and SG would reach 90% confidence respectively 13.5 days, 4 days and 13 hours after the true acceleration moment, if the total monitoring period is 6 months.

For linear trends (α=2) in the inverse velocity diagram, the application of GWMA and SG improved the forecast accuracies, respectively, by 60-75% and 90-95%. An improvement of 65-72% for GWMA and at least 89% for SG was noted for non-linear trends ($\alpha \neq 2$). Analyzing the time-series of actual failed cases from the literature also confirmed the GWMA and SG satisfy the expectation of accurate forecasts. It was observed that employing GWMA and SG, on average, led to respectively 60-80% and 90-100% improvement in the forecast as well. An interesting conclusion was that a higher filtration bandwidth would lead to larger errors when using GWMA as opposed to the expectation, while no such observation was made for SG. This, called the "bandwidth paradox", emphasizes that considerations should be taken into account when setting the filtration bandwidth and higher values would not necessarily lead to an improved forecast.

In conclusion, the adoption of any other SMA alternatives discussed here improves the reliability of EWSs, as they prompt the monitoring systems to act timely and meaningful.

7.1.2. InSAR Element

7.1.2.1. Combined Precision

Mathematical calculations showed that the error induced by the simplifying assumption in vertical and eastward components of velocity is linearly correlated to the northward component. For the Oldman River Dam case, the effect on the vertical component was found 55 times more than the impact on the northward component. This highlights the vulnerability of interpretations in the vertical plane to this assumption. For true movements due North, the vertical component is exposed to a downward error with a magnitude of 17.06% of the northward velocity component. The same is also true when the true movements are due South; however, the direction of the error vector would be upward. This, in particular, is detrimental for translational landslides in Canada, sliding on sub-horizontal shear surfaces with limited vertical velocity which may be rendered moving upward. The induced error in the eastward component is only 0.31% of the northward component which highlights the immunity of this component to the simplifying assumption. The 17.06% and 0.31% coefficients are a function of the geometry of acquisitions (i.e., incidence and heading angles). To ensure a minimum error in the vertical component, the difference between incidence angles of ascending and descending orbits should be minimized. To minimize the error in the eastward component, both incidence angles should be lowered as much as possible. As a result, a low similar incidence angle of both geometries should be used which may entail other geometrical distortions in InSAR analysis itself. This fact undermines the suitability of using simplifying assumptions for phenomena with sizable northward components such as landslides.

A framework was developed and successfully applied to the case of Oldman River Dam. The proposed approach adopts the effect of simplifying the assumption's error along with InSAR's inherent accuracy in estimating LOS velocities. Spillway LOS accuracy was found to vary from 0 to 2 mm/yr while this range increases to 3.5~5.2 mm/yr for the active area on the embankment. The combined precision, taking into account both sources of uncertainty, was found to be 0.72 and 2.78 mm/yr on average for the spillway and active area on the embankment. Comparing them against the interpreted average velocity for these two regions of interest reveals that the combined precision is 33~57% of 1.26 and 8.29 mm/yr. This highlights, the significance of estimating the combined precision when reporting InSAR and not relying on the estimated magnitudes alone. In addition, it shows that the simplifying assumption is not the best decomposing practice and other techniques should be too evaluated for each site.

7.1.2.2. Accuracy of topography-informed assumptions

The accuracy of SPFM, SPFM-LSM, APFM and STFM was evaluated in decomposing a total of 445 SAR scenes obtained by Sentinel-1 and Radarsat-2 on the Thompson River Valley. All the mentioned topography-informed assumptions were evaluated in terms of interpreting the magnitude and the geometry of velocity vectors.

Results of InSAR direct analysis showed a north-biased interpretation of vectors by SPFM and SPFM-LSM leading to a large error in the aspect angle. Further mathematical investigations demonstrated that SPFM-based methods manifest any variance in LOS velocity as a geometrical rotation toward the South-North direction (polar-biasing). It was also observed that these methods are less preferred for slopes with strong east/west aspects as SPFM's tendency for polar-biasing was found to be inversely related to the northward gradient. By super-imposing the variance on SPFM's main assumption, a mathematical expression, called "aspect characteristic surface" which is a function of ground gradients is proposed as follows (Eq. 7. 1):

$$\tan \beta_e = \frac{a+1}{b\left(\frac{1}{i_N}\right) - a\left(\frac{i_E}{i_N}\right) + c}, \tag{7. 1}$$

where $a = dV_E/V_E$, $b = dV_V/V_E$, $c = 1/\tan\beta$, and β and β_e are true and erroneous aspect angles, respectively. Eq. 7. 1 is a homographic function of $1/i_N$ and i_E/i_N, and coefficients a, b, and c could be estimated by regression analysis. Fitting a surface which follows Eq. 7. 1 on a group of scatterers believed to be moving in a relatively single direction leads to retrieving the constant c. It is possible to back-calculate the true aspect angle by having the value of c constant. Aspect characteristic surface is then beneficial in practice to reduce the error of SPFM

APFM, on the other hand, was able to interpret the aspect angle with limited error yet showed a considerable deviation in the travel angle. A mathematical investigation called error propagation analysis showed that APFM reflects the LOS variances by steeper travel angles. This is because APFM strictly dictates the vectors to face the aspect angle and the only remaining degree of freedom is the dip of vectors in the vertical plane.

In the case of STFM, LOS variances were not found to be contributing to geometrical distortions because the aspect and travel angles are strictly enforced by the topography. This characteristic sometimes leads to the interpretation of vectors aiming upslope, caused by hummocky terrain. Another disadvantage of STFM is that yields very large velocities when the ground is steep.

In conclusion, it is observed that a single method of the existing topography-informed assumptions cannot satisfy all of the expectations and a hybrid approach is recommended. For translational landslides, APFM is suggested for procuring the magnitude and the aspect angle in conjunction with leveraging SPFM to interpret the travel angle. The use of SPFM-LSM is recommended to be adjourned to the cases where all the incorporated SAR stacks hold high spatial resolution.

7.2. Recommendations for Future Studies

7.2.1. Data Analysis Element

1. It is now known that having a kernel with tapered ends is more efficient since they give less contribution to those measurements temporally distant from the point of interest. However, GWMA and SG filters are not the only ones, and Figure 7- 1 displays a list of well-known kernels in statistics which can be used to evaluate further filters. The formulas shown in Figure 7- 1 are non-normalized in the vertical axis (*K*(*u*)) and configured for a horizontal axis parameter (*u*) varying between -1 and +1.

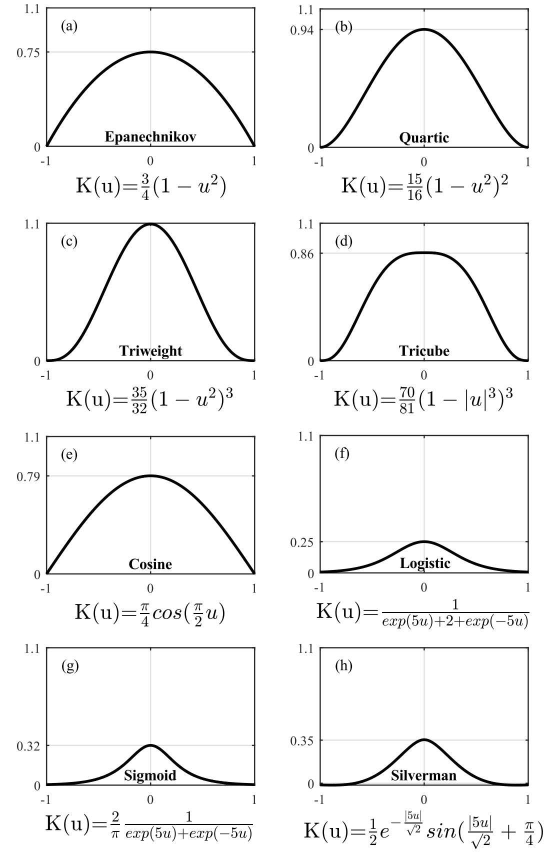

Figure 7- 1. Suggested kernels for candidate filters

2. Many disadvantages of the SG filter, as well as its advantages, are rooted in the negative values of its kernel. As a result, it is speculated that maintaining these negative values but fracturing their intensity and spreading them across the filtration should improve SG performance. This can be achieved by fitting higher-order polynomials in the filtration window, instead of parabolic shapes which was used here. Early results on the data reported by Geocubes on the Ten-mile landslide confirmed it but a comprehensive investigation using the numerical analysis of synthetic database is necessary. Figure 7- 2 displays the kernel of SG with the polynomial degrees from 2 to 8 with increments of 2.

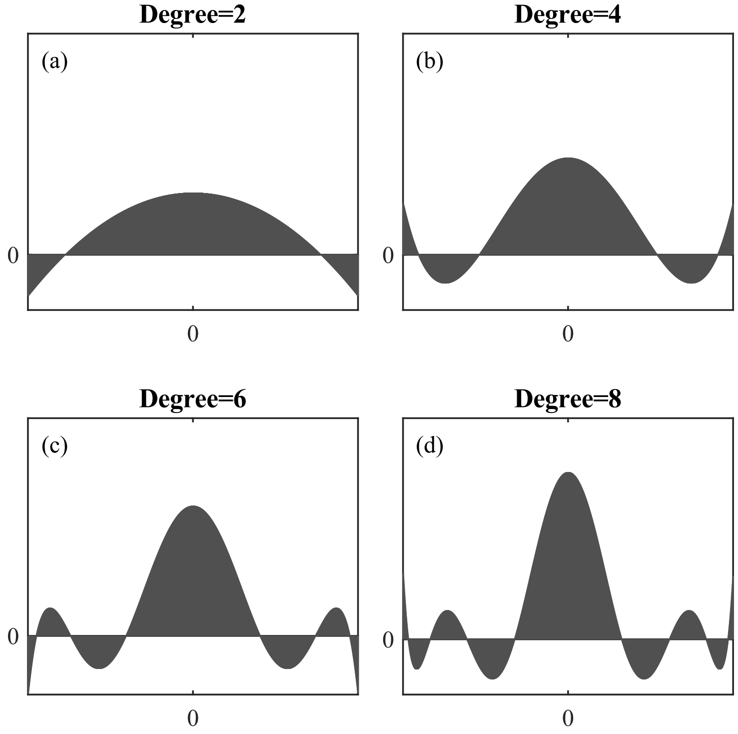

Figure 7- 2. Kernel of SG at degrees of (a) 2, (b) 4, (c) 6 and (d) 8

3. Multi-passing is applying a filter over and over on an already filtered dataset. If p is the bandwidth of the filter, after n passes, the equivalent bandwidth is $p'=n(p-1)+1$. It is known that the time complexity of a filter, denoted by $\mathcal{O}()$, with the bandwidth of h, is $\mathcal{O}(h^2)$. Therefore, the time complexity of a filter with the bandwidth of p' is Eq. 7. 2:

$$\mathcal{O}(p'^2)=\mathcal{O}((\mathrm{n}(p\text{-}1)+1)^2)=\mathcal{O}(\mathrm{n}^2(p\text{-}1)^2+2\mathrm{n}(p\text{-}1)+1), \qquad (7.2)$$

where it is a larger value than $n\mathcal{O}(p^2)$. As a result, multi-passing results in reducing the time complexity and the computation demand by using a filter with lower bandwidth. Its advantage will be consequently a timelier and more efficient performance of a monitoring system. Mathematically, multi-passing an SMA filter provides results similar to GWMA since the self-convolution of a constant kernel goes toward a normal distribution. It is beneficial, in future studies, to find an optimized value of the number of passes. In the context of real-time monitoring with an asymmetric window, multi-passing only leads to a large lag and finding a solution to either eliminate or minimize the lag would satisfy the goal.

7.2.2. InSAR element

1. Based on the theoretical calculations, the portion of the northward component that is translated into an error, due to the simplifying assumption, along the vertical axis is now known (α –Table 5- 2 & Table 5- 3). Two different α values could be obtained by analysing a SAR stack obtained at different incidence angles from a redundant orbital geometry (i.e., ascending or descending). The relationship between true, denoted by capital subscripts, and erroneous components, denoted by small subscripts, are as follows:

$$\mathrm{V}_{\mathrm{v}_1}\text{-}\mathrm{V}_{\mathrm{V}}=\alpha_1\mathrm{V}_{\mathrm{N}}, \qquad (7.3)$$

$$\mathrm{V}_{\mathrm{v}_2}\text{-}\mathrm{V}_{\mathrm{V}}=\alpha_2\mathrm{V}_{\mathrm{N}}, \qquad (7.4)$$

By rearranging terms in Eqs. 7. 3 and 7. 4 to have V_V on the same side and equating them, the northward component can be computed:

$$V_N=\frac{V_{v_2}-V_{v_1}}{\alpha_2-\alpha_1}. \tag{7. 5}$$

The same process can be repeated by looking into the errors induced along eastward. These two back-calculated northward components are probably different due to the LOS variance and other errors produced by the post-processing stages. Studies on other sites where the direction of velocities are known by *in situ* measurements would be useful to establish what ratio of vertical component, contributes to the calculation of the true northward component.

2. In Chapter 6, only descending Radarsat-2 scenes are studied. Utilizing ascending Radarsat-2 scenes in the same framework would help with identifying how much SPFM-LSM is truly advantageous. Additionally, coupling the least-squares method with APFM and STFM will provide insights if their drawbacks can be mitigated this way. These analyses could be initial steps to define geometrical cut-offs for STFM as well.

3. Aspect characteristic surface, detailed in Chapter 6, is potentially a measure for understanding a more accurate aspect angle of movement when using SPFM. Although the investigation on the Ripley landslide showed promising results, future studies on other sites where more positioning units exist could provide more validation. Moreover, evaluations of topography-informed assumptions in other movement mechanisms such as rotational landslides or areas at the risk of rockfalls would cast light on the performance of each method in different settings.

4. Similar to the methodology adopted to develop the aspect characteristic surface, calculations can result in Eq. 7. 6 which describes the erroneous travel angle (η_e) as a function of aspect angle:

$$\tan \eta_e = \frac{1+a}{b+c\sin\beta + d\cos\beta}, \tag{7. 6}$$

where $a = \mathrm{d}V_V / V_V$, $b = 1/\tan\eta$, $c = \mathrm{d}V_E / V_V$, $d = \mathrm{d}V_N / V_V$, η is the true travel angle and dV_V, dV_E and dV_N indicates the error in the vertical, eastward and northward components of velocity. Constants *a*, *b*, *c* and *d* are to be interpreted from regression analysis over a group of scatterers believed to travel identically. Eq. 7. 6, which can be correspondingly called travel characteristic surface, is a possible technique to minimize the error in travel angle observed in APFM. Further studies are required to confirm if this could be applied in practice.

References

Ajvazi, B., & Czimber, K. (2019). A COMPARATIVE ANALYSIS OF DIFFERENT DEM INTERPOLATION METHODS IN GIS: CASE STUDY OF RAHOVEC, KOSOVO. *Geodesy and Cartography*, *45*(5), 43–48. https://doi.org/10.3846/gac.2019.7921

Ao, M., Zhang, L., Shi, X., Liao, M., & Dong, J. (2019). Measurement of the three-dimensional surface deformation of the Jiaju landslide using a surface-parallel flow model. *Remote Sensing Letters*, *10*(8), 776–785. https://doi.org/10.1080/2150704X.2019.1608601

Atzeni, C., Barla, M., Pieraccini, M., & Antolini, F. (2015). Early Warning Monitoring of Natural and Engineered Slopes with Ground-Based Synthetic-Aperture Radar. *Rock Mechanics and Rock Engineering*, *48*(1), 235–246. https://doi.org/10.1007/s00603-014-0554-4

Azadnejad, S., Maghsoudi, Y., & Perissin, D. (2019). Investigating the effect of the physical scattering mechanism of the dual-polarization sentinel-1 data on the temporal coherence optimization results. *International Journal of Remote Sensing*, *40*(18), 7033–7047. https://doi.org/10.1080/01431161.2019.1597309

Bally, A. W., Gordy, P. L., & Steward, G. A. (1966). Structure, seismic data, and orogenic evolution of southern Canadian Rocky Mountains. *Bulletin of Canadian Petroleum Geology*, *14*(3), 337–381.

Bar, N., Arrieta, M., Espino, A., Diaz, C., Mosquea, L. A., Mojica, B., McQuillan, A., Baldeon, G., & Falorni, G. (2022). Back-analysis of ductile slope failure mechanisms and validation with aerial photogrammetry, InSAR and GbRAR to proactively manage economic risks to protect the mine plan. In R. E. Hammah, T. E. Yacoub, A. McQuillan, & J. Curran (Eds.), *The Evolution of Geotech – 25 Year* (pp. 512–526). CRC Press.

Bechor, N. B. D., & Zebker, H. A. (2006). Measuring two-dimensional movements using a single InSAR pair. *Geophysical Research Letters*, *33*(16), L16311. https://doi.org/10.1029/2006GL026883

Bekaert, D. P. S., Handwerger, A. L., Agram, P., & Kirschbaum, D. B. (2020). InSAR-based detection method for mapping and monitoring slow-moving landslides in remote regions with steep and mountainous terrain: An application to Nepal. *Remote Sensing of Environment*, *249*, 111983. https://doi.org/10.1016/j.rse.2020.111983

Benoit, L., Briole, P., Martin, O., & Thom, C. (2014). Real-time deformation monitoring by a wireless network of low-cost GPS. *Journal of Applied Geodesy*, *8*(2). https://doi.org/10.1515/jag-2013-0023

Benoit, L., Briole, P., Martin, O., Thom, C., Malet, J.-P., & Ulrich, P. (2015). Monitoring landslide displacements with the Geocube wireless network of low-cost GPS. *Engineering Geology*, *195*, 111–121. https://doi.org/10.1016/j.enggeo.2015.05.020

Bentivenga, M., Bellanova, J., Calamita, G., Capece, A., Cavalcante, F., Gueguen, E., Guglielmi, P., Murgante, B., Palladino, G., Perrone, A., Saganeiti, L., & Piscitelli, S. (2021). Geomorphological and geophysical surveys with InSAR analysis applied to the Picerno earth flow (southern Apennines, Italy). *Landslides*, *18*(1), 471–483. https://doi.org/10.1007/s10346-020-01499-z

Berardino, P., Fornaro, G., Lanari, R., & Sansosti, E. (2002). A new algorithm for surface deformation monitoring based on small baseline differential SAR interferograms. *IEEE*

Transactions on Geoscience and Remote Sensing, *40*(11), 2375–2383. https://doi.org/10.1109/TGRS.2002.803792

BGC Engineering Inc. (2015). *CN Lillooet Sub. M. 167.7 (Fountain Slide) September 2015 Drilling and Instrumentation. Project report to Canadian National Railway*.

BGC Engineering Inc. (2016). *CN Lillooet Sub. M. 167.7 (Ten Mile Slide) April 2016 Drilling and Instrumentation. Project report to Canadian National Railway*.

Biagini, L., Macciotta, R., Gräpel, C., Tappenden, K., & Skirrow, R. (2022). Characteristics, Kinematics and Contributing Factors of Compound and Translational Landslides in the Interior Plains of Canada. *Geosciences*, *12*(8), 289. https://doi.org/10.3390/geosciences12080289

Bianchini, S., Herrera, G., Mateos, R., Notti, D., Garcia, I., Mora, O., & Moretti, S. (2013). Landslide Activity Maps Generation by Means of Persistent Scatterer Interferometry. *Remote Sensing*, *5*(12), 6198–6222. https://doi.org/10.3390/rs5126198

Bishop, N., Evans, S., Petley, D., & Unger, A. (2008). *The geotechnics of glaciolacustrine sediments and associated landslides near Ashcroft (British Columbia) and the Grand Coulee Dam (Washington)*. The 4th GeoHazards Canadian Geotechnical Society Conference.

Blais-Stevens, A., & Hungr, O. (2008). Landslide Hazards and their mitigation along the sea to sky corridor, British Columbia. *4th Canadian Conference on Geohazards*. IV GeoHazards.

Bobrowsky, P., Huntley, D., Neelands, P., MacLeod, R., Mariampillai, D., Hendry, M., Macciotta, R., Reeves, H., & Chambers, J. (2017). *Ripley Landslide—Canada's premier landslide* *field laboratory*. Abstracts and Proceedings of Geological Society of America Annual Meeting.

Bobrowsky, P. T., & Dominguez, M. J. (2012). *Landslide susceptibility map of Canada* (7228; p. 7228). https://doi.org/10.4095/291902

Bovis, M. J. (1985). Earthflows in the Interior Plateau, southwest British Columbia. *Canadian Geotechnical Journal*, *22*(3), 313–334. https://doi.org/10.1139/t85-045

Boyd, J. M., Hinds, D. V., Moy, D., & Rogers, C. (1973). Two simple devices for monitoring movements in rock slopes. *Quarterly Journal of Engineering Geology*, *6*(3–4), 295–302. https://doi.org/10.1144/GSL.QJEG.1973.006.03.12

Bozzano, F., Mazzanti, P., & Moretto, S. (2018). Discussion to: 'Guidelines on the use of inverse velocity method as a tool for setting alarm thresholds and forecasting landslides and structure collapses' by T. Carlà, E. Intrieri, F. Di Traglia, T. Nolesini, G. Gigli and N. Casagli. *Landslides*, *15*(7), 1437–1441. https://doi.org/10.1007/s10346-018-0976-2

Carlà, T., Farina, P., Intrieri, E., Botsialas, K., & Casagli, N. (2017). On the monitoring and early-warning of brittle slope failures in hard rock masses: Examples from an open-pit mine. *Engineering Geology*, *228*, 71–81. https://doi.org/10.1016/j.enggeo.2017.08.007

Carlà, T., Intrieri, E., Di Traglia, F., Nolesini, T., Gigli, G., & Casagli, N. (2017). Guidelines on the use of inverse velocity method as a tool for setting alarm thresholds and forecasting landslides and structure collapses. *Landslides*, *14*(2), 517–534. https://doi.org/10.1007/s10346-016-0731-5

Carlà, T., Intrieri, E., Raspini, F., Bardi, F., Farina, P., Ferretti, A., Colombo, D., Novali, F., & Casagli, N. (2019). Perspectives on the prediction of catastrophic slope failures from satellite InSAR. *Scientific Reports*, *9*(1), 14137. https://doi.org/10.1038/s41598-019-50792-y

Carlà, T., Macciotta, R., Hendry, M., Martin, D., Edwards, T., Evans, T., Farina, P., Intrieri, E., & Casagli, N. (2018). Displacement of a landslide retaining wall and application of an enhanced failure forecasting approach. *Landslides*, *15*(3), 489–505. https://doi.org/10.1007/s10346-017-0887-7

Carri, A., Valletta, A., Cavalca, E., Savi, R., & Segalini, A. (2021). Advantages of IoT-Based Geotechnical Monitoring Systems Integrating Automatic Procedures for Data Acquisition and Elaboration. *Sensors*, *21*(6), 2249. https://doi.org/10.3390/s21062249

Casagli, N., Frodella, W., Morelli, S., Tofani, V., Ciampalini, A., Intrieri, E., Raspini, F., Rossi, G., Tanteri, L., & Lu, P. (2017). Spaceborne, UAV and ground-based remote sensing techniques for landslide mapping, monitoring and early warning. *Geoenvironmental Disasters*, *4*(1), 9. https://doi.org/10.1186/s40677-017-0073-1

Cenni, N., Fiaschi, S., & Fabris, M. (2021). Integrated use of archival aerial photogrammetry, GNSS, and InSAR data for the monitoring of the Patigno landslide (Northern Apennines, Italy). *Landslides*, *18*(6), 2247–2263. https://doi.org/10.1007/s10346-021-01635-3

Chae, B.-G., Park, H.-J., Catani, F., Simoni, A., & Berti, M. (2017). Landslide prediction, monitoring and early warning: A concise review of state-of-the-art. *Geosciences Journal*, *21*(6), 1033–1070. https://doi.org/10.1007/s12303-017-0034-4

Chang, C., & Wang, G. (2022). Creep of clayey soil induced by elevated pore-water pressure: Implication for forecasting the time of failure of rainfall-triggered landslides. *Engineering Geology*, *296*, 106461. https://doi.org/10.1016/j.enggeo.2021.106461

Chen, H., Zhao, C., Sun, R., Chen, L., Wang, B., & Li, B. (2022). Two-dimensional deformation monitoring of karst landslides in Zongling, China, with multi-platform distributed scatterer InSAR technique. *Landslides*, *19*(7), 1767–1777. https://doi.org/10.1007/s10346-022-01860-4

Chen, M., & Jiang, Q. (2020). An early warning system integrating time-of-failure analysis and alert procedure for slope failures. *Engineering Geology*, *272*, 105629. https://doi.org/10.1016/j.enggeo.2020.105629

Clague, J. J., & Bobrowsky, P. T. (2010). *Natural Hazards in Canada*. *37*(1), 17–37.

Clague, J. J., & Evans, S. G. (2003). Geologic Framework of Large Historic Landslides in Thompson River Valley, British Columbia. *Environmental and Engineering Geoscience*, *9*(3), 201–212. https://doi.org/10.2113/9.3.201

Clayton, C., Barnett, R., & Slater, M. (2020). Case study: Back-analysis of a historical open pit highwall failure at a coal mine in Canada. *Proceedings of the 2020 International Symposium on Slope Stability in Open Pit Mining and Civil Engineering*, 873–888. https://doi.org/10.36487/ACG_repo/2025_57

Cleveland, W. S. (1979). Robust Locally Weighted Regression and Smoothing Scatterplots. *Journal of the American Statistical Association*, *74*(368), 829–836. https://doi.org/10.1080/01621459.1979.10481038

Cleveland, W. S. (1981). LOWESS: A Program for Smoothing Scatterplots by Robust Locally Weighted Regression. *The American Statistician*, *35*(1), 54. https://doi.org/10.2307/2683591

Cleveland, W. S., & Devlin, S. J. (1988). Locally Weighted Regression: An Approach to Regression Analysis by Local Fitting. *Journal of the American Statistical Association*, *83*(403), 596–610. https://doi.org/10.1080/01621459.1988.10478639

Clifford, P. (1994). Monte Carlo methods. In John L. Stanford & Stephen B. Vardeman (Eds.), *Statistical methods for Physical Science*. Academic Press.

Coggan, J. S., & Pine, R. J. (1996). Application of distinct-element modelling to assess slope stability at Delabole slate quarry, Cornwall, England. *TRANSACTIONS OF THE INSTITUTION OF MINING AND METALLURGY SECTION A-MINING TECHNOLOGY*, *105*, A22–A30.

Cotton, W. R. (1972). *Preliminary geologic map of the Franciscan rocks in the central part of the Diablo Range, Santa Clara and Alameda Counties, California*. https://doi.org/10.3133/mf343

Davachi, M. M., Baggott, B. L., McKeown, J. D., & Peters, J. E. (1989). *The Design and Construction of the Oldman River Dam and Dyke*. The 30th CANCOLD Annual General Meeting.

Davachi, M. M., Sinclair, B. J., Hartmaier, H. H., Baggott, B. L., & Peters, J. E. (1991). Determination of the Oldman River Dam foundation shear strength. *Canadian Geotechnical Journal*, *28*(5), 698–707. https://doi.org/10.1139/t91-084

Davies, L., & Gather, U. (1993). The Identification of Multiple Outliers. *Journal of the American Statistical Association*, *88*(423), 782–792. https://doi.org/10.1080/01621459.1993.10476339

Deane, E. (2020). *The Application of Emerging Monitoring Technologies on Very Slow Vegetated Landslides*. University of Alberta.

Deane, E., Macciotta, R., Hendry, M. T., Gräpel, C., & Skirrow, R. (2020). Leveraging historical aerial photographs and digital photogrammetry techniques for landslide investigation—A practical perspective. *Landslides*, *17*(8), 1989–1996. https://doi.org/10.1007/s10346-020-01437-z

Deng, L., Smith, A., Dixon, N., & Yuan, H. (2021). Machine learning prediction of landslide deformation behaviour using acoustic emission and rainfall measurements. *Engineering Geology*, *293*, 106315. https://doi.org/10.1016/j.enggeo.2021.106315

Desmet, P. J. J. (1997). *Effects of interpolation errors on the analysis of DEMs*. *6*, 563–580.

Desrues, M., Malet, J.-P., Brenguier, O., Carrier, A., Mathy, A., & Lorier, L. (2022). Landslide kinematics inferred from in situ measurements: The Cliets rock-slide (Savoie, French Alps). *Landslides*, *19*(1), 19–34. https://doi.org/10.1007/s10346-021-01726-1

Di Traglia, F., De Luca, C., Manzo, M., Nolesini, T., Casagli, N., Lanari, R., & Casu, F. (2021). Joint exploitation of space-borne and ground-based multitemporal InSAR measurements for volcano monitoring: The Stromboli volcano case study. *Remote Sensing of Environment*, *260*, 112441. https://doi.org/10.1016/j.rse.2021.112441

Dick, G. J., Eberhardt, E., Cabrejo-Liévano, A. G., Stead, D., & Rose, N. D. (2015). Development of an early-warning time-of-failure analysis methodology for open-pit mine slopes utilizing ground-based slope stability radar monitoring data. *Canadian Geotechnical Journal*, *52*(4), 515–529. https://doi.org/10.1139/cgj-2014-0028

Doberstein, D. (2012). *Fundamentals of gps receivers: A hardware approach*. Springer Science+Business Media, LLC.

Donati, D., Stead, D., Lato, M., & Gaib, S. (2020). Spatio-temporal characterization of slope damage: Insights from the Ten Mile Slide, British Columbia, Canada. *Landslides*, *17*(5), 1037–1049. https://doi.org/10.1007/s10346-020-01352-3

Duhamel, P., & Vetterli, M. (1990). Fast fourier transforms: A tutorial review and a state of the art. *Signal Processing*, *19*(4), 259–299. https://doi.org/10.1016/0165-1684(90)90158-U

Eriksen, H. Ø., Lauknes, T. R., Larsen, Y., Corner, G. D., Bergh, S. G., Dehls, J., & Kierulf, H. P. (2017). Visualizing and interpreting surface displacement patterns on unstable slopes using multi-geometry satellite SAR interferometry (2D InSAR). *Remote Sensing of Environment*, *191*, 297–312. https://doi.org/10.1016/j.rse.2016.12.024

Eshraghian, A., Martin, C. D., & Cruden, D. M. (2005). Landslides in the Thompson River valley between Ashcroft and Spences Bridge, British Columbia. In Hungr et al. (Ed.), *Landslide Risk Management* (pp. 437–446). CRC Press.

Eshraghian, A., Martin, C. D., & Cruden, D. M. (2007). Complex Earth Slides in the Thompson River Valley, Ashcroft, British Columbia. *Environmental and Engineering Geoscience*, *13*(2), 161–181. https://doi.org/10.2113/gseegeosci.13.2.161

Eshraghian, A., Martin, C. D., & Morgenstern, N. R. (2008a). Hazard analysis of an active slide in the Thompson River Valley, Ashcroft, British Columbia, Canada. *Canadian Geotechnical Journal*, *45*(3), 297–313. https://doi.org/10.1139/T07-085

Eshraghian, A., Martin, C. D., & Morgenstern, N. R. (2008b). Movement triggers and mechanisms of two earth slides in the Thompson River Valley, British Columbia, Canada. *Canadian Geotechnical Journal*, *45*(9), 1189–1209. https://doi.org/10.1139/T08-047

Fan, H., Wang, L., Wen, B., & Du, S. (2021). A New Model for three-dimensional Deformation Extraction with Single-track InSAR Based on Mining Subsidence Characteristics. *International Journal of Applied Earth Observation and Geoinformation*, *94*, 102223. https://doi.org/10.1016/j.jag.2020.102223

Ferretti, A. (2014). *Satellite InSAR Data: Reservoir Monotoring from Space*. EAGE.

Ferretti, A., Fumagalli, A., Novali, F., Prati, C., Rocca, F., & Rucci, A. (2011). A New Algorithm for Processing Interferometric Data-Stacks: SqueeSAR. *IEEE Transactions on Geoscience and Remote Sensing*, *49*(9), 3460–3470. https://doi.org/10.1109/TGRS.2011.2124465

Ferretti, A., Prati, C., & Rocca, F. (2001). Permanent scatterers in SAR interferometry. *IEEE Transactions on Geoscience and Remote Sensing*, *39*(1), 8–20. https://doi.org/10.1109/36.898661

Fuhrmann, T., & Garthwaite, M. C. (2019). Resolving Three-Dimensional Surface Motion with InSAR: Constraints from Multi-Geometry Data Fusion. *Remote Sensing*, *11*(3), 241. https://doi.org/10.3390/rs11030241

Fukuzono, T. (1985a). A Method to Predict the Time of Slope Failure Caused by Rainfall Using the Inverse Number of Velocity of Surface Displacement. *Landslides*, *22*(2), 8-13_1. https://doi.org/10.3313/jls1964.22.2_8

Fukuzono, T. (1985b). *A new method for predicting the failure time of a slope failure*. 145–150.

Fukuzono, T. (1990). Recent studies on time prediction of slope failure. *Landslide News*, *4*, 9–12.

Gaib, S., Wilson, B., & Lapointe, E. (2012). Design, construction and monitoring of a test section for the stabilization of an active slide area utilizing soil mixed shear keys installed using cutter soil mixing. *ISSMGE - TC 211*, *3*, 147–158.

Ghazifard, A., Moslehi, A., Safaei, H., & Roostaei, M. (2016). Effects of groundwater withdrawal on land subsidence in Kashan Plain, Iran. *Bulletin of Engineering Geology and the Environment*, *75*(3), 1157–1168. https://doi.org/10.1007/s10064-016-0885-3

Gigli, G., Fanti, R., Canuti, P., & Casagli, N. (2011). Integration of advanced monitoring and numerical modeling techniques for the complete risk scenario analysis of rockslides: The case of Mt. Beni (Florence, Italy). *Engineering Geology*, *120*(1–4), 48–59. https://doi.org/10.1016/j.enggeo.2011.03.017

Glover, T., Craddock, T., & Harder, L. Jr. (1997). *Castaic Dam left abutment stability evaluation*. 105–126.

González, F. (2022). InSAR-based mapping of ground deformation caused by industrial waste disposals: The case study of the Huelva phosphogypsum stack, SW Spain. *Bulletin of Engineering Geology and the Environment*, *81*(8), 304. https://doi.org/10.1007/s10064-022-02809-6

Goorabi, A., Karimi, M., Yamani, M., & Perissin, D. (2020). Land subsidence in Isfahan metropolitan and its relationship with geological and geomorphological settings revealed by Sentinel-1A InSAR observations. *Journal of Arid Environments*, *181*, 104238. https://doi.org/10.1016/j.jaridenv.2020.104238

Government of Canada. (2022). *Historical Hydrometric Data of Station 05AA032* [dataset]. https://wateroffice.ec.gc.ca/mainmenu/historical_data_index_e.html

Grebby, S., Sowter, A., Gluyas, J., Toll, D., Gee, D., Athab, A., & Girindran, R. (2021). Advanced analysis of satellite data reveals ground deformation precursors to the Brumadinho Tailings Dam collapse. *Communications Earth & Environment*, *2*(1), 2. https://doi.org/10.1038/s43247-020-00079-2

Guo, G., Wang H., Bell, D., Bi, Y., & Greer, K. (2003). KNN model-based approach in classification. In OTM Confederated International Conferences. *On the Move to Meaningful Internet Systems*, 986–996.

Guthrie, R. (2013). *Socio-economic significance, Canadian technical guidelines and best practices related to landslides: A national initiative for loss reduction* (7311; p. 7311). https://doi.org/10.4095/292241

Hall, C. A. Jr. (1978). *Geologic map of Twitchell Dam and parts of Santa Maria and Tepusquet Canyon quadrangles, Santa Barbara County, California*. https://doi.org/10.3133/mf933

Hampel, F. R. (1971). A General Qualitative Definition of Robustness. *The Annals of Mathematical Statistics*, *42*(6), 1887–1896. https://doi.org/10.1214/aoms/1177693054

Han, Q., Sassa, K., & Mikoš, M. (2021). International Programme on Landslides (IPL): A Programme of the ICL for Landslide Disaster Risk Reduction. In K. Sassa, M. Mikoš, S. Sassa, P. T. Bobrowsky, K. Takara, & K. Dang (Eds.), *Understanding and Reducing Landslide Disaster Risk* (pp. 187–203). Springer International Publishing. https://doi.org/10.1007/978-3-030-60196-6_11

Hanegan, G. L. (1973). *Geology, seismicity, and environmental impact* (D. E. Moran, J. E. Slosson, R. O. Stone, & C. A. Yelverton, Eds.; pp. 201–211). Association of Engineering Geologists Special Publication.

Hao, S., Yang, H., & Elsworth, D. (2017). An accelerating precursor to predict "time-to-failure" in creep and volcanic eruptions. *Journal of Volcanology and Geothermal Research*, *343*, 252–262. https://doi.org/10.1016/j.jvolgeores.2017.07.009

Harris, F. J. (1978). On the use of windows for harmonic analysis with the discrete Fourier transform. *Proceedings of the IEEE*, *66*(1), 51–83. https://doi.org/10.1109/PROC.1978.10837

Helmstetter, A., Sornette, D., Grasso, J.-R., Andersen, J. V., Gluzman, S., & Pisarenko, V. (2004). Slider block friction model for landslides: Application to Vaiont and La Clapière landslides: SLIDER BLOCK MODEL FOR LANDSLIDES. *Journal of Geophysical Research: Solid Earth*, *109*(B2). https://doi.org/10.1029/2002JB002160

Hendry, M. T., Chalcroft, D., Zaidi, H., & Iqbal, M. J. (2019). *Instrumentation data review and long-term trends of displacement at the Oldman River Dam: A case study*. 1–15.

Hendry, M. T., Macciotta, R., Martin, C. D., & Reich, B. (2015). Effect of Thompson River elevation on velocity and instability of Ripley Slide. *Canadian Geotechnical Journal*, *52*(3), 257–267. https://doi.org/10.1139/cgj-2013-0364

Henry, M. (2022). An ultra-precise fast fourier transform. *Science Talks*, *4*, 100097. https://doi.org/10.1016/j.sctalk.2022.100097

Her, Y., Heatwole, C. D., & Kang, M. S. (2015). Interpolating SRTM Elevation Data to Higher Resolution to Improve Hydrologic Analysis. *JAWRA Journal of the American Water Resources Association*, *51*(4), 1072–1087. https://doi.org/10.1111/jawr.12287

Herrera, G., Fernández-Merodo, J. A., Mulas, J., Pastor, M., Luzi, G., & Monserrat, O. (2009). A landslide forecasting model using ground based SAR data: The Portalet case study. *Engineering Geology*, *105*(3–4), 220–230. https://doi.org/10.1016/j.enggeo.2009.02.009

Herrera, G., Gutiérrez, F., García-Davalillo, J. C., Guerrero, J., Notti, D., Galve, J. P., Fernández-Merodo, J. A., & Cooksley, G. (2013). Multi-sensor advanced DInSAR monitoring of very slow landslides: The Tena Valley case study (Central Spanish Pyrenees). *Remote Sensing of Environment*, *128*, 31–43. https://doi.org/10.1016/j.rse.2012.09.020

Hongtao, N. (2020). Smart safety early warning model of landslide geological hazard based on BP neural network. *Safety Science*, *123*, 104572. https://doi.org/10.1016/j.ssci.2019.104572

Houston, M. (2001). *Proposed Dunvegan Hydroelectric Project*. Canadian Dam Association.

Hu, J., Li, Z. W., Ding, X. L., Zhu, J. J., Zhang, L., & Sun, Q. (2014). Resolving three-dimensional surface displacements from InSAR measurements: A review. *Earth-Science Reviews*, *133*, 1–17. https://doi.org/10.1016/j.earscirev.2014.02.005

Hu, J., Motagh, M., Guo, J., Haghighi, M. H., Li, T., Qin, F., & Wu, W. (2022). Inferring subsidence characteristics in Wuhan (China) through multitemporal InSAR and hydrogeological analysis. *Engineering Geology*, *297*, 106530. https://doi.org/10.1016/j.enggeo.2022.106530

Hu, X., Wang, T., Pierson, T. C., Lu, Z., Kim, J., & Cecere, T. H. (2016). Detecting seasonal landslide movement within the Cascade landslide complex (Washington) using time-series SAR imagery. *Remote Sensing of Environment*, *187*, 49–61. https://doi.org/10.1016/j.rse.2016.10.006

Hu, X., Wu, S., Zhang, G., Zheng, W., Liu, C., He, C., Liu, Z., Guo, X., & Zhang, H. (2021). Landslide displacement prediction using kinematics-based random forests method: A case study in Jinping Reservoir Area, China. *Engineering Geology*, *283*, 105975. https://doi.org/10.1016/j.enggeo.2020.105975

Hungr, O., Evans, S. G., & Hazzard, J. (1999). Magnitude and frequency of rock falls and rock slides along the main transportation corridors of southwestern British Columbia. *Canadian Geotechnical Journal*, *36*(2), 224–238. https://doi.org/10.1139/t98-106

Huntley, D., Bobrowsky, P., Charbonneau, F., Journault, J., Macciotta, R., & Hendry, M. (2017). Innovative Landslide Change Detection Monitoring: Application of Space-Borne InSAR Techniques in the Thompson River Valley, British Columbia, Canada. In M. Mikoš, Ž. Arbanas, Y. Yin, & K. Sassa (Eds.), *Advancing Culture of Living with Landslides* (pp. 219–229). Springer International Publishing. https://doi.org/10.1007/978-3-319-53487-9_25

Huntley, D., Rotheram-Clarke, D., Pon, A., Tomaszewicz, A., Leighton, J., Cocking, R., & Joseph, J. (2021). Benchmarked RADARSAT-2, SENTINEL-1 and RADARSAT Constellation

Mission Change-Detection Monitoring at North Slide, Thompson River Valley, British Columbia: Ensuring a Landslide-Resilient National Railway Network. *Canadian Journal of Remote Sensing*, *47*(4), 635–656. https://doi.org/10.1080/07038992.2021.1937968

Husaini, O., & Ratnasamy, M. (2001). An early warning system for active landslides. *Quarterly Journal of Engineering Geology and Hydrogeology*, *34*(3), 299–305. https://doi.org/10.1144/qjegh.34.3.299

International Strategy for Disaster Reduction. (2009). *UNISDR Terminology on Diasaster Risk Reduction*. United Nations. http://www.unisdr.org

Intrieri, E., Bardi, F., Fanti, R., Gigli, G., Fidolini, F., Casagli, N., Costanzo, S., Raffo, A., Di Massa, G., Capparelli, G., & Versace, P. (2017). Big data managing in a landslide early warning system: Experience from a ground-based interferometric radar application. *Natural Hazards and Earth System Sciences*, *17*(10), 1713–1723. https://doi.org/10.5194/nhess-17-1713-2017

Intrieri, E., Carlà, T., & Gigli, G. (2019). Forecasting the time of failure of landslides at slope-scale: A literature review. *Earth-Science Reviews*, *193*, 333–349. https://doi.org/10.1016/j.earscirev.2019.03.019

Intrieri, E., & Gigli, G. (2016). Landslide forecasting and factors influencing predictability. *Natural Hazards and Earth System Sciences*, *16*(12), 2501–2510. https://doi.org/10.5194/nhess-16-2501-2016

Intrieri, E., Gigli, G., Mugnai, F., Fanti, R., & Casagli, N. (2012). Design and implementation of a landslide early warning system. *Engineering Geology*, *147–148*, 124–136. https://doi.org/10.1016/j.enggeo.2012.07.017

Intrieri, E., Raspini, F., Fumagalli, A., Lu, P., Del Conte, S., Farina, P., Allievi, J., Ferretti, A., & Casagli, N. (2018). The Maoxian landslide as seen from space: Detecting precursors of failure with Sentinel-1 data. *Landslides*, *15*(1), 123–133. https://doi.org/10.1007/s10346-017-0915-7

Jackson, L. E. (2002). Landslides and landscape evolution in the Rocky Mountains and adjacent Foothills area, southwestern Alberta, Canada. In *Reviews in Engineering Geology* (Vol. 15, pp. 325–344). Geological Society of America. https://doi.org/10.1130/REG15-p325

Jaspar, J. L., & Peters, N. (1979). Foundation performance of Gardiner Dam. *Canadian Geotechnical Journal*, *16*(4), 758–788. https://doi.org/10.1139/t79-083

Jia, H., Wang, Y., Ge, D., Deng, Y., & Wang, R. (2022). InSAR Study of Landslides: Early Detection, Three-Dimensional, and Long-Term Surface Displacement Estimation—A Case of Xiaojiang River Basin, China. *Remote Sensing*, *14*(7), 1759. https://doi.org/10.3390/rs14071759

Jo, M.-J., Jung, H.-S., & Won, J.-S. (2017). Measurement of precise three-dimensional volcanic deformations via TerraSAR-X synthetic aperture radar interferometry. *Remote Sensing of Environment*, *192*, 228–237. https://doi.org/10.1016/j.rse.2017.02.022

Joughin, I. R., Kwok, R., & Fahnestock, M. A. (1998). Interferometric estimation of three-dimensional ice-flow using ascending and descending passes. *IEEE Transactions on Geoscience and Remote Sensing*, *36*(1), 25–37. https://doi.org/10.1109/36.655315

Journault, J., Macciotta, R., Hendry, M. T., Charbonneau, F., Huntley, D., & Bobrowsky, P. T. (2018). Measuring displacements of the Thompson River valley landslides, south of

Ashcroft, BC, Canada, using satellite InSAR. *Landslides*, *15*(4), 621–636. https://doi.org/10.1007/s10346-017-0900-1

Ju, N., Huang, J., He, C., Van Asch, T. W. J., Huang, R., Fan, X., Xu, Q., Xiao, Y., & Wang, J. (2020). Landslide early warning, case studies from Southwest China. *Engineering Geology*, *279*, 105917. https://doi.org/10.1016/j.enggeo.2020.105917

Kang, Y., Lu, Z., Zhao, C., Xu, Y., Kim, J., & Gallegos, A. J. (2021). InSAR monitoring of creeping landslides in mountainous regions: A case study in Eldorado National Forest, California. *Remote Sensing of Environment*, *258*, 112400. https://doi.org/10.1016/j.rse.2021.112400

Karl, J. H. (1989). *An introduction to digital signal processing*. Academic Press.

Kehtarnavaz, N. (2008). Frequency Domain Processing. In *Digital Signal Processing System Design* (pp. 175–196). Elsevier. https://doi.org/10.1016/B978-0-12-374490-6.00007-6

Kellndorfer, J., Cartus, O., Lavalle, M., Magnard, C., Milillo, P., Oveisgharan, S., Osmanoglu, B., Rosen, P. A., & Wegmüller, U. (2022). Global seasonal Sentinel-1 interferometric coherence and backscatter data set. *Scientific Data*, *9*(1), 73. https://doi.org/10.1038/s41597-022-01189-6

Khorrami, M., Abrishami, S., Maghsoudi, Y., Alizadeh, B., & Perissin, D. (2020). Extreme subsidence in a populated city (Mashhad) detected by PSInSAR considering groundwater withdrawal and geotechnical properties. *Scientific Reports*, *10*(1), 11357. https://doi.org/10.1038/s41598-020-67989-1

Khorrami, M., Alizadeh, B., Ghasemi Tousi, E., Shakerian, M., Maghsoudi, Y., & Rahgozar, P. (2019). How Groundwater Level Fluctuations and Geotechnical Properties Lead to Asymmetric Subsidence: A PSInSAR Analysis of Land Deformation over a Transit Corridor in the Los Angeles Metropolitan Area. *Remote Sensing*, *11*(4), 377. https://doi.org/10.3390/rs11040377

Khoshlahjeh Azar, M., Hamedpour, A., Maghsoudi, Y., & Perissin, D. (2021). Analysis of the Deformation Behavior and Sinkhole Risk in Kerdabad, Iran Using the PS-InSAR Method. *Remote Sensing*, *13*(14), 2696. https://doi.org/10.3390/rs13142696

Kintzer, F. C. (1980). *Geology and Landslides at Calaveras Reservoir, Alameda and Santa Clara Counties, California*. California State University.

Komac, M., Holley, R., Mahapatra, P., Van Der Marel, H., & Bavec, M. (2015). Coupling of GPS/GNSS and radar interferometric data for a 3D surface displacement monitoring of landslides. *Landslides*, *12*(2), 241–257. https://doi.org/10.1007/s10346-014-0482-0

Kothari, U. C., & Momayez, M. (2018). New approaches to monitoring, analyzing and predicting slope instabilities. *Journal of Geology and Mining Research*, *10*(1), 1–14. https://doi.org/10.5897/JGMR2017.0272

Lacasse, S., & Nadim, F. (2009). Landslide Risk Assessment and Mitigation Strategy. In K. Sassa & P. Canuti (Eds.), *Landslides – Disaster Risk Reduction* (pp. 31–61). Springer Berlin Heidelberg. https://doi.org/10.1007/978-3-540-69970-5_3

Lannacone, J. P., & Falorni, G. (2016). *Towards InSAR guidelines for landslide monitoring*. The 69th Conference of Canadian Geotechnical Society.

Leroueil, S. (2001). Natural slopes and cuts: Movement and failure mechanisms. *Géotechnique*, *51*(3), 197–243. https://doi.org/10.1680/geot.2001.51.3.197

Li, L. (2011). *Separablity of deformations and measurement noises of GPS time series with modified Kalman filter for landslide monitoring in real-time* [Rheinische Friedrich-Wilhelms-Universität Bonn]. https://nbn-resolving.org/urn:nbn:de:hbz:5N-26054

Li, M., Zhang, L., Ding, C., Li, W., Luo, H., Liao, M., & Xu, Q. (2020). Retrieval of historical surface displacements of the Baige landslide from time-series SAR observations for retrospective analysis of the collapse event. *Remote Sensing of Environment*, *240*, 111695. https://doi.org/10.1016/j.rse.2020.111695

Lian, C., Zeng, Z., Yao, W., & Tang, H. (2015). Multiple neural networks switched prediction for landslide displacement. *Engineering Geology*, *186*, 91–99. https://doi.org/10.1016/j.enggeo.2014.11.014

Liu, H., Shah, S., & Jiang, W. (2004). On-line outlier detection and data cleaning. *Computers & Chemical Engineering*, *28*(9), 1635–1647. https://doi.org/10.1016/j.compchemeng.2004.01.009

Liu, X., Wang, Y., Yan, S., Shao, Y., Zhou, H., & Li, Y. (2019). Ground subsidence characteristics associated with urbanization in East China analyzed with a Sentinel-1A-based InSAR time series approach. *Bulletin of Engineering Geology and the Environment*, *78*(6), 4003–4015. https://doi.org/10.1007/s10064-018-1383-6

Liu, X., Zhao, C., Zhang, Q., Yin, Y., Lu, Z., Samsonov, S., Yang, C., Wang, M., & Tomás, R. (2021). Three-dimensional and long-term landslide displacement estimation by fusing C-and L-band SAR observations: A case study in Gongjue County, Tibet, China. *Remote Sensing of Environment*, *267*, 112745. https://doi.org/10.1016/j.rse.2021.112745

Lucieer, A., Jong, S. M. D., & Turner, D. (2014). Mapping landslide displacements using Structure from Motion (SfM) and image correlation of multi-temporal UAV photography. *Progress in Physical Geography: Earth and Environment*, *38*(1), 97–116. https://doi.org/10.1177/0309133313515293

Luck, S. J. (2014). *Time and Frequency: A Closer Look at Filtering and Time-Frequency Analysis* (pp. 1–27).

Ma, P., Cui, Y., Wang, W., Lin, H., & Zhang, Y. (2021). Coupling InSAR and numerical modeling for characterizing landslide movements under complex loads in urbanized hillslopes. *Landslides*, *18*(5), 1611–1623. https://doi.org/10.1007/s10346-020-01604-2

Macciotta, R., Carlà, T., Hendry, M., Evans, T., Edwards, T., Farina, P., & Casagli, N. (2017). The 10-Mile Slide and Response of a Retaining Wall to Its Continuous Deformation. In M. Mikoš, Ž. Arbanas, Y. Yin, & K. Sassa (Eds.), *Advancing Culture of Living with Landslides* (pp. 553–562). Springer International Publishing. https://doi.org/10.1007/978-3-319-53487-9_65

Macciotta, R., Hendry, M., & Martin, C. D. (2016). Developing an early warning system for a very slow landslide based on displacement monitoring. *Natural Hazards*, *81*(2), 887–907. https://doi.org/10.1007/s11069-015-2110-2

Macciotta, R., Hendry, M., Martin, C. D., Elwood, D., Lan, H., Huntley, D., Bobrowsky, P., Sladen, W., Bunce, C., Choi, E., & Edwards, T. (2014). *Monitoring of the Ripley Landslide in the Thompson River Valley, BC*. The 6th Geohazards of Canadian Geotechnical Society.

Macciotta, R., & Hendry, M. T. (2021). Remote Sensing Applications for Landslide Monitoring and Investigation in Western Canada. *Remote Sensing*, *13*(3), 366. https://doi.org/10.3390/rs13030366

Macciotta, R., Rodriguez, J., Hendry, M., Martin, C. D., Edwards, T., & Evans, T. (2017). *The 10-mile Slide north of Lillooet, British Columbia–history, characteristics and monitoring*. The 3rd north American symposium on landslides.

Miao, F., Wu, Y., Xie, Y., & Li, Y. (2018). Prediction of landslide displacement with step-like behavior based on multialgorithm optimization and a support vector regression model. *Landslides*, *15*(3), 475–488. https://doi.org/10.1007/s10346-017-0883-y

Michoud, C., Bazin, S., Blikra, L. H., Derron, M.-H., & Jaboyedoff, M. (2013). Experiences from site-specific landslide early warning systems. *Natural Hazards and Earth System Sciences*, *13*(10), 2659–2673. https://doi.org/10.5194/nhess-13-2659-2013

Milczarek, W., Kopeć, A., Głąbicki, D., & Bugajska, N. (2021). Induced Seismic Events—Distribution of Ground Surface Displacements Based on InSAR Methods and Mogi and Yang Models. *Remote Sensing*, *13*(8), 1451. https://doi.org/10.3390/rs13081451

Mondini, A. C., Guzzetti, F., Chang, K.-T., Monserrat, O., Martha, T. R., & Manconi, A. (2021). Landslide failures detection and mapping using Synthetic Aperture Radar: Past, present and future. *Earth-Science Reviews*, *216*, 103574. https://doi.org/10.1016/j.earscirev.2021.103574

Morgenstern, N. R. (1989). *Recent experience with dam foundations on clay-shale in western Canada*. *4*, 2201–2208.

Morgenstern, N. R., & Simmons, J. V. (1982). *Analysis of the movements of Gardiner dam*. *4*, 1003–1027.

Motagh, M., Shamshiri, R., Haghshenas Haghighi, M., Wetzel, H.-U., Akbari, B., Nahavandchi, H., Roessner, S., & Arabi, S. (2017). Quantifying groundwater exploitation induced subsidence in the Rafsanjan plain, southeastern Iran, using InSAR time-series and in situ measurements. *Engineering Geology*, *218*, 134–151. https://doi.org/10.1016/j.enggeo.2017.01.011

Mufundirwa, A., Fujii, Y., & Kodama, J. (2010). A new practical method for prediction of geomechanical failure-time. *International Journal of Rock Mechanics and Mining Sciences*, *47*(7), 1079–1090. https://doi.org/10.1016/j.ijrmms.2010.07.001

Ng, A. H.-M., Ge, L., Zhang, K., & Li, X. (2012). Estimating horizontal and vertical movements due to underground mining using ALOS PALSAR. *Engineering Geology*, *143–144*, 18–27. https://doi.org/10.1016/j.enggeo.2012.06.003

Nilsen, T. H. (1972). *Preliminary photointerpretation map of landslide and other surficial deposits of the Mount Hamilton quadrangle and parts of the Mount Boardman and San Jose quadrangles, Alameda and Santa Clara Counties, California*. https://doi.org/10.3133/mf339

Pearson, R. K. (2002). Outliers in process modeling and identification. *IEEE Transactions on Control Systems Technology*, *10*(1), 55–63. https://doi.org/10.1109/87.974338

Pecoraro, G., & Calvello, M. (2021). Integrating local pore water pressure monitoring in territorial early warning systems for weather-induced landslides. *Landslides*, *18*(4), 1191–1207. https://doi.org/10.1007/s10346-020-01599-w

Perissin, D., & Wang, T. (2012). Repeat-Pass SAR Interferometry With Partially Coherent Targets. *IEEE Transactions on Geoscience and Remote Sensing*, *50*(1), 271–280. https://doi.org/10.1109/TGRS.2011.2160644

Porter, M., Hove, J. V., Barlow, P., Froese, C., Bunce, C., Skirrow, R., Lewycky, D., & Bobrowsky, P. (2019). The estimated economic impacts of prairie landslides in wester Canada. *72nd Canadian Geotechnical Society Conference*. Geo St. John’s.

Porter, M., Savigny, K., Keegan, T., Bunce, C., & McKay, C. (2002). *Controls on stability of the Thompson River landslides*. The 55th Conference of Canadian Geotechnical Society.

Rajaby, E., & Sayedi, S. M. (2022). A structured review of sparse fast Fourier transform algorithms. *Digital Signal Processing*, *123*, 103403. https://doi.org/10.1016/j.dsp.2022.103403

Reid, M. E., Godt, J. W., LaHusen, R. G., Slaughter, S. L., Badger, T. C., Collins, B. D., Schulz, W. H., Baum, R. L., Coe, J. A., Harp, E. L., Schmidt, K. M., Iverson, R. M., Smith, J. B., Haugerud, R. A., & George, D. L. (2021). When hazard avoidance is not an option: Lessons learned from monitoring the postdisaster Oso landslide, USA. *Landslides*, *18*(9), 2993–3009. https://doi.org/10.1007/s10346-021-01686-6

Ren, K., Yao, X., Li, R., Zhou, Z., Yao, C., & Jiang, S. (2022). 3D displacement and deformation mechanism of deep-seated gravitational slope deformation revealed by InSAR: A case study in Wudongde Reservoir, Jinsha River. *Landslides*, *19*(9), 2159–2175. https://doi.org/10.1007/s10346-022-01905-8

Rodriguez, J., Deane, E., Hendry, M. T., Macciotta, R., Evans, T., Gräpel, C., & Skirrow, R. (2021). Practical evaluation of single-frequency dGNSS for monitoring slow-moving landslides. *Landslides*, *18*(11), 3671–3684. https://doi.org/10.1007/s10346-021-01737-y

Rodriguez, J., Hendry, M., Macciotta, R., & Evans, T. (2018). *Cost-effective landslide monitoring GPS system: Characteristics, implementation, and results*. GeoHazards7.

Rodriguez, J., Macciotta, R., Hendry, M., Edwards, T., & Evans, T. (2017). *Slope hazards and risk engineering in the Canadian railway network through the Cordillera*. 163–168.

Rodriguez, J., Macciotta, R., Hendry, M. T., Roustaei, M., Gräpel, C., & Skirrow, R. (2020). UAVs for monitoring, investigation, and mitigation design of a rock slope with multiple failure mechanisms—A case study. *Landslides*, *17*(9), 2027–2040. https://doi.org/10.1007/s10346-020-01416-4

Roque, D., Lima, J. N., Perissin, D., Falcão, A. P., Lemos, J. V., & Fonseca, A. M. (2021). Integrated InSAR and GNSS Monitoring Subsystem for an Arch Dam and Reservoir Banks. *Journal of Surveying Engineering*, *147*(3), 05021003. https://doi.org/10.1061/(ASCE)SU.1943-5428.0000361

Rose, N. D., & Hungr, O. (2007). Forecasting potential rock slope failure in open pit mines using the inverse-velocity method. *International Journal of Rock Mechanics and Mining Sciences*, *44*(2), 308–320. https://doi.org/10.1016/j.ijrmms.2006.07.014

Rotheram-Clarke, D., Huntley, D., LeSueur, P., Cocking, R., Joseph, J., & MacLeod, R. (2022). *Direct comparison of RADARSAR Constellation Mission InSAR, UAD derived point cloud comparison & RTK GNSS deformation monitoring GNSS deformation monitoring at North*

Slide, Thompson River Valley, British Columbia. The 75th Conference of Canadian Geotechnical Society.

Rousseeuw, P. J., & Hubert, M. (2011). Robust statistics for outlier detection. *WIREs Data Mining and Knowledge Discovery*, *1*(1), 73–79. https://doi.org/10.1002/widm.2

Roy, P., Martha, T. R., Khanna, K., Jain, N., & Kumar, K. V. (2022). Time and path prediction of landslides using InSAR and flow model. *Remote Sensing of Environment*, *271*, 112899. https://doi.org/10.1016/j.rse.2022.112899

Saito, M. (1969). *Forecasting time of slope failure by tertiary creep*. *2*, 677–683.

Saito, M., & Uezawa, M. (1961). *Failure of soil due to creep*. *1*, 315–318.

Salgado, C. M., Azevedo, C., Proença, H., & Vieira, S. M. (2016). Noise Versus Outliers. In Mit Critical Data, *Secondary Analysis of Electronic Health Records* (pp. 163–183). Springer International Publishing. https://doi.org/10.1007/978-3-319-43742-2_14

Samsonov, S., Dille, A., Dewitte, O., Kervyn, F., & d’Oreye, N. (2020). Satellite interferometry for mapping surface deformation time series in one, two and three dimensions: A new method illustrated on a slow-moving landslide. *Engineering Geology*, *266*, 105471. https://doi.org/10.1016/j.enggeo.2019.105471

Samsonov, S., Gonzalez, P. J., Tiampo, K., & d’Oreye, N. (2013). Spatio-temporal analysis of ground deformation occurring near Rice Lake, Saskatchewan, and observed by Radarsat-2 DInSAR during 2008–2011. *Canadian Journal of Remote Sensing*, *39*(1), 27–33. https://doi.org/10.5589/m13-005

Samsonov, S., & Tiampo, K. (2006). Analytical Optimization of a DInSAR and GPS Dataset for Derivation of Three-Dimensional Surface Motion. *IEEE Geoscience and Remote Sensing Letters*, *3*(1), 107–111. https://doi.org/10.1109/LGRS.2005.858483

Samsonov, S., Tiampo, K., Rundle, J., & Li, Z. (2007). Application of DInSAR-GPS Optimization for Derivation of Fine-Scale Surface Motion Maps of Southern California. *IEEE Transactions on Geoscience and Remote Sensing*, *45*(2), 512–521. https://doi.org/10.1109/TGRS.2006.887166

Sauer, E. K. (1984). A landslide in clay shale in the north saskatchewan river valley, canada. *Engineering Geology*, *20*(4), 279–300. https://doi.org/10.1016/0013-7952(84)90057-7

Savitzky, Abraham., & Golay, M. J. E. (1964). Smoothing and Differentiation of Data by Simplified Least Squares Procedures. *Analytical Chemistry*, *36*(8), 1627–1639. https://doi.org/10.1021/ac60214a047

Scammell, P. (2013). *Evaluation of Gardiner Dam's ongoing movement*. University of Saskatchewan.

Scammell, P., Sharma, S., & Johnson, R. (2012). *Evaluation of on-going displacement of Gardiner Dam embankment*. The Canadian Dam Association Annual Conference.

Schafer, M. B. (2016). *Kinematics and Controlling Mechanics of Slow-moving Ripley Landslide*. University of Alberta.

Schafer, R. (2011). What Is a Savitzky-Golay Filter? [Lecture Notes]. *IEEE Signal Processing Magazine*, *28*(4), 111–117. https://doi.org/10.1109/MSP.2011.941097

Schlögl, M., Gutjahr, K., & Fuchs, S. (2022). The challenge to use multi-temporal InSAR for landslide early warning. *Natural Hazards*, *112*(3), 2913–2919. https://doi.org/10.1007/s11069-022-05289-9

Schuster, R. L. (2006). *Interaction of dams and landslides: Case studies and mitigation*. U.S. Geological Survey.

Schuster, R. L., & Highland, L. M. (2001). *Socioeconomic and environmental impacts of landslides in the Western Hemisphere* (01–276). U.S. Geological Survey.

Scoppettuolo, M. R., Cascini, L., & Babilio, E. (2020). Typical displacement behaviours of slope movements. *Landslides*, *17*(5), 1105–1116. https://doi.org/10.1007/s10346-019-01327-z

Segalini, A., Valletta, A., & Carri, A. (2018). Landslide time-of-failure forecast and alert threshold assessment: A generalized criterion. *Engineering Geology*, *245*, 72–80. https://doi.org/10.1016/j.enggeo.2018.08.003

Sharifi, S., Abrishami, S., Dias, D., & Dastpak, P. (2022). Behavior of Axially and Eccentrically Loaded Trapezoidal Shell Footings Resting on a Granular Assembly. *International Journal of Geomechanics*, *22*(8), 04022119. https://doi.org/10.1061/(ASCE)GM.1943-5622.0002442

Sharifi, S., Hendry, M., & Macciotta, R. (2022). *InSAR time-series displacement analysis on the Oldman River Dam, southern Alberta*. The 8th GeoHazards Conference of Canadian Geotechnica Society.

Sharifi, S., Hendry, M. T., Macciotta, R., & Evans, T. (2022). Evaluation of filtering methods for use on high-frequency measurements of landslide displacements. *Natural Hazards and Earth System Sciences*, *22*(2), 411–430. https://doi.org/10.5194/nhess-22-411-2022

Sharifi, S., Macciotta, R., & Hendry, M. (2021). *Reduction of stochastic noise in instrumentation readings: A comparison of simple moving average and Savitzky-Golay filters*. The 74th Canadian Geotechnical Society Conference.

Sharifi, S., Macciotta, R., & Hendry, M. T. (2022). Algorithms to enhance detection of landslide acceleration moment and time-to-failure forecast using time-series displacements. *Engineering Geology*, *309*, 106832. https://doi.org/10.1016/j.enggeo.2022.106832

Shi, X., Xu, Q., Zhang, L., Zhao, K., Dong, J., Jiang, H., & Liao, M. (2019). Surface displacements of the Heifangtai terrace in Northwest China measured by X and C-band InSAR observations. *Engineering Geology*, *259*, 105181. https://doi.org/10.1016/j.enggeo.2019.105181

Shi, X., Zhang, L., Zhou, C., Li, M., & Liao, M. (2018). Retrieval of time series three-dimensional landslide surface displacements from multi-angular SAR observations. *Landslides*, *15*(5), 1015–1027. https://doi.org/10.1007/s10346-018-0975-3

Simons, M., & Rosen, P. A. (2007). Interferometric Synthetic Aperture Radar Geodesy. In *Treatise on Geophysics* (pp. 391–446). Elsevier. https://doi.org/10.1016/B978-044452748-6.00059-6

Sinclair, B. J., Hartmaier, H. H., Davachi, M. M., & Peters, J. E. (1989). *Geology of the Oldman River Dam Site*. The 30th CANCOLD Annual Meeting.

Smith, B., & Sandwell, D. (2003). Coulomb stress accumulation along the San Andreas Fault system: COULOMB STRESS ALONG THE SAN ANDREAS FAULT. *Journal of Geophysical Research: Solid Earth*, *108*(B6). https://doi.org/10.1029/2002JB002136

Smith, S. W. (2013). *Digital signal processing: A practical guide for engineers and scientists*. Newnes.

Soltanieh, A., & Macciotta, R. (2022a). Updated Understanding of the Ripley Landslide Kinematics Using Satellite InSAR. *Geosciences*, *12*(8), 298. https://doi.org/10.3390/geosciences12080298

Soltanieh, A., & Macciotta, R. (2022b). Updated Understanding of the Thompson River Valley Landslides Kinematics Using Satellite InSAR. *Geosciences*, *12*(10), 359. https://doi.org/10.3390/geosciences12100359

Stanton, R. B. (1898). The Great Land-Slides on the Canadian Pacific Railway in British Columbia.(Includes Plate and Appendix). *Minutes of the Proceedings of the Institution of Civil Engineers*, *132*(1898), 1–20. https://doi.org/10.1680/imotp.1898.19167

Sun, Q., Hu, J., Zhang, L., & Ding, X. (2016). Towards Slow-Moving Landslide Monitoring by Integrating Multi-Sensor InSAR Time Series Datasets: The Zhouqu Case Study, China. *Remote Sensing*, *8*(11), 908. https://doi.org/10.3390/rs8110908

Sun, Q., Zhang, L., Ding, X. L., Hu, J., Li, Z. W., & Zhu, J. J. (2015). Slope deformation prior to Zhouqu, China landslide from InSAR time series analysis. *Remote Sensing of Environment*, *156*, 45–57. https://doi.org/10.1016/j.rse.2014.09.029

Tan, Q., Wang, P., Hu, J., Zhou, P., Bai, M., & Hu, J. (2020). The application of multi-sensor target tracking and fusion technology to the comprehensive early warning information extraction of landslide multi-point monitoring data. *Measurement*, *166*, 108044. https://doi.org/10.1016/j.measurement.2020.108044

Tappenden, K. M., & Skirrow, R. K. (2020). Vision for Geotechnical Asset Management at Alberta Transportation. *73rd Canadian Geotechnical Society Conference*. GeoVirtual.

Tarighat, F., Foroughnia, F., & Perissin, D. (2021). Monitoring of Power Towers' Movement Using Persistent Scatterer SAR Interferometry in South West of Tehran. *Remote Sensing*, *13*(3), 407. https://doi.org/10.3390/rs13030407

Taunk, K., De, S., Verma, S., & Swetapadma, A. (2019). *A brief review of nearest neighbor algorithm for learning and classification*. The 2019 International Conference on Intelligent Computing and Control Systems.

Thiebes, B., Bell, R., Glade, T., Jäger, S., Mayer, J., Anderson, M., & Holcombe, L. (2014). Integration of a limit-equilibrium model into a landslide early warning system. *Landslides*, *11*(5), 859–875. https://doi.org/10.1007/s10346-013-0416-2

Thirugnanam, H., Ramesh, M. V., & Rangan, V. P. (2020). Enhancing the reliability of landslide early warning systems by machine learning. *Landslides*, *17*(9), 2231–2246. https://doi.org/10.1007/s10346-020-01453-z

Tofani, V., Raspini, F., Catani, F., & Casagli, N. (2013). Persistent Scatterer Interferometry (PSI) Technique for Landslide Characterization and Monitoring. *Remote Sensing*, *5*(3), 1045–1065. https://doi.org/10.3390/rs5031045

Vaziri, A., Moore, L., & Ali, H. (2010). Monitoring systems for warning impending failures in slopes and open pit mines. *Natural Hazards*, *55*(2), 501–512. https://doi.org/10.1007/s11069-010-9542-5

Voight, B. (1988). A method for prediction of volcanic eruptions. *Nature*, *332*(6160), 125–130. https://doi.org/10.1038/332125a0

Wang, G. (2011). GPS Landslide Monitoring: Single Base vs. Network Solutions — A case study based on the Puerto Rico and Virgin Islands Permanent GPS Network. *Journal of Geodetic Science*, *1*(3). https://doi.org/10.2478/v10156-010-0022-3

Wang, S., Wang, J., Wu, W., Cui, D., Su, A., & Xiang, W. (2020). Creep properties of clastic soil in a reactivated slow-moving landslide in the Three Gorges Reservoir Region, China. *Engineering Geology*, *267*, 105493. https://doi.org/10.1016/j.enggeo.2020.105493

Wang, Y., Dong, J., Zhang, L., Zhang, L., Deng, S., Zhang, G., Liao, M., & Gong, J. (2022). Refined InSAR tropospheric delay correction for wide-area landslide identification and monitoring. *Remote Sensing of Environment*, *275*, 113013. https://doi.org/10.1016/j.rse.2022.113013

Wang, Y., Liu, D., Dong, J., Zhang, L., Guo, J., Liao, M., & Gong, J. (2021). On the applicability of satellite SAR interferometry to landslide hazards detection in hilly areas: A case study of Shuicheng, Guizhou in Southwest China. *Landslides*, *18*(7), 2609–2619. https://doi.org/10.1007/s10346-021-01648-y

Wang, Z., Yu, S., Tao, Q., Liu, G., Hao, H., Wang, K., & Zhou, C. (2018). A method of monitoring three-dimensional ground displacement in mining areas by integrating multiple InSAR methods. *International Journal of Remote Sensing*, *39*(4), 1199–1219. https://doi.org/10.1080/01431161.2017.1399473

Wasowski, J., & Bovenga, F. (2014). Investigating landslides and unstable slopes with satellite Multi Temporal Interferometry: Current issues and future perspectives. *Engineering Geology*, *174*, 103–138. https://doi.org/10.1016/j.enggeo.2014.03.003

Wasowski, J., & Pisano, L. (2020). Long-term InSAR, borehole inclinometer, and rainfall records provide insight into the mechanism and activity patterns of an extremely slow urbanized landslide. *Landslides*, *17*(2), 445–457. https://doi.org/10.1007/s10346-019-01276-7

Woods, A., Hendry, M. T., Macciotta, R., Stewart, T., & Marsh, J. (2020). GB-InSAR monitoring of vegetated and snow-covered slopes in remote mountainous environments. *Landslides*, *17*(7), 1713–1726. https://doi.org/10.1007/s10346-020-01408-4

Woods, A., Macciotta, R., Hendry, M. T., Stewart, T., & Marsh, J. (2021). Updated understanding of the deformation characteristics of the Checkerboard Creek rock slope through GB-InSAR monitoring. *Engineering Geology*, *281*, 105974. https://doi.org/10.1016/j.enggeo.2020.105974

Yang, Z. F., Li, Z. W., Zhu, J. J., Preusse, A., Yi, H. W., Wang, Y. J., & Papst, M. (2017). An Extension of the InSAR-Based Probability Integral Method and Its Application for Predicting 3-D Mining-Induced Displacements Under Different Extraction Conditions. *IEEE Transactions on Geoscience and Remote Sensing*, *55*(7), 3835–3845. https://doi.org/10.1109/TGRS.2017.2682192

Yao, W., Zeng, Z., Lian, C., & Tang, H. (2015). Training enhanced reservoir computing predictor for landslide displacement. *Engineering Geology*, *188*, 101–109. https://doi.org/10.1016/j.enggeo.2014.11.008

Yao, Z., Xie, J., Tian, Y., & Huang, Q. (2019). Using Hampel Identifier to Eliminate Profile-Isolated Outliers in Laser Vision Measurement. *Journal of Sensors*, *2019*, 1–12. https://doi.org/10.1155/2019/3823691

Yi, Z., Xingmin, M., Allesandro, N., Tom, D., Guan, C., Colm, J., Yuanxi, L., & Xiaojun, S. (2022). Characterization of pre-failure deformation and evolution of a large earthflow using InSAR monitoring and optical image interpretation. *Landslides*, *19*(1), 35–50. https://doi.org/10.1007/s10346-021-01744-z

Yin, Y., Wang, H., Gao, Y., & Li, X. (2010). Real-time monitoring and early warning of landslides at relocated Wushan Town, the Three Gorges Reservoir, China. *Landslides*, *7*(3), 339–349. https://doi.org/10.1007/s10346-010-0220-1

Yoshizawa, T., Hirobayashi, S., & Misawa, T. (2011). Noise reduction for periodic signals using high-resolution frequency analysis. *EURASIP Journal on Audio, Speech, and Music Processing*, *2011*(1), 5. https://doi.org/10.1186/1687-4722-2011-426794

Zavodni, Z. M., & Broadbent, C. D. (1978). *Slope Failure Kinematics*. The 19th U.S. Symposium on Rock Mechanics (USRMS).

Zhang, J., Wang, Z. P., Zhang, G. D., & Xue, Y. D. (2020). Probabilistic prediction of slope failure time. *Engineering Geology*, *271*, 105586. https://doi.org/10.1016/j.enggeo.2020.105586

Zhang, W., Xiao, R., Shi, B., Zhu, H., & Sun, Y. (2019). Forecasting slope deformation field using correlated grey model updated with time correction factor and background value optimization. *Engineering Geology*, *260*, 105215. https://doi.org/10.1016/j.enggeo.2019.105215

Zhang, Y., Ma, H., & Yu, Z. (2021). Application of the method for prediction of the failure location and time based on monitoring of a slope using synthetic aperture radar. *Environmental Earth Sciences*, *80*(21), 706. https://doi.org/10.1007/s12665-021-09989-6

Zhang, Y., Meng, X., Jordan, C., Novellino, A., Dijkstra, T., & Chen, G. (2018). Investigating slow-moving landslides in the Zhouqu region of China using InSAR time series. *Landslides*, *15*(7), 1299–1315. https://doi.org/10.1007/s10346-018-0954-8

Zhang, Y., Tang, J., He, Z., Tan, J., & Li, C. (2021). A novel displacement prediction method using gated recurrent unit model with time series analysis in the Erdaohe landslide. *Natural Hazards*, *105*(1), 783–813. https://doi.org/10.1007/s11069-020-04337-6

Zhou, C., Cao, Y., Hu, X., Yin, K., Wang, Y., & Catani, F. (2022). Enhanced dynamic landslide hazard mapping using MT-InSAR method in the Three Gorges Reservoir Area. *Landslides*, *19*(7), 1585–1597. https://doi.org/10.1007/s10346-021-01796-1

Zhou, C., Yin, K., Cao, Y., & Ahmed, B. (2016). Application of time series analysis and PSO–SVM model in predicting the Bazimen landslide in the Three Gorges Reservoir, China. *Engineering Geology*, *204*, 108–120. https://doi.org/10.1016/j.enggeo.2016.02.009

Zhou, X.-P., Liu, L.-J., & Xu, C. (2020). A modified inverse-velocity method for predicting the failure time of landslides. *Engineering Geology*, *268*, 105521. https://doi.org/10.1016/j.enggeo.2020.105521

Zhu, W., Zhang, Q., Ding, X., Zhao, C., Yang, C., Qu, F., & Qu, W. (2014). Landslide monitoring by combining of CR-InSAR and GPS techniques. *Advances in Space Research*, *53*(3), 430–439. https://doi.org/10.1016/j.asr.2013.12.003

Zhu, Y., Yao, X., Yao, L., Zhou, Z., Ren, K., Li, L., Yao, C., & Gu, Z. (2022). Identifying the Mechanism of Toppling Deformation by InSAR: A Case Study in Xiluodu Reservoir, Jinsha River. *Landslides*, *19*(10), 2311–2327. https://doi.org/10.1007/s10346-022-01908-5

Zimek, A., & Filzmoser, P. (2018). There and back again: Outlier detection between statistical reasoning and data mining algorithms. *WIREs Data Mining and Knowledge Discovery*, *8*(6). https://doi.org/10.1002/widm.1280